Reconstructing seawater carbonate chemistry using foraminiferal B/Ca

Yuhao Dai

A thesis submitted for the degree of Doctor of Philosophy of
The Australian National University

Research School of Earth Sciences, ANU
June 2018

Declaration

I, Yuhao Dai, declare that this thesis is my original research performed during the academic program towards the degree of Doctor of Philosophy of The Australian National University. This thesis does not incorporate any material either previously submitted for a degree or diploma at any university, previously published or written by another person, except where due reference is made in the text.

Acknowledgments

The research presented in this thesis could not have been done without the support from many people. I would like to acknowledge their help here.

I would like to express my sincere gratitude to Jimin Yu, my PhD supervisor, for offering me the opportunity to work on the unique samples presented in this thesis, for his patience, motivation, and immense knowledge. His guidance helped me in all the time of research and writing of this thesis. Besides my supervisor, I also want to thank other members on my supervisory panel, Steve Eggins, Michael Ellwood, and Eelco Rohling, for their advices and insightful comments, and for bringing different perspectives to my project.

My gratitude also goes to people who helped me with my lab work. Thanks to William Howard and Bradley Opdyke for their assistance in organizing sampling of two sediment cores used in this thesis. Thank you Fei Zhang and Zhangdong Jin for teaching me how to identify and pick foraminifera. Thank you Les Kinsley for helping tune and fix the ICP-MS. Thank you Laura Rodriguez-Sanz for showing me how to prepare samples for stable isotopes. I thank my officemates, Jiade, Katie, and Pujiao, for many discussions and their help with lab works. I thank fellow OCG students and postdocs, especially Gianluca, Kate, and Oscar for many stimulating discussions.

This research was financially made possible with support from the Australian Research Council Discovery Grants (DP140101393) and Future Fellowship (FT140100993), both awarded to Jimin Yu. I am grateful to the Research School of Earth Sciences for granting me the International Postgraduate Research Scholarship and the ANU Research Supplementary Scholarship, which gave me the opportunity to pursue a PhD at the ANU. I am also very grateful for the financial support from Research School of Earth Sciences and the Vice Chancellor's travel grant, which enabled me to present my research at international conferences.

Last but not least, I would thank my family and friends for encouraging

and supporting me throughout my pursuit of PhD.

Abstract

Planktonic B/Ca holds promise of reconstructing the surface seawater carbonate chemistry, which is linked to the past levels of atmospheric partial pressure of CO_2. However, it is still not clear to what extent the carbonate chemistry control on planktonic B/Ca is complicated by physiological activities of foraminifera. In this thesis, the environmental controls on B/Ca in two planktonic foraminiferal species, *Globigerinoides ruber* (white) and *Globigerinoides sacculifer* (without final sac-like chamber), are examined using core-top samples from the Atlantic Ocean. For an accurate estimation of the ambient calcification environments, the calcification depths and seasonality of the studied species at these core-top locations are determined by planktonic Mg/Ca. The dissolution effect on B/Ca, which is evident from planktonic B/Ca data from three depth transects, proves to have little impact on the interpretation of planktonic B/Ca data from the Atlantic core-tops. While the carbonate chemistry control on planktonic B/Ca can be detected from these core-top data, a strong calcification rate control on planktonic B/Ca is demonstrated by the correlation between B/Ca and Sr/Ca, where Sr/Ca is employed as an indicator of the calcification rate. This calcification rate control on planktonic B/Ca complicates the direct link between planktonic B/Ca and seawater carbonate chemistry. Nevertheless, based on the different responses of B/Ca in the two studied species to the calcification rate, it is possible that B/Ca in some species are less susceptible to this influence, and thus can be employed for carbonate chemistry reconstructions.

Benthic B/Ca is a recently developed quantitative proxy for deepwater carbonate ion concentration ($[CO_3^{2-}]$). In this thesis, deepwater $[CO_3^{2-}]$ variations during the last 150 thousand years are reconstructed using two cores from the deep Southwestern Pacific, a critical but not fully investigated region to regulate the carbon inventory in the deep ocean. Since Marine Isotope Stage (MIS) 5a, the deep the SW Pacific $[CO_3^{2-}]$ varied in concert with benthic

carbon isotopes ($\delta^{13}C_b$). These covariations, on the timescale of ~10 kyr, are similar to those observed in the deep Atlantic. This suggests that the deep SW Pacific [CO_3^{2-}] could be affected by changes in the Atlantic Overturning Circulation and the biological pump. However, the deep SW Pacific [CO_3^{2-}] showed little change during Termination II (T II), despite that variations of $\delta^{13}C_b$, neodymium isotopes (ε_{Nd}), and foraminifer-bound nitrogen isotopes ($\delta^{15}N_{pf}$) were similar to those during Termination I (T I). This difference is interpreted as the result of coral reef regrowth on continental shelves, which decreased the whole ocean [CO_3^{2-}] and counteracted the [CO_3^{2-}] increase due to the influences from Atlantic Overturning Circulation and the biological pump changes during T II.

Contents

List of Figures

List of Tables

Chapter 1

Introduction

The atmospheric partial pressure of CO_2 (pCO_2) measured in air bubbles from ice cores fluctuates approximately between 180 ppm and 280 ppm (Petit et al., 1999; Monnin and Barnola, 2001; Lüthi et al., 2008), and is strongly correlated with the Antarctic air temperature over the last 800 kyr (Jouzel et al., 2007; Lüthi et al., 2008). Processes in the ocean are acknowledged to be responsible for the fluctuation of atmospheric pCO_2 (Broecker, 1982; Sigman and Boyle, 2000; Sigman et al., 2010), although the detailed mechanisms are still emerging. Proxies based on B/Ca in foraminiferal shells are important tools to reconstruct seawater carbonate chemistry contributing to improving our understanding about the carbon cycle. Planktonic B/Ca hold promise of reconstructing the surface seawater carbonate chemistry. As surface ocean is directly in contact with the atmosphere, surface seawater carbonate chemistry is closely linked to the atmospheric pCO_2 level. Planktonic B/Ca can thus be used to estimate atmospheric pCO_2 beyond the age range covered by ice core records (*e.g.*, Allen et al., 2012; Penman et al., 2014; Babila et al., 2016). Within the age range covered by ice core records, reconstruction of surface seawater carbonate chemistry at key locations can be potentially used to reconstruct outgassing of CO_2 from the ocean. Benthic B/Ca can help reconstruct deep-water $[CO_3^{2-}]$ (Yu and Elderfield, 2007). Deep-water $[CO_3^{2-}]$ is directly linked to the carbon inventory in the deep ocean (*e.g.*, Yu and

Elderfield, 2007; Yu et al., 2010b; Allen et al., 2015; Gottschalk et al., 2015).

In this introduction, backgrounds related to seawater carbonate chemistry and boron chemistry are summarized. The outline of this thesis is then presented.

1.1 Seawater carbonate chemistry

There are three primary inorganic forms of carbon dioxide in seawater: aqueous carbon dioxide ($CO_2(aq)$), bicarbonate ion (HCO_3^-), and carbonate ion (CO_3^{2-}). At thermodynamical equilibrium, $[CO_2(aq)]$ is linked to pCO_2 following Henry's law:

$$\begin{aligned} CO_2(g) &\overset{K_0}{\rightleftharpoons} CO_2(aq), \\ K_0 &= \frac{[CO_2(aq)]}{P_{CO_2}}, \end{aligned} \tag{1.1}$$

where K_0 is CO_2 solubility coefficient in seawater. Inorganic carbonate species are linked through the following equations:

$$\begin{aligned} CO_2(aq) + H_2O \rightleftharpoons H_2CO_3 &\overset{K_1}{\rightleftharpoons} HCO_3^- + H^+ \overset{K_2}{\rightleftharpoons} CO_3^{2-} + 2H^+, \\ K_1 = \frac{[HCO_3^-][H^+]}{[CO_2]},\ K_2 &= \frac{[CO_3^{2-}][H^+]}{[HCO_3^-]}, \end{aligned} \tag{1.2}$$

where K_1 and K_2 are the first and second dissociation constants of carbonic acid, respectively. These equilibrium constants depend on temperature, pressure, and salinity in seawater. When these parameters are known, the concentrations of three carbonate species and pH can be calculated from two conservative variables: dissolved inorganic carbon (DIC) and alkalinity (ALK) (Zeebe and Wolf-Gladrow, 2001). DIC is the sum of all three dissolved inorganic carbon species in seawater:

$$DIC = [CO_2(aq)] + [HCO_3^-] + [CO_3^{2-}]. \tag{1.3}$$

ALK represents 'the excess of proton acceptors over proton donors' in seawater (Zeebe and Wolf-Gladrow, 2001), that can be defined as:

$$ALK = 2[CO_3^{2-}] + [HCO_3^-] + [B(OH)_4^-] + [OH^-] - [H^+] + minor\ components. \tag{1.4}$$

To date, these two conservative variables are difficult to estimate by proxies directly. However, boron-based proxies can help reconstruct some variables of the carbonate system.

1.2 Boron chemistry

1.2.1 Boron in seawater

Proxies based on boron in foraminiferal shells have become useful tools for reconstructing seawater carbonate chemistry. The theoretical foundation of these proxies is boron's systematics in seawater. Boron has two major dissolved species in seawater: boron acid ($B(OH)_3$) and borate ion ($B(OH)_4^-$). The relative abundances of these two species are pH-dependent (Figure 1-1A):

$$B(OH)_3 + H_2O = B(OH)_4^- + H^+. \tag{1.5}$$

This equilibrium depends on temperature, salinity, and pressure, the influences of which are all incorporated in pK_B^*, the boron disassociation constant (Dickson, 1990b). pK_B^* is 8.60 at standard surface seawater conditions (T = 25 °C, S = 34.7) (Dickson, 1990b). pK_B^* is close to pH of seawater, making changes between the two boron species sensitive to variations of carbonate chemistry. As can be seen in Figure 1-1A, the concentration of $B(OH)_4^-$ in seawater increases with increasing pH, when the total boron concentration is constant.

There are two stable isotopes of boron: ^{10}B and ^{11}B, with natural abundance of 19.82% and 80.18%, respectively (Rosman and Taylor, 1998). The

fractionation between ^{10}B and ^{11}B can be described by the following equation:

$$^{10}B(OH)_3 + {}^{11}B(OH)_4^- = {}^{11}B(OH)_3 + {}^{10}B(OH)_4^-. \quad (1.6)$$

The equilibrium constant of this reaction ($^{11-10}K_B$) is 1.0272 at 25 °C in seawater (Klochko et al., 2006), indicating that the lighter isotope (^{10}B) is enriched in $B(OH)_4^-$. As a result, δ^{11}B, which is the offset between ratios of two boron isotopes in samples and the standard material (Equation 1.7), is also pH-dependent (Figure 1-1B).

$$\delta^{11}B(‰) = \left(\frac{^{11}B/^{10}B_{sample}}{^{11}B/^{10}B_{standard}} - 1\right) \times 1000 \quad (1.7)$$

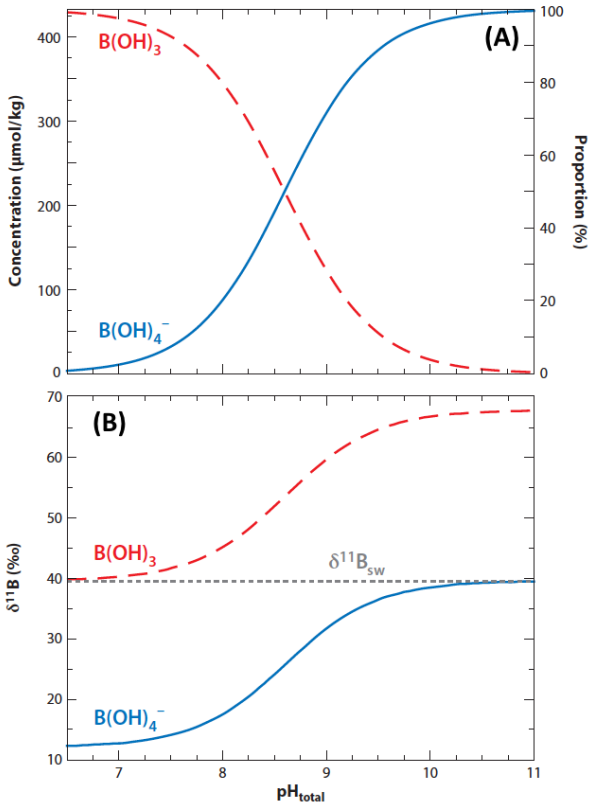

Figure 1-1: Variation in concentrations (A) and isotopic compositions (B) of $B(OH)_4^-$ and $B(OH)_3$ with pH. The compositions are calculated at standard surface seawater conditions, where T = 25 °C, S = 35, with $pK_B^* = 8.60$ (Dickson, 1990b), $^{11-10}K_B = 1.0272$ (Klochko et al., 2006), and $\delta^{11}B_{sw} = 39.61‰$ (Foster et al., 2010). This figure is from Foster and Rae (2016).

1.2.2 Incorporation of boron into $CaCO_3$

Based on varying boron concentrations in modern marine carbonates and $\delta^{11}B$ offsets between marine carbonates and seawater (Hemming and Hanson, 1992), it is proposed that $B(OH)_4^-$, the charged boron species, is predominantly incorporated into $CaCO_3$, via the following reaction:

$$CaCO_3 + B(OH)_4^- = Ca(HBO_3) + HCO_3^- + H_2O. \tag{1.8}$$

The partition coefficient between $CaCO_3$ and seawater, K_D, is defined by Equation (1.8):

$$K_D = \frac{[HBO_3^{2-}/CO_3^{2-}]_{CaCO_3}}{[B(OH)_4^-/HCO_3^-]_{seawater}} = \frac{[B/Ca]_{CaCO_3}}{[B(OH)_4^-/HCO_3^-]_{seawater}}. \tag{1.9}$$

Following the proposal of Hemming and Hanson (1992), both $\delta^{11}B$ and B/Ca of marine carbonates should be able to reflect changes in seawater carbonate chemistry.

Inorganic $CaCO_3$. The predominant incorporation of $B(OH)_4^-$ into $CaCO_3$ is supported by the pH control on both $\delta^{11}B$ and B/Ca. The correlation between $\delta^{11}B$ of inorganic $CaCO_3$ and pH is comparable to the correlation between $\delta^{11}B$ of $B(OH)_4^-$ and pH (Sanyal et al., 2000). It is also observed in inorganic $CaCO_3$ precipitation experiments that B/Ca in $CaCO_3$ increases with pH (Hemming et al., 1995; Sanyal et al., 2000; He et al., 2013; Uchikawa et al., 2015; Kaczmarek et al., 2016).

In contrast, some recent studies (Noireaux et al., 2015; Uchikawa et al., 2015) show evidence that the incorporation of boron into $CaCO_3$ is more complicated than the proposition of Hemming and Hanson (1992). $\delta^{11}B$ and B/Ca in inorganic $CaCO_3$ are both deviated from that expected from the theory of dominant $B(OH)_4^-$ incorporation. $\delta^{11}B$ in calcite was offset from that of $B(OH)_4^-$ towards the more positive values, while $\delta^{11}B$ in aragonite equals to

that of $B(OH)_4^-$ (Noireaux et al., 2015). These authors attributed to the offsets of $\delta^{11}B$ in calcite to the incorporation of $B(OH)_3$, and suggested that the incorporation of $B(OH)_3$ into $CaCO_3$ depends on the concentration of $B(OH)_3$ (Noireaux et al., 2015). Apart from the evidence from $\delta^{11}B$, B/Ca in several inorganic $CaCO_3$ precipitation experiments also suggested incorporation of both boron species (Gabitov et al., 2014; Uchikawa et al., 2015; Kaczmarek et al., 2016). A strong calcification rate control on B/Ca in inorganic $CaCO_3$ demonstrated that boron tended to be more easily incorporated into $CaCO_3$ at high precipitation rates, which is interpreted as the result of the incorporation of $B(OH)_3$ (Uchikawa et al., 2015). Incorporation of $B(OH)_3$ into calcite is consistent with the surface kinetic model for isotopic fractionation in calcite (DePaolo, 2011). According to this model, high $B(OH)_3$ concentrations or high precipitation rates (Noireaux et al., 2015; Uchikawa et al., 2015) can enhance the chance of $B(OH)_3$ being incorporated into $CaCO_3$.

Foraminiferal $CaCO_3$. The incorporation of boron into foraminiferal calcite is further complicated by physiological processes of foraminifera and symbionts. The influences of these processes on B/Ca are known as 'vital effects'. The composition of foraminiferal calcite is affected by the chemical composition of the calcifying fluid and the microenvironment (De Nooijer et al., 2014). Firstly, the chemical composition of calcifying fluid is regulated by foraminifera. One well-understood process is that foraminifera remove H^+ from the calcifying fluid to promote calcification (Zeebe and Sanyal, 2002). Secondly, within the microenvironment of the foraminifera, pH could be lowered by calcification and respiration (Zeebe et al., 1999; Wolf-Gladrow et al., 1999), and could be raised by photosynthesis of the symbiont (Bé et al., 1982; Rink et al., 1998). These changes lead to distinct boron speciation in the calcifying fluid and microenvironment from that in the ambient seawater. The different boron chemistry of the calcifying fluid and microenvironment deviates B/Ca in foraminiferal calcite from that expected from the chemistry of

the ambient seawater. The vital effect on foraminiferal B/Ca is evident from 1) inter-species difference in B/Ca and δ^{11}B (as summarized in Henehan et al. (2016)), which reflects the physiological difference of different species, and 2) intra-shell B/Ca heterogeneity (Allen et al., 2011; Branson et al., 2015; Holland et al., 2017), which possibly reflects physiological cycles of a single specimen.

1.2.3 B/Ca in foraminiferal calcite as paleoceanographic proxies

Despite the complexity in boron incorporation in foraminiferal calcite, B/Ca in both planktonic and benthic foraminiferal calcite have been proved to be useful tools for paleoceanographic reconstructions.

Planktonic B/Ca. B/Ca in planktonic foraminifera has been proposed as a proxy for surface seawater carbonate chemistry (Yu et al., 2007b; Foster, 2008; Allen et al., 2011, 2012), based on the proposal that $B(OH)_4^-$ is the only species incorporated into the calcite (Hemming and Hanson, 1992; Sanyal et al., 2000). Strong correlations between B/Ca and $\frac{[B(OH)_4^-]}{[HCO_3^-]}$ have been observed in core-top studies for *Globigerina bulloides* and *Globorotalia inflata* (Yu et al., 2007b) and in culture experiments for *Orbulina universa*, *Globigerinoides ruber* (pink), and *Globigerinoides sacculifer* (with the sac-like chamber) (Allen et al., 2011, 2012). These correlations are the foundation of the use of planktonic B/Ca as a proxy for surface seawater carbonate chemistry. Nevertheless, other controls on planktonic B/Ca, *e.g.*, calcification rate and vital effect, have also been identified (Babila et al., 2014; Henehan et al., 2015; Salmon et al., 2016). These controls sometimes overwrite the influence of carbonate chemistry on B/Ca (Babila et al., 2014; Henehan et al., 2015; Salmon et al., 2016). To establish planktonic B/Ca as a reliable proxy, knowledge about competing controls on planktonic B/Ca is needed.

Benthic B/Ca. B/Ca in two epifaunal benthic foraminifera *Cibicidoides wuellersorfi* and *Cibicidoides mundulus* have strong correlations with bottom water carbonate saturation state ($\Delta[CO_3^{2-}]$), defined as the difference between *in situ* $[CO_3^{2-}]$ and the saturated $[CO_3^{2-}]$ of calcite (Figure 1-2). This strong empirical correlation is supported by large numbers of core-tops from different ocean basins (Yu and Elderfield, 2007; Rae et al., 2011; Raitzsch et al., 2011; Brown et al., 2011; Yu et al., 2013) (Figure 1-2). Although the reason for the correlations of B/Ca in *C. wuellersorfi* and *C.mundulus* with $\Delta[CO_3^{2-}]$ remains to be investigated, benthic B/Ca is a useful tool for deepwater carbonate chemistry reconstruction (*e.g.*, Yu et al., 2010b, 2014, 2016; Allen et al., 2015; Gottschalk et al., 2015). Compared with $\delta^{11}B$, benthic B/Ca permits consistent reconstructions requiring fewer shells (Yu et al., 2010b).

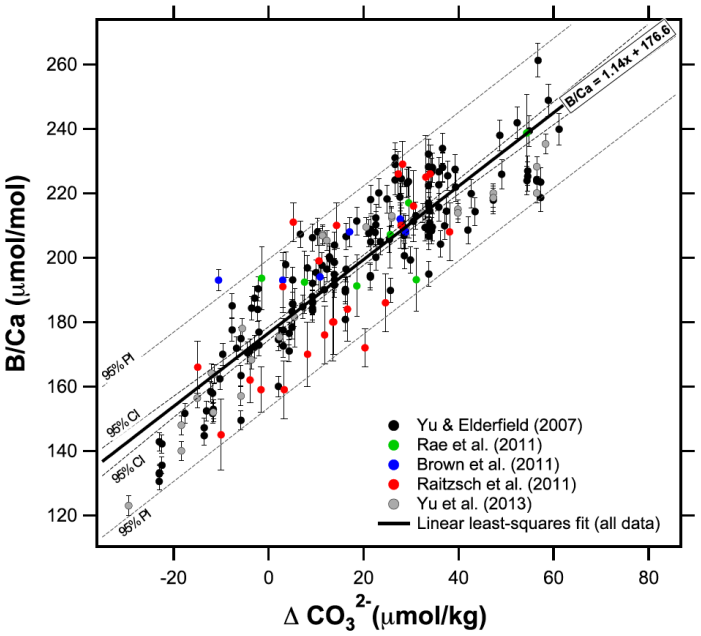

Figure 1-2: Calibration of B/Ca in *C. wuellerstorfi* as a proxy for deepwater $\Delta[CO_3^{2-}]$. This figure is from Allen et al. (2015). Core-top data are from (Yu and Elderfield, 2007; Rae et al., 2011; Raitzsch et al., 2011; Brown et al., 2011; Yu et al., 2013).

Dissolution effect. Partial dissolution can potentially influence the original B/Ca in foraminiferal shells, similar to other trace element to calcium ratios (Russell et al., 1994; Brown and Elderfield, 1996; Dekens et al., 2002; Regen-

berg et al., 2006). No dissolution effect has been observed for benthic B/Ca (Yu and Elderfield, 2007). However, based on existing literature, planktonic B/Ca seems to have different responses to dissolution. B/Ca in *Globigerinoides sacculifer* (Wara et al., 2003; Seki et al., 2010; Coadic et al., 2013) can be lowered by dissolution, while B/Ca in *Globorotalia inflata* is resistant to dissolution (Yu et al., 2007b). For a faithful application of planktonic B/Ca as a proxy for surface seawater carbonate chemistry, more work is needed for B/Ca in various planktonic species.

1.3 Outline of the thesis

This thesis is comprised of two parts, focusing on planktonic and benthic B/Ca, respectively. The first part of the thesis investigates environmental controls on planktonic B/Ca.

Chapter 2 focuses on the influence of dissolution on planktonic B/Ca, that may alter the original B/Ca signals recorded during growth after deposition of foraminiferal shells onto the seafloor. By investigating core-tops collected at three depth transects from different ocean basins, it is demonstrated that B/Ca in *G. ruber* (w) and *G. sacculifer* (w/o sac) can be lowered in undersaturated conditions, while B/Ca in some other species cannot. Methods to correct for such a dissolution effect on B/Ca for core-tops and downcore samples are proposed.

To more accurately estimate parameters of calcifying environments of the planktonic foraminifera, calcification depth and the seasonality of the studied species need to be specified. To this end, Chapter 3 constrains the calcification depths and seasonality of *G. ruber* (w) and *G. sacculifer* (w/o sac). This is achieved by employing a realistic dissolution correction to Mg/Ca and examining temperature sensitivities derived from Mg/Ca with hydrological data. In this way, the salinity effect on planktonic Mg/Ca is also reevaluated. A strong salinity effect on planktonic Mg/Ca is discounted.

Based on conclusions of Chapter 2 and 3, environmental controls on B/Ca in *G. ruber* (w) and *G. sacculifer* (w/o sac) are investigated in Chapter 4. Dissolution correction derived from Chapter 2 is tested to see whether it can affect the interpretation of environmental controls on B/Ca or not. Calcification depths and seasonality derived in Chapter 3 are used to estimate properties of the ambient calcifying environment. A strong carbonate chemistry control on B/Ca is observed for *G. sacculifer* (w/o sac) and partly for *G. ruber* (w), which is consistent with previous culture studies. For B/Ca in both species, a strong calcification rate control on B/Ca is observed.

The second part of the thesis addresses the deep water carbonate chemistry reconstruction using B/Ca in *C. wuellerstorfi*. Chapter 5 refines the approximation of deep water $[CO_3^{2-}]$ from DIC and ALK by examining modern hydrological data. A decrease in the sensitivity of $[CO_3^{2-}]$ to (ALK - DIC) is observed with decreasing $[CO_3^{2-}]$, which can help better quantify the carbon inventory in deep ocean from $[CO_3^{2-}]$.

In Chapter 6, the carbonate chemistry history in the deep Southwestern Pacific for the last 150 kyr is reconstructed by B/Ca in *C. wuellerstorfi* from two sediment cores. The new records are discussed in the context of published deep ocean $[CO_3^{2-}]$ records to investigate the deep ocean carbon inventory.

Chapter 2

Dissolution effect on planktonic foraminiferal B/Ca*

2.1 Introduction

It is well documented that trace element to calcium ratios of foraminiferal shells can be altered by partial dissolution on the seafloor (Russell et al., 1994; Brown and Elderfield, 1996; Dekens et al., 2002; Regenberg et al., 2006). Therefore, dissolution effects on foraminiferal shells can have crucial impacts on paleoceanographic proxies. Several studies have revealed significant dissolution effects on planktonic foraminiferal B/Ca. B/Ca in both extant and extinct species is reported to be affected by post-depositional processes on the seafloor (Wara et al., 2003; Seki et al., 2010; Coadic et al., 2013; Edgar et al., 2015). Other existing data, although limited, appear to suggest little influence of dissolution on B/Ca in some planktonic species. For example, a few core-top data from the North Atlantic show that B/Ca in *Globorotalia inflata* is resistant to dissolution (Yu et al., 2007b). For reliable reconstructions, it is necessary to evaluate post-mortem dissolution influences on B/Ca in different species. At present, available data are insufficient to fully explore the

*This chapter is modified from a published paper during the PhD project: Dai Y., Yu J. and Johnstone H. J. H. (2016) Distinct Responses of Planktonic Foraminiferal B/Ca to Dissolution on Seafloor. *Geochem. Geophys. Geosyst.*, 17, 1339-1348.

dissolution effect on B/Ca in different planktonic foraminiferal species. Before environmental controls on planktonic B/Ca are examined, dissolution effects on planktonic foraminiferal B/Ca would be evaluated. B/Ca in four planktonic foraminiferal species from core-top samples at three depth transects from the three major oceans, are measured to test whether there are species-specific dissolution effects on B/Ca in different planktonic foraminiferal species.

2.2 Materials and Methods

2.2.1 Samples

B/Ca in four planktonic species: *G. sacculifer* (w/o sac), *G. ruber* (w), *Neogloboquadrina dutertrei*, and *Pulleniatina obliquiloculata* are presented. Mg /Ca and shell weights for the samples used in this study have been previously published (Johnstone et al., 2010, 2011). These species are chosen based on their living habitats, symbiont conditions, shell wall structure and resistance to dissolution. *G. sacculifer* (w/o sac) and *G. ruber* (w) are spinose species that inhabit in the surface mixed layer, harboring dinoflagellates as symbiont (Hemleben et al., 1989), and their shells are susceptible to dissolution according to the planktonic foraminifer solubility rank of (Berger, 1970), which is based on changing species composition of planktonic foraminifera in under-saturated environment. *N.dutertrei* and P. obliquiloculata are non-spinose species living in the thermocline, harboring chrysophycophytes as symbiont, and their shells are more resistant to dissolution compared to those of *G. ruber* (w) and *G. sacculifer* (w/o sac)(Berger, 1970; Gastrich, 1987; Hemleben et al., 1989).

Foraminifera shells are from 28 core-top samples obtained from three depth transects in the Caribbean Sea, the Southwestern Indian Ocean, and the Ontong Java Plateau (Figure 2-1). All core-tops are verified to be Holocene in age, and the age difference within the Caribbean Sea and the Southwestern Indian Ocean transect is smaller than 3 kyr (Regenberg et al., 2006; Wilson et al., 2012). It is assumed that surface conditions and hence comparable chemical

compositions (*e.g.*, B/Ca and Mg/Ca) of shells before any dissolution at each transect are similar, due to the constrained geographic coverage of core-top samples. Nevertheless, it should be noted that compared to the Caribbean Sea and the Ontong Java Plateau transects, samples from the Southwestern Indian Ocean cover a wider geographic region, which could cause some variations in the initial B/Ca in foraminiferal shells. Excluding data from the Indian Ocean depth transect would not affect the conclusions.

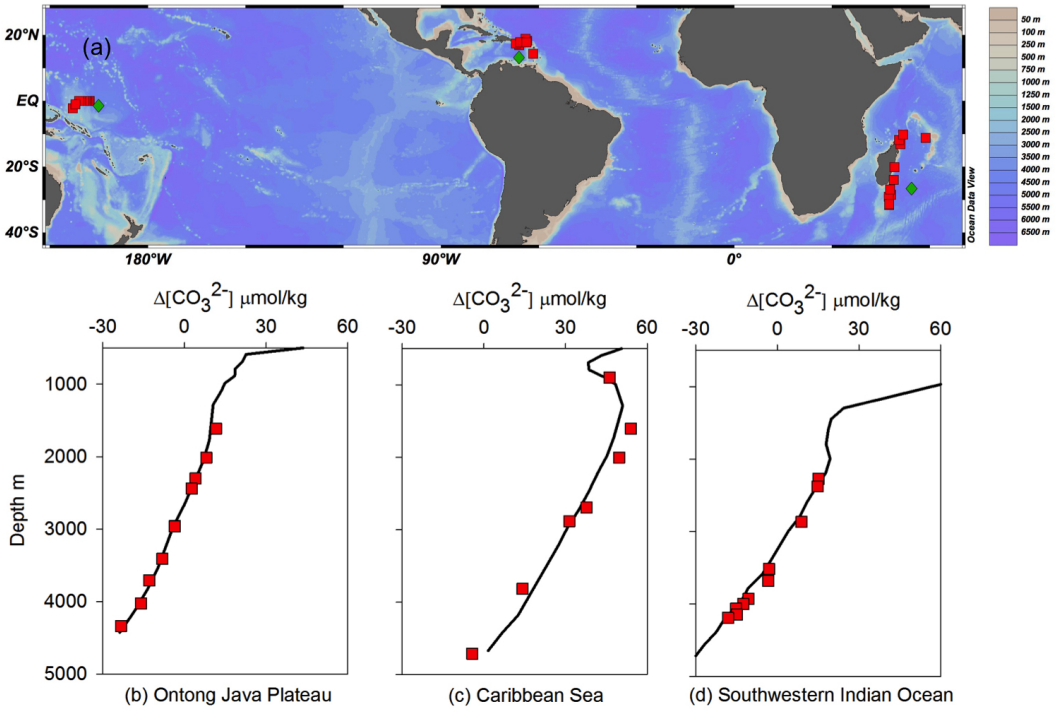

Figure 2-1: Hydrology of the core-tops. (a): Location of the core-tops (red squares) and nearby GLODAP stations (green diamonds) selected for $\Delta[CO_3^{2-}]$ profiles; (b)-(d): $\Delta[CO_3^{2-}]$ of core-tops plotted with $\Delta[CO_3^{2-}]$ depth profile of a nearby GLODAP station for three depth transects.

2.2.2 Hydrological data calculations

Bottom water calcite saturation states, $\Delta[CO_3^{2-}]$, defined by $\Delta[CO_3^{2-}] = [CO_3^{2-}]_{\text{insitu}} - [CO_3^{2-}]_{\text{saturation}}$, were estimated using data from the Global Ocean Data Analysis Project (GLODAP) database (Key et al., 2004). Anthropogenic CO_2 was removed to derive preindustrial dissolved inorganic carbon (DIC) (Sabine et al., 2004). Bottom water $[CO_3^{2-}]$ were calculated using

CO2sys.xls (Lewis et al., 1998), following the method and constants used previously (Yu and Elderfield, 2007). Our calculation reveals a large range in bottom water $\Delta[CO_3^{2-}]$ from -23 to 54 μmol/kg at the three depth transects, making these core-top samples ideal to investigate dissolution effects on B/Ca.

2.3 Results

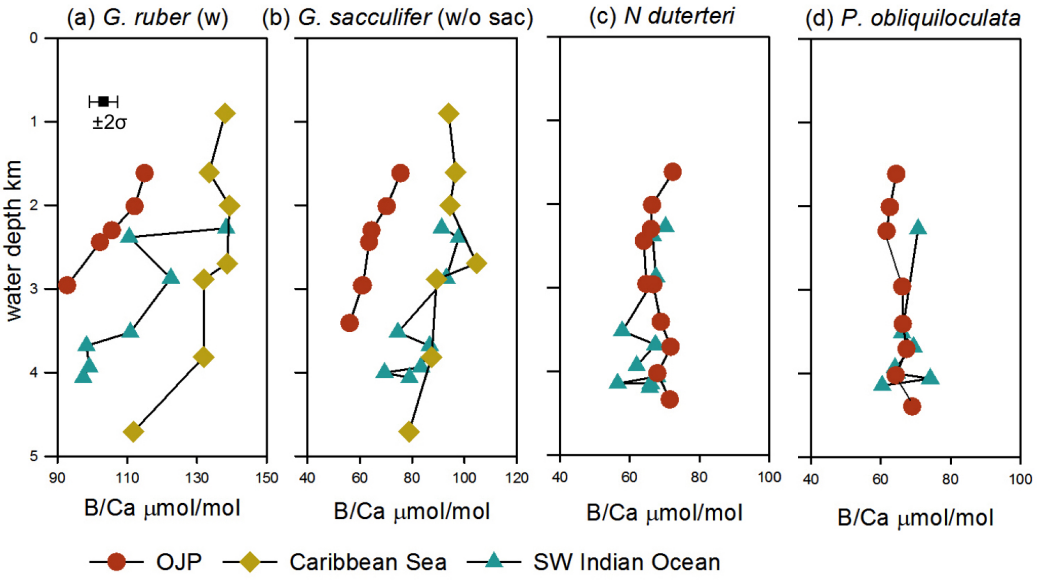

Figure 2-2: Planktonic B/Ca in four species versus water depth from three depth transects: (a) *G. ruber* (w), (b) *G. sacculifer* (w/o sac), (c) *N. dutertrei*, and (d) *P. obliquiloculata*. Error bar in (a) represents $\pm 2\sigma$ range of the consistent standard.

Figure 2-2 shows B/Ca in the four studied planktonic species from three depth transects. In the Caribbean Sea, B/Ca in *G. ruber* (w) remains roughly stable at 135 $\pm$ 4 μmol/mol above 3.8 km (1 standard deviation, the same below), and is lowered by 23 μmol/mol ($\sim$17%) from 3.8 to 5.0 km. For the Southwestern Indian and the Ontong Java Plateau transects, B/Ca in *G. ruber* (w) appears to show continuous declines throughout the entire depth ranges. B/Ca in *G. ruber* (w) decreases by 20% from 1.6 km to 3.0 km depth at the Ontong Java Plateau, and decreases by 30% from 2.3 km to 4.1 km depth in the Southwestern Indian Ocean. Large scatter in B/Ca is seen between 2 and 3 km water depth at the Indian Ocean transect, perhaps reflecting less

homogeneous surface conditions associated with these core-tops.

Similar trends are observed in *G. sacculifer* (w/o sac) from these three depth transects. At the Caribbean Sea depth transect, *G. sacculifer* (w/o sac) shows a roughly stable B/Ca of 94 ± 6 μmol/mol above 3.8 km and a 15 μmol/mol (16%) decline below this depth. B/Ca in *G. sacculifer* (w/o sac) decreases by 26% from 1.6 km to 3.7 km at the Ontong Java Plateau, and by 24% from 2.3 km to 4.1 km in the Southwestern Indian Ocean.

In contrast, *N. dutertrei* and *P. obliquiloculata* show no decreasing trend in B/Ca with water depth at the two depth transects in the Indian and Pacific Oceans. Instead, B/Ca in these two species exhibit roughly stable values. At the Ontong Java Plateau, B/Ca are 68 ± 3 μmol/mol and 65 ± 2 μmol/mol in *N. dutertrei* and *P. obliquiloculata*, respectively. In the Southwestern Indian Ocean, B/Ca are 65 ± 4 μmol/mol and 67 ± 5 μmol/mol in *N. dutertrei* and *P. obliquiloculata*, respectively.

2.4 Discussion

2.4.1 Species-specific dissolution effects on planktonic B/Ca

Previous studies have shown that dissolution in the bottom water significantly lowers shell weights and Mg/Ca of these studied species (Broecker and Clark, 2001a; De Villiers, 2005; Regenberg et al., 2006; Johnstone et al., 2010, 2011). Therefore shell weights and Mg/Ca are employed as indicators of dissolution in this study.

Figure 2-3 shows the correlations of B/Ca with shell weight and Mg/Ca. B/Ca in *G. sacculifer* (w/o sac) and *G. ruber* (w) strongly correlates with Mg/Ca and shell weight at the Ontong Java Plateau (Table 2.1, $r^2 = 0.94$ with shell weight, $r^2 = 0.60$ with Mg/Ca for *G. sacculifer* (w/o sac); $r^2 = 0.84$ with shell weight, $r^2 = 0.62$ with Mg/Ca for *G. ruber* (w)). In the Southwestern Indian Ocean, B/Ca in these species sometimes show relatively poor correlations with Mg/Ca and shell weight, possibly due to large variations in

their initial values. Despite the scatter, the overall decreasing trend of B/Ca with decreasing shell weight and Mg/Ca is similar to that seen at Ontong Java Plateau. Because variations in shell weight and Mg/Ca are thought to result from dissolution on the seafloor, the generally positive correlations shown in Figure 2-3 suggest that decline of B/Ca in *G. sacculifer* (w/o sac) and *G. ruber* (w) are also results of dissolution. This is consistent with the previous observation on *G. sacculifer* (w/o sac)(Seki et al., 2010; Coadic et al., 2013).

In contrast, B/Ca in *N. dutertrei* and *P. obliquiloculata* remains roughly invariant, although their shell weights and Mg/Ca show large changes. In the Southwestern Indian Ocean and the Ontong Java Plateau, shell weights of *N. dutertrei* and *P. obliquiloculata* decline 38-50% and 31-40% from the shallowest to deepest sites, respectively; Mg/Ca in *N. dutertrei* and *P. obliquiloculata* declines 41-61% and 53-57%, respectively. These decreases in shell weights suggest substantial dissolution of shells. No statistically significant change in B/Ca thus suggests B/Ca in these two species is not sensitive to dissolution (Figure 2-3). Similarly, dissolution appears to impose little influence on B/Ca in *G. inflata* (Yu et al., 2007b).

Our results suggest that dissolution effects on planktonic foraminiferal B/Ca are species-specific. On the one hand, B/Ca in spinose mixed layer dwellers, *G. sacculifer* (w/o sac) and *G. ruber* (w) is sensitive to dissolution. On the other hand, B/Ca in nonspinose thermocline dwellers, *G. inflata*, *N. dutertrei*, and *P. obliquiloculata* is not sensitive to dissolution.

2.4.2 Reasons for different dissolution responses

Dissolution of foraminiferal shell is a selective process, in which more soluble parts of the shell are removed first. High-Mg phase is known to be more soluble in $CaCO_3$(Brown and Elderfield, 1996; Bassinot et al., 2004; Johnstone et al., 2011), and Mg is heterogeneously distributed within shells of planktonic species (Eggins et al., 2003; Sadekov et al., 2013; Branson et al., 2013). Therefore, dissolution effects on Mg/Ca are similar in various planktonic species

Location	Slope	r^2	n	t ($\alpha = 0.05$)	P
1) B/Ca-shell weight					
	G. sacculifer (w/o sac)				
SW Indian	1.9 ± 0.3	0.86	8	6.07	<0.001
OJP	2.2 ± 0.3	0.94	7	8.85	<0.001
	G. ruber (w)				
SW Indian	2.8 ± 2.4	0.20	7	1.12	0.264
OJP	2.8 ± 0.7	0.84	6	4.58	<0.001
	N. dutertrei				
SW Indian	-0.2 ± 0.3	0.04	10	0.58	0.564
OJP	0.8 ± 0.4	0.39	10	2.26	0.024
	P. obliquiloculata				
SW Indian	0.7 ± 0.4	0.33	7	1.57	0.117
OJP	-0.3 ± 0.1	0.47	8	2.31	0.021
2) B/Ca-Mg/Ca					
	G. sacculifer (w/o sac)				
SW Indian	12.7 ± 8.8	0.26	8	1.45	0.093
OJP	17.5 ± 6.5	0.60	7	2.69	0.016
SLR[a]	15.8 ± 2.3	0.91	7	6.94	<0.001
	G. ruber (w)				
SW Indian	14.3 ± 5.0	0.62	7	2.84	0.012
OJP	24.0 ± 9.7	0.62	6	2.46	0.024
	N. dutertrei				
SW Indian	3.0 ± 3.9	0.07	10	0.76	0.233
OJP	-2.3 ± 2.7	0.09	10	0.88	0.200
	P. obliquiloculata				
SW Indian	5.2 ± 5.8	0.14	7	0.91	0.198
OJP	-3.0 ± 1.4	0.43	8	2.14	0.033
3) B/Ca-$\Delta[CO_3^{2-}]$					
	G. sacculifer (w/o sac)				
SW Indian	0.68 ± 0.17	0.74	8	4.09	0.002
OJP	0.90 ± 0.09	0.95	7	9.72	<0.001
SLR[a]	0.32 ± 0.06	0.90	5	5.20	0.002
	G. ruber (w)				
SW Indian	0.64 ± 0.28	0.57	6	2.32	0.030
OJP	1.01 ± 0.35	0.68	6	2.90	0.014

[a]: data from [Coadic et al., 2013].

Table 2.1: Summary of regression analyses.

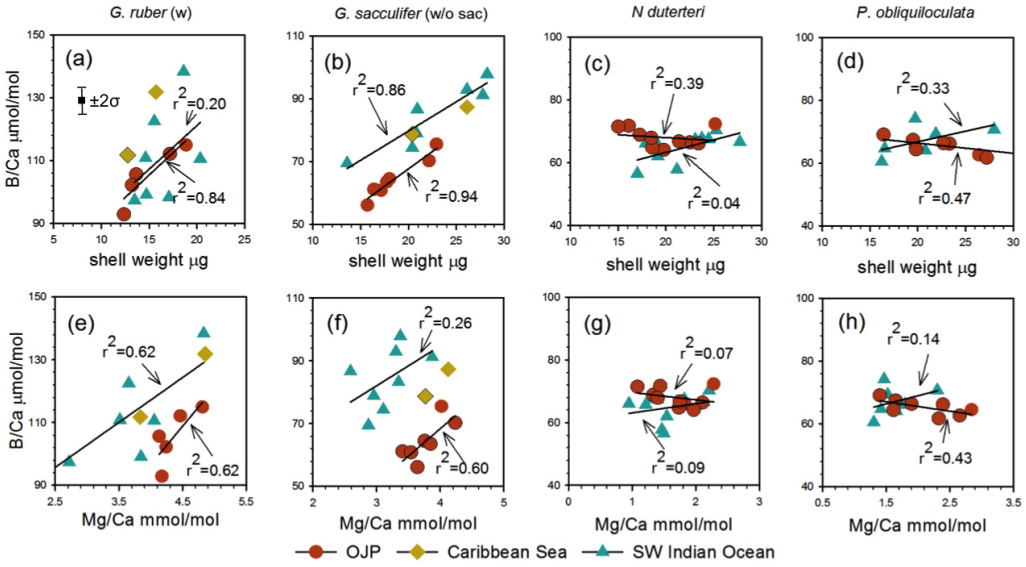

Figure 2-3: Planktonic B/Ca versus shell weights (a-d) and Mg/Ca (e-h). In the Caribbean Sea, only data with $\Delta[CO_3^{2-}]$ lower than critical $\Delta[CO_3^{2-}]$ for dissolution are shown. Solid lines show the best linear fit of data. Error bar in (a) represents $\pm 2\sigma$ range of the consistent standard. B/Ca in *G. ruber* (w) and *G. sacculifer* (w/o sac) are significantly correlated with shell weight and Mg/Ca, suggesting strong dissolution effects on B/Ca in these two species. By contrast, no significantly correlation is observed for B/Ca in *N. dutertrei* or *P. obliquiloculata*, implying negligible dissolution influence on B/Ca in these species. Shell weight data are from (Johnstone et al., 2010); Mg/Ca data are from (Johnstone et al., 2011).

(Regenberg et al., 2014). A similar dissolution effect on B/Ca in *G. sacculifer* (w/o sac) and *G. ruber* (w) to that on Mg/Ca would suggest that B is not homogeneously distributed within shell of these species and that high-B phases are preferentially removed by dissolution. Currently, the distribution of B within foraminiferal shell is investigated in two species: symbiont-bearing planktonic species *O. universa* and symbiont-bearing benthic species *Amphistegina lessonii*(Allen et al., 2011; Branson et al., 2013). B banding was observed in both species. It is reasonable to speculate that B banding is also present within shell of *G. sacculifer* (w/o sac) and *G. ruber* (w). Due to the lack of studies on symbiont-barren species, B distribution within *N. dutertrei* and *P. obliquiloculata* examined in this study cannot be speculated. Neverthe-

less, if B were preferentially removed by dissolution, minimal dissolution effect on B/Ca in these two non-spinose species would suggest that B is relatively homogeneously distributed.

The reason for different distribution patterns of boron within a foraminiferal shell might be related to symbiont activities. According to studies on δ^{11}B, the pH of microenvironment surrounding foraminifera can be elevated by symbiont activities(Hönisch et al., 2003; Zeebe et al., 2003; Rollion-Bard and Erez, 2010). When pH is raised by stronger symbiont activity, the concentration of $B(OH)_4^-$ is raised as well, so that more B could be incorporated into the foraminiferal shell. *G. sacculifer* (w/o sac) and *G. ruber* (w) have strong symbiont activities, so that diurnal changing symbiont activity can generate heterogeneity of B within the shell. Although *N. dutertrei*, and *P. obliquiloculata* also harbor algal (Gastrich, 1987), symbiont activity is weaker because they calcify at deeper depths where light intensity is much lower. Therefore, it is reasonable to infer that B is more homogeneously distributed within shell of these species.

2.4.3 Correlation with bottom water $\Delta[CO_3^{2-}]$

Bottom water $\Delta[CO_3^{2-}]$ is responsible for dissolution of planktonic foraminiferal shells on the seafloor (Berger, 1970; Brown and Elderfield, 1996). A reduction in shell weight and Mg/Ca is initiated above the calcite saturation horizon at a threshold $\Delta[CO_3^{2-}]$ value (Lohmann, 1995; Broecker et al., 1999; Johnstone et al., 2011; Regenberg et al., 2014). According to our observations, we adopt 21.3 $\pm$ 6.6 μmol/mol as the threshold $\Delta[CO_3^{2-}]$ for dissolution effect on Mg/Ca (Regenberg et al., 2014), and assume B/Ca in *G. sacculifer* (w/o sac) and *G. ruber* (w) begins to be influenced by dissolution at this $\Delta[CO_3^{2-}]$. It is notable that the threshold $\Delta[CO_3^{2-}]$ for the dissolution effect on B/Ca cannot be derived from our data set. However, as B/Ca values below chosen threshold value are evidently lowered by dissolution effect, we can investigate the sensitivity of B/Ca change to $\Delta[CO_3^{2-}]$ using available data.

Figure 2-4 shows that the sensitivity of B/Ca to $\Delta[CO_3^{2-}]$ varies be-

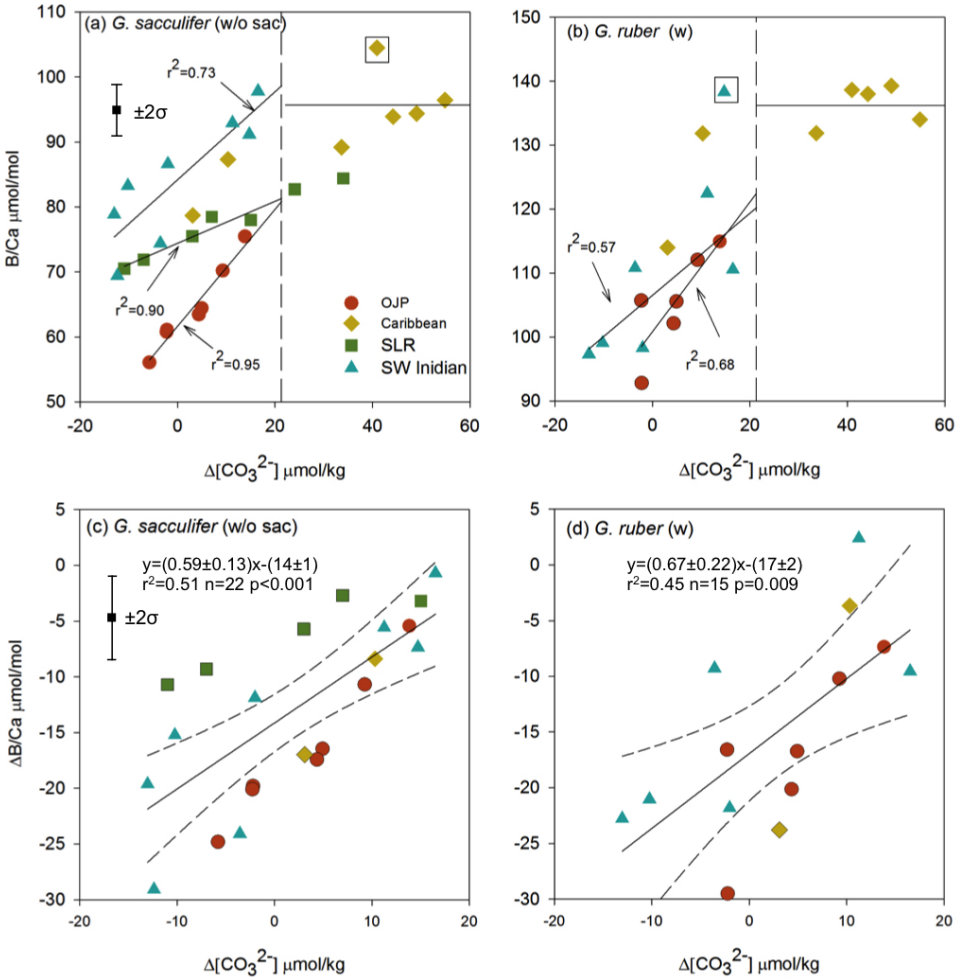

Figure 2-4: B/Ca in *G. sacculifer* (w/o sac) and *G. ruber* (w) versus bottom seawater $\Delta[CO_3^{2-}]$. Data from Sierra Leone Rise are from (Coadic et al., 2013). Panel (a) and (b) show original B/Ca versus $\Delta[CO_3^{2-}]$, questionable data points are framed within boxes. Dashed lines indicate the threshold $\Delta[CO_3^{2-}]$ value for the onset discernible dissolution effects on Mg/Ca (Regenberg et al., 2014). For the Caribbean Sea data, black solid lines show the average B/Ca above the threshold $\Delta[CO_3^{2-}]$. Regression lines of data below threshold $\Delta[CO_3^{2-}]$ are extrapolated to threshold $\Delta[CO_3^{2-}]$ to estimate initial B/Ca. Panel (c) and (d) show ΔB/Ca and $\Delta[CO_3^{2-}]$. Regression lines show average B/Ca loss rate with decreasing $\Delta[CO_3^{2-}]$. Dashed lines are the 95% confidence intervals. Error bars in (a) and (c) represent $\pm 2\sigma$ range of the consistent standard.

tween species in the different depth transects, from 0.69 to 0.90 μmol/mol per μmol/kg $\Delta[CO_3^{2-}]$ change for *G. sacculifer* (w/o sac), and 0.64 to 1.01

μmol/mol per μmol/kg $\Delta[CO_3^{2-}]$ change for *G. ruber* (w) for depth transects from this study. Compared to data from this study, B/Ca in *G. sacculifer* (w/o sac) from Sierra Leone Rise is significantly less sensitive to bottom water $\Delta[CO_3^{2-}]$ change (0.32 μmol/mol per μmol/kg $\Delta[CO_3^{2-}]$ change) (Coadic et al., 2013), which suggests dissolution effect on B/Ca might vary at different locations.

To derive sensitivity of B/Ca to $\Delta[CO_3^{2-}]$ change on a global scale, we translate the initial B/Ca to ΔB/Ca, decline of B/Ca caused by dissolution. We first define $B/Ca_{initial}$ as B/Ca at threshold $\Delta[CO_3^{2-}]$ for dissolution, assuming this is where B/Ca starts to be lowered by dissolution. Different choices of the threshold $\Delta[CO_3^{2-}]$ value to translate B/Ca change from different depth transects do not affect the conclusion on sensitivity, as shown by sensitivity tests. $B/Ca_{initial}$ is calculated by extrapolating regression line to threshold $\Delta[CO_3^{2-}]$ at the Ontong Java Plateau and the Southwestern Indian Ocean depth transects, and by averaging B/Ca above threshold $\Delta[CO_3^{2-}]$ at the Caribbean Sea depth transect. Measured B/Ca is then translated to ΔB/Ca:

$$\Delta B/Ca = B/Ca_{measured} B/Ca_{initial}. \tag{2.1}$$

Correlation between ΔB/Ca in both species from all three depth transects and $\Delta[CO_3^{2-}]$ is significant. The sensitivity of ΔB/Ca in G. sacculifer (w/o sac) to $\Delta[CO_3^{2-}]$ is 0.59 $\pm$ 0.13 μmol/mol per μmol/kg $\Delta[CO_3^{2-}]$ change (r^2 = 0.51, n = 22, p <0.001, Figure 2-4c). ΔB/Ca at Sierra Leone Rise from Coadic et al. (2013) is systematically higher than ΔB/Ca from this study, and diverges from the trend defined by data from this study, possibly reflecting regional dependence of dissolution sensitivity. The sensitivity of ΔB/Ca in *G. ruber* (w) is 0.67 $\pm$ 0.22 μmol/mol per μmol/kg $\Delta[CO_3^{2-}]$ change (r^2 = 0.45, n = 15, p = 0.009, Figure 2-4d). These results, integrating data from different oceans, provide a first-order estimation of the sensitivity of B/Ca in *G. sacculifer* (w/o sac) and *G. ruber* (w) to dissolution effects.

2.4.4 Correlation with coexisting benthic B/Ca

The correlation of planktonic B/Ca in *G. sacculifer* (w/o sac) and *G. ruber* (w) with bottom water $\Delta[CO_3^{2-}]$ indicates that planktonic B/Ca can be corrected given knowledge of bottom water $\Delta[CO_3^{2-}]$. As suggested by Coadic et al. (2013), for downcore reconstruction, an independent proxy for $\Delta[CO_3^{2-}]$ can be employed to correct for the dissolution effects on planktonic B/Ca. Given that benthic B/Ca is an established quantitative proxy for bottom water $\Delta[CO_3^{2-}]$ change and is not affected by dissolution (Yu and Elderfield, 2007), it follows that $\Delta[CO_3^{2-}]$ reconstructed from the same sediment sample as planktonic B/Ca could be used to correct for dissolution bias of planktonic B/Ca. Accordingly, here we attempt to use benthic B/Ca to evaluate how planktonic B/Ca records can be altered by bottom water $\Delta[CO_3^{2-}]$ change in sediment cores.

Sites with planktonic B/Ca evidently affected by dissolution are chosen for the following analysis. We begin by comparing our core-top planktonic B/Ca in *G. sacculifer* (w/o sac) and *G. ruber* (w) to published benthic B/Ca in *C. wuellerstorfi* (data are from (Yu and Elderfield, 2007)) from the Ontong Java Plateau, the Southwestern Indian Ocean, and the Caribbean Sea. Planktonic and benthic B/Ca from different depth transects are translated to relative change within each depth transect. This makes data from different depth transects comparable:

$$B/Ca_{diff} = B/Ca_{measured} - B/Ca_{mean}. \tag{2.2}$$

It is revealed that all data from these three areas show a positive correlation between planktonic B/Ca and benthic B/Ca. B/Ca in *G. sacculifer* (w/o sac) and *G. ruber* (w) decreases 0.38 $\pm$ 0.11and 0.60 $\pm$ 0.07 μmol/mol per μmol/mol B/Ca change in *C. wuellerstorfi*, respectively (Figure 2-5).

The comparison made above shows that B/Ca change can be 35-55% of benthic B/Ca change, when planktonic B/Ca is subject to the influence of

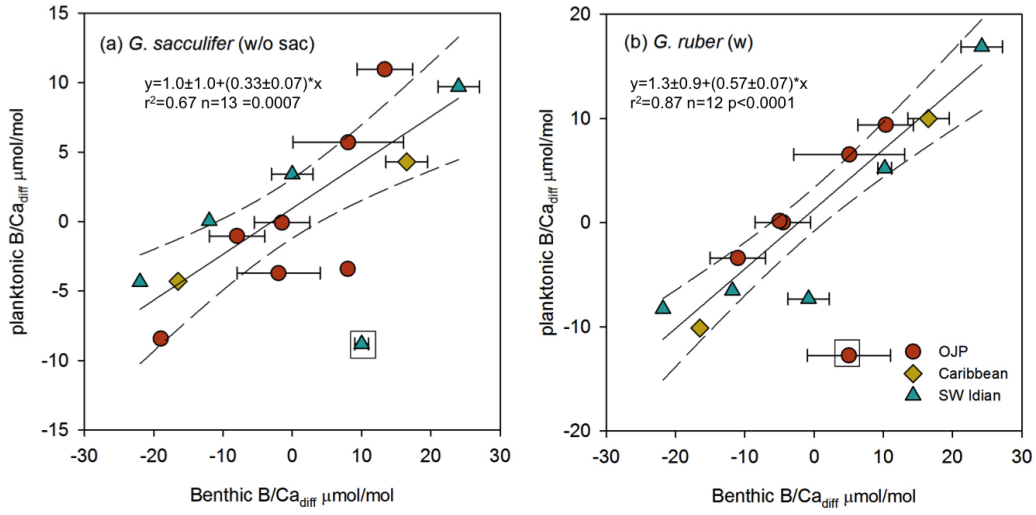

Figure 2-5: B/Ca in *G. sacculifer* (w/o sac) and *G. ruber* (w) versus co-existing B/Ca in *C. wuellerstorfi* (Yu and Elderfield, 2007). Horizontal error bars indicate available standard errors of benthic B/Ca (Yu and Elderfield, 2007). Questionable data points are framed within boxes and excluded from regression analysis. Solid lines and dashed lines are regression lines and 95% confidence internals, respectively, for the predicted planktonic B/Ca decline based on benthic B/Ca.

dissolution. Glacial-interglacial difference of deep water $\Delta[CO_3^{2-}]$ can be as large as 50 μmol/kg, based on reconstructions via various proxies (Broecker and Clark, 2001b; Marchitto et al., 2005; Yu et al., 2010a; Doss and Marchitto, 2013), equivalent to 57 μmol/mol variation of B/Ca variations in *C. wuellerstorfi* (Yu and Elderfield, 2007). According to the correlations we observe, this would alter the planktonic B/Ca by 18-28 μmol/mol, if $\Delta[CO_3^{2-}]$ of one certain site is always below the threshold $\Delta[CO_3^{2-}]$ value for planktonic B/Ca decline. This dissolution effect is substantial compared to glacial-interglacial change in planktonic B/Ca of 25 μmol/mol (Yu and Elderfield, 2007; Foster, 2008; Palmer et al., 2010; Yu et al., 2013). With the sensitivity of planktonic B/Ca change to benthic B/Ca change here and the threshold $\Delta[CO_3^{2-}]$ value for planktonic B/Ca decline, it is feasible to correct for dissolution effects on planktonic B/Ca, if a benthic B/Ca record is available.

2.5 Conclusions

In this study, we have measured B/Ca in four planktonic foraminiferal species in core-top samples from three depth transects to investigate dissolution effects on planktonic B/Ca. We find that the dissolution effects on planktonic B/Ca are species-specific. Among the four species examined, B/Ca in *G. sacculifer* (w/o sac) and *G. ruber* (w) shows significant decreases with progressive dissolution, while B/Ca in *N. dutertrei* and *P. obliquiloculata* is negligibly influenced by dissolution. The reason for species-specific responses of B/Ca in different species to dissolution might be related to the micro-scale distribution of B in foraminiferal shells. Decline of B/Ca in *G. sacculifer* (w/o sac) and *G. ruber* (w) can be empirically correlated with bottom water $\Delta[CO_3^{2-}]$ and B/Ca in coexisting benthic foraminifera, providing a means to correct for dissolution effects on planktonic B/Ca in sediment cores.

Chapter 3

Revisiting salinity effect on planktonic foraminiferal Mg/Ca

3.1 Introduction

Planktonic foraminiferal Mg/Ca is a widely used proxy for past sea surface temperatures (*e.g.*, Elderfield and Ganssen, 2000; Lea et al., 2003). Bulk shell Mg/Ca of planktonic foraminifera is observed to increase with seawater temperatures, as shown by studies based on sediment traps, core-tops, and cultured specimens (Anand et al., 2003; Dekens et al., 2002; Lea et al., 1999; Nürnberg et al., 1996). For example, based on Mg/Ca in multiple planktonic species, Anand et al. (2003) established a calibration:

$$Mg/Ca = (0.38 \pm 0.02) \times e^{(0.09 \pm 0.003) \times T}. \tag{3.1}$$

This calibration has been routinely employed to reconstruct sea surface temperatures from planktonic Mg/Ca.

Apart from temperature, planktonic Mg/Ca is also found to be susceptible to several other parameters including deepwater saturation state (Brown and Elderfield, 1996; Regenberg et al., 2006, 2014), surface seawater carbonate chemistry (Lea et al., 1999; Russell et al., 2004; Evans et al., 2016b), seawater

Mg/Ca (Evans et al., 2016a), and salinity (Kısakurek et al., 2008; Arbuszewski et al., 2010; Hönisch et al., 2013). Of relevance to this study, an influence of salinity on planktonic foraminiferal Mg/Ca would introduce uncertainties into temperature reconstructions. However, there is currently no consensus on the magnitude of the salinity effect on planktonic Mg/Ca, since culture experiments and core-top studies gave contrasting results. Culture experiments showed a weak salinity effect, at 3-6% per salinity unit change, on planktonic Mg/Ca (Lea et al., 1999; Kısakurek et al., 2008; Dueñas-Bohórquez et al., 2009; Hönisch et al., 2013). Core-top studies, on the other hand, suggested much stronger salinity effects ranging from 15 to 30% per salinity unit change on Mg/Ca in a widely used species *Globigerinoides ruber* (white) (Arbuszewski et al., 2010; Ferguson et al., 2008; Mathien-Blard and Bassinot, 2009). The large salinity effects on core-top *G. ruber* (w) Mg/Ca are inferred from discrepancies of Mg/Ca-derived temperatures (termed T_{Mg}) with sea surface temperatures (SST) from modern hydrological data and with temperatures estimated from foraminifera-seawater $\delta^{18}O$ offsets (termed T_{iso}) (Arbuszewski et al., 2010; Ferguson et al., 2008; Mathien-Blard and Bassinot, 2009). In these core-top studies, *G. ruber* (w) Mg/Ca were poorly correlated with SST, but the correlation was significantly improved when sea surface salinity (SSS) was included in the multivariate regression analyses. A large salinity effect on *G. ruber* (w) Mg/Ca was also implied by a strong positive correlation between SSS and 'excess Mg/Ca' (Mg/Ca_{xs}), where Mg/Ca_{xs} is defined as the difference between measured Mg/Ca and Mg/Ca calculated from either hydrological temperatures or T_{iso} (Equation (3.2), Arbuszewski et al., 2010; Ferguson et al., 2008; Mathien-Blard and Bassinot, 2009).

$$Mg/Ca_{xs} = Mg/Ca_{measured} - Mg/Ca_{expected}, \tag{3.2}$$

where $Mg/Ca_{expected}$ represent Mg/Ca estimated from either hydrological data or oxygen isotope data. The large salinity effect on *G. ruber* (w) Mg/Ca, if

valid, would compromise the reliability of planktonic Mg/Ca as a proxy for sea surface temperature reconstructions. For example, the effect of 1 unit change in salinity on Mg/Ca would be equivalent to that of 1.7-3.3°C change in temperature, based on a salinity sensitivity of 15-30% per salinity unit change (Arbuszewski et al., 2010; Ferguson et al., 2008; Mathien-Blard and Bassinot, 2009).

Several attempts have been made to reconcile the contrasting salinity effects derived from core-top and culture studies. Firstly, it was suggested that a large salinity effect could result from post-depositional alterations that overprint Mg/Ca of pristine foraminiferal shells. The large salinity effect reported for the Mediterranean Sea samples (Ferguson et al., 2008) was later questioned by the presence of high-Mg overgrowths on the shells (Boussetta et al., 2011; Hoogakker et al., 2009). Secondly, the poor correlation between T_{Mg} and SST for the Atlantic core-tops (Arbuszewski et al., 2010) was partially attributed to overcorrecting post-depositional dissolution influences on Mg/Ca (Hertzberg and Schmidt, 2013; Hönisch et al., 2013). Thirdly, variations of *G. ruber* (w) Mg/Ca of the Atlantic core-top samples (Arbuszewski et al., 2010) might be in part driven by latitude-dependent variations in the calcification depth and seasonality of this species. By invoking variable calcification depths and seasonality along the Atlantic meridional transect, the correlation between T_{Mg} and hydrological temperatures could be significantly improved (Hertzberg and Schmidt, 2013; Hönisch et al., 2013). However, the salinity effect derived from the Atlantic core-tops (Arbuszewski et al., 2010) has not been fully resolved. *G. ruber* (w) T_{Mg} remain higher than the hydrological temperatures at high salinity sites, and the correlation between salinity and Mg/Ca_{xs} (Arbuszewski et al., 2010) is still strong after taking seasonality and calcification into account (Figure 3-1) (Hönisch et al., 2013).

In this chapter, salinity effects on planktonic Mg/Ca are investigated by analyzing Mg/Ca in *G. ruber* (white, *sensu stricto*) and *Globigerinoides sacculifer* (without final sac-like chamber) from core-tops in the open Atlantic.

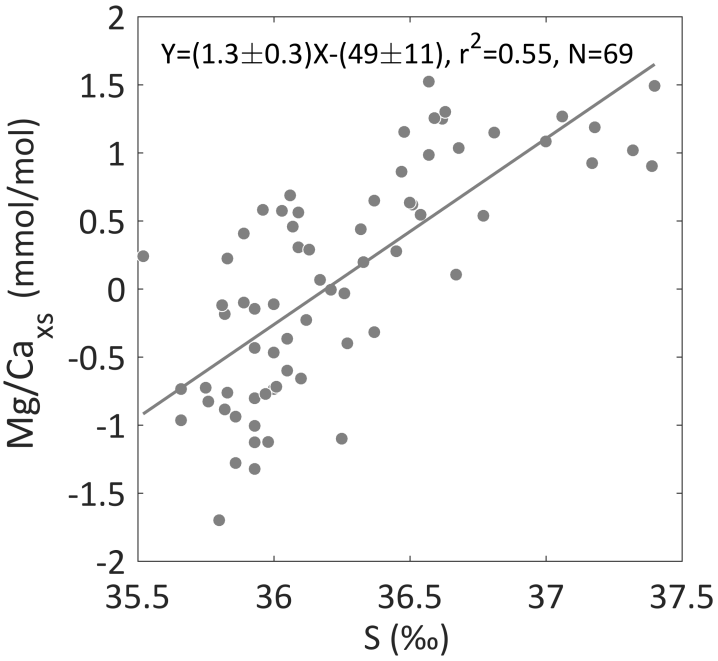

Figure 3-1: Correlation between Mg/Ca_{xs} and salinity in (Arbuszewski et al., 2010), after reinterpreted by (Hönisch et al., 2013). Hönisch et al. (2013) attempted to dismiss the salinity effect on *G. ruber* (w) Mg/Ca observed from data in (Arbuszewski et al., 2010). They discarded the dissolution corrections applied to Mg/Ca and invoked varying seasonality and calcification depths for different core-top sites. By doing so, the correlation between Mg/Ca and hydrological temperatures was significantly improved. However, there was still a strong correlation between Mg/Ca_{xs} and salinities, indicating a strong salinity effect on *G. ruber* (w) Mg/Ca.

Both species are mixed-layer species favoring tropical and subtropical surface waters (*e.g.*, Bé and Hamlin, 1967; Fairbanks et al., 1982; Hemleben et al., 1989; Tolderlund and Bé, 1971), with *G. sacculifer* (w/o sac) dwelling slightly deeper in the mixed layer (Fairbanks et al., 1982; Ravelo and Fairbanks, 1992). *G. ruber* (w) has been the focus of previous studies. Among *G. ruber* (w) sites in this study, 34 of them were measured and used to argue for strong salinity effects (Arbuszewski et al., 2010). The salinity effect on *G. sacculifer* (w/o sac) Mg/Ca has been determined in culture experiments (Hönisch et al., 2013), but not yet been explored in core-top studies. New *G. ruber* (w) Mg/Ca from this study are lower than the published values, making re-evaluation of the potential salinity effect on planktonic Mg/Ca necessary. Specifically, the large

salinity effects, previously inferred from the offsets of T_{Mg} from hydrological temperatures and T_{iso} are re-examined.

In the context of this thesis, it is important to constrain the calcification depth and seasonality for the studied species, in order to better estimate the environmental parameters. If the salinity effect on Mg/Ca is small, the calcification depth and seasonality of *G. ruber* (w) and *G. sacculifer* (w/o sac) can be determined.

3.2 Materials and methods

3.2.1 Materials

The core-tops are selected from a meridional core-top transect along the Mid-Atlantic Ridge covering large ranges in latitude (35°S to 45°N) and water depth (1.7 to 5.2 km) (Figure 3-2). Ages of most of these core-tops are verified to be the Late Holocene (0-6 kyr), based on radiocarbon dating, oxygen isotope stratigraphy, or carbonate content (Arbuszewski et al., 2010; Cléroux et al., 2013). *G. ruber* (w) and *G. sacculifer* (w/o sac) shells were picked from 57 and 60 core-tops, respectively.

For each sample, 50 shells from the 250-355 μm size fraction were picked. The narrow size fraction range can minimize potential size effects on Mg/Ca (Elderfield et al., 2002; Friedrich et al., 2012). Foraminiferal shells were crushed, rinsed with Milli-Q water and methanol, and checked under a microscope to remove foreign particles using a single-haired brush (Yu et al., 2007a). In a clean lab, all *G. ruber* (w) samples were cleaned with both oxidative and reductive steps (Boyle and Keigwin, 1985; Barker et al., 2003). All *G. sacculifer* (w/o sac) samples were first oxidatively cleaned, and 15 of these samples were split into two subsamples. One subsample was further reductively cleaned. Mg/Ca in the subsamples with reductive step are 2.2% lower than those without ($Mg/Ca_r = 0.978 \times Mg/Ca_o$, n=15, $r^2 = 0.97$, intercept forced to zero, Figure 3-3). This difference introduces no more than 0.2 °C bias in T_{Mg} cal-

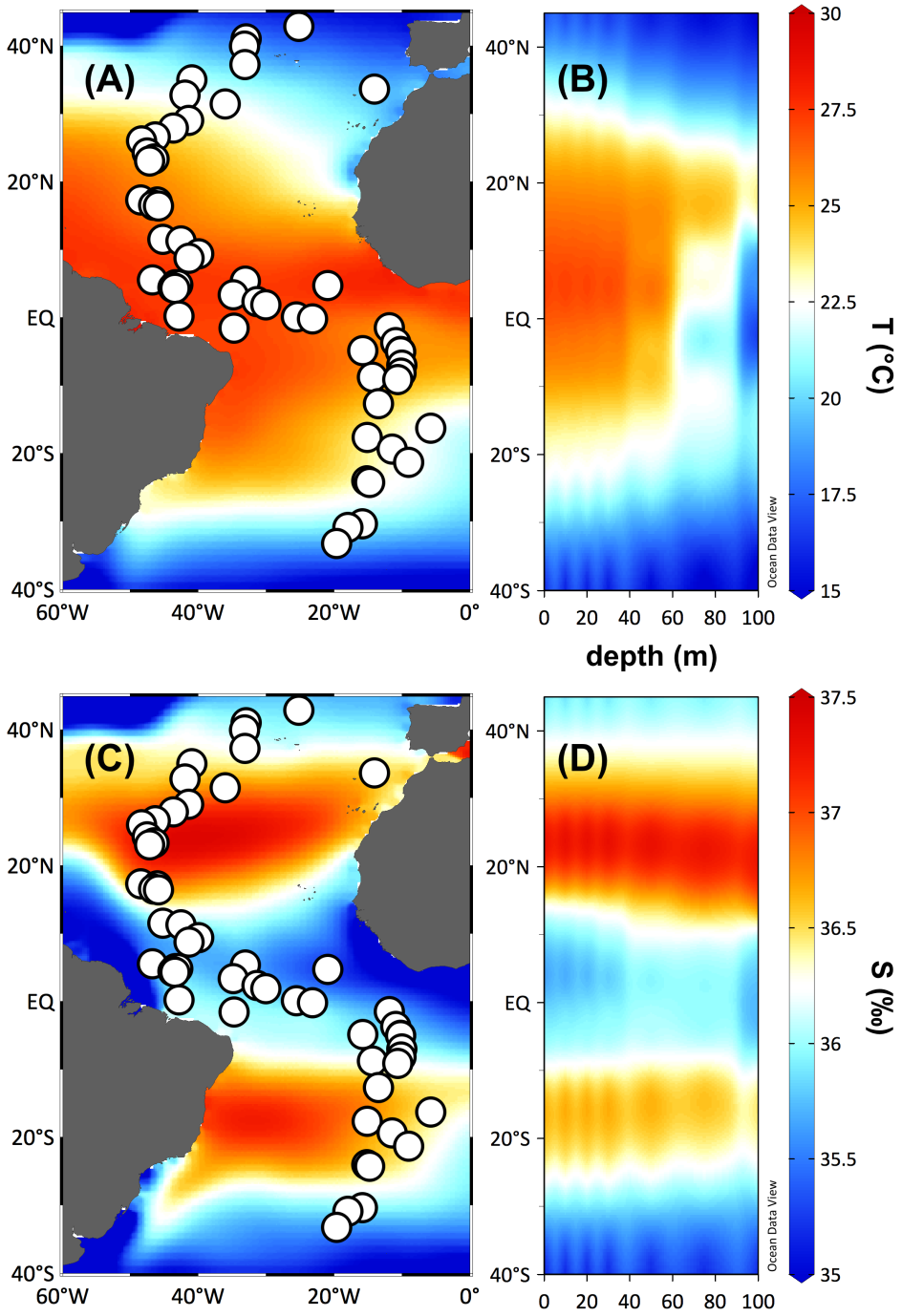

Figure 3-2: Panel (A) and (C) show annual mean SST and SSS, respectively (WOA 09, Locarnini et al., 2010; Antonov et al., 2010). White circles indicate core-top sites. Panel (B) and (D) show the annual mean temperature and salinity in upper 100 m along the Mid-Atlantic Ridge.

culated from Mg/Ca with or without the reductive step, negligible compared to the uncertainty of calibrations. Therefore, no correction was applied to *G.*

sacculifer (w/o sac) Mg/Ca cleaned by different methods.

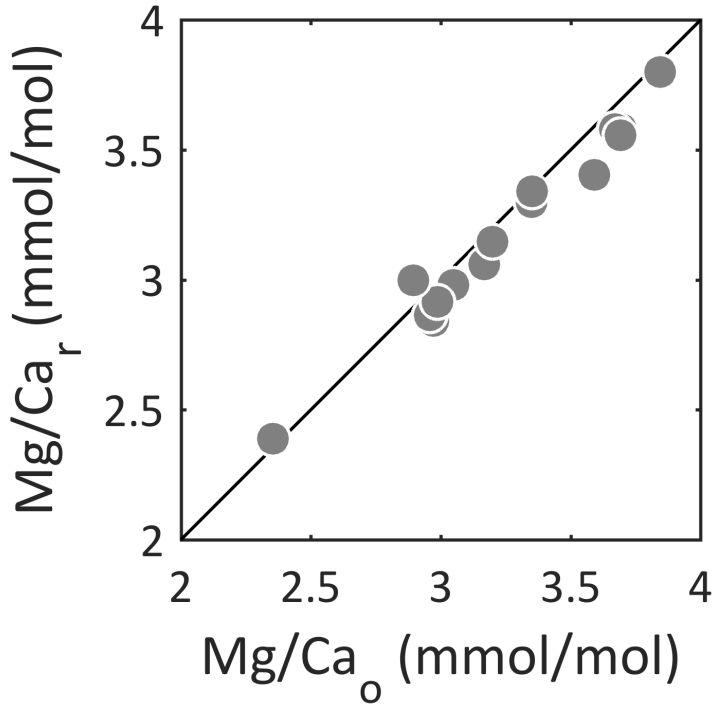

Figure 3-3: Effects of different cleaning methods on *G. sacculifer* (w/o sac) Mg/Ca. Comparison between *G. sacculifer* (w/o sac) Mg/Ca in two subsamples cleaned with oxidative step only (Mg/Ca_o) and with both oxidative and reductive steps (Mg/Ca_r). The black line is the 1:1 line.

3.2.2 Mg/Ca measurement

Trace element to calcium ratios of dissolved foraminiferal samples were measured on a Varian 820 ICP-MS at the Australian National University (ANU) following the method of Yu et al. (2005). Analytical precision for Mg/Ca is better than 2% (2σ). Other ratios including Fe/Ca, Mn/Ca, and Al/Ca were measured to monitor potential contaminations from Fe/Mn hydroxide coatings and the effectiveness of clay removal. There is no correlation between Mg/Ca and Fe/Ca, Mn/Ca, or Al/Ca in foraminiferal calcite samples, suggesting a minimal influence of contamination phases on Mg/Ca results in this study.

Two carbonate reference materials, BAM RS3 and CMSI 1767 (Greaves et al., 2008), were also measured along with samples to test the accuracy of

Mg/Ca measurements. The measured Mg/Ca of BAM RS3 and CMSI 1767 are 0.80 ± 0.02 mmol/mol (n = 3, 2σ) and 5.58 ± 0.08 mmol/mol (n = 4, 2σ), respectively, which are within 1.4 % (2σ) of the accepted values (Greaves et al., 2008).

For inter-laboratory comparisons, Mg/Ca in 9 dissolved foraminiferal samples, 2 calibration standard solutions used at the ANU, and 2 carbonate reference materials (BAM RS3 and CMSI 1767) were also measured in the Lamont-Doherty Earth Observatory of Columbia University (LDEO). The Mg/Ca difference between ANU and LDEO is smaller than 0.16 mmol/mol, except for one standard solution (Mg/Ca_{ANU} = 3.02 mmol/mol, Mg/Ca_{LDEO} = 2.81 mmol/mol) (Figure 3-4). The overall agreement between Mg/Ca obtained from both laboratories suggests a minimal inter-laboratory offset in Mg/Ca measurements.

3.2.3 Hydrological data calculation

Modern hydrological datasets are employed to estimate the hydrological conditions at each core-top site. Seasonal and annual mean sea surface temperatures and salinities are extracted from the World Ocean Atlas 2009 dataset (WOA09) (Antonov et al., 2010; Locarnini et al., 2010). To evaluate the dissolution effect on Mg/Ca, deep water calcite saturation state ($\Delta[CO_3^{2-}]$, defined as the difference between *in-situ* $[CO_3^{2-}]$ and saturation $[CO_3^{2-}]$) is calculated from carbonate chemistry data (total alkalinity, dissolved inorganic carbon (DIC), anthropogenic CO_2, phosphate concentration, and silicate concentration) using the Global Ocean Data Analysis Program database (GLODAP, v1.1) (Key et al., 2004). The DIC is corrected to the preindustrial level by removing the anthropogenic CO_2 (Sabine et al., 2004). The $\Delta[CO_3^{2-}]$ is calculated by CO2sys v2.1 (Lewis et al., 1998), using the same constants as in Yu and Elderfield (2007).

3.3 Comparison with published data

The new *G. ruber* (w) Mg/Ca, measured by both ANU and LDEO, are on average 12% lower than those reported in Arbuszewski et al. (2010) (Figure 3-4). Explaining the higher Mg/Ca in Arbuszewski et al. (2010) requires further investigation, but is out the scope of the current study. Yet, it is possible that slightly different cleaning procedures might be responsible for the Mg/Ca contrast. In this study, all contaminants visible under a microscope were removed prior to the oxidative step to ensure samples free of dirty particles, which could be bleached and mistaken as clean shell fragments after the oxidative step (Yu et al., 2007a).

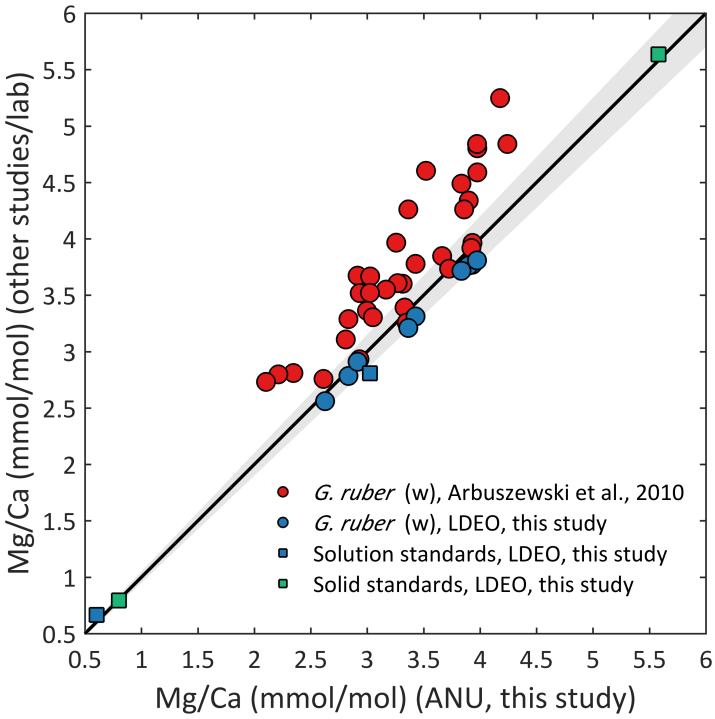

Figure 3-4: Comparison of Mg/Ca between different studies and labs. Green squares, blue squares, and blue circles represent results for solid carbonate standards, solution standards, and dissolved foraminiferal solutions, measured at ANU and LDEO, respectively. Red circles show foraminiferal samples measured by this study and Arbuszewski et al. (2010). The solid line with shading is the 1:1 line with ±2% uncertainty, corresponding to the analytical precision.

Following the same multivariate regression analysis method used by Ar-

buszewski et al. (2010), the new data in this study suggest that the salinity effect on *G. ruber* (w) Mg/Ca would be 14% per salinity unit change:

$$Mg/Ca = 0.0055 \times e^{0.054\times T+0.14\times S},\ r^2 = 0.79,\ n = 57,\ G.\ ruber\ (w). \quad (3.3)$$

Compared to the 27% per salinity unit change reported by Arbuszewski et al. (2010), it represents ~13% decrease in the salinity effect on *G. ruber* (w) Mg/Ca. This suggests that the higher and possibly biased Mg/Ca are partially responsible for the large salinity effect reported by Arbuszewski et al. (2010). This is the incentive to revisit the previous efforts discounting a strong salinity effect on the Atlantic core-top *G. ruber* (w) Mg/Ca (Hönisch et al., 2013; Hertzberg and Schmidt, 2013).

To address the poor correlation between T_{Mg} and SST for the Atlantic core-top *G. ruber* (w), previous studies have invoked influences of post-depositional dissolution (Hertzberg and Schmidt, 2013) and latitude-dependent variations in calcification depths and seasonality of *G. ruber* (w) (Hönisch et al., 2013). These two arguments will be discussed in the following two sections.

3.4 Dissolution effect on Mg/Ca

Post-depositional dissolution can lower foraminiferal Mg/Ca and lead to an underestimation of temperature (Brown and Elderfield, 1996; Regenberg et al., 2006, 2014; Johnstone et al., 2011). Foraminiferal calcite dissolution occurs in both bottom waters and pore waters, when they are under-saturated with respect to calcite owing to low *in situ* $[CO_3^{2-}]$ or high saturation $[CO_3^{2-}]$ (Berger, 1970; Archer and Maier-Reimer, 1994). The effect of dissolution can be corrected using an independent parameter (Dekens et al., 2002; Regenberg et al., 2006, 2014). Currently, there are two methods to correct for the dissolution effect on planktonic foraminiferal Mg/Ca: bottom water $[CO_3^{2-}]$-based (Regenberg et al., 2006, 2014; Johnstone et al., 2011) and water depth-based (Dekens et al., 2002) correcting methods. Dissolution corrections are needed

for core-tops, as post-depositional dissolution is expected at some sites, where the overlying bottom waters are undersaturated. I compare the effects of these two dissolution correction methods on planktonic T_{Mg} interpretation.

Declines in planktonic Mg/Ca caused by dissolution are empirically correlated with bottom water $\Delta[CO_3^{2-}]$ below a threshold $\Delta[CO_3^{2-}]$ value (Brown and Elderfield, 1996; Regenberg et al., 2006, 2014; Johnstone et al., 2011). As deep water saturation $[CO_3^{2-}]$ is correlated to pressure and thus water depth, Dekens et al. (2002) used water depth to account for dissolution effects. The relationships used for corrections in the Atlantic are:

$$G.\ ruber\ (w):\ Mg/Ca = 0.38 \times e^{0.09\left(T - 0.61 \times (core\ depth)\right)}, \quad core\ depth > 2.8\ km, \tag{3.4}$$

$$G.\ sacculifer\ (w/o\ sac):\ Mg/Ca = 0.37 \times e^{0.09\left(T - 0.36 \times (core\ depth)\right)}, \quad core\ depth > 2.8\ km. \tag{3.5}$$

Alternatively, dissolution effects on Mg/Ca can be corrected using bottom water $\Delta[CO_3^{2-}]$. Regenberg et al. (2014) developed a series of species-specific correction calibrations based on core-top samples:

$$G.\ ruber\ (w):\ \Delta Mg/Ca = (0.054 \pm 0.019) \times (17.9 \pm 6.6 - \Delta[CO_3^{2-}]), \quad \Delta[CO_3^{2-}] < 17.9 \pm 6.6\ \mu mol/kg, \tag{3.6}$$

$$G.\ sacculifer\ (w/osac):\ \Delta Mg/Ca = (0.054 \pm 0.019) \times (20.2 \pm 6.6 - \Delta[CO_3^{2-}]), \quad \Delta[CO_3^{2-}] < 20.2 \pm 6.6\ \mu mol/kg. \tag{3.7}$$

To compare these two dissolution correction methods, I calculate temperature corrections (ΔT) applied to the T_{Mg} from both methods. For the depth-based correction, ΔT is the difference between T_{Mg} calculated from Equation 3.4 or 3.5 and Equation (3.1). For the $\Delta[CO_3^{2-}]$-based correction, ΔT is the difference between T_{Mg} calculated from Mg/Ca using Equation (3.1), with or

without dissolution correction according to Equation 3.6 or 3.7.

A comparison of ΔT based on these two correction methods is shown in Figure 3-5. For *G. ruber* (w), $\Delta[CO_3^{2-}]$-based ΔT increases from ∼0°C for sites close to the $\Delta[CO_3^{2-}]$ threshold to ∼4°C for sites ∼15 μmol/kg below the saturation horizon. For *G. sacculifer* (w/o sac), $\Delta[CO_3^{2-}]$-based ΔT shows a similar pattern, but a larger ΔT magnitude owing to several more undersaturated sites. By comparison, depth-based ΔT of *G. ruber* (w) surges from 0 to ∼1.8°C at the threshold depth of 2.8 km, and increases towards ∼2.7°C at 4.5 km. Depth-based ΔT of *G. sacculifer* (w/o sac) is similar to that of *G. ruber* (w), with a smaller variation of ∼1.1 to 1.8°C.

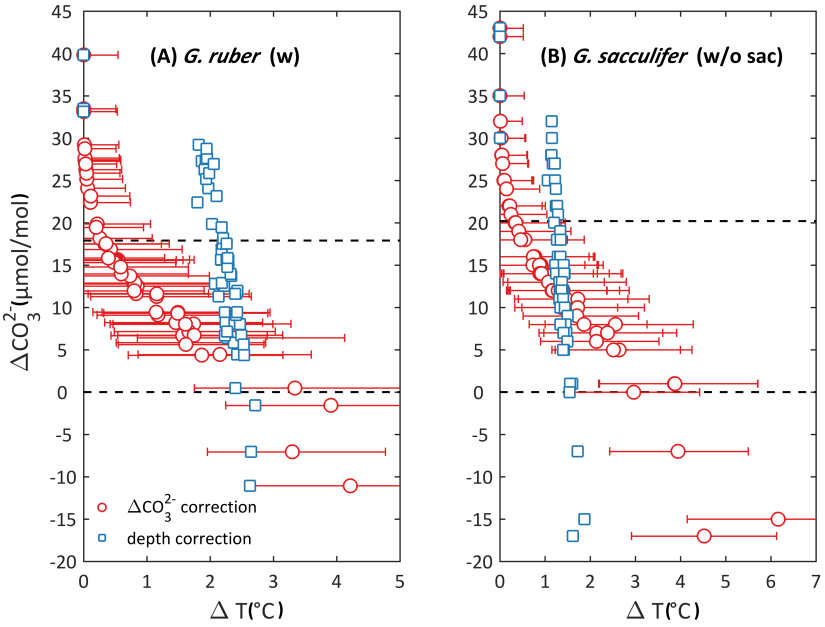

Figure 3-5: $\Delta[CO_3^{2-}]$-based correction (red circles) and depth-dependent correction (blue squares), for *G. ruber* (w) (A) and *G. sacculifer* (w/o sac) (B). The errorbars of $\Delta[CO_3^{2-}]$-based corrections are 68% probability intervals from a Monte-Carlo simulation. The dashed lines show threshold values of $\Delta[CO_3^{2-}]$-based correction and calcite saturation horizon. No errorbars are shown for depth-based dissolution correction, because uncertainties are not derived in (Dekens et al., 2002).

Based on the comparison above, the $\Delta[CO_3^{2-}]$-based dissolution correction is preferred for the following three reasons. Firstly, as can be seen in the Atlantic core-top data, the $\Delta[CO_3^{2-}]$-based dissolution correction is smooth

near the threshold $\Delta[CO_3^{2-}]$, while the depth-based dissolution correction introduces an abrupt transition of ΔT near the threshold depth, which is not realistic. Secondly, the $\Delta[CO_3^{2-}]$-based dissolution correction can provide a meaningful correction to downcore records, while depth-based correction cannot. On the glacial-interglacial timescale, the bottom water $\Delta[CO_3^{2-}]$ can change dramatically (Yu and Elderfield, 2007; Yu et al., 2010b; Gottschalk et al., 2015), resulting in varying dissolution effects. This variation can be captured by the $\Delta[CO_3^{2-}]$-based dissolution correction with an independent proxy for $\Delta[CO_3^{2-}]$, but not by the depth-based dissolution correction, owing to the relatively small water depth variation ($<$ 130 m, Grant et al., 2014) and low sensitivities of ΔT to water depth. Thirdly, by reanalyzing data from the depth transects in Dekens et al. (2002), Hönisch et al. (2013) found that the depth-based correction tends to overcorrect (undercorrect) Mg/Ca above (below) the calcite saturation horizon.

One caveat of the $\Delta[CO_3^{2-}]$-based dissolution correction is the uncertainty introduced to Mg/Ca, especially in more undersaturated bottom waters. The 1σ of ΔMg/Ca of both species increase from 0.16 mmol/mol at the $\Delta[CO_3^{2-}]$ threshold to 0.47 and 0.52 mmol/mol at the saturation horizon for *G. ruber* (w) and *G. sacculifer* (w/o sac), respectively. At the most undersaturated sites in this study, these uncertainties in Mg/Ca are equivalent to $\sim$1.8°C uncertainties in T_{Mg}. As the temperature corrections applied are larger than the 2σ in T_{Mg} introduced by dissolution correction, $\Delta[CO_3^{2-}]$-based dissolution correction improves the 'pristine' signal in Mg/Ca despite the large uncertainties introduced. For this reason, $\Delta[CO_3^{2-}]$-based dissolution corrections are applied to all affected sites in the following discussions, with the uncertainty ranges propagated.

3.5 Calcification depth and seasonality

The salinity effects on *G. ruber* (w) Mg/Ca were inferred from the weak correlations between Mg/Ca and temperatures and the strong correlations between Mg/Ca_{xs} and salinity (Mathien-Blard and Bassinot, 2009; Arbuszewski et al., 2010). Hertzberg and Schmidt (2013) and Hönisch et al. (2013) improved the correlation between *G. ruber* (w) T_{Mg} in (Arbuszewski et al., 2010) and hydrological temperatures, by invoking variable calcification depths and seasonality of *G. ruber* (w) at different latitudes. Hertzberg and Schmidt (2013) found that using annual mean temperatures at 30 m for the tropical latitude sites and mean temperatures at 30 m for the temperate latitude sites can improve the correlation between *G. ruber* (w) T_{Mg} and hydrological temperatures. Hönisch et al. (2013) found that the average habitat depth of *G. ruber* (w) is deeper at tropical latitudes than at temperate latitudes, by comparing *G. ruber* (w) T_{Mg} with seasonal temperatures at different depths. By invoking varying calcification depths and seasonality, previous work discounted, to some extent, but not all, the salinity effect on *G. ruber* (w) Mg/Ca. Indeed, although *G. ruber* (w) and *G. sacculifer* (w/o sac) are often regarded as tropical-subtropical species living in the mixed-layer (*e.g.*, Bé and Hamlin, 1967; Fairbanks et al., 1982; Tolderlund and Bé, 1971; Hemleben et al., 1989), studies based on plankton net, sediment trap, and oxygen isotopes of planktonic foraminifera all suggest that seasonality and calcification depths of these species vary at different latitudes (Tolderlund and Bé, 1971; Žarić et al., 2005; Jonkers and Kučera, 2015, 2017). Following previous studies, the effects of changing calcification depth and seasonality on the interpretation of planktonic foraminiferal Mg/Ca from the Atlantic meridional transect are explored here. Specifically, I 1) examine the correlations between dissolution-corrected Mg/Ca and hydrological temperatures at different depths in different seasons, and the correlations between corresponding Mg/Ca_{xs} and hydrological salinities, and 2) calculate the salinity effects on planktonic Mg/Ca using

the multivariate regression method.

3.5.1 *G. ruber* (w)

Dissolution-corrected *G. ruber* (w) Mg/Ca is compared with annual mean, summer (July to September in the North Hemisphere, and January to March in the South Hemisphere), and winter (July to September in the South Hemisphere, and January to March in the North Hemisphere) hydrological temperatures at 0, 30, and 50 m. The depths and the seasons of the hydrological temperatures represent the 'hypothesized' calcification depths and the seasons of *G. ruber* (w), respectively. By including all the combinations, no prior knowledge about the calcification depths and the seasonality of *G. ruber* (w) is involved.

Correlations between Mg/Ca and hydrological temperatures, with varying calcification depths and the seasonality, are shown in Figure 3-6. Regardless of the 'hypothesized' calcification depths and seasons, these Mg/Ca-T correlations are always significant (r^2 from 0.48 to 0.63), compared to that reported in (Arbuszewski et al., 2010) (r^2 = 0.19). The Mg/Ca-T correlations become stronger, by increasing calcification depths. By contrast, The Mg/Ca-T correlations are less sensitive to seasonality variations. The strongest Mg/Ca-T correlation is achieved when *G. ruber* (w) calcifies at 50 m during summer.

The correlations between Mg/Ca_{xs} and hydrological salinities are shown in Figure 3-7. Although significant ($r^2 = 0.11$ to 0.37, with p values all < 0.05), these Mg/Ca_{xs}-S correlations are much weaker compared to that reported in (Arbuszewski et al., 2010) (r^2 = 0.77). Mg/Ca_{xs} are more strongly correlated with salinities, at shallower calcification depths. Changing seasonality does not have obvious impacts on the significance of the Mg/Ca_{xs}-S correlations.

Multivariate regression analyses are conducted between Mg/Ca and temperatures and salinities at different depths during various seasons. The results of the regression analyses (r^2 values and sensitivities of Mg/Ca to temperatures and salinities) are summarized in Table 3.1. r^2 values of the multivariate

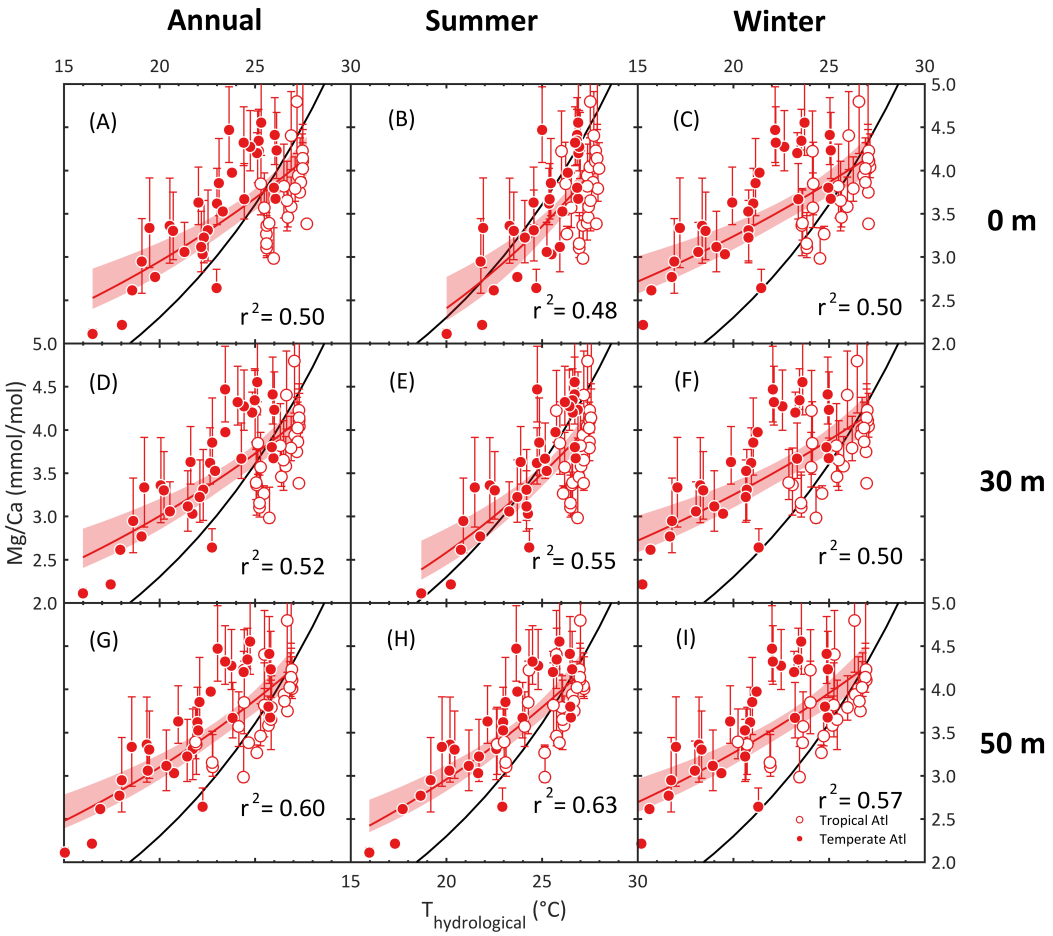

Figure 3-6: Comparison between dissolution-corrected *G. ruber* (w) Mg/Ca and hydrological temperatures, at different depths during different seasons. The empty and filled dots are data from the tropical and the temperate Atlantic, respectively. The errorbars indicate $\pm 1\sigma$ errors of the dissolution corrected Mg/Ca. The analytical error of Mg/Ca is comparable to the size of dots. The red curves with the envelops are the exponential regressions with 95% confidence intervals. The black curves represent the calibration curve from Anand et al. (2003).

regressions range from 0.57 to 0.69, higher than r^2 values of the corresponding regressions between Mg/Ca and temperatures (0.48 to 0.63). The salinity effects on *G. ruber* (w) Mg/Ca vary from 9.6 to 15.6% per salinity unit, when different hydrological data are used. The lowest salinity effect can be achieved by using summer hydrological data at 50 m water depth.

Compared to Arbuszewski et al. (2010), *G. ruber* (w) Mg/Ca from the Atlantic meridional transect in this study are more strongly correlated to hy-

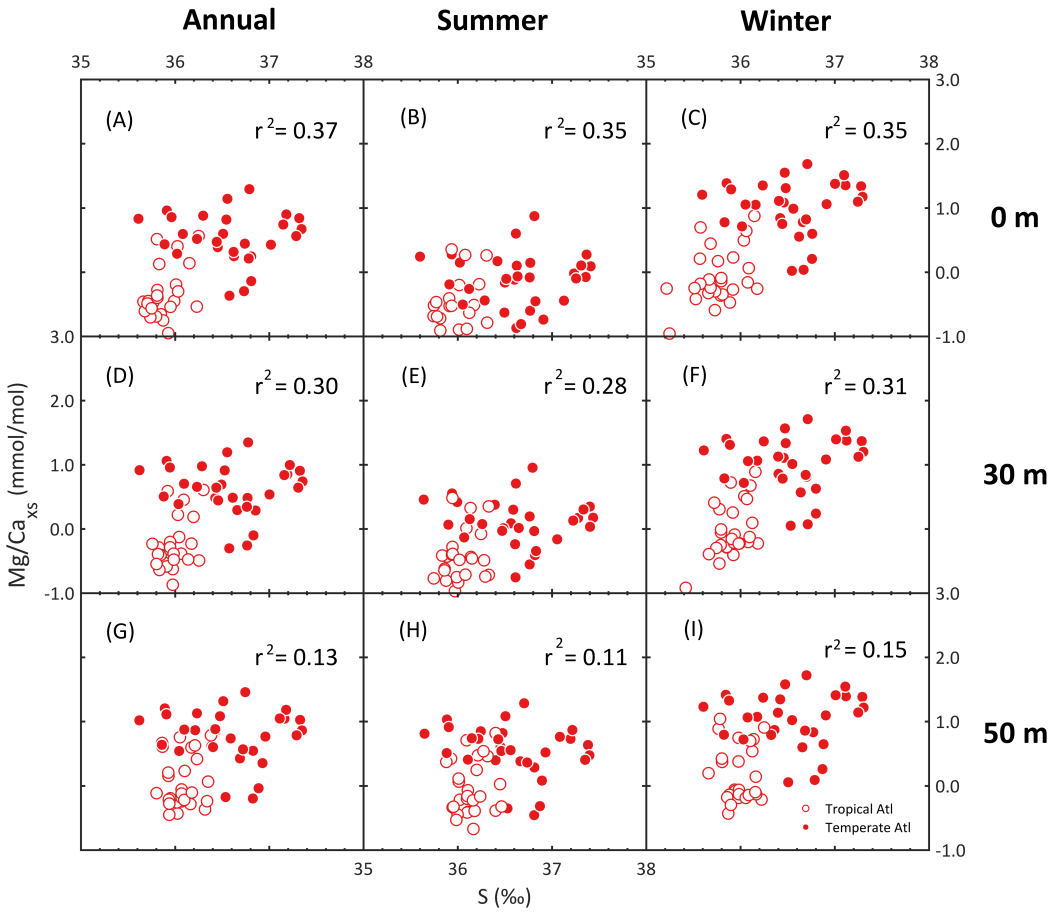

Figure 3-7: Comparisons between *G. ruber* (w) Mg/Ca_{xs} and hydrological salinity, at different depths during different seasons. The empty and filled dots are data from the tropical and the temperate Atlantic, respectively.

Season	Depth m	r^2	T sens. % per °C	S sens. % per unit
Annual Mean	0	0.65	4.9	13.2
	30	0.66	4.6	13.8
	50	0.69	4.3	11.9
Summer	0	0.57	6.8	10.1
	30	0.63	6.0	10.0
	50	0.69	4.7	**9.6**
Winter	0	0.65	4.1	13.3
	30	0.68	3.9	15.6
	50	0.69	3.9	13.7

Table 3.1: Sensitivities of *G. ruber* (w) Mg/Ca to temperature and salinity derived from multivariate regression analyses.

drological temperatures, and the corresponding Mg/Ca_{xs} are less significantly correlated with salinities. These observations indicate a weaker salinity effect on *G. ruber* (w) Mg/Ca. Nevertheless, the salinity effect on *G. ruber* (w) Mg/Ca is still evident, due to the significant correlations between Mg/Ca_{xs} and salinities and more significant correlations when salinity is included in the regression analyses.

For the next step, the salinity effect on *G. ruber* (w) Mg/Ca is further investigated by invoking variations of calcification depth and seasonality at various latitude ranges. Specifically, multivariate regressions are carried out between Mg/Ca and temperatures and salinities, where the temperatures and salinities are allowed to come from different depths and seasons in various latitude ranges. The reason for doing so is that seasonality and calcification depths of *G. ruber* (w) can vary at different latitudes (Tolderlund and Bé, 1971; Žarić et al., 2005; Jonkers and Kučera, 2015, 2017), and these variations can affect the interpretation of *G. ruber* (w) Mg/Ca from (Arbuszewski et al., 2010) (Hönisch et al., 2013; Hertzberg and Schmidt, 2013).

The detailed method is described as follows. Each core-top site is first categorized as either 'tropical' or 'temperate' based on latitude, because *G. ruber* (w) is a mixed-layer species favoring tropical and subtropical waters (Bé and Hamlin, 1967; Fairbanks et al., 1982; Hemleben et al., 1989; Tolderlund and Bé, 1971), so that calcification depths and seasonality of *G. ruber* (w) can be different at tropical and temperate latitudes. Core-tops sites between 10°S and 15°N are deemed as tropical sites, while sites north of 15°N and south of 10°S are classified as temperate sites. It is notable that the core-tops within the subtropical gyres with relatively high salinity fall within the temperate latitudes (Figure 3-2). Hydrological data are constructed by specifying the calcification depths and seasons at the temperate and the tropical latitudes, respectively. Here, based on current understanding of calcification depth and seasonality of *G. ruber* (w), several conditions are applied to reduce the combinations of calcification depths and seasonality at the temperate and the tropical latitude.

As *G. ruber* (w) prefer tropical warm waters (Bé and Hamlin, 1967; Hemleben et al., 1989; Tolderlund and Bé, 1971), it is expected that *G. ruber* (w) do not prefer 1) calcifying at deeper depth at temperate latitudes than at tropical latitudes, 2) calcifying in winter at temperate latitudes, 3) or calcifying in the cooler season at temperate latitudes compared to tropical latitudes. Therefore, depths of hydrological data at temperate latitudes are assumed to calcify no deeper than those at tropical latitudes, not in winter, and during seasons no cooler than those at tropical latitudes. In total, 30 combinations of hydrological data are investigated. Regression analyses are carried out between *G. ruber* (w) Mg/Ca and hydrological data to find out the minimum and maximum of salinity effects on *G. ruber* (w) Mg/Ca.

The results of regression analyses are shown in Figure 3-8. Here, salinity sensitivities, temperature sensitivities, and r^2 are presented by the shadings of the grids, against different combinations of seasonality (x axes) and calcification depth (y axes) at temperate and tropical latitudes (see caption for an example).

The salinity effect on *G. ruber* (w) Mg/Ca varies with T-S of selected depths and seasons. The salinity sensitivity of *G. ruber* (w) Mg/Ca ranges from -2.5 to 13.8 % per salinity unit (Figure 3-8A), compared to 9.6-15.6 % per salinity unit using T-S for constant seasons and depths (r^2 = 0.57 to 0.69, temperature sensitivity = 3.9 to 6.8 % per °C, see Table 3.1 for details). I use temperature sensitivities and r^2 to infer the most likely calcification depths and seasonality of *G. ruber* (w) thus constraining the salinity effect on Mg/Ca.

Firstly, the temperature sensitivities derived from the multivariate regressions are required to fall within the published sensitivity range. The sensitivities of *G. ruber* (w) Mg/Ca to temperature derived from multivariate regressions range from 4 to 8 % per °C (Figure 3-8B). By comparison, the temperature sensitivities of *G. ruber* (w) Mg/Ca vary from 6.8 to 10.2 % per °C based on culture experiments and sediment traps (Lea et al., 2000; Anand et al., 2003; McConnell and Thunell, 2005; Kısakurek et al., 2008). These

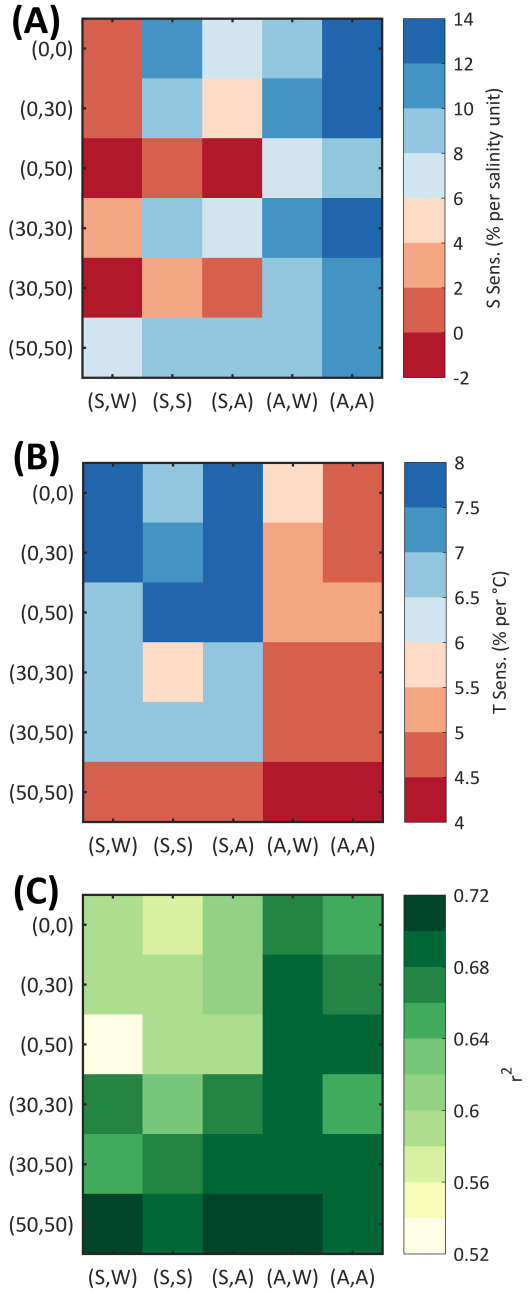

Figure 3-8: Summary of the regression analyses between *G. ruber* (w) Mg/Ca and T, S. Panel (A) and (B) show the sensitivities of *G. ruber* (w) Mg/Ca to salinity and temperature, respectively. Panel (C) shows the r^2 of multivariate regressions. The x axises represent combinations of calcification seasons for temperate and tropical regions (W = winter, S = summer, A = annual mean). The y axises represent combinations of calcification depths for temperate and tropical regions. For example, in all panes, the top-right corner represents the result derived from annual mean hydrological data at 0 m at temperate latitudes and annual mean hydrological data at 0 m at tropical latitudes.

published temperature sensitivities are not likely to be strongly compromised by potential salinity effects. For culture studies, salinity is hold constant (Lea et al., 2000; Kısakurek et al., 2008). For sediment trap studies, seasonal variation of salinity at trap sites is small (Anand et al., 2003; McConnell and Thunell, 2005). To make temperature sensitivities from core-top data in this study comparable to the published values, it is necessary to use summer hydological data $<$ 50 m at temperate latitudes (Figure 3-8B).

Secondly, the r^2 of the regressions should be relatively high. r^2 of the correlations vary between 0.52 to 0.72 (Figure 3-8C). When seasonality of *G. ruber* (w) is assigned as summer at temperate latitudes, r^2 values of correlations generally increase with increasing calcification depths at temperate latitudes.

Using constraints from both temperature sensitivities and r^2 values of correlations, several conclusions on the calcification depths and seasonality of *G. ruber* (w) can be drawn. At temperate latitudes, calcification of *G. ruber* (w) is biased towards summer, at the calcification depth of 30 m. At tropical latitudes, the seasonality of *G. ruber* (w) is not obvious, and the calcification depth is around 30 and 50 m. When *G. ruber* (w) from the tropical region is assigned to calcify at 50 m, the highest r^2 value is reached while the temperature sensitivity is within the published range.

Based on the constrained seasonality and calcification depths of *G. ruber* (w) as described above, the salinity effects on *G. ruber* (w) Mg/Ca are from 0.0 to 10.0 % per salinity unit. When r^2 value is the highest, the salinity effect is 1.8±3.1 % per salinity unit (1σ):

$$ln(Mg/Ca) = (0.018 \pm 0.031) \times S + (0.070 \pm 0.007) \times T - (1.1 \pm 1.1), \quad r^2 = 0.68. \tag{3.8}$$

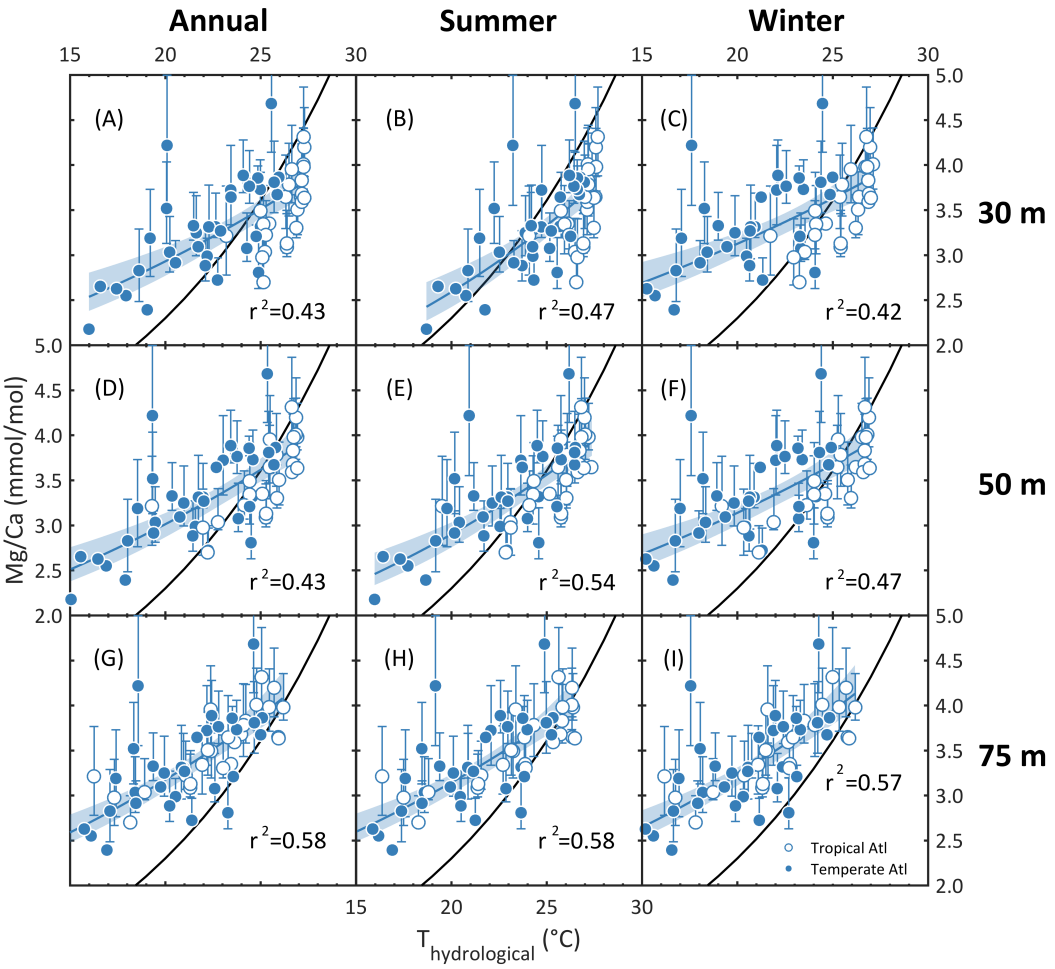

Figure 3-9: Comparisons between dissolution-corrected *G. sacculifer* (w/o sac) Mg/Ca and hydrological temperatures, at different calcification depths and seasons. The empty and filled dots are data from the tropical and the temperate Atlantic, respectively. The errorbars represent 1σ uncertainty of the dissolution corrected Mg/Ca. The analytical error of Mg/Ca is comparable to the size of symbols. The blue curves with the envelops are the exponential regressions with 95% confidence intervals. The black curves represent the calibration curve from Anand et al. (2003).

3.5.2 *G. sacculifer* (w/o sac)

G. sacculifer (w/o sac) Mg/Ca is analyzed by the same approach as *G. ruber* (w) Mg/Ca. Correlations between Mg/Ca and temperatures and between Mg/Ca_{xs} and salinities are investigated to test whether there is detectable salinity effects on *G. sacculifer* (w/o sac) Mg/Ca. Dissolution-corrected *G. sacculifer* (w/o sac) Mg/Ca are compared with annual mean, summer, and

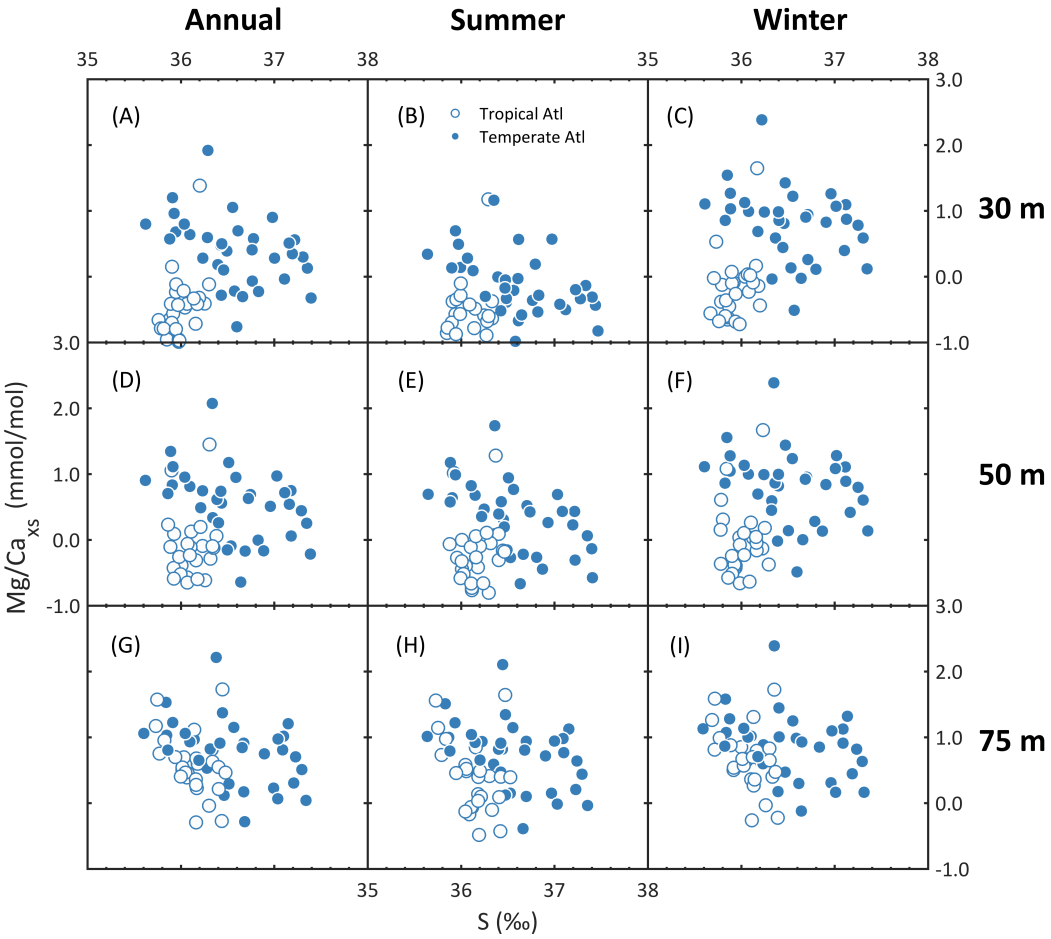

Figure 3-10: Comparisons between *G. sacculifer* (w/o sac) Mg/Ca_{xs} and hydrological salinity, at different calcification depths and seasons. The empty and filled dots are data from the tropical and the temperate Atlantic, respectively.

winter hydrological temperatures at 30, 50, and 75 m (Figure 3-9). *G. sacculifer* (w/o sac) Mg/Ca_{xs} are compared with the corresponding hydrological salinities (Figure 3-10). Deeper calcification depths than *G. ruber* (w) are chosen for *G. sacculifer* (w/o sac) because *G. sacculifer* (w/o sac) seems to dwell deeper than *G. ruber* (w) (Fairbanks et al., 1982; Ravelo and Fairbanks, 1992). *G. sacculifer* (w/o sac) Mg/Ca are significantly correlated with temperatures at all chosen calcification depths and seasons, with r^2 ranging from 0.43 to 0.58 (Figure 3-9). Different from *G. ruber* (w), *G. sacculifer* (w/o sac) Mg/Ca_{xs} are only correlated to salinity at calcification depth of 30 m (r^2 =0.07, p = 0.04), whereas for the rest cases, *G. sacculifer* (w/o sac) Mg/Ca_{xs}

are not significantly correlated with salinities (r^2 <0.05, p > 0.05, Figure 3-10). However, calcification depth is not likely to be 30 m for *G. sacculifer* (w/o sac), if there is a salinity effect on Mg/Ca. In multivariate regression analyses between *G. sacculifer* (w/o sac) Mg/Ca, temperature, and salinity at 30 m in different seasons, the temperature sensitivities are between 2.8 to 3.7 % per °C, significantly lower than the published range of 4.8 to 9.0 % per °C from culture and sediment trap studies (Nürnberg et al., 1996; Anand et al., 2003). Because the hydrological data, with which a salinity effect can be detected, fail to reconstruct temperature sensitivities comparable to the published ranges, it is concluded that core-top data suggest little salinity effect on *G. sacculifer* (w/o sac) Mg/Ca.

Although there is no obvious salinity effect on *G. sacculifer* (w/o sac) Mg/Ca, the calcification depths and seasonality of *G. sacculifer* (w/o sac) can be determined in a similar way to *G. ruber* (w). Regression analyses between Mg/Ca and temperatures are conducted, instead of a multivariate regression with both temperature and salinity. The temperatures are allowed to be different between the 'temperate' and the 'tropical' latitudes, with the same definition as for *G. ruber* (w). Salinity is excluded in the regression analyses, because little salinity effects on *G. sacculifer* (w/o sac) can be detected. Temperature sensitivities and r^2 values of regressions are used to constrain the seasonal preference and calcification depth of *G. sacculifer* (w/o sac).

The result of regression analyses is shown in Figure 3-11. The temperature sensitivities of *G. sacculifer* (w/o sac) Mg/Ca range between 3.5 and 5.9 % per °C, in comparison to the published range of 4.8 to 9.0 % per °C from culture and sediment trap studies (Nürnberg et al., 1996; Anand et al., 2003). To reach the most compatible temperature sensitivities between core-tops in this study and culture and sediment traps (Nürnberg et al., 1996; Anand et al., 2003), it is necessary to assume that *G. sacculifer* (w/o sac) at the temperate latitudes calcify at 30 m during summer (Figure 3-11A). For the tropical latitudes, *G. sacculifer* (w/o sac) may calcify around 30-50 m, insensitive to seasonality.

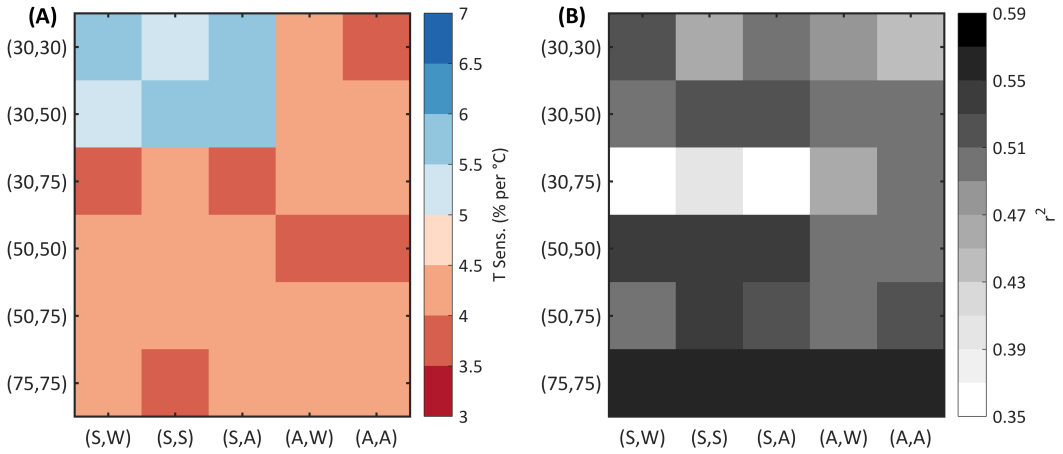

Figure 3-11: Summary of the regression analyses between *G. sacculifer* (w/o sac) Mg/Ca and hydrological data. Panel (A) shows the sensitivities of *G. sacculifer* (w/o sac) Mg/Ca to temperature, respectively. Panel (C) shows the r^2 of the multivariate regressions. The x axises represent the change in seasons of the hydrological data. Letters in the parentheses are the seasons of the hydrological data at temperate and tropical latitudes, respectively (W = winter, S = summer, A = annual mean). The y axises represent the change in depth of the hydrological data. Numbers in the parentheses are the depths of the hydrological data at temperate and tropical latitudes (in the unit of m), respectively.

Within these combinations of calcification depths and seasonality, r^2 values are comparable (Figure 3-11B), so that r^2 values cannot help further constrain calcification depths and seasonality.

Overall, similar to *G. ruber* (w), at the temperate latitude, *G. sacculifer* (w/o sac) can be demonstrated to calcify at 30 m during summer, while at the tropical latitudes, *G. sacculifer* (w/o sac) may calcify deeper than at the temperate latitudes, with no seasonal bias.

3.5.3 Calcification depth and seasonality

The seasonality and calcification depth of *G. ruber* (w) and *G. sacculifer* (w/o sac) deduced from Mg/Ca are consistent with previous observations (Tolderlund and Bé, 1971; Žarić et al., 2005; Jonkers and Kučera, 2015, 2017). *G. ruber* (w) and *G. sacculifer* (w/o sac) are thought to be mixed-layer species favoring tropical and subtropical surface waters (*e.g.*, Bé and Hamlin, 1967;

Fairbanks et al., 1982; Hemleben et al., 1989; Tolderlund and Bé, 1971). Seasonality of these two species is well registered in the moderate North Atlantic (Tolderlund and Bé, 1971; Deuser, 1987). Between 32°N and 44°N in the Atlantic, high abundance of *G. ruber* (w) and *G. sacculifer* (w/o sac) are associated with thermal maxima during summer (Tolderlund and Bé, 1971). At tropical latitude, seasonal appearance of these two species shows less predictable patterns (Žarić et al., 2005; Jonkers and Kučera, 2015). Jonkers and Kučera (2015) concluded that these warm-water species do not demonstrate a clear seasonality in tropical waters, but their occurrence tends to be narrowed to warmer seasons at temperate latitudes. Based on comparison between Mg/Ca and hydrological data, it is found in this study that seasonality of these two species is biased towards summer at temperate latitudes, while there is no seasonal preference at tropical latitude. These findings are consistent with previous studies.

Defining calcification depth of the planktonic foraminifera is challenging as most foraminifera migrate though the water column in their life cycles (Duplessy et al., 1981; Hemleben et al., 1989). Although regarded as 'mixed-layer' species, both *G. ruber* (w) and *G. sacculifer* (w/o sac) are present in upper 100 m in many plankton tow studies (Jones, 1967; Tolderlund and Bé, 1971; Fairbanks et al., 1980, 1982; Ravelo and Fairbanks, 1992). Many previous studies (Ravelo and Fairbanks, 1992; Hönisch et al., 2013; Jonkers and Kučera, 2017) and this study calculate the 'empirical' calcification depth by comparing proxy-based temperature estimates with hydrological temperatures. This depth represents the apparent average calcification depth of the species. The deeper calcification depth of *G. ruber* (w) and *G. sacculifer* (w/o sac) at tropical latitudes than at moderate latitudes derived based on Mg/Ca in this study is consistent with that derived from $\delta^{18}O_c$ (Jonkers and Kučera, 2017). The ~50 m calcification depth of *G. ruber* (w) found in this study is also consistent with the maximum concentration of *G. ruber* (w) observed ~50 m during April and May between 2°S and 2°N (Jones, 1967).

3.5.4 Salinity effect

Based on the new Atlantic meridional transect core-top data, *G. ruber* (w) Mg/Ca is affected by salinity, but *G. sacculifer* (w/o sac) Mg/Ca seems not. The salinity effect on *G. ruber* (w) Mg/Ca is 13.2±2.8% per salinity unit without considering variations of seasonality and calcification depth in different latitude ranges. When these variations are taken into account, the salinity effect on *G. ruber* (w) Mg/Ca is reduced to 0.0-10.0 % per salinity unit, which is much weaker than that in (Arbuszewski et al., 2010). The salinity effect can be as low as 1.8±3.1% per salinity unit, if *G. ruber* (w) is assumed to calcify at 30 m during summer at temperate latitude and at 50 m all year round at tropical latitude. This choice of the calcification depth and seasonality is supported by current knowledge about calcification depth and seasonality of *G. ruber* (w), as discussed in section 3.5.3. In this case, the derived salinity effect is comparable to those obtained from culture experiments (Lea et al., 1999; Kısakurek et al., 2008; Dueñas-Bohórquez et al., 2009; Hönisch et al., 2013).

No salinity effect on *G. sacculifer* (w/o sac) Mg/Ca can be detected, in contrast to *G. ruber* (w). In a culture experiment, *G. sacculifer* (w/o sac) Mg/Ca is observed to be affected by salinity (Hönisch et al., 2013). The reason for the absence of the salinity effect on *G. sacculifer* (w/o sac) is unclear, but it is suspected to be related with the uncertainties in *G. sacculifer* (w/o sac) Mg/Ca introduced by dissolution correction. The salinity effect on *G. sacculifer* (w/o sac), if present, would be small, according to that culture study (Hönisch et al., 2013) and the result for *G. ruber* (w). It is possible that such a small salinity effect could be disguised by the uncertainties incurred by dissolution correction, so that it is not detectable from the core-top data. This is evident from the overall lower r^2 values between *G. sacculifer* (w/o sac) Mg/Ca and temperatures compared to r^2 values between *G. ruber* (w) Mg/Ca and temperatures.

Taken together, Mg/Ca in neither *G. ruber* (w) nor *G. sacculifer* (w/o

sac) are strongly affected by salinity, although a statistically significant salinity influence can be detected for *G. ruber* (w) Mg/Ca. These results are consistent with culture studies, and resolve the long-standing debate regarding the salinity effect on planktonic Mg/Ca. This salinity effect on *G. ruber* (w) Mg/Ca is negligible compared to the influence of temperatures in the open ocean on the glacial-interglacial timescale. This warrants Mg/Ca as a reliable paleotemperature proxy on this timescale.

3.6 Salinity effects inferred from Mg/Ca and $\delta^{18}O_c$

Apart from the discrepancy between T_{Mg} and hydrological temperatures, a strong salinity effect on *G. ruber* (w) Mg/Ca was also inferred from the discrepancy between T_{Mg} and T_{iso} (Mathien-Blard and Bassinot, 2009; Arbuszewski et al., 2010) (see Section 3.1 for details). Here, I compare T_{Mg} with T_{iso}, and calculate Mg/Ca_{xs} from these two temperature estimates. Mg/Ca_{xs} are then compared with salinity to test for any salinity effect. This complements the comparison between T_{Mg} and hydrological temperatures.

	Reference	n
G. ruber (w)	(This study) (Mg/Ca), (Arbuszewski et al., 2010) ($\delta^{18}O_c$)	33
	(Dekens et al., 2002)	18
	(Mathien-Blard and Bassinot, 2009)	11
G. sacculifer (w/o sac)	(This study)	38
	(Dekens et al., 2002)	18

Table 3.2: Source of paired Mg/Ca-$\delta^{18}O_c$ data in the open Atlantic.

Paired Mg/Ca-$\delta^{18}O_c$ for *G. ruber* (w) and *G. sacculifer* (w/o sac) are compiled from Mg/Ca-$\delta^{18}O_c$ in the open Atlantic from this and previous studies (Table 3.2). T_{Mg} are calculated from dissolution-corrected Mg/Ca using Equation 3.1, and T_{iso} are calculated from $\delta^{18}O_c$ and hydrological salinity. To calculate T_{iso}, $\delta^{18}O_{sw}$ is first estimated from S using regional $\delta^{18}O_{sw}$-S covariations based on paired $\delta^{18}O_{sw}$-S measurements (Schmidt et al., 1999) (Equation 3.9). In the open Atlantic, $\delta^{18}O_{sw}$ strongly covaries with salinity

(Schmidt et al., 1999):

$$\delta^{18}O_{sw} = M \times S + N, \tag{3.9}$$

where M and N are latitude-dependent coefficients of the correlation determined by the paired $\delta^{18}O_{sw}$-S measurements in the upper Atlantic seawater (<200 m) as compiled in (Schmidt et al., 1999) (Figure 3-12, Table 3.3). A gridded $\delta^{18}O_{sw}$ map based on the paired $\delta^{18}O_{sw}$-S measurements compiled in (Schmidt et al., 1999) is available, but $\delta^{18}O_{sw}$ at any site without $\delta^{18}O_{sw}$-S measurement nearby (within 550 km) still largely depends on the regional $\delta^{18}O_{sw}$-S covariation (LeGrande and Schmidt, 2006). $\delta^{18}O_{sw}$ derived from the regional $\delta^{18}O_{sw}$-S covariation are generally consistent with data extracted from the gridded map in the Atlantic (LeGrande and Schmidt, 2006) (Figure 3-12B-D). With $\delta^{18}O_{sw}$ estimated from salinity, T_{iso} is calculated from $\delta^{18}O_c$ and $\delta^{18}O_{sw}$ using the low light calibration of Bemis et al. (1998) (Equation 3.10):

$$\begin{aligned} T_{iso} &= 16.5 \pm 0.2 - (4.8 \pm 0.16) \times (\delta^{18}O_c - \delta^{18}O_{sw} + 0.27), \\ T_{iso} &= 16.5 \pm 0.2 - (4.8 \pm 0.16) \times (\delta^{18}O_c - M \times S - N + 0.27). \end{aligned} \tag{3.10}$$

It is noted that using salinity at different water depths or seasons generates similar T_{iso} (variation < 0.5°C), because variation of salinity at any particular site is small.

	Latitude range	M	N	RMSE	n
North Atlantic*	15-40°N	0.52	-18.01	0.25	213
Tropical Atlantic	10°S-15°N	0.14	-4.41	0.34	337
South Atlantic	10-40°S	0.49	-16.95	0.12	98

*: Mediterranean sites are excluded.

Table 3.3: Summary of regional $\delta^{18}O_{sw}$-S correlation in the open Atlantic.

The comparisons between T_{Mg} and T_{iso} for both species are shown in Figure 3-13A, B. *G. ruber* (w) T_{Mg} and T_{iso} are significantly correlated, with an r^2 value of 0.55. In the North Atlantic, *G. ruber* (w) T_{Mg} and T_{iso} gen-

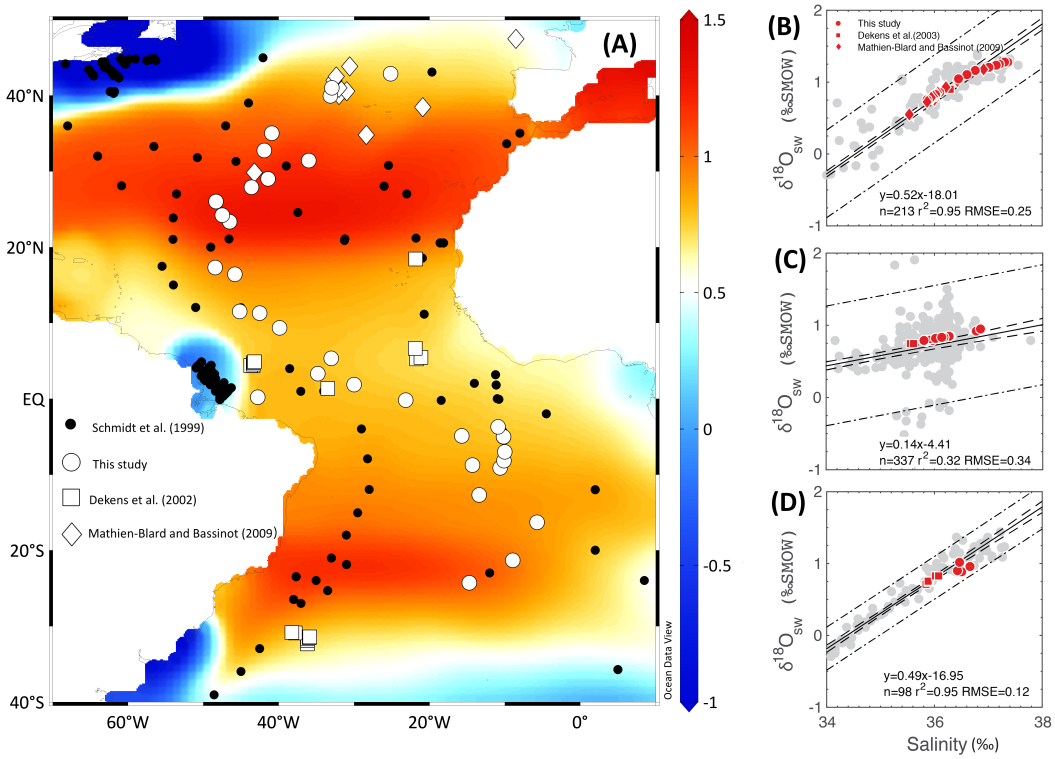

Figure 3-12: Regional $\delta^{18}O_{sw}$-S correlations in the open Atlantic. (A): Sea surface $\delta^{18}O_{sw}$ map of the Atlantic. Data are from LeGrande and Schmidt (2006). Black dots are sites with both measured $\delta^{18}O_{sw}$ and salinity from Schmidt et al. (1999). White symbols are *G. ruber* (w) core top sites with published $\delta^{18}O_c$ in the open Atlantic. (B)-(D): Comparison between $\delta^{18}O_{sw}$ calculated from regional $\delta^{18}O_{sw}$-S covariation and extracted from gridded map (LeGrande and Schmidt, 2006) in the north, tropical, and south Atlantic, respectively. Grey dots are $\delta^{18}O_{sw}$-S data compiled in (Schmidt et al., 1999), showing regional covariations between $\delta^{18}O_{sw}$ and salinity in upper 200 m seawater. Red symbols are $\delta^{18}O_{sw}$ estimated using gridded map of LeGrande and Schmidt (2006) versus annual salinity at 30 m at all the core-top sites in the north, tropical, and south Atlantic respectively. Solid lines are regression lines for data from Schmidt et al. (1999). Dashed lines and dash-dot lines are functional and observation prediction intervals at 95% confidence level, respectively. Different shapes of symbols represent data sources: circle, this study (Mg/Ca) and Arbuszewski et al. (2010) ($\delta^{18}O_c$); square, Dekens et al. (2002); diamond, Mathien-Blard and Bassinot (2009).

erally plot along the 1:1 line, with most T_{Mg} and T_{iso} within a ±2°C range. In the South Atlantic, *G. ruber* (w) T_{Mg} is on average higher than T_{iso}. In the tropical Atlantic, *G. ruber* (w) T_{Mg} is on average lower than T_{iso}. Similar

patterns are seen for T_{Mg} and T_{iso} of *G. sacculifer* (w/o sac) (Figure 3-13B). The different T_{Mg}-T_{iso} patterns in different latitude ranges might result from insufficient $\delta^{18}O_{sw}$ data coverage in the tropical and South Atlantic. As detailed by Hönisch et al. (2013), the current $\delta^{18}O_{sw}$-S measurements are mostly clustered in the western tropical and south Atlantic, it is possible that $\delta^{18}O_{sw}$-S correlation defined in the western Atlantic may not be representative of the $\delta^{18}O_{sw}$-S correlation at the core-top sites, which causes the offset between T_{iso} and T_{Mg}. It is argued here that the similar temperature estimates from Mg/Ca and $\delta^{18}O_c$ in the North Atlantic, where the $\delta^{18}O_{sw}$-S correlation is well-defined, can demonstrate these two proxies are consistent with each other.

Mg/Ca_{xs} of both species are compared with salinity in Figure 3-13C, D. Mg/Ca_{xs} of neither species show any correlation with salinity. *G. ruber* (w) Mg/Ca_{xs} in the North Atlantic varies within ± 0.5 mmol/mol range. In response to the offsets between T_{Mg} and T_{iso}, *G. ruber* (w) Mg/Ca_{xs} in the South and tropical Atlantic are biased towards positive and negative values, respectively. Nevertheless, when data from the entire Atlantic meridional transect are combined, *G. ruber* (w) Mg/Ca_{xs} is not correlated with salinity. *G. sacculifer* (w/o sac) Mg/Ca_{xs} does not show a correlation with salinity either. The lack of correlation between Mg/Ca_{xs} and salinity for both *G. ruber* (w) and *G. sacculifer* (w/o sac) discounts a salinity effect on *G. ruber* (w) and *G. sacculifer* (w/o sac) Mg/Ca from the comparison between Mg/Ca and $\delta^{18}O_c$. This corroborates the conclusion based on the comparison between Mg/Ca and hydrological temperature as shown in Section 3.5.

3.7 Conclusions

In this chapter, I reevaluate the salinity effects on Mg/Ca in *G. ruber* (w) and *G. sacculifer* (w/o sac) using the Atlantic meridional core-tops. This is done by comparing Mg/Ca in these species with hydrological temperatures and with temperatures estimated from $\delta^{18}O_c$. No salinity effect on *G. sacculifer*

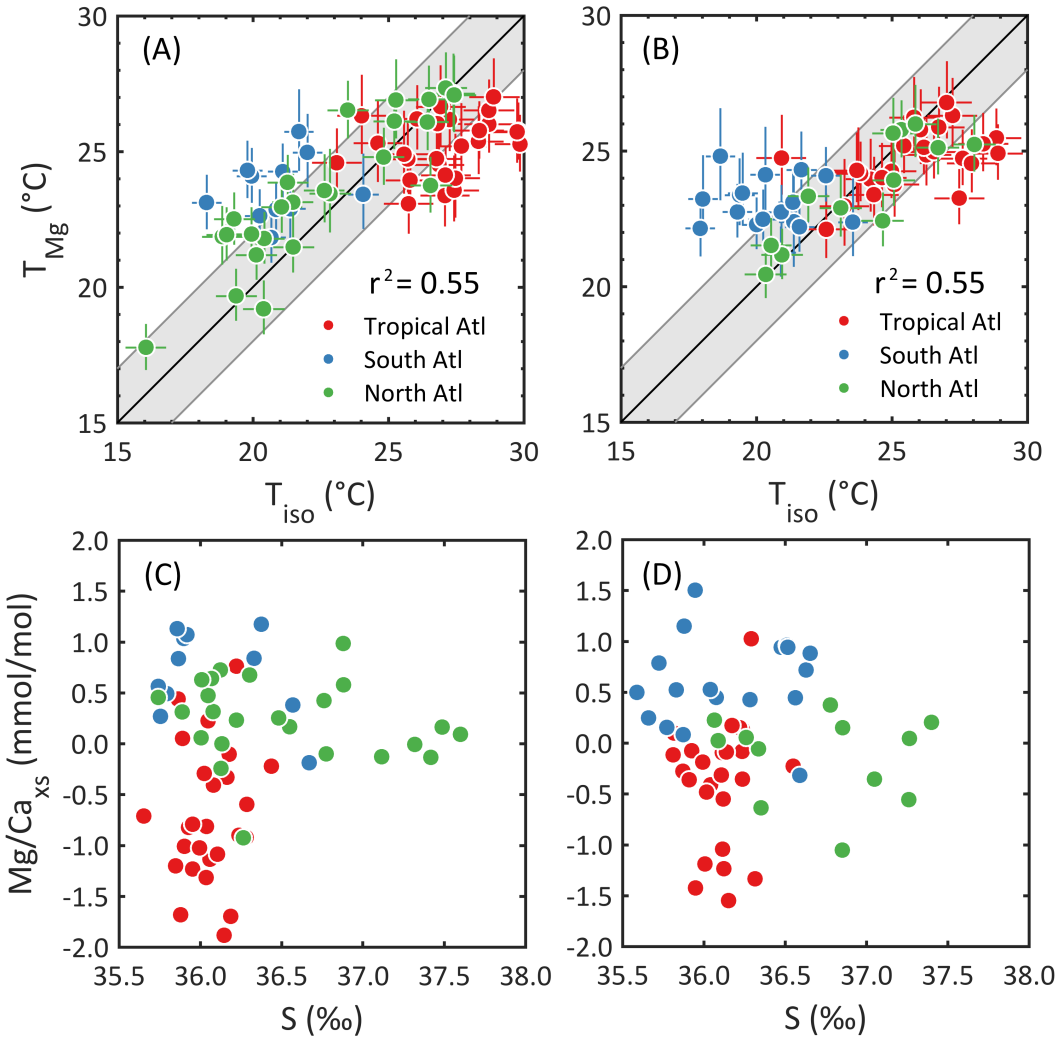

Figure 3-13: Panel (A) and (B): comparisons between T_{Mg} and T_{iso} for *G. ruber* (w) and *G. sacculifer* (w/o sac), respectively. The error bars are $\pm 1\sigma$ uncertainty generated from Monte-Carlo methods. The solid lines with gray envelops are 1:1 lines with ± 2°C uncertainties, which is roughly $\pm 2\sigma$ uncertainty for both temperature estimates. Panel (C) and (D): comparisons between Mg/Ca_{xs} and salinity for *G. ruber* (w) and *G. sacculifer* (w/o sac), respectively. Red, blue, and green dots represent data from the tropical, South, and North Atlantic, respectively.

(w/o sac) Mg/Ca is detected from comparisons of Mg/Ca with temperatures from either hydrological data or from oxygen isotopes. On the other hand, *G. ruber* (w) Mg/Ca is observed to be influenced by salinity, based on a comparison of Mg/Ca with hydrological data. However, the salinity effect on *G. ruber* (w) Mg/Ca derived in this study is much smaller than reported by pre-

vious core-top studies (Arbuszewski et al., 2010; Mathien-Blard and Bassinot, 2009). When variations of seasonality and calcification depths of *G. ruber* (w) are taken into account, a small salinity effect comparable to that observed in culture experiments can be obtained. Therefore, it is argued here that the long-standing debate on the salinity effect on planktonic Mg/Ca between core-tops and culture studies can be reconciled by acknowledging seasonality and calcification depths of planktonic foraminifera from varying latitudes. Consequently, using planktonic Mg/Ca as a proxy for sea surface temperature is negligibly affected by salinity variations, in the open ocean, on the glacial-interglacial timescale. At the same time, attention should be paid to temperatures reconstructed from Mg/Ca, because the reconstructed temperature is associated with the preferred calcification depths and seasons of the studied foraminiferal species.

Chapter 4

Environmental controls on planktonic B/Ca

4.1 Introduction

Planktonic B/Ca has been regarded as a promising proxy for surface seawater carbonate chemistry (Yu et al., 2007b; Allen et al., 2012; Penman et al., 2014). This is based on pH-dependent boron speciation in seawater and preferred incorporation of charged boron species, $B(OH)_4^-$, into calcite (Figure 4-1) (Hemming and Hanson, 1992). The effect of carbonate chemistry on planktonic B/Ca have indeed been observed (Yu et al., 2007b; Foster, 2008; Allen et al., 2011, 2012). Some recent observations suggested that planktonic B/Ca might be strongly affected by vital effects (Babila et al., 2014; Salmon et al., 2016). These vital effects, if valid, could compromise the use of planktonic B/Ca to reconstruct surface seawater carbonate chemistry.

The main objective of this chapter is to investigate environmental controls on B/Ca in planktonic foraminiferal shells using core-top samples from the Atlantic meridional transect. Previous studies on planktonic foraminiferal B/Ca are first summarized. Environmental controls on B/Ca in *G. ruber* (w) and *G. sacculifer* (w/o sac) from the Atlantic meridional transect are discussed subsequently.

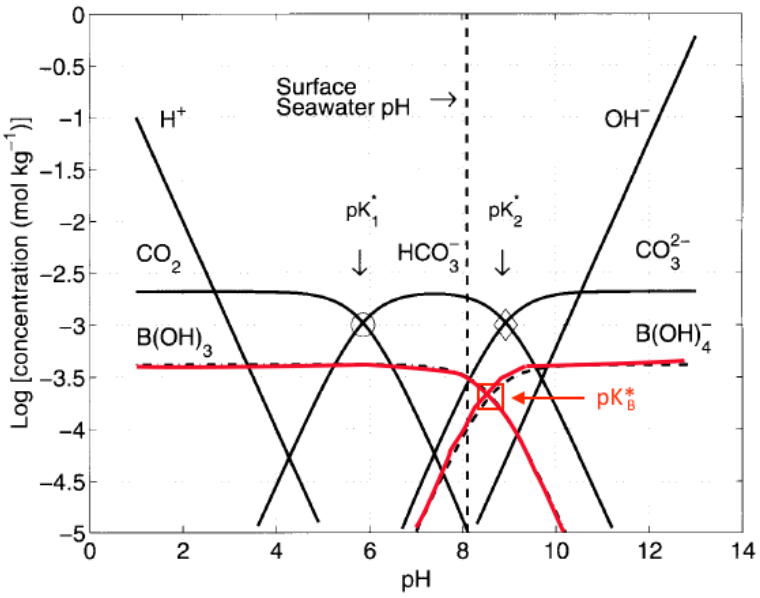

Figure 4-1: Bjerrum plot of carbonate and borate systems, at T = 25 °C, S = 35. As pK_B is close to the average surface seawater pH, the relative abundances of $B(OH)_3$ and $B(OH)_4^-$ are sensitive to carbonate system change. This figure is modified from (Zeebe and Wolf-Gladrow, 2001).

4.2 Previous work

4.2.1 Carbonate chemistry control

If $B(OH)_4^-$ is the only species incorporated into calcite as previously proposed (Hemming and Hanson, 1992; Sanyal et al., 2000; Yu et al., 2007b), carbonate chemistry would exert a primary control on B/Ca in foraminiferal calcite. A carbonate chemistry control on planktonic B/Ca has been reported by both core-top (Yu et al., 2007b; Foster, 2008) and culture studies (Allen et al., 2011, 2012; Henehan et al., 2015). Positive correlations between B/Ca and $\frac{[B(OH)_4^-]}{[HCO_3^-]}$ have been observed for *Globigerina bulloides*, *Globorotalia inflata*, and *Globigerinoides sacculifer* from core-tops (Yu et al., 2007b; Foster, 2008). These core-top studies also found that K_D, defined as the ratio of B/Ca in planktonic foraminiferal shell to $\frac{[B(OH)_4^-]}{[HCO_3^-]}$ in seawater (Equation 1.8) is not constant, but covaries with temperature or $[CO_3^{2-}]$, hinting at a secondary control on boron incorporation through K_D (Yu et al., 2007b; Foster, 2008).

In culture studies, positive correlations between B/Ca and $\frac{[B(OH)_4^-]}{[HCO_3^-]}$ have also been observed for *Orbulina universa*, *Globigerinoides ruber* (pink and white), and *G. sacculifer* (Allen et al., 2011, 2012; Henehan et al., 2015). However, no temperature effect on planktonic foraminiferal B/Ca was observed in culture studies, suggesting that the temperature control on B/Ca discovered in core-top studies possibly resulted from the influence of the hydrological parameter(s) covarying with temperature (Allen et al., 2011, 2012).

Several questions regarding controlling factors on planktonic B/Ca have been raised by both core-top and culture studies. Firstly, the sensitivity of B/Ca to $[B(OH)_4^-]$ was significantly higher when $[B(OH)_4^-]$ was raised by increasing total boron concentration in seawater than by adjusting seawater pH in culture experiments (Allen et al., 2011). The cause for this difference remains unknown, but *O. universa* $\delta^{11}B$ data excluded the possibility of significant incorporation of $B(OH)_3$ (Sanyal et al., 2000; Henehan et al., 2016). Secondly, B/Ca in a few species were correlated with salinity in culture studies, which still lacks plausible explanations (Allen et al., 2011, 2012). Allen et al. (2012) tried to explain this salinity effect on B/Ca by investigating the influence of salinity on equilibrium constants and ion strength, but found these influences were too small to account for the observed B/Ca variation. Thirdly, B/Ca were not correlated to $\frac{[B(OH)_4^-]}{[HCO_3^-]}$ for *G. ruber* (w) according to core-top and sediment trap studies. The variation of *G. ruber* B/Ca was larger than predicted from seawater carbonate chemistry (Foster, 2008; Henehan et al., 2015; Babila et al., 2014). To account for the weak correlations between seawater carbonate chemistry and planktonic B/Ca, many studies have invoked 'vital effects' on planktonic B/Ca.

4.2.2 Vital effect

Vital effects refer to impacts on B/Ca in shell calcite that are imposed by physiological activities of foraminifera. Mineralization of foraminiferal $CaCO_3$

is highly mediated by metabolic processes within foraminifera (*e.g.*, Erez, 2003; De Nooijer et al., 2014). Nucleation and growth of calcite are regulated by organic templates formed during calcification. The composition of the calcifying fluid is manipulated by foraminifera. The chemical microenvironment surrounding the organism is affected by calcification and respiration of the foraminifera itself and photosynthesis of symbiotic organisms. For these three reasons, foraminiferal B/Ca can deviate from the prediction based on ambient seawater carbonate chemistry following the proposition of Hemming and Hanson (1992). Recent studies have focused on two aspects of vital effects: modification of carbonate chemistry of the microenvironment and calcification rate of foraminifera.

Modification of microenvironments. In the immediate vicinity of a foraminiferal shell, diffusion is the only way for ions to transport (*e.g.*, Zeebe et al., 1999; Wolf-Gladrow et al., 1999). A chemical gradient develops between the microenvironment and the ambient seawater, due to the low rate of ion diffusion and slow equilibrium of calcification, respiration, and photosynthesis of symbionts. In the microenvironment, calcification and respiration release CO_2 lowering pH, while photosynthesis of symbionts takes up CO_2 raising pH. The relative strengths of these competing processes affect B/Ca in $CaCO_3$ by regulating pH of the microenvironment, since relative proportions of $B(OH)_4^-$ and $B(OH)_3$ are pH dependent, and $B(OH)_4^-$ is preferentially incorporated into calcites.

The influence of the altered microenvironments on planktonic B/Ca has been supported by intra-shell B/Ca variation of a planktonic foraminiferal species *O. universa* (Holland et al., 2017). Because Mg-banding within *O. universa* shells reflects diurnal cycles (Eggins et al., 2004; Spero et al., 2015), the phase relation of B-banding with Mg-banding can be used to determine the relation of B-banding to the diurnal cycle. Within an *O. universa* shell, B-banding tracks Mg-banding, showing high B/Ca within diurnal banding and

low B/Ca within nocturnal banding (Holland et al., 2017). This is consistent with the idea that symbiont photosynthesis can increase B/Ca in foraminiferal shells by raising pH, thus the proportion of boron in the calcifying fluid as $B(OH)_4^-$.

The influence of the microenvironment chemistry on planktonic B/Ca has also been inferred from B/Ca in bulk samples. In a sediment trap study, monthly fluctuations of *G. ruber* (w) B/Ca were in accord with the daily peak light intensities (Babila et al., 2014). This correlation was attributed to the influence of the pH in the microenvironment on planktonic B/Ca. These authors proposed that pH in the microenvironment was increased by photosynthesis, in response to increasing light intensity. The physiological activities were also thought to be responsible for inter-species B/Ca differences (Henehan et al., 2016). Without photosynthesis raising the microenvironment pH, symbiont-barren species tend to have lower B/Ca compared to symbiont-bearing species (Yu et al., 2007b; Henehan et al., 2016).

Calcification rate. It has been demonstrated that the B partition coefficient can be promoted by high calcification rates, which suggests the incorporation of $B(OH)_3$ into calcite (Gabitov et al., 2014; Uchikawa et al., 2015; Kaczmarek et al., 2016). Several studies suggested that the calcification rate can influence B/Ca in foraminiferal calcite, based on the correlations between B/Ca and several indicators of the calcification rate. For example, B/Ca in several planktonic foraminiferal species from sediment traps are correlated to shell area density (shell density), which was attributed to a calcification rate control (Salmon et al., 2016). A calcification rate control has also been inferred from correlations between B/Ca in two symbiont-barren species and $[CO_3^{2-}]$, since the calcification rate is thought to increase with increasing ambient $[CO_3^{2-}]$ (Krupinski et al., 2017). Unfortunately, due to the difficulty in quantifying foraminiferal calcification rates, direct evidence for a calcification rate control on planktonic foraminiferal B/Ca is still lacking.

4.3 Materials and methods

4.3.1 Sample preparation and B/Ca measurement

B/Ca were measured in *G. ruber* (w) and *G. sacculifer* (w/o sac) from core-tops from the Atlantic meridional transect. These core-tops cover broad ranges in latitude (35 °S to 45 °N) and water depth (1.7 km to 5.2 km) (Figure 4-2). *G. ruber* (w) and *G. sacculifer* (w/o sac) shells were picked from 57 and 60 core-tops, respectively. For each sample, 50 tests from the 250-355 μm size fraction were picked. The narrow size fraction range was used to minimize a potential size effect on B/Ca (Ni et al., 2007). These shells were crushed, rinsed with Milli-Q water and methanol, and checked under a microscope to remove foreign particles using a single-haired brush (Yu et al., 2007a). In a clean lab, *G. ruber* (w) samples were cleaned with both oxidative and reductive steps (Boyle and Keigwin, 1985; Barker et al., 2003). All *G. sacculifer* (w/o sac) samples were firstly oxidatively cleaned. Fifteen of these samples were then split into two subsamples, one of which was further reductively cleaned. B/Ca of the subsamples cleaned with the reductive step are 3% higher than those cleaned by the oxidative step only ($B/Ca_r = 1.034 \times B/Ca_o$, n=15, $r^2 = 0.81$, intercept forced to zero, Figure 4-3). Such a difference is comparable to the analytical precision of ~3% (see the next paragraph), confirming minimal B/Ca bias introduced by cleaning methods (Yu and Elderfield, 2007). No correction is thus applied to B/Ca for *G. sacculifer* (w/o sac) cleaned by different methods.

B/Ca were measured along with Mg/Ca and other trace element to calcium ratios on a Varian 820 ICP-MS at the Australian National University (ANU) following the method of Yu et al. (2005). The analytical precision for B/Ca, based on repeated analyses of an in-house solution standard, is 2.7% (151.4±4.2 μmol/mol, 2σ). Other ratios including Fe/Ca, Mn/Ca, and Al/Ca were also measured to monitor potential contaminations from Fe/Mn hydroxide coatings and the effectiveness of clay removal. There are no correlations

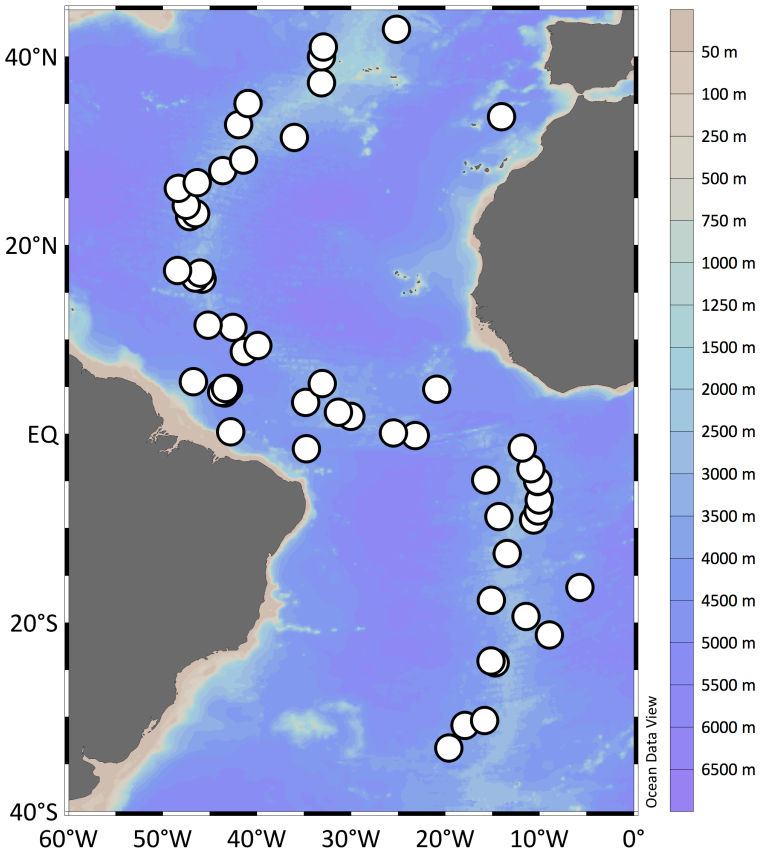

Figure 4-2: A map showing core-tops locations and water depths.

between B/Ca and Fe/Ca, Mn/Ca, or Al/Ca for foraminiferal samples measured, suggesting a minimal influence of contamination phases on B/Ca results in this study.

4.3.2 Environmental parameter calculation

To evaluate possible influences from ambient seawater condition on B/Ca in planktonic foraminiferal shells, environmental parameters for *G. ruber* (w) and *G. sacculifer* (w/o sac) are estimated at their preferred calcification depths, based on detailed work in Chapter 3. Seasonal temperature, salinity, nutrient concentration data are extracted from the WOA2009 dataset (Locarnini et al., 2010; Antonov et al., 2010). Seawater total alkalinity (ALK), dissolved inorganic carbon (DIC), and anthropogenic CO_2 are extracted from GLODAP dataset (Key et al., 2004). DIC is corrected to the preindustrial level by remov-

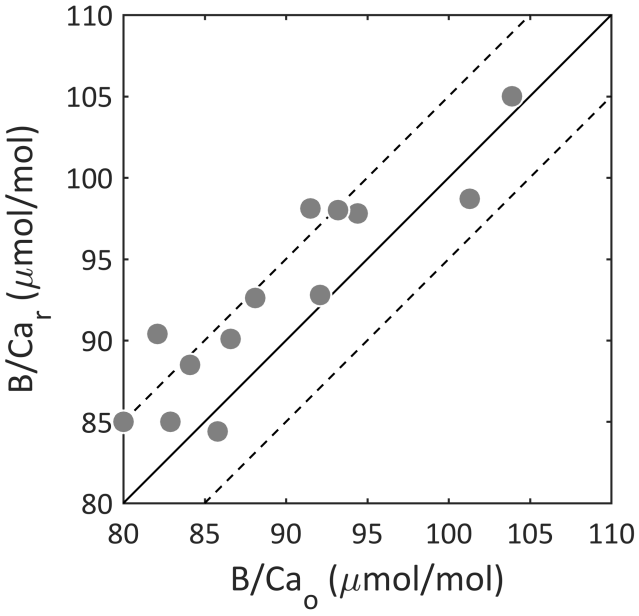

Figure 4-3: Effect of cleaning methods on B/Ca. B/Ca_r: *G. sacculifer* (w/o sac) B/Ca of subsamples cleaned with both reductive and oxidative steps, B/Ca_o *G. sacculifer* (w/o sac) B/Ca of subsamples cleaned with oxidative step only. The solid black line is the 1:1 line, and the dashed black lines represent the ± 5 μmol/mol range.

ing the anthropogenic CO_2 (Sabine et al., 2004). Total boron concentration is estimated from salinity based on the relationship from (Lee et al., 2010). These data are used to calculate $[CO_3^{2-}]$, $[HCO_3^-]$, and $[B(OH)_4^-]$, by CO2sys v2.1 (Lewis et al., 1998), using the same constants as in (Yu and Elderfield, 2007).

4.4 Results

B/Ca in *G. ruber* (w) and *G. sacculifer* (w/o sac) along the Atlantic meridional transect are shown in Figure 4-4. These core-tops are divided into the tropical, South, and North Atlantic sites, because the average B/Ca differ in different latitude ranges. The tropical Atlantic sites are between 10°S and 15°N. The North and South Atlantic sites are north of 15°N and south of 10°S, respectively. The meridional distributions of B/Ca in *G. ruber* (w) and *G.*

sacculifer (w/o sac) are different. *G. ruber* (w) B/Ca are the highest in the tropical Atlantic, with the average of 112 ± 6 μmol/mol (n = 27, standard deviation). *G. ruber* (w) B/Ca are 107 ± 6 μmol/mol (n = 19) and 95 ± 5 μmol/mol (n = 11) in the North and South Atlantic, respectively. For *G. sacculifer* (w/o sac), B/Ca are higher in the North Atlantic, with the average of 93 ± 6 μmol/mol (n = 21), compared to 84 ± 3 μmol/mol (n = 39) in the South and the tropical Atlantic. Owing to the difference in the meridional distributions of B/Ca in both species, the inter-species B/Ca differences are apparently greater in the tropical Atlantic.

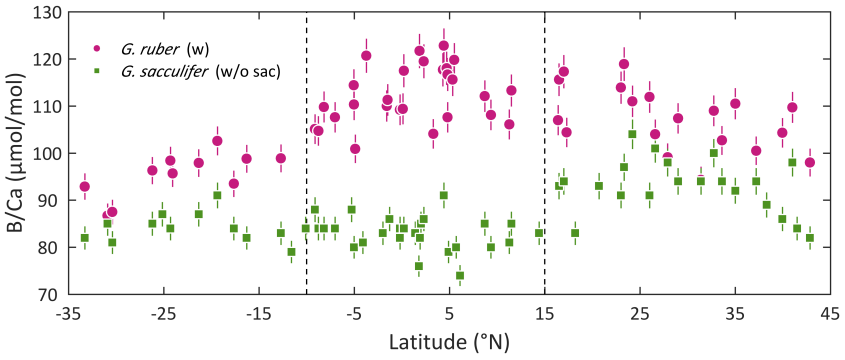

Figure 4-4: Core-top B/Ca data. The magenta circles and the green squares represent B/Ca in *G. ruber* (w) and *G. sacculifer* (w/o sac), respectively. Errorbars show the 3% relative standard deviation. The dashed lines indicate the latitude boundaries of the North, tropical, and South Atlantic.

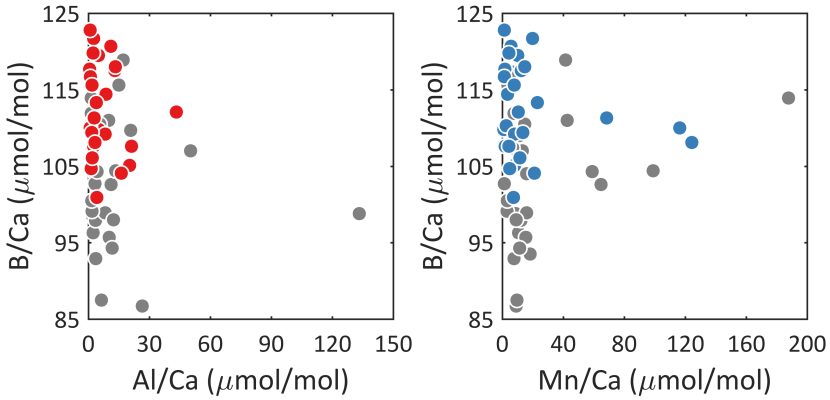

Figure 4-5: Cross plot of *G. ruber* (w) B/Ca versus Al/Ca and Mn/Ca. The gray dots are the North and South Atlantic core-tops, and the red and blue dots are the tropical Atlantic core-tops.

The varying inter-species B/Ca gradients in different latitude ranges are unexpected. However, it is argued here that this is a robust feature, rather

than the result of contamination to the *G. ruber* (w) B/Ca with the apparent higher values, *G. ruber* (w) B/Ca in the tropical Atlantic, specifically. First, it is unreasonable that only *G. ruber* (w) samples at tropical latitudes were contaminated during sample preparation, as all the *G. ruber* (w) samples were treated together in a random order in the lab. Second, *G. ruber* (w) samples were thoroughly cleaned. No correlations are observed between B/Ca and Al/Ca or Mn/Ca, and average Al/Ca and Mn/Ca of *G. ruber* (w) from tropical latitudes are not higher than those from temperate latitudes (Figure 4-5). Third, new *G. ruber* (w) B/Ca from this study are comparable to published results for the Atlantic (Foster, 2008; Henehan et al., 2015). Therefore, contamination to the shells is unlikely a contributor to the higher *G. ruber* (w) B/Ca from the tropical Atlantic. Data with high Al/Ca and Mn/Ca are also included in further discussion.

4.5 Environmental controls on B/Ca in planktonic foraminifera

The potential environmental controls of seawater carbonate chemistry, salinity, $[PO_4^{3-}]$, and temperature on B/Ca in *G. ruber* (w) and *G. sacculifer* (w/o sac) are discussed in this section, following the previous core-top and culture studies (Yu et al., 2007b; Allen et al., 2011, 2012; Henehan et al., 2015). Owing to the regional differences in B/Ca of both *G. ruber* (w) and *G. sacculifer* (w/o sac), regression analyses are carried out between B/Ca and environmental parameters with or without including data from the tropical Atlantic. Correlations between *G. ruber* (w) and *G. sacculifer* (w/o sac) B/Ca with environmental parameters are summarized in Figure 4-6, 4-7, and Table 4.1.

G. ruber (w) B/Ca are not correlated to $\frac{[B(OH)_4^-]}{[HCO_3^-]}$, $[CO_3^{2-}]$, pH, salinity or $[PO_4^{3-}]$, but are correlated to temperature (Figure 4-6, and Table 4.1). When tropical *G. ruber* (w) B/Ca are excluded, the correlations of B/Ca with

$\frac{[B(OH)_4^-]}{[HCO_3^-]}$, $[CO_3^{2-}]$, salinity, and $[PO_4^{3-}]$ become significant. The tropical *G. ruber* (w) B/Ca are above the regression lines defined by *G. ruber* (w) B/Ca at temperate latitudes, while ranges of the environmental parameters in the tropical Atlantic are within those in the temperate Atlantic. It seems that *G. ruber* (w) B/Ca in the tropical Atlantic are further influenced by another process, which will be discussed later in this chapter (Section 4.6). For now, they are excluded from the discussion about environmental controls on B/Ca mentioned by previous studies.

G. sacculifer (w/o sac) B/Ca are significantly correlated to $\frac{[B(OH)_4^-]}{[HCO_3^-]}$, $[CO_3^{2-}]$, $[PO_4^{3-}]$, and salinity, but not with pH or temperature (Figure 4-7, Table 4.1). Including data from the tropical Atlantic or not, the significance of the correlations is similar. The sensitivities of *G. sacculifer* (w/o sac) B/Ca to $\frac{[B(OH)_4^-]}{[HCO_3^-]}$, $[CO_3^{2-}]$, $[PO_4^{3-}]$, and salinity are also similar with or without including data from tropical latitudes.

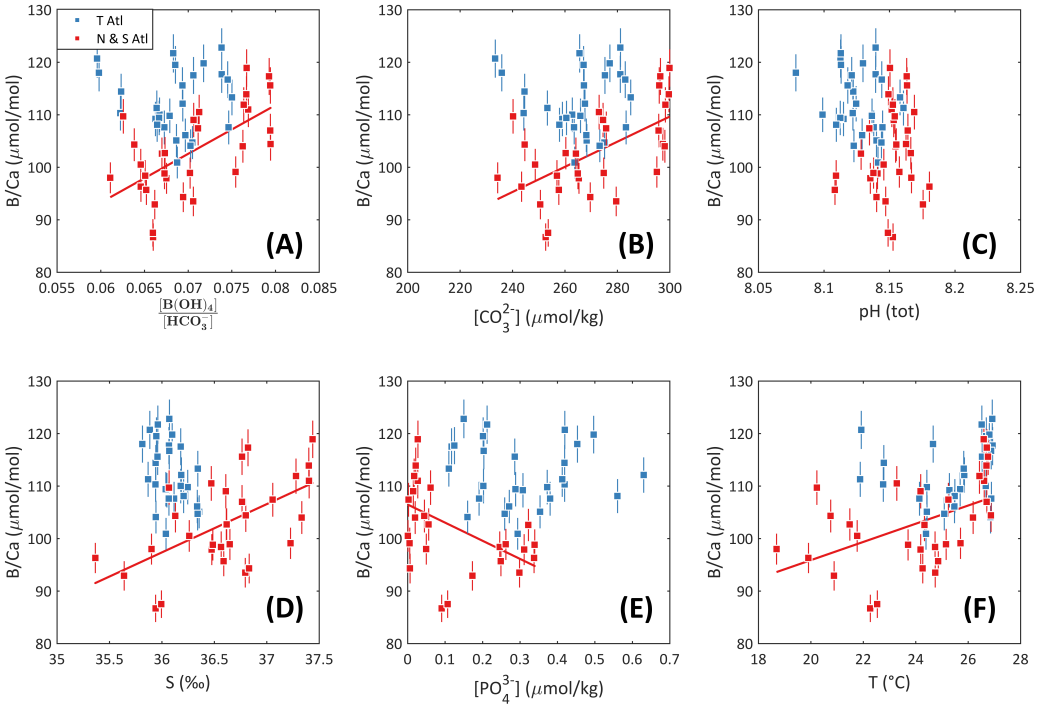

Figure 4-6: *G. ruber* (w) B/Ca compared with surface seawater environmental parameters. Red and blue squares are data from the temperate and tropical Atlantic, respectively. The red lines show the regression results from the temperate Atlantic, when the correlations are significant ($p < 0.05$).

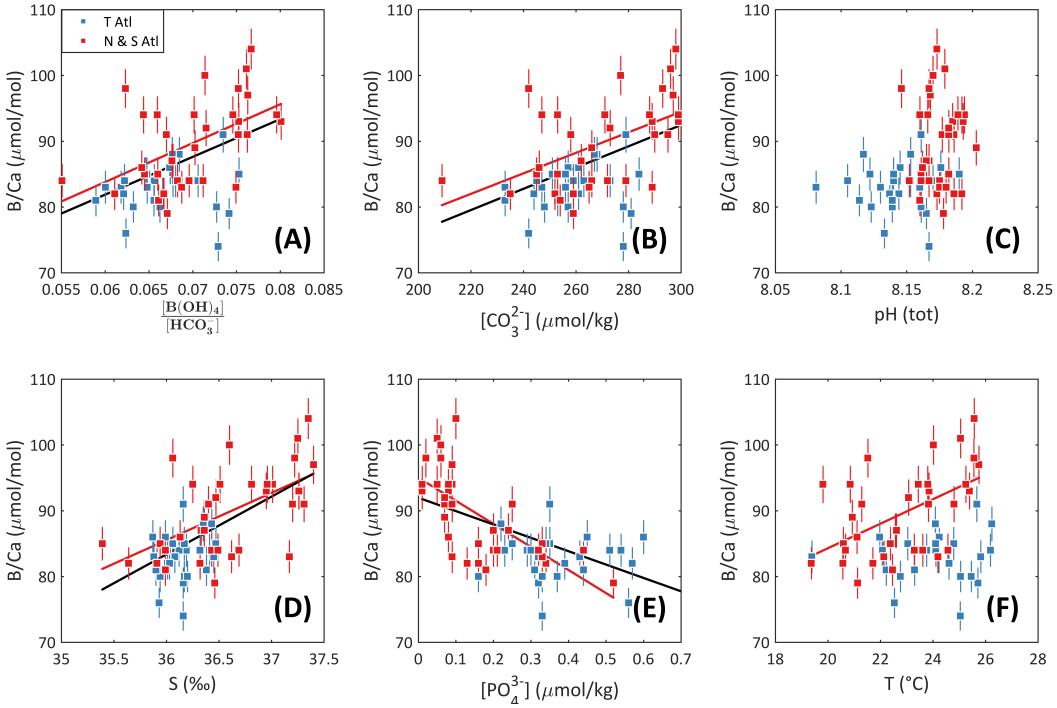

Figure 4-7: *G. sacculifer* (w/o sac) B/Ca compared with surface seawater environmental parameters. Red and blue squares are data from the temperate and tropical Atlantic, respectively. The red lines show the regression results from the temperate Atlantic, while the black lines are the regression results for all data. The regression line is shown if the correlation is significant ($p < 0.05$).

		$\frac{[B(OH)_4^-]}{[HCO_3^-]}$	$[CO_3^{2-}]$	pH	S	$[PO_4^{3-}]$	T
				G. ruber (w)			
All	r^2	0.06	0.06	0.09	0.00	0.01	0.23
	p	0.064	0.069	0.02	0.886	0.391	<0.001
N & S Atl	r^2	0.40	0.37	0.03	0.33	0.27	0.24
	p	<0.001	<0.001	0.31	0.001	0.003	0.006
				G. sacculifer (w/o sac)			
All	r^2	0.23	0.24	0.12	0.41	0.36	0.03
	p	<0.001	<0.001	0.006	<0.001	<0.001	0.169
N & S Atl	r^2	0.26	0.27	0.00	0.33	0.46	0.27
	p	0.002	0.002	0.867	<0.001	<0.001	0.002

Table 4.1: Summary of regression analyses of *G. ruber* (w) and *G. sacculifer* (w/o sac) B/Ca with various environmental parameters.

4.5.1 Effects of dissolution correction

As described in Chapter 2, B/Ca in both *G. ruber* (w) and *G. sacculifer* (w/o sac) are susceptible to post-depositional dissolution. Dissolution corrections are applied to B/Ca to test whether dissolution correction could affect the correlations between B/Ca and environmental parameters. As discussed in Chapter 2, based on data from depth transects, the dissolution sensitivities of B/Ca to $\Delta[CO_3^{2-}]$ are 0.67 ± 0.22 and 0.59 ± 0.13 μmol/mol per μmol/kg for *G. ruber* (w) and *G. sacculifer* (w/o sac), respectively. However, due to the lack of dissolution-free samples, the threshold $\Delta[CO_3^{2-}]$ of the dissolution effect on B/Ca is not well constrained. It is thus difficult to correct for the dissolution effect directly. Although B/Ca declines are accompanied by a decline in Mg/Ca at different depth transects, the threshold $\Delta[CO_3^{2-}]$ for dissolution effects on B/Ca is not necessarily the same as that for Mg/Ca, because high Mg/Ca phases in the foraminiferal shell is not associated with high-B phases (Branson et al., 2015). In fact, some observation suggests Mg/Ca and B/Ca are anti-phased within the shell of a planktonic foraminiferal species *O. universa* (Holland et al., 2017).

As the correlations between B/Ca and environmental parameters are relatively weak, and the root-mean-square errors (RMSEs) of the correlations are large, it is suspected that dissolution may not be able to notably improve the correlations between B/Ca and environmental parameters. To test the influence of dissolution correction on the interpretation of the environmental controls on B/Ca, sensitivity tests using a series of $\Delta[CO_3^{2-}]$ thresholds are carried out. The effectiveness of dissolution correction is assessed by comparing sensitivities of B/Ca to environmental parameters and r^2 of the correlations with or without employing the correction.

Sensitivities of B/Ca to environmental parameters and r^2 are summarized in Table 4.2. Sensitivities of B/Ca to environmental parameters are not significantly changed by the dissolution correction for both species in most cases. r^2 values of B/Ca in neither *G. ruber* (w) nor *G. sacculifer* (w/o sac) with

any environmental parameters is significantly improved when the dissolution correction is included. Based on these two observations, applying dissolution correction will not change the conclusions based on uncorrected B/Ca. Although dissolution effect on B/Ca is clear for data from depth transects (Chapter 2), it appears that invoking the dissolution correction does not help better constrain environmental controls on planktonic B/Ca in the core-top data. This may be because, in a core-top set, dissolution on the seafloor only plays a minor role in contributing to the variability of B/Ca compared to parameters of the living environment. Therefore, dissolution corrections to B/Ca are not invoked in the further investigation of the environmental controls on B/Ca.

***G. ruber* (w) (N & S Atl)**

threshold $\Delta[CO_3^{2-}]$	$\frac{[B(OH)_4^-]}{[HCO_3^-]}$		$[CO_3^{2-}]$		$[PO_4^{3-}]$		S	
	r^2	sens.[a]	r^2	sens.[b]	r^2	sens.[c]	r^2	sens.[d]
Uncorrected	0.40	928	0.37	0.24	0.27	-34.5	0.34	9.2
10 μmol/kg	0.39	881	0.35	0.22	0.31	-35.4	0.32	8.5
21.3 μmol/kg	0.34	857	0.34	0.22	0.14	-22.5	0.24	7.8
30 μmol/kg	0.34	868	0.34	0.23	0.14	-14	0.24	7.8

***G. sacculifer* (w/o sac) (all)**

threshold $\Delta[CO_3^{2-}]$	$\frac{[B(OH)_4^-]}{[HCO_3^-]}$		$[CO_3^{2-}]$		$[PO_4^{3-}]$		S	
	r^2	sens.[a]	r^2	sens.[b]	r^2	sens.[c]	r^2	sens.[d]
Uncorrected	0.23	574	0.24	0.16	0.36	-20.3	0.41	8.8
10 μmol/kg	0.21	599	0.22	0.17	0.34	-21.4	0.37	9.0
21.3 μmol/kg	0.19	544	0.19	0.15	0.25	-17.4	0.25	7.2
30 μmol/kg	0.15	536	0.16	0.15	0.16	-15.8	0.20	7.3

[a]: unit μmol/mol, [b]: unit μmol/mol per μmol/kg, [c]: unit μmol/mol per μmol/kg, [d]: unit μmol/mol per ‰.

Table 4.2: Effect of dissolution correction on correlations between B/Ca and environmental parameters.

4.5.2 Carbonate chemistry parameters

B/Ca in *G. ruber* (w) and *G. sacculifer* (w/o sac) are significantly correlated to $\frac{[B(OH)_4^-]}{[HCO_3^-]}$ and $[CO_3^{2-}]$, but not pH (Figure 4-6, 4-7, and Table 4.1). This is coherent with carbonate chemistry controls on B/Ca in *G. ruber* and *G.*

sacculifer observed in culture experiments (Allen et al., 2012; Henehan et al., 2015).

$\frac{[\mathbf{B(OH)_4^-}]}{[\mathbf{HCO_3^-}]}$. $\frac{[B(OH)_4^-]}{[HCO_3^-]}$ has a significant correlation with B/Ca in both *G. ruber* (w) and *G. sacculifer* (w/o sac) (Figure 4-6, 4-7, and Table 4.1). This is consistent with the idea that $B(OH)_4^-$, the charged boron species, is the primary boron species incorporated into foraminiferal calcite (Hemming and Hanson, 1992; Yu et al., 2007b). The sensitivities of B/Ca in *G. ruber* (w) and *G. sacculifer* (w/o sac) to $\frac{[B(OH)_4^-]}{[HCO_3^-]}$ derived from the core-tops in this study are similar to those observed in culture studies (Figure 4-8) (Allen et al., 2012; Henehan et al., 2015). Owing to the large size of the core-top dataset, the 95% confidence interval of the core-top regression is much smaller than that of the culture regression. The 95% prediction interval of the core-top regression is comparable to the 95% confidence interval of the culture regression (Figure 4-8A). With the narrower 95% confidence interval of the core-top calibration, the predictability of the average B/Ca at given $\frac{[B(OH)_4^-]}{[HCO_3^-]}$ is improved, based on the new core-top data.

The correlation between B/Ca and $\frac{[B(OH)_4^-]}{[HCO_3^-]}$ is absent in another previous core-top study for *G. ruber* (w) of mixed morphologies (Henehan et al., 2015). This might be the result of combining *G. ruber* (w) *sensu stricto* and *sensu lato*, which have different habitat depths and temperature preferences (Wang, 2000; Sadekov et al., 2008). If only *G. ruber* (w, *sensu stricto*) from the dataset in (Henehan et al., 2015) are used, a 'small but statistically significant' carbonate chemistry control could be detected (Henehan et al., 2015). It is also noted that *G. ruber* (w) B/Ca reported in (Henehan et al., 2015) from marginal seas are ~30 μmol/mol higher than the maximum value from this study, while the carbonate chemistry parameters from those sites in (Henehan et al., 2015) are within the ranges of this study. It is speculated here that the absence of the correlation between *G. ruber* (w) B/Ca and carbonate chemistry parameters in (Henehan et al., 2015) might also be the result of another influence on B/Ca

at some sites. This is in analogy with the lack of a correlation between *G. ruber* (w) B/Ca and carbonate chemistry parameter for all core-tops in this study, which would be discussed in a separate section (Section 4.6).

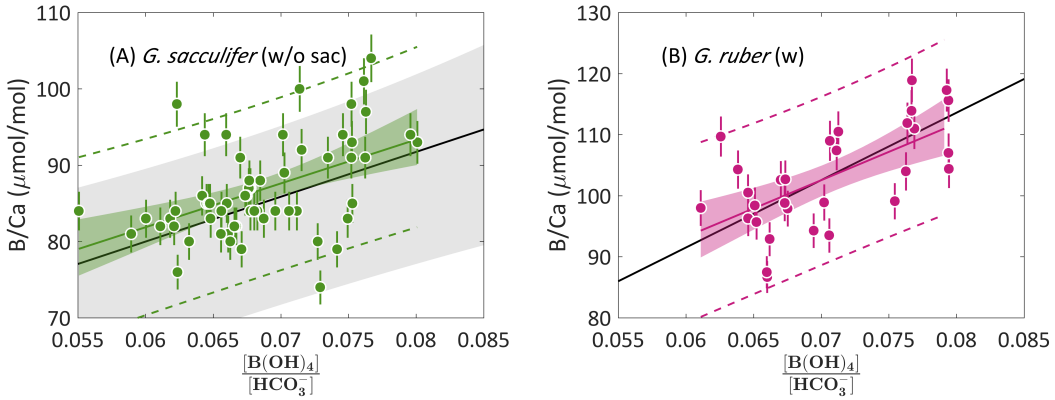

Figure 4-8: Sensitivities of B/Ca in *G. ruber* (w) and *G. sacculifer* (w/o sac) to $\frac{[B(OH)_4^-]}{[HCO_3^-]}$ from core-top and culture studies. Green and magenta circles are core-top data in this study (all data for *G. sacculifer* (w/o sac) and temperate latitude data for *G. ruber* (w)). Green and magenta lines with shades in both panels are regression lines with 95% confidence intervals of core-top data. Broken curves are 95% prediction interval of core-top data. The black lines are the regression lines from culture studies, which are shifted downwards to coincide with B/Ca in this study (Allen et al., 2012; Henehan et al., 2015). The gray shading in Panel (A) is the 95% confidence intervals for culture data. No confidence band is shown in Panel (B) for culture data, because the regression line is defined by 3 data points.

Despite the significant correlations of *G. sacculifer* (w/o sac) and *G. ruber* (w) B/Ca with $\frac{[B(OH)_4^-]}{[HCO_3^-]}$, the large prediction bands of the regressions may impair the use of planktonic B/Ca as a means for reconstructing seawater $\frac{[B(OH)_4^-]}{[HCO_3^-]}$. These large prediction bands can be attributed to the variable calcification conditions within the Atlantic transect in this study. As will be discussed in Section 4.6.2 and reported in other studies (Salmon et al., 2016), planktonic B/Ca could be largely affected by calcification rate. It has been suggested that the calcification rate is related to the conditions of the ecological niche rather than any single environmental parameter on a global basis (De Villiers, 2004). Therefore, calcification rates of foraminifera across a large latitude range may not be reflected by environmental parameters. The offset

of B/Ca at any particular site from the regression line is the result of site-specific calcification conditions. When a large number of sites from across the Atlantic are combined, the discrepancy of the calcification conditions is canceled out, and the sensitivity of planktonic B/Ca to $\frac{[B(OH)_4^-]}{[HCO_3^-]}$ generated by the core-top data is similar to that derived from the culture studies where the living environment of foraminifera is less variable.

$[CO_3^{2-}]$. The correlations of *G. ruber* (w) and *G. sacculifer* (w/o sac) B/Ca with $[CO_3^{2-}]$ are also significant (Figure 4-6, 4-7, and Table 4.1). Instead of $\frac{[B(OH)_4^-]}{[HCO_3^-]}$, $[CO_3^{2-}]$ has been recognized as the primary carbonate chemistry control on B/Ca in two symbiont-barren planktonic foraminiferal species, *Neogloboquadrina incompta* and *Globigerina bulloides* (Krupinski et al., 2017). These authors attributed the correlation between B/Ca and $[CO_3^{2-}]$ to the influence of calcification rate, based on the higher r^2 of B/Ca with $[CO_3^{2-}]$ compared to B/Ca with $\frac{[B(OH)_4^-]}{[HCO_3^-]}$. However, a similar conclusion that the correlation between B/Ca and $[CO_3^{2-}]$ originated from calcification rate control cannot be drawn based on data in this study. $\frac{[B(OH)_4^-]}{[HCO_3^-]}$ and $[CO_3^{2-}]$ are highly correlated in this study, and correlations of B/Ca with $[CO_3^{2-}]$ and $\frac{[B(OH)_4^-]}{[HCO_3^-]}$ are of comparable significance (Figure 4-6, 4-7, and Table 4.1). It is not possible to argue for a major $[CO_3^{2-}]$ control on B/Ca based on the difference in r^2 of correlations.

pH. Similar to other core-top studies (Yu et al., 2007b; Foster, 2008; Henehan et al., 2015; Krupinski et al., 2017), correlations between planktonic B/Ca and pH are less significant than correlations between planktonic B/Ca and other carbonate chemistry parameters (Figure 4-6F, 4-7F, and Table 4.1). This discounts the direct influence of pH on planktonic foraminiferal B/Ca. The lack of a correlation between B/Ca and pH is expected, as the relation between pH and $\frac{[B(OH)_4^-]}{[HCO_3^-]}$ is not straightforward. To derive pH from $\frac{[B(OH)_4^-]}{[HCO_3^-]}$, ALK or DIC are needed. Although planktonic B/Ca is influenced by seawater carbonate

chemistry, this influence is not directly reflected by pH.

In summary, B/Ca in *G. ruber* (w) and *G. sacculifer* (w/o sac) from core-tops lend support to the idea that carbonate chemistry exerts the primary control over B/Ca in planktonic foraminifera. The scatter of B/Ca, on the other hand, may be attributed to variable calcification conditions at different sites. Such a scatter of B/Ca in these two symbiont-bearing species makes it difficult to employ B/Ca in symbiont-bearing planktonic foraminiferal species to reconstruct carbonate chemistry on the glacial-interglacial timescale. For example, the LGM-Holocene B/Ca difference in *G. ruber* (w) is ~15 μmol/mol in a core from the Caribbean Sea (Foster, 2008). This difference is within the 95% prediction interval. Nevertheless, B/Ca in symbiont-bearing planktonic foraminiferal species still holds the promise of reconstructing the past carbonate system chemistry with a larger amplitude for time intervals such as PETM (Penman et al., 2014; Babila et al., 2016).

4.5.3 Salinity

B/Ca in *G. ruber* (w) and *G. sacculifer* (w/o sac) are significantly correlated with salinity (Figure 4-6D, 4-7D, and Table 4.1). Similar salinity dependencies of planktonic B/Ca have also been observed in other core-top and culture studies (Allen et al., 2012; Henehan et al., 2015; Krupinski et al., 2017). However, as salinity is correlated with many other environmental parameters, including carbonate chemistry parameters (*e.g.*, $r^2 = 0.59$ for salinity and $\frac{[B(OH)_4^-]}{[HCO_3^-]}$), it follows that the correlation might be an artifact of the carbonate chemistry control on planktonic B/Ca. In order to isolate the salinity effect on B/Ca, the B/Ca component without the influence of carbonate chemistry, residual B/Ca, is calculated following the method of (Henehan et al., 2015), by normalizing measured B/Ca to the same $\frac{[B(OH)_4^-]}{[HCO_3^-]}$ employing the correlation

between B/Ca and $\frac{[B(OH)_4^-]}{[HCO_3^-]}$ derived in the current study:

$$B/Ca_{residual} = B/Ca_{measured} - \left(\frac{[B(OH)_4^-]}{[HCO_3^-]}_{in\ situ} - \frac{[B(OH)_4^-]}{[HCO_3^-]}_{ref}\right) \times k, \quad (4.1)$$

where $\frac{[B(OH)_4^-]}{[HCO_3^-]}_{ref}$ is at a constant reference value of 0.04 and k is the sensitivity of B/Ca to $\frac{[B(OH)_4^-]}{[HCO_3^-]}$ derived in this study.

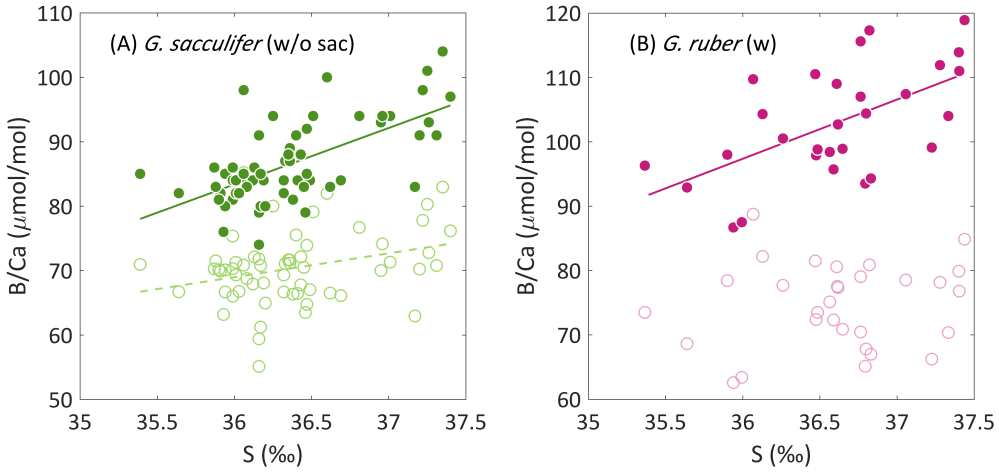

Figure 4-9: B/Ca and residual B/Ca compared to salinity (A): *G. sacculifer* (w/o sac), (B): *G. ruber* (w). The filled circles are measured B/Ca, and the and empty circles are residual B/Ca with the carbonate chemistry contribution removed. Regression lines are shown when the correlations are significant ($p<0.05$).

Salinity effects on B/Ca in *G. sacculifer* (w/o sac) and *G. ruber* (w) in this study are substantially reduced when the contribution of the carbonate chemistry is removed. For *G. sacculifer* (w/o sac), the sensitivity of B/Ca to salinity is 8.8 μmol/mol per salinity unit, while the sensitivity of residual B/Ca is 3.7 μmol/mol per salinity unit. The correlation between *G. sacculifer* (w/o sac) residual B/Ca and salinity is still significant ($p = 0.02$) (Figure 4-9). For *G. ruber* (w), the salinity effect of B/Ca is 9.2 μmol/mol per salinity unit, and there is no significant correlation between residual B/Ca and salinity ($p = 0.49$) (Figure 4-9). These results are in contrast to those from culture studies, where the variation of carbonate chemistry ($\frac{[B(OH)_4^-]}{[HCO_3^-]}$) associated with salinity could only account for ~20% of salinity effects on B/Ca (Allen et al.,

2012). The salinity effect observed in culturing experiments (Allen et al., 2012) may be related to the effect of total boron concentration ($[B]_{sw}$) on B/Ca observed in culturing experiments (Allen et al., 2011). As observed by these authors, the sensitivity of *O. universa* B/Ca to $\frac{[B(OH)_4^-]}{[HCO_3^-]}$ was nine times higher when $[B(OH)_4^-]$ was elevated by increasing $[B]_{sw}$ than that when $[B(OH)_4^-]$ was elevated by increasing pH in culture experiments (Allen et al., 2011). When the salinity was changed in culture experiments, $[B]_{sw}$ was implicitly changed simultaneously, exerting an influence on B/Ca. Among the core-tops, the $[B]_{sw}$ variability associated with salinity (~250 μmol/kg) was less than half of that in culture experiments (~600 μmol/kg) (Allen et al., 2011). The different $[B]_{sw}$ change among core-tops compared to that in culturing experiments may be the reason why a larger proportion of the salinity effect on B/Ca can be explained by covariation of salinity and carbonate chemistry parameters in the current core-top study.

In conclusion, the salinity effect on planktonic B/Ca is the result of covariation of salinity with other environmental parameters, specifically carbonate chemistry parameters in the current core-top study.

4.5.4 Phosphate

B/Ca in both *G. ruber* (w) and *G. sacculifer* (w/o sac) are negatively correlated with $[PO_4^{3-}]$ in this study (Figure 4-6E, 4-7E, and Table 4.1), in contrast to the positive correlation of *G. ruber* (w) B/Ca with $[PO_4^{3-}]$ reported in (Henehan et al., 2015). Henehan et al. (2015) propose that the correlation between *G. ruber* (w) B/Ca and $[PO_4^{3-}]$ may originate from the effect of $[PO_4^{3-}]$ on the calcification rate or crystallographic processes. The reason for an opposite direction of the correlations in this study from that in (Henehan et al., 2015) is elusive. Nevertheless, this discrepancy at least suggests that the effect of $[PO_4^{3-}]$ on planktonic B/Ca may not be straightforwardly represented by the correlations between B/Ca and $[PO_4^{3-}]$.

4.5.5 Temperature

G. ruber (w) B/Ca is positively correlated with temperature, while *G. sacculifer* (w/o sac) B/Ca is not (Figure 4-6, 4-7, and Table 4.1). The potential influence of temperature on planktonic B/Ca is explored here by comparing B/Ca directly with temperature. K_D, which was employed in some earlier investigations (Wara et al., 2003; Yu et al., 2007b; Foster, 2008), is not considered, since it may be confounded by the correlation of temperature with carbonate chemistry parameters (Allen and Hönisch, 2012).

In comparison to the results in this study, no temperature effect on B/Ca was observed for *G. sacculifer* (w/o sac) or *G. ruber* (p) previously (Allen et al., 2012). If there is no temperature effect on planktonic B/Ca as suggested by a culture study (Allen et al., 2012), the correlation between *G. ruber* (w) B/Ca and temperature must be originated from the covariation of temperature with another parameter or process that can influence *G. ruber* (w) B/Ca.

4.6 Elevated *G. ruber* (w) B/Ca in the tropical Atlantic

4.6.1 Light intensity

The elevated *G. ruber* (w) B/Ca in the tropical Atlantic could originate from environmental parameters not investigated in the previous section but capable of affecting planktonic B/Ca. One parameter is light intensity. It has been reported by a sediment trap study that monthly *G. ruber* (w) B/Ca fluctuated with a magnitude of ~30 μmol/mol, larger than expected from carbonate chemistry variation (Babila et al., 2014). These changes in *G. ruber* (w) B/Ca covaried with the monthly peak light intensity, supporting an influence of varying photosynthesis strength associated with the peak light intensity on B/Ca (Babila et al., 2014). Indeed, the chemical composition of the microenvironment is mediated by light availability (Jorgensen et al., 1985; Rink

et al., 1998; Wolf-Gladrow et al., 1999). As the seawater light intensity varies meridionally, vertically, and seasonally, it is possible that light intensities of the calcifying environments could result in variations in B/Ca of *G. ruber* (w) and *G. sacculifer* (w/o sac) which have different calcification depths and seasonality at different latitudes. Here, light intensity in seawater is assessed to evaluate its potential influence on planktonic B/Ca.

Zonal average light intensities of the upper 100 m seawater in the Atlantic are estimated using satellite data for the boreal summer, the austral summer, and annual mean. The light intensity is calculated by the daily mean photosynthetically available radiation (PAR) and diffusive attenuation coefficient for downwelling irradiance at 490 nm (Kd_490) using the Giovanni database (https://giovanni.gsfc.nasa.gov/) (Figure 4-10). The light intensities calculated from satellite observation are on a different timescale from the lab observation and the previous sediment trap study. The satellite-based data are daily average, and thus in the unit of mol m^{-2} d^{-1}. The light intensities in lab observations and sediment trap studies are both instant values (Jorgensen et al., 1985; Rink et al., 1998; Babila et al., 2014), and are in the unit of μmol m^{-2} s^{-1}. The daylight hour is assumed to be 12 h at all latitudes, to bring the units of light intensities together. Two caveats are that there are considerable daily fluctuations in light intensity, and that the daylight hours vary at different latitudes. Nevertheless, with these caveats, the satellite-observed daily average values can help illustrate the meridional light intensity variation, which can ultimately evaluate strengths of vital activities in response to light intensities at varying latitudes.

To date, saturation and compensation light intensities are only directly measured for two symbiotic planktonic foraminiferal species: *G. sacculifer* (Jorgensen et al., 1985) and *O. universa* (Rink et al., 1998). The light saturation intensity and compensation light intensity of *G. sacculifer* is 160-170 μmol m^{-2} s^{-1} and 26-30 μmol m^{-2} s^{-1}, respectively (Jorgensen et al., 1985). These data are used to approximate the compensation light intensity of the

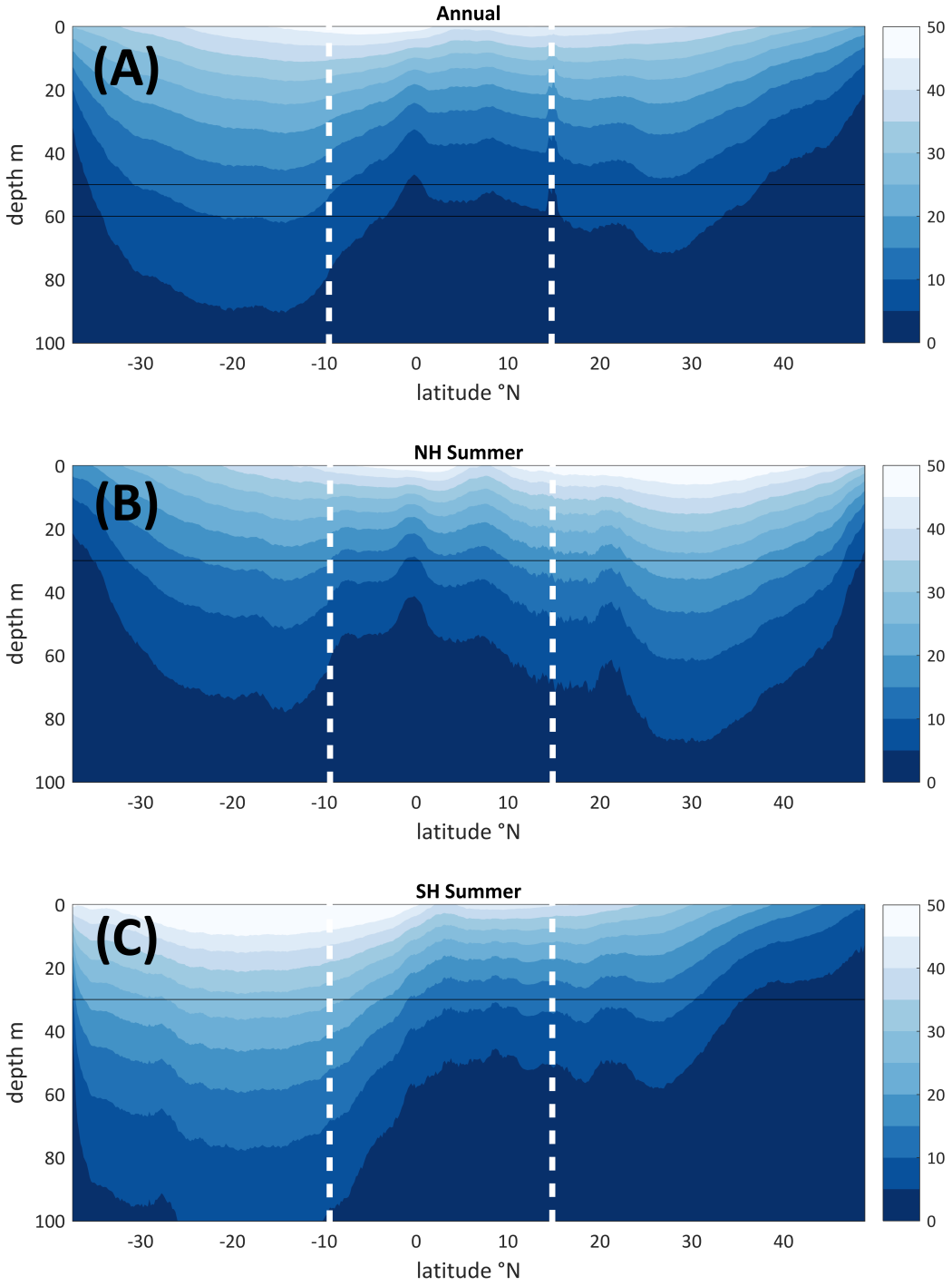

Figure 4-10: Zonal averaged light intensity of the Atlantic in the upper 100 m: (A) Annual mean, (B) boreal summer, (C) austral summer. Unit of light intensity is $mol\ m^{-2}\ d^{-1}$. The thick dashed white lines show the boundaries of the north, tropical, and south Atlantic.

two species studied in this study, with the caveat that the strengths of light absorption could be different between *G. ruber* (w) and *G. sacculifer* (w/o sac) (Hemleben et al., 1989).

At temperate latitudes, both *G. ruber* (w) and *G. sacculifer* (w/o sac) prefer shallower calcification depths during summer (*e.g.*, Jonkers and Kučera, 2017, and Chapter 3 in this study). The daily average light intensities at 30 m during summer are 15-25 mol m^{-2} d^{-1} in the North Atlantic and 20-30 mol m^{-2} d^{-1} in the South Atlantic, equivalent to 350-580 μmol m^{-2} s^{-1} and 460-690 μmol m^{-2} s^{-1}, respectively. These daily average light intensities are twice of the light saturation intensity, indicating that the light intensity is high enough to sustain photosynthesis close to the saturation level during the most of the daytime.

At tropical latitudes, both *G. ruber* (w) and *G. sacculifer* (w/o sac) calcify deeper than at temperate latitudes, and do not show obvious seasonal preferences. The annual mean light intensities at 50 m in the tropical Atlantic are lower than 5-10 mol m^{-2} d^{-1}, equivalent to 120-230 μmol m^{-2} s^{-1}. The daily average light intensity is comparable to the light saturation intensity, suggesting a lower level of photosynthetic activities compared to the temperate Atlantic.

pH in the microenvironment of symbiotic foraminifera could be raised by photosynthesis (*e.g.*, Wolf-Gladrow et al., 1999; Zeebe et al., 1999). Therefore, a higher light intensity and an associated stronger photosynthetic activity, raises pH in the microenvironment, which would lead to higher B/Ca as observed by a sediment trap study (Babila et al., 2014). It follows that B/Ca at tropical latitudes, where the average light intensity of the calcification microenvironment is lower, are expected to be lower. This is consistent with the relatively lower *G. sacculifer* (w/o sac) B/Ca at tropical latitudes, but not with the relatively higher *G. ruber* (w) B/Ca at tropical latitudes. Therefore, it seems unlikely that elevated *G. ruber* (w) B/Ca in the tropical Atlantic is caused by light intensities.

4.6.2 Calcification rate

Another possible cause of the elevated *G. ruber* (w) B/Ca in the tropical Atlantic is that B/Ca is affected by a process that cannot be directly connected to a certain environmental parameter, such as calcification. The calcification rate can influence planktonic foraminiferal B/Ca, which is inferred from the correlations between B/Ca and calcification rate indicators, *e.g.*, test size (Ni et al., 2007), test area density (Salmon et al., 2016), and $[CO_3^{2-}]$ (Krupinski et al., 2017). An ideal calcification rate indicator could alternatively be a shell chemistry property internally determined by calcification, as an 'internal standard' for calcification rate. Two candidates are Sr/Ca and calcium isotopes (*e.g.*, Tang et al., 2008).

Here, Sr/Ca is employed as a calcification rate indicator to investigate the influence of the calcification rate on planktonic B/Ca, as it is often measured along with other trace element to calcium ratios. A calcification rate control on Sr/Ca has been well established by inorganic calcite precipitation experiments (Lorens, 1981; Tesoriero and Pankow, 1996; Tang et al., 2008). A control on Sr/Ca in biological calcite has also been inferred for coccolithophores (Stoll et al., 2002; Rickaby et al., 2002) and foraminifera (Lea et al., 1999; Erez, 2003; Russell et al., 2004; Kısakurek et al., 2008; Kısakürek et al., 2011; Dueñas-Bohórquez et al., 2009; Holland et al., 2017). More relevant to this study, Sr/Ca in *G. ruber* (Kısakurek et al., 2008) and *G. sacculifer* (Erez, 2003; Dueñas-Bohórquez et al., 2009) have both been observed to be correlated to the calcification rate. Besides, Sr/Ca of *G. ruber* (w) and *G. sacculifer* (w/o sac) are comparable, as the interspecies difference of Sr uptake by these two species is minimal as shown in various culture experiments (as summarized in Allen et al., 2016).

When B/Ca and Sr/Ca in both *G. ruber* (w) and *G. sacculifer* (w/o sac) are plotted together, there is a strong covariation between these two ratios ($r^2 = 0.68, N = 117, p < 0.001$, Figure 4-11A). The covariation between B/Ca and Sr/Ca in *G. ruber* (w) is weaker, but still significant ($r^2 = 0.28$, N = 57,

$p < 0.001$). Average B/Ca and Sr/Ca in *G. ruber* (w) from the tropical and temperate Atlantic coincide with the trend defined by data of both species. *G. ruber* (w) Sr/Ca is 0.02 ± 0.03 mmol/mol higher in the tropical Atlantic than in the temperate Atlantic, corresponding to the 9 ± 10 μmol/mol increase in B/Ca. If Sr/Ca reflect calcification rates of these two species, the covariation of B/Ca and Sr/Ca suggest a calcification rate control on B/Ca. The different calcification rates of these two species can account for the inter-species B/Ca difference. The more elevated B/Ca in *G. ruber* (w) than in *G. sacculifer* (w/o sac) is accompanied by the higher calcification rate of *G. ruber* (w), as indicated by Sr/Ca. The regional Sr/Ca and B/Ca gradients of *G. ruber* (w) also coincides with the trend defined by data of both species, suggesting that the overall higher growth rate is responsible for the higher B/Ca of *G. ruber* (w) at tropical latitudes. When residual B/Ca is derived by normalizing $\frac{[B(OH)_4^-]}{[HCO_3^-]}$ to the same value (Equation 4.1), the correlation between residual B/Ca and Sr/Ca is still significant (Figure 4-11B). Such a strong correlation suggests that the influence of calcification rate on planktonic B/Ca is independent of the carbonate chemistry control.

While some studies have suggested a possible influence of calcification rate on planktonic B/Ca (Salmon et al., 2016; Krupinski et al., 2017), direct measurements of calcification rate of planktonic foraminifera do not seem to support such an influence. In an inorganic calcite precipitation experiment, calcification rates promote boron incorporation into inorganic calcite above a threshold calcification rate (Uchikawa et al., 2015). Many studies attempted to compare the measured calcification rates with the threshold calcification rate in the inorganic calcite precipitation experiment (Uchikawa et al., 2015), to test the influence of the calcification rate on B/Ca (Allen et al., 2016; Holland et al., 2017; Haynes et al., 2017). To date, these measured calcification rates fall 1 to 2 orders smaller than the threshold calcification rate (Allen et al., 2016; Holland et al., 2017; Haynes et al., 2017), indicating no calcification rate control. Nevertheless, the calcification rate of foraminifera varies dramatically

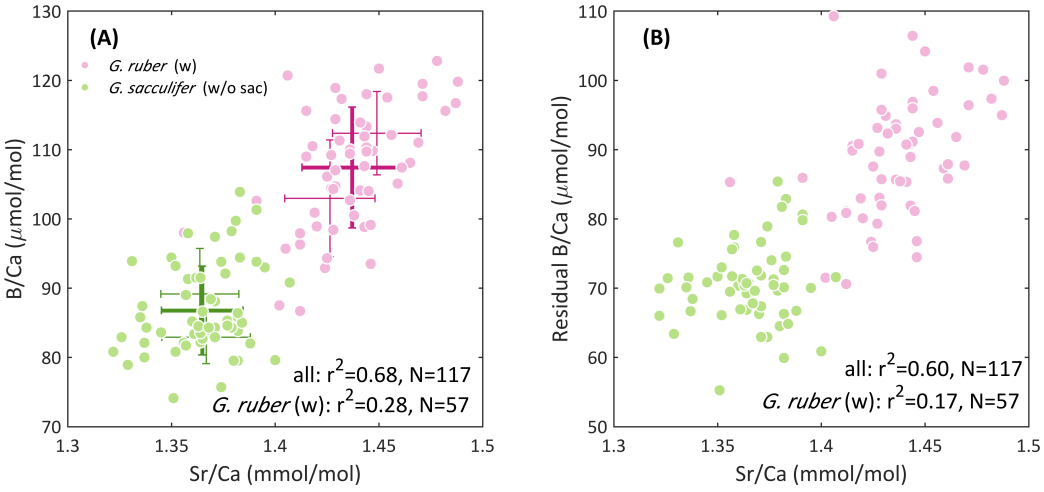

Figure 4-11: Comparisons between (A) B/Ca and Sr/Ca, (B) residual B/Ca and Sr/Ca. Magenta and green circles are data of G. ruber (w) and G. sacculifer (w/o sac), respectively. In Panel (A) the bold magenta and green crosses demonstrate the average B/Ca and Sr/Ca with 1σ ranges for G. ruber (w) and G. sacculifer (w/o sac), respectively. The thin crosses show the average B/Ca and Sr/Ca with 1σ ranges for G. ruber (w) in the tropical and the temperate Atlantic.

during their life cycles, as suggested by the intra-shell heterogeneity of trace elements (*e.g.*, Eggins et al., 2004; Spero et al., 2015). It is argued that the instantaneous calcification rate can be high enough to initiate the calcification rate control on boron incorporation and thus to exert an influence on B/Ca of the bulk shell, although the average calcification rate is below the threshold value. The calcification rates corresponding to the apparent boron partition coefficients of *G. ruber* (w) and *G. sacculifer* (w/o sac) B/Ca as calculated in Uchikawa et al. (2015) lie within the regime where calcification rate promotes boron incorporation (Figure 4-12). Should $B(OH)_3$ be incorporated into planktonic foraminiferal calcite at high calcification rates in a similar way to inorganic calcite, the calcification rate would have the potential to exert a control on planktonic B/Ca. As a result, the imprints of environmental controls on planktonic B/Ca can be overwhelmed by the influence of the calcification rate, as seen for *G. ruber* (w) B/Ca from the tropical Atlantic.

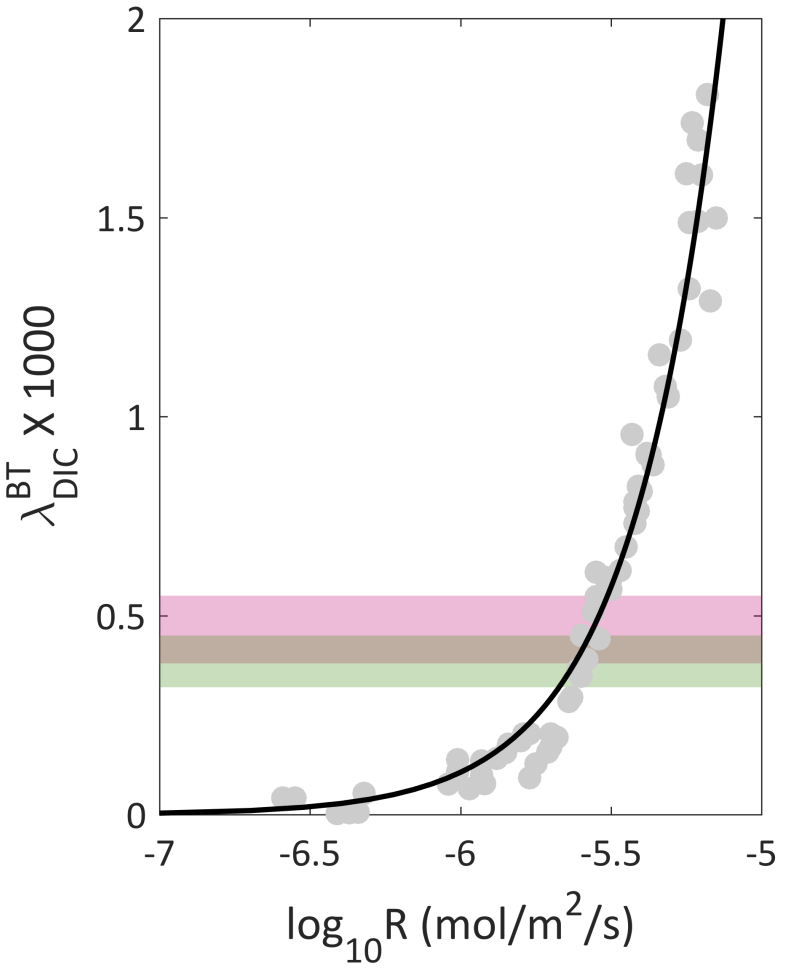

Figure 4-12: Partition coefficients of B/Ca in *G. ruber* (w) and *G. sacculifer* (w/o sac) from core-tops in comparison to inorganic calcite. Gray circles are inorganic calcite data (Uchikawa et al., 2015), and the black curve is the regression line. The magenta and green bars indicate the ranges of partition coefficients calculated from core-top *G. ruber* (w) and *G. sacculifer* (w/o sac) B/Ca, respectively.

4.7 Conclusions

In this chapter, environmental controls on B/Ca in two symbiont-bearing planktonic foraminiferal species *G. ruber* (w) and *G. sacculifer* (w/o sac) are examined using core-tops from the meridional Atlantic transect. With similar ranges of environmental parameters, *G. ruber* (w) B/Ca at tropical latitudes are higher than those from temperate latitudes. This is attributed to the

relatively greater calcification rates of *G. ruber* (w) from tropical latitudes as indicated by shell Sr/Ca. *G. ruber* (w) B/Ca affected by calcification rate to a lesser degree and *G. sacculifer* (w/o sac) B/Ca show similar correlations with carbonate chemistry parameters to those observed in culture studies, confirming seawater carbonate chemistry as an important controlling factor on planktonic B/Ca. The meridional variations of B/Ca in these two planktonic species from the core-tops are likely resulted from the competing influences of the calcification rate and seawater carbonate chemistry. The calcification rate control on planktonic B/Ca would complicate a direct link between planktonic B/Ca and seawater carbonate chemistry. Nevertheless, according to different B/Ca responses of *G. ruber* (w) and *G. sacculifer* (w/o sac) to calcification rate, should B/Ca in some planktonic species be less susceptible to growth rate changes, B/Ca could be employed for carbonate chemistry reconstructions.

Chapter 5

$[CO_3^{2-}]$: A Key Parameter to Deep Water Carbonate Chemistry

5.1 Introduction

Deep-water $[CO_3^{2-}]$ is directly linked to the amount of carbon stored in the deep ocean reservoir. Processes capable of affecting the deep ocean carbon reservoir include invasion and release of CO_2, dissolution and preservation of $CaCO_3$, remineralization and formation of organic matters, and water mass mixing. All these processes leave imprints on deep-water $[CO_3^{2-}]$. In the carbonate chemistry system, $[CO_3^{2-}]$ is determined by DIC and ALK at a given temperature, salinity, and pressure (Figure 5-1), and can be approximated by the difference between ALK and DIC (Broecker et al., 1982):

$$[CO_3^{2-}] \cong ALK - DIC. \tag{5.1}$$

The influences of temperature, salinity, and pressure on deepwater $[CO_3^{2-}]$ are negligible (Broecker et al., 1982). Equation (5.1) ignores contribution of dissolved $[CO_2]$ and carbonic acid to DIC and approximates the carbonate alkalinity as the total alkalinity (Broecker et al., 1982).

Equation (5.1) can help qualify $[CO_3^{2-}]$ change induced by different pro-

cesses affecting the deep ocean carbon reservoir. Preservation and dissolution of $CaCO_3$ changes ALK and DIC at a ratio of 2:1:

$$Ca^{2+} + 2HCO_3^- \underset{dissolution}{\overset{preservation}{\rightleftharpoons}} CaCO_3 + H_2O + CO_2. \tag{5.2}$$

Therefore, preservation of $CaCO_3$ decreases $[CO_3^{2-}]$ and dissolution increases $[CO_3^{2-}]$ (Figure 5-1). Invasion and release of CO_2 only involves changes in DIC, and thus decreases and increases $[CO_3^{2-}]$, respectively. The chemical composition of organic matters in the ocean has a near-constant ratio of three major nutrient elements: C, N, and P, which is known as the Redfield ratio (Redfield, 1934). Although it is later found that this ratio is not constant in different oceans (e. g., Teng et al., 2014), the classic Redfield ratio can help exemplify formation and remineralization of organic matters. Formation and remineralization of organic matters removes and releases CO_2, respectively, involving minor changes in ALK:

$$\begin{aligned} 106CO_2 + 16NO_3^- + HPO_4^{2-} + 122H_2O + 18H^+ \underset{remineralization}{\overset{formation}{\rightleftharpoons}} \\ (CH_2O)_{106}(NH_3)_{16}H_3PO_4 + 138O_2. \end{aligned} \tag{5.3}$$

Therefore, the influence of formation of organic matters on $[CO_3^{2-}]$ is similar to that of CO_2 release, while the influence of remineralization of organic matters on $[CO_3^{2-}]$ is similar to that of CO_2 invasion (Figure 5-1). Because it is difficult to quantify ALK and DIC directly, a lot of work has been devoted to reconstruct $[CO_3^{2-}]$ to infer changes of ALK and DIC (e. g., Arrhenius, 1952; Howard and Prell, 1994; Hodell et al., 2001; Anderson and Archer, 2002; Marchitto et al., 2005; Yu and Elderfield, 2007). A lot of our knowledge about past changes of seawater carbonate chemistry relies on Equation 5.1.

Useful as it is to help understand the variability of seawater $[CO_3^{2-}]$, Equation 5.1 falls short of quantifying $[CO_3^{2-}]$ precisely. Recently, it was discovered that $[CO_3^{2-}]$ is correlated to ALK-DIC in the deep Atlantic Ocean with a

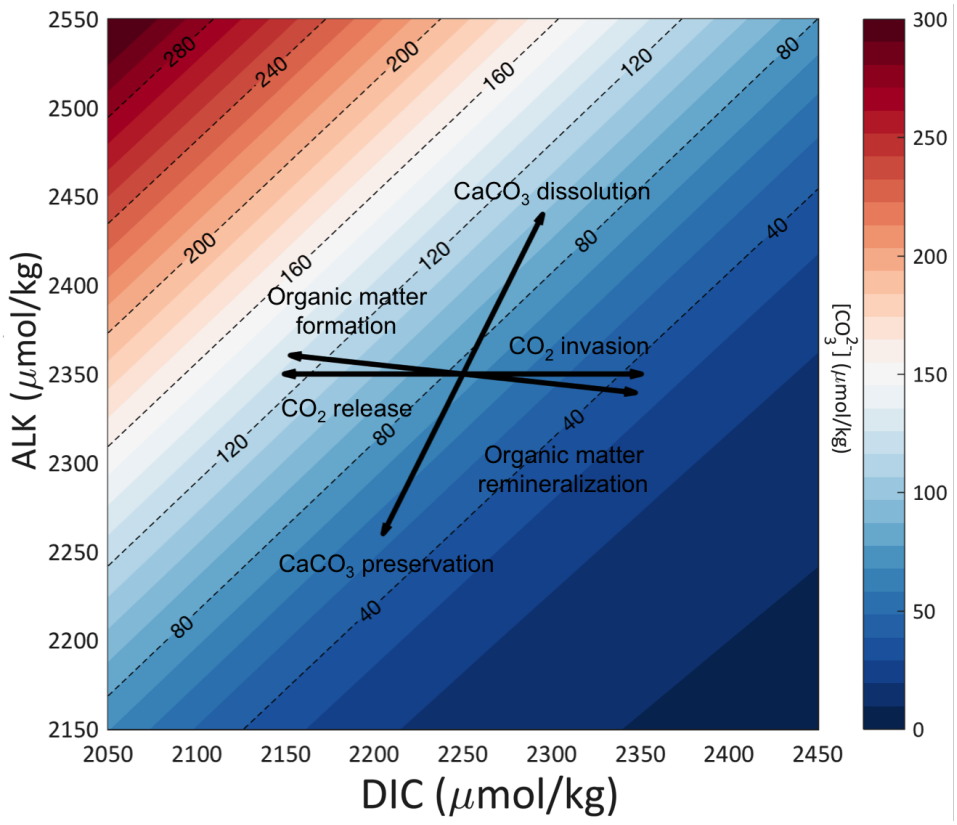

Figure 5-1: $[CO_3^{2-}]$ as a function of ALK and DIC. $[CO_3^{2-}]$ is calculated at T = 1 °C, P = 3600 dbar, S = 35. Invasion/release of CO_2 only affects DIC and hence decreases/increases $[CO_3^{2-}]$. Dissolution/preservation of $CaCO_3$ increases/decreases ALK and DIC in 2:1 ratio, and hence increases/decreases $[CO_3^{2-}]$. Remineralization/formation of organic matters increases/decreases DIC and only has a small effect on ALK, and hence decreases/increases $[CO_3^{2-}]$.

coefficient 'k' and an interception of 'b' (Yu et al., 2016):

$$[CO_3^{2-}] = k \times (ALK - DIC) + b$$
$$k = 0.59 \pm 0.01, b = 16 \pm 1, r^2 = 0.98 \tag{5.4}$$

The strong correlation could be employed to quantify the change in the DIC in the deep water with a knowledge of change in ALK. However, the k value seems to be variable when simulated in different boundary conditions (Yu et al., 2016). This could cause variation in estimation of deep-water DIC change outside the Atlantic Ocean. As the core sites studied in Chapter 6 of this thesis sit in the Southwest Pacific, it is highly likely that the k value

could be different from the Atlantic value. To better understand past changes of seawater carbonate chemistry in the SW Pacific, I explore the relationship between $[CO_3^{2-}]$ and ALK-DIC in the deep ocean (water depth $>$ 2.5 km) using the GLODAP (Global Data Analysis Project) dataset (Key et al., 2004) and a series of artificial carbonate systems. The correlation between $[CO_3^{2-}]$ and ALK-DIC observed in a hydrological dataset (GLODAP) is supplemented by carbonate system data generated from random ALK and DIC. The variation of the k values in the GLODAP dataset is derived by imposing a small change in the carbonate chemistry. Such a variation of k values is also supported by analysis of the artificial dataset.

5.2 Methods

5.2.1 GLODAP dataset

Data from GLODAP dataset with both ALK and DIC data are selected for the analysis. DIC from GLODAP dataset are corrected to the preindustrial level by subtracting *in situ* DIC by anthropogenic CO_2, where anthropogenic CO_2 data are from Sabine et al. (2004). In cases where anthropogenic CO_2 are not available, they are assumed to be zero. This assumption only affects $\sim$8% percent of the total data. Removal of sites without anthropogenic CO_2 data does not influence the conclusion of this chapter. From ALK and DIC all the carbonate chemistry parameters ($[CO_3^{2-}]$, pH, and etc) can be calculated, with the knowledge of temperature, pressure, salinity, and minor contributors to ALK (phosphate and silicate) (Zeebe and Wolf-Gladrow, 2001). Here negative phosphate and silicate values from the GLODAP dataset are made to be zero. The carbonate chemistry variables are calculated by an adapted CO2sys2.1 MATLAB code (Lewis et al., 1998), using K_1 and K_2 from Mehrbach et al. (1973), $K_{HSO_4^-}$ from Dickson (1990a), and total boron concentration and salinity correlation from Lee et al. (2010). Carbonate system variables are calculated at the *in situ* conditions and are also normalized

to the same constant output condition (T = 3 °C, P = 2500 dbar, and S = 35).

5.2.2 Artificial data

100,000 artificial carbonate systems are simulated from random ALK and DIC values covering the variability within the modern ocean (Figure 5-2A), at random modern deep ocean conditions, where temperatures range from 0 to 3 °C, pressures range from 2500 to 5500 dBar, and salinities range from 34.5 to 35.5. Minor contributors to ALK (phosphate and silicate) are omitted for simplicity of the simulation. Similar to GLODAP dataset, from ALK and DIC, with temperature, pressure, and salinity, all carbonate chemistry variables can be calculated, using the same program and constants as the calculation of GLODAP. These artificial carbonate chemistry data are also both calculated in the in situ condition and normalized to a constant output condition, where T = 3 °C, P = 2500 dBar, and S = 35. To get the trend of $[CO_3^{2-}]$ at varying ALK-DIC, the simulated carbonate systems are grouped into bins based on ALK-DIC (width = 0.1 μmol/kg). $[CO_3^{2-}]$ in each bin is averaged and smoothed by a Gaussian filter.

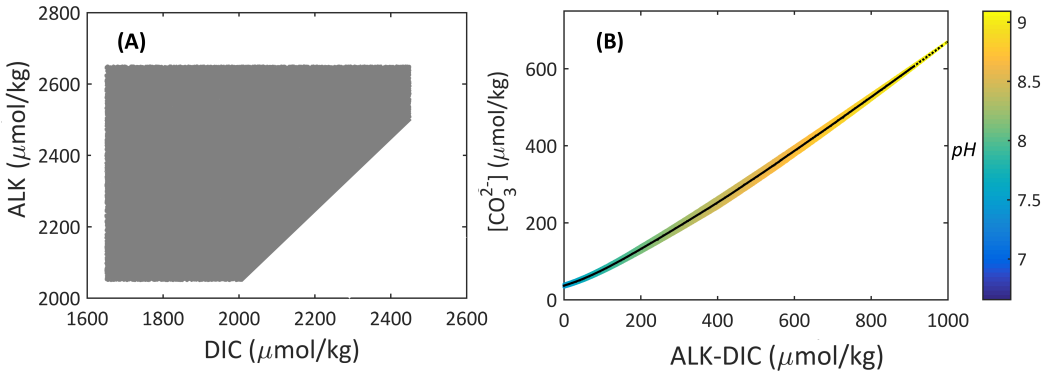

Figure 5-2: $[CO_3^{2-}]$ calculated from random ALK and DIC. (A): ALK and DIC input. (B): Correlation between $[CO_3^{2-}]$ at random deep ocean condition and ALK-DIC. Color shading shows all the calculated $[CO_3^{2-}]$ within each ALK-DIC bin, and the black curve is the smoothed average $[CO_3^{2-}]$. Note that the results for artificial carbonate systems with ALK < DIC, which are not realistic in the ocean, are not shown in (B).

5.3 Results and discussion

5.3.1 $[CO_3^{2-}]$

$[CO_3^{2-}]$ of artificial carbonate systems are plotted with ALK-DIC in Figure 5-2B. Despite that ALK and DIC are randomly distributed, $[CO_3^{2-}]$ calculated from ALK and DIC is strongly related to ALK-DIC. Such a dependence demonstrates that the correlation between $[CO_3^{2-}]$ and ALK-DIC derived in the hydrological dataset by Yu et al. (2016) is not an artifact of covariation of ALK and DIC in the modern ocean. Moreover, the average $[CO_3^{2-}]$ of the simulated carbonate systems at constant and random deep ocean conditions are within 1 standard deviation of each other (Figure 5-3). These consistent results suggests that variations in temperature, salinity, and pressure within the deep ocean conditions only have a marginal influence on the covariation of $[CO_3^{2-}]$ and ALK-DIC.

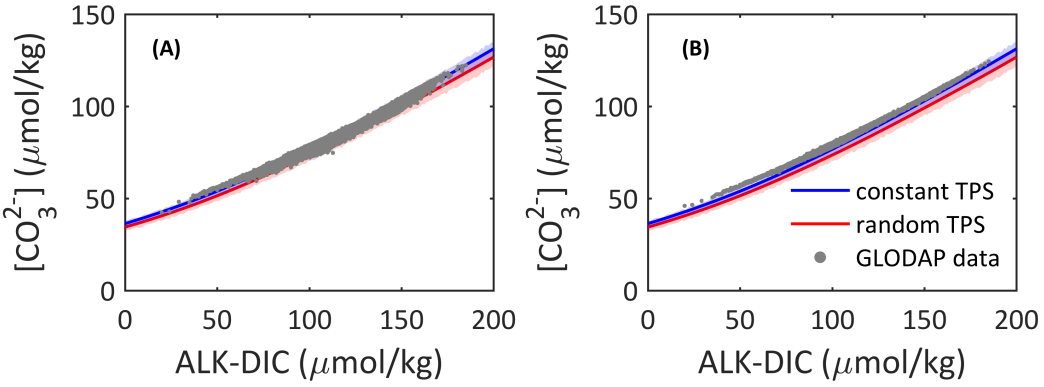

Figure 5-3: Comparison between $[CO_3^{2-}]$ at GLODAP sites and $[CO_3^{2-}]$ calculated from random ALK and DIC. Red and blue curves represent average $[CO_3^{2-}]$ calculated from random ALK and DIC at random and constant deep ocean conditions, respectively. Envelopes are $\pm 1\sigma$ uncertainties associated with the averages. Grey dots in Panel (A) and (B) are the GLODAP $[CO_3^{2-}]$ data at *in situ* and normalized constant condition, respectively.

The GLODAP $[CO_3^{2-}]$ data are within the 1σ ranges of the artificial data at both *in situ* and normalized conditions (Figure 5-3). The spread of $[CO_3^{2-}]$ is smaller under the normalized condition. The correlations between $[CO_3^{2-}]$ and ALK-DIC are consistent between the GLODAP data and artificial data.

This suggests that the correlation between $[CO_3^{2-}]$ and ALK-DIC applies to ALK and DIC ranges wider than those observed in the modern ocean.

5.3.2 k value

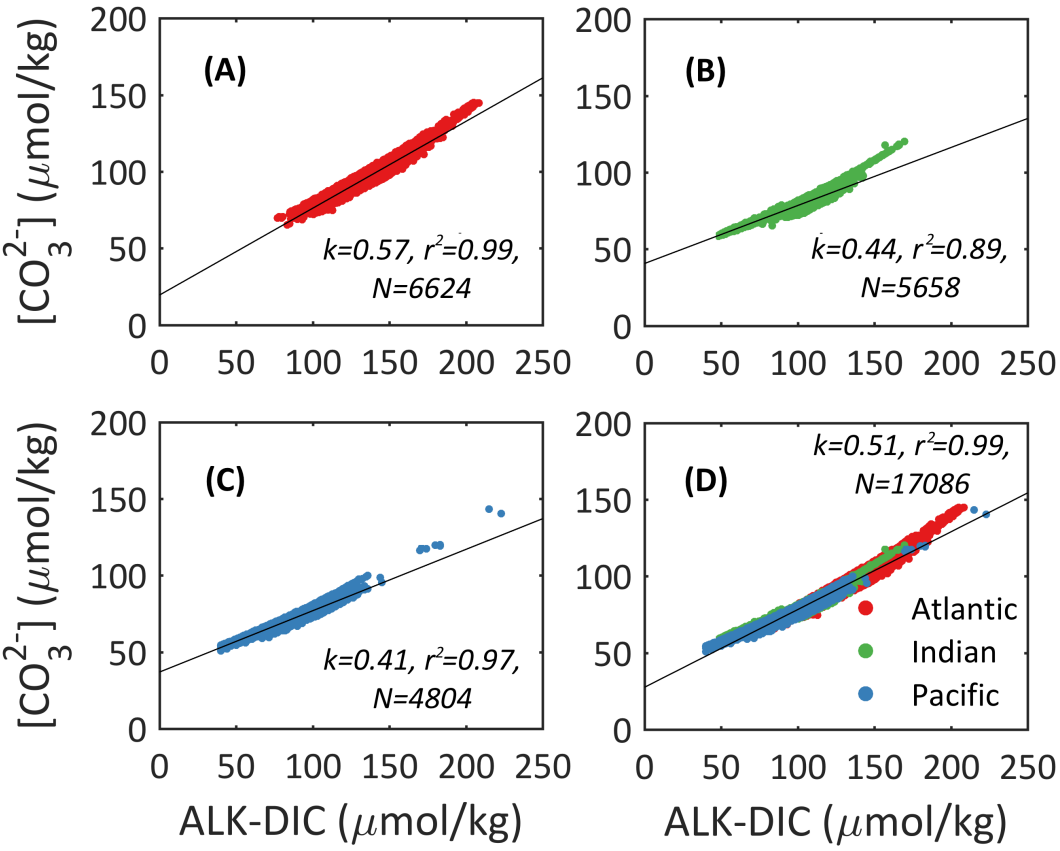

Figure 5-4: Correlations between *in situ* $[CO_3^{2-}]$ and ALK-DIC in the deep ocean at GLODAP sites (>2.5 km).

The correlations between deepwater $[CO_3^{2-}]$ and ALK-DIC from the GLODAP dataset for *in situ* and normalized conditions are shown in Figure 5-4 and 5-5, respectively. k values can be derived from the regression between $[CO_3^{2-}]$ and ALK-DIC. At the *in situ* condition, k values vary from 0.41 in the Pacific to 0.57 in the Atlantic. The k value of the global ocean is 0.51. The k value of the Atlantic (k = 0.57) is consistent withs the result of Yu et al. (2016) (k = 0.59). The difference between k values in this study and Yu et al. (2016) might be caused by a minor difference in data selection. The k values in the Atlantic Ocean are higher than the k values in the Indian and the Pacific Ocean (k =

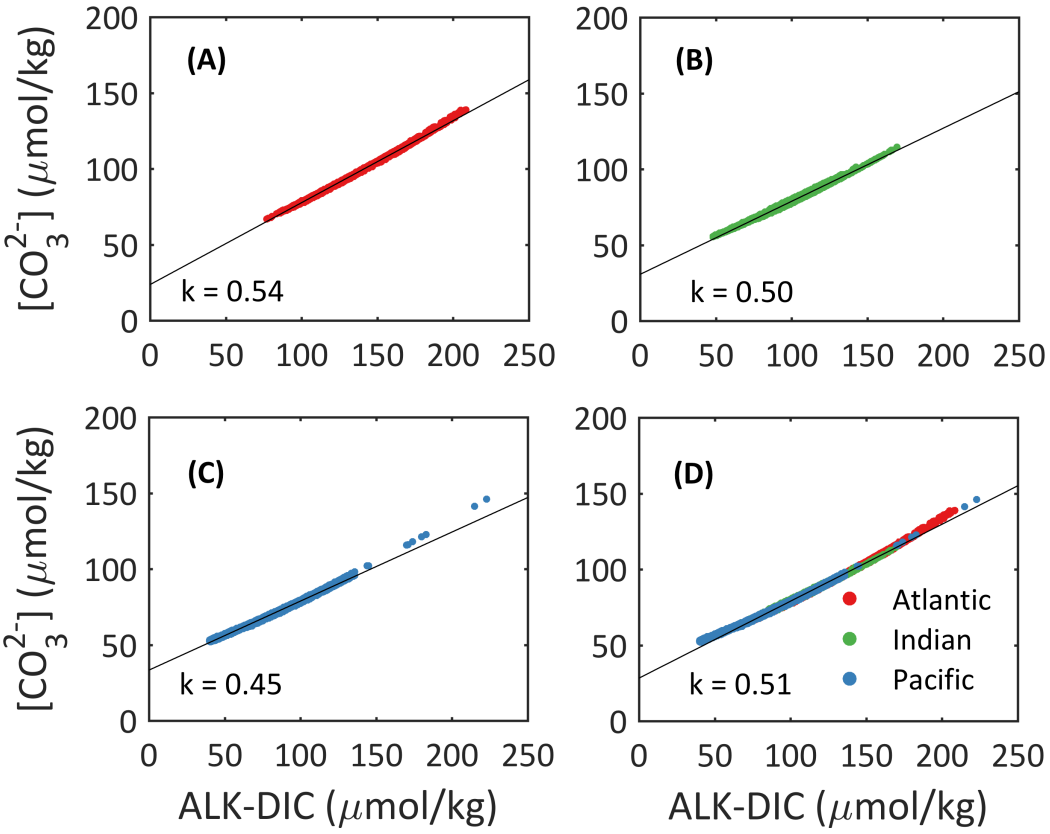

Figure 5-5: Correlations between normalized $[CO_3^{2-}]$ and ALK-DIC in the deep ocean at GLODAP sites (>2.5 km).

0.44 for the Indian Ocean, k = 0.41 for the Pacific Ocean). Under the normalized condition, the variability of k values is reduced. Compared to k values at the *in situ* condition, k values calculated under normalized conditions are lower in the Atlantic but still remain the highest (k = 0.54), and higher in the Pacific and Indian.

For both *in situ* and the normalized conditions, when the data from global deep ocean are plotted together, the curvature of the data array suggests that the k values seem to depend on $[CO_3^{2-}]$ (Figure 5-4 and 5-5). This potential variation of k with $[CO_3^{2-}]$ is thus further explored based on both artificial and GLODAP data.

Based on the artificial data, k values are calculated as the derivatives of the smoothed $[CO_3^{2-}]$ to ALK-DIC. The k values calculated for *in situ* and normalized conditions are similar. The k value increases from 0.35 to 0.59

within the typical deepwater $[CO_3^{2-}]$ range of 50 to 150 μmol/kg (Figure 5-6). The k values increase from 0.35 to ~0.52 in the $[CO_3^{2-}]$ range of 50 to 100 μmol/kg. At higher $[CO_3^{2-}]$, the increment of k values is smaller than 0.07 in the $[CO_3^{2-}]$ range of 100 to 150 μmol/kg.

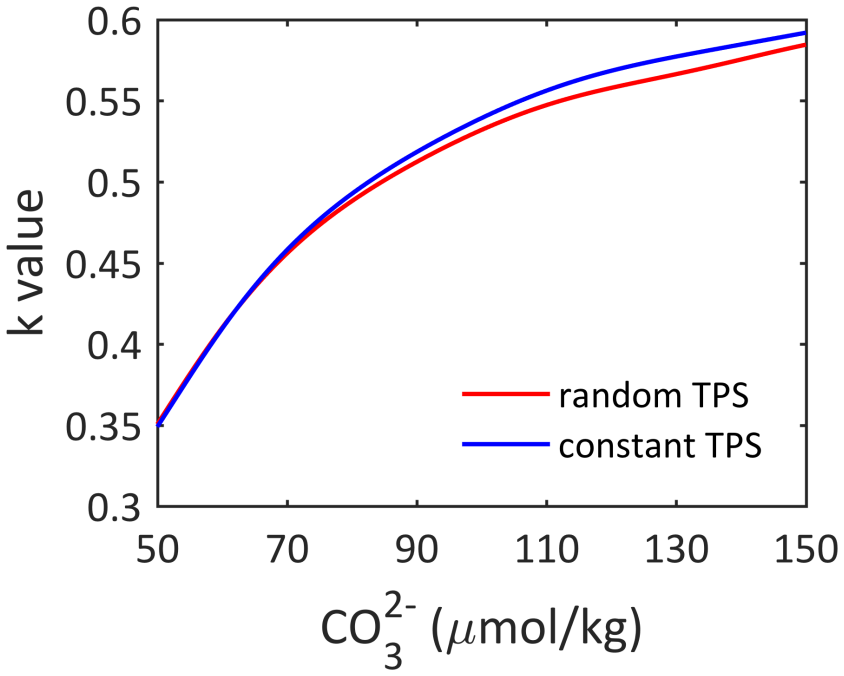

Figure 5-6: k values at different $[CO_3^{2-}]$ calculated using artificial data.

To derive k values using GLODAP data, $[CO_3^{2-}]$ at each site is recalculated from ALK and DIC with small increments. One potential issue of this calculation is that $[CO_3^{2-}]$ calculated at the same ALK-DIC increment, but different ratios of ALK to DIC are different (Figure 5-1), which would result in different k values. To overcome this issue, I define the increments of ALK and DIC by an increment of $[PO_4^{3-}]$ ($\pm$ 0.01 μmol/kg) via the Redfield Ratio of 1:16:106 (Redfield, 1934) and rain ratio (the mole ratio between carbon released by remineralization of organic matter and $CaCO_3$) of 4:1 (Broecker et al., 1982). The robustness of the choice of Redfield Ratio and rain ratio is then tested by sensitivity tests.

The choice of Redfield ratio and rain ratio is based on the assumption that these ratios are somewhat constant throughout the ocean, which is not

the case. There is currently no consensus on the exact stoichiometry of the Redfield ratio (C/P), and inverse-model studies suggest that C/P can better fit modern hydrological observations if it varies in different oceans (Teng et al., 2014). There is no globally consistent rain ratio either (*e.g.*, Hain et al., 2014). Besides, both Redfield ratio and rain ratio might change on the glacial-interglacial timescale. If the k value is sensitive to the Redfield ratio or rain ratio, the k value derived from the modern data may not be applied directly to paleo-reconstructions. To this end, I test the sensitivities of k value to various Redfield ratios and rain ratios. The k value is calculated at different C/P and rain ratios using the same $[PO_4^{3-}]$ increment. Figure 5-7 demonstrates that k value is not sensitive to changes in neither Redfield ratio nor rain ratio. The average k value in the Atlantic only shows a small variation (0.48 to 0.52, Figure 5-7), with dramatic changes in both Redfield ratio and rain ratio. The small variability of the average k value validates the k value calculated from the $[PO_4^{3-}]$ increment, with assumptions on the regeneration of both organic matter and $CaCO_3$.

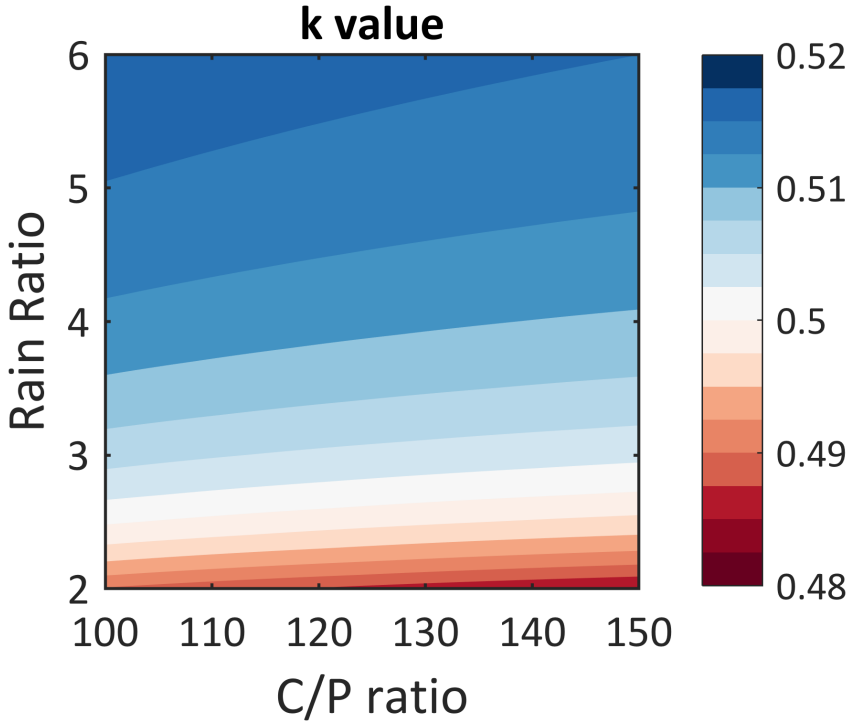

Figure 5-7: Average deep Atlantic k values calculated at various Redfield ratios and rain ratios.

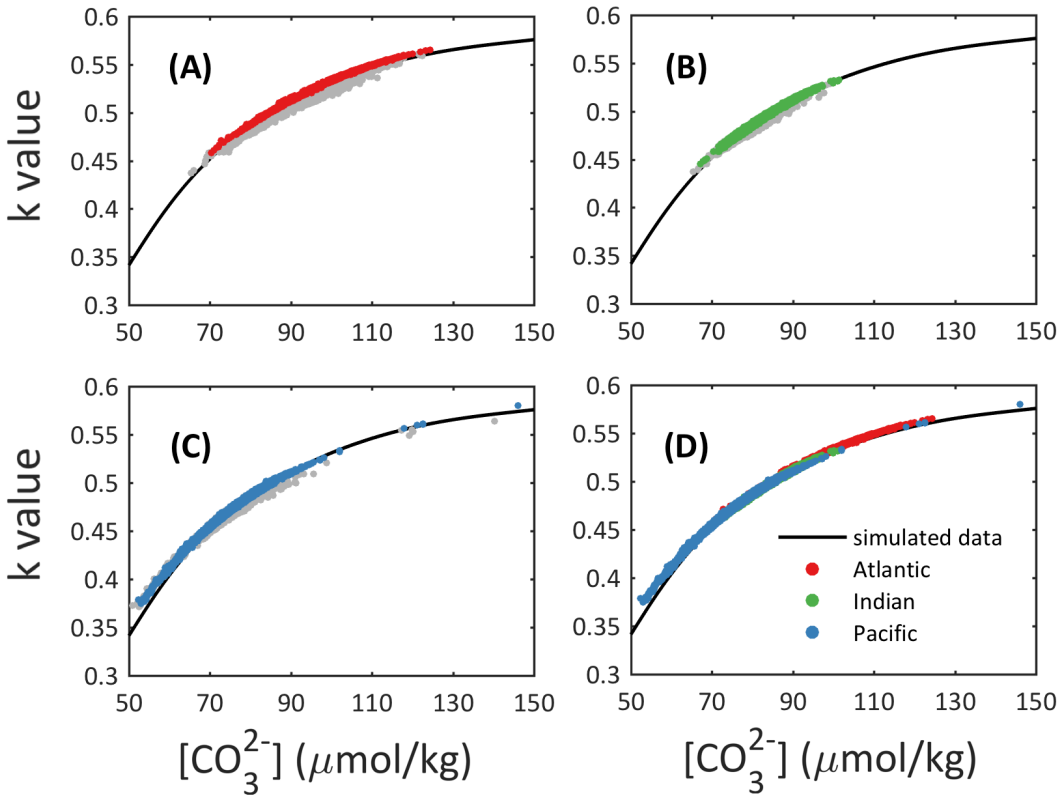

Figure 5-8: k values at different $[CO_3^{2-}]$ calculated from the deep ocean (water depth $>$ 2.5 km) using GLODAP data in three ocean basins: (A) the Atlantic Ocean, (B) the Indian Ocean, (C) the Pacific Ocean, and (D) the global ocean. The black curves in all panels are calculated from artificial data at the constant condition. The gray dots in panel (A)-(C) are k values computed from GLODAP data at in situ conditions while the red, green, and blue dots are k values calculated at the normalized condition. In panel (D), only k values in the normalized condition are shown.

The k values calculated from GLODAP data in the three ocean basins are shown in Figure 5-8. The k values are similar for the *in situ* and the normalized conditions. The spread of k values is slightly larger for the *in situ* condition than the normalized condition. K values calculated from the GLODAP data are consistent with those calculated from the artificial carbonate system data. In the Pacific Ocean, the k value can be as low as 0.4, while in the Atlantic, the k value can be as high as 0.57. Similar to the results from the artificial carbonate systems, k value is less sensitive to $[CO_3^{2-}]$ change at high $[CO_3^{2-}]$ (Figure 5-8).

The consistent dependence of k values on $[CO_3^{2-}]$ determined from the simulated data and the GLODAP data demonstrates that the variation of k value is intrinsically determined by the carbonate system and does not rely on the exact level of ALK and DIC. In other words, the k-$[CO_3^{2-}]$ relationship applies to all seawater carbonate system, which is useful to estimate the carbon inventory of the deep ocean. It is suggested that response of $[CO_3^{2-}]$ to ALK-DIC is not linear. Take the modern ocean as an example, a given $[CO_3^{2-}]$ change in the Indo-Pacific suggests a larger change in ALK-DIC in the Indo-Pacific than compared to the Atlantic, with a factor of $\sim$1.5.

5.4 Conclusions

In this chapter, the relationship between $[CO_3^{2-}]$ and ALK-DIC is investigated using modern hydrological data and artificial carbonate system data. The correlation between $[CO_3^{2-}]$ and ALK-DIC exists beyond the modern range of ALK and DIC. This confirms that this correlation is not an artifact of the covariation of ALK and DIC in the modern ocean. Therefore, the $[CO_3^{2-}]$-(ALK-DIC) correlation is a robust feature that can be employed to quantify past DIC change using $[CO_3^{2-}]$. It is further demonstrated that the sensitivity of $[CO_3^{2-}]$ to ALK-DIC is dependent on $[CO_3^{2-}]$. The $[CO_3^{2-}]$ change is more sensitive to ALK and DIC changes at high $[CO_3^{2-}]$ values. The improved relationship between $[CO_3^{2-}]$ and (ALK - DIC) can help better quantify the carbon inventory in the deep ocean, especially in the deep Indo-Pacific where $[CO_3^{2-}]$ values are lower than those in the Atlantic.

Chapter 6

Deep SW Pacific carbonate chemistry during the last glacial cycle

6.1 Introduction

The Southern Ocean has been recognized as an important player in regulating atmospheric pCO_2 on the glacial-interglacial timescale (Sigman et al., 2010, and references therein). It has been proposed that more carbon is sequestered into the deep Southern Ocean during the glacial times,which ultimately contributed to the low atmospheric pCO_2 during ice ages (Sigman and Boyle, 2000; Sigman et al., 2010, and references therein).

The accumulation of carbon in the deep Southern Ocean during glacials and the release of carbon during deglacials can be considered based on the closed-system and open-system responses (Sigman and Boyle, 2000). Closed-system responses redistribute carbon within the ocean-atmosphere system, which are mainly driven by the biological pump and global circulation (Sigman and Boyle, 2000). The Southern Ocean, where carbon rich deep water upwells to the surface, is a window for direct carbon exchange between the deep ocean and the atmosphere. In the modern ocean the annual carbon flux is close to

zero, as the summer CO_2 uptake and winter CO_2 release generally cancel out (Takahashi et al., 2009). The deep water upwelling in the modern Southern Ocean is also rich in nutrients, which are not completely consumed at surface before returning to the subsurface (Sigman and Boyle, 2000, and references therein). The incomplete use of nutrients allows sequestered carbon to escape to the atmosphere (Takahashi et al., 2009), but also offers an opportunity to enhance carbon sequestration into the deep ocean if nutrients can be more efficiently utilized (*e.g.*, Martin, 1990; Francois et al., 1997; Martínez-García et al., 2014). Circulation of deep water in the Southern Ocean, especially the upwelling of deep water also control the exchange of carbon between the surface and deep Southern Ocean (Anderson et al., 2009; Burke and Robinson, 2012). Besides, changes in the efficiency of sea-air exchange, possibly related to shift in southern westerly winds (Toggweiler et al., 2006) and sea ice coverage (Stephens and Keeling, 2000) can also affect the CO_2 flux within the Southern Ocean.

Changes in seawater carbonate chemistry caused by closed-system processes can affect interactions between the ocean carbon reservoir and the labile parts of the sedimentary carbon reservoirs on the seafloor and continental shelves. These processes are known as open-system processes (Sigman and Boyle, 2000). The change of deepwater carbonate chemistry can affect alkalinity balance by altering $CaCO_3$ preservation on the seafloor (Broecker and Peng, 1987; Boyle, 1988). Sea level fluctuations can shift the locus of carbonate deposition between the deep sea and continental shelves, contributing to seawater alkalinity inventory change (Berger, 1982; Opdyke and Walker, 1992).

The Pacific Sector of the Southern Ocean is a crucial region for the carbon inventory in the deep ocean, as it connects the vast deep waters in the Pacific Ocean with the atmosphere. Deepwater carbonate chemistry in the South Pacific provides important information about the carbon inventory change on the glacial-interglacial timescale. To date, deepwater carbonate chemistry in the deep South Pacific is still not well quantified for the last full glacial cycle.

Most of our knowledge about the deepwater carbonate chemistry in this region relies on a qualitative proxy, carbonate content in the sediment ($\%CaCO_3$) (*e.g.*, Howard and Prell, 1994). In this chapter, deepwater carbonate chemistry in the Southwestern Pacific Ocean during the last glacial cycle is reconstructed using benthic B/Ca in two sediment cores (GC34 and MD97-2106) located on the South Tasman Rise.

6.1.1 Modern Southern Ocean hydrography

Circulation in the Southern Ocean is largely dominated by the Antarctic Circumpolar Current (ACC), which flows eastwards continuously and isolates Antarctic. The ACC is mainly forced by westerlies between 40 and 60 °S (Talley et al., 2011). The westerlies also drive the northwards Ekman transport under the influence of Coriolis force.

Fronts and zones. Owing to the ACC, nearly zonal fronts defined by pronounced meridional gradients of surface properties are developed in the Southern Ocean (Figure 6-1A). The Subtropical Front (STF) marks the northernmost boundary of all Southern Ocean phenomena (Talley et al., 2011). The STF separates the cold and fresh subantarctic water from the warm and saline subtropical water (Orsi et al., 1995). In the Tasman Region, the equatorwards subantarctic water overrides the the polarwards subtropical water, forming the Subtropical Front Zone (STFZ) (Hamilton, 2006). The north and the south STF in the Tasman Region can be defined as the 10 and 12 °C temperature contour at 100 m water depth (Orsi et al., 1995). Within the ACC, there are three fronts from the north to south: the Subantarctic Front (SAF), the Polar front (PF), and the Southern ACC Front (SACCF). All these three fronts are strong eastwards flow. The SAF is the northern edge of the ACC, and can be identified as the 4 °C temperature contour at 200 m (Orsi et al., 1993; Belkin and Gordon, 1996). The PF is the northern edge of the shallow temperature minimum that can be represented by 2 °C temperature contour at 200 m (Orsi

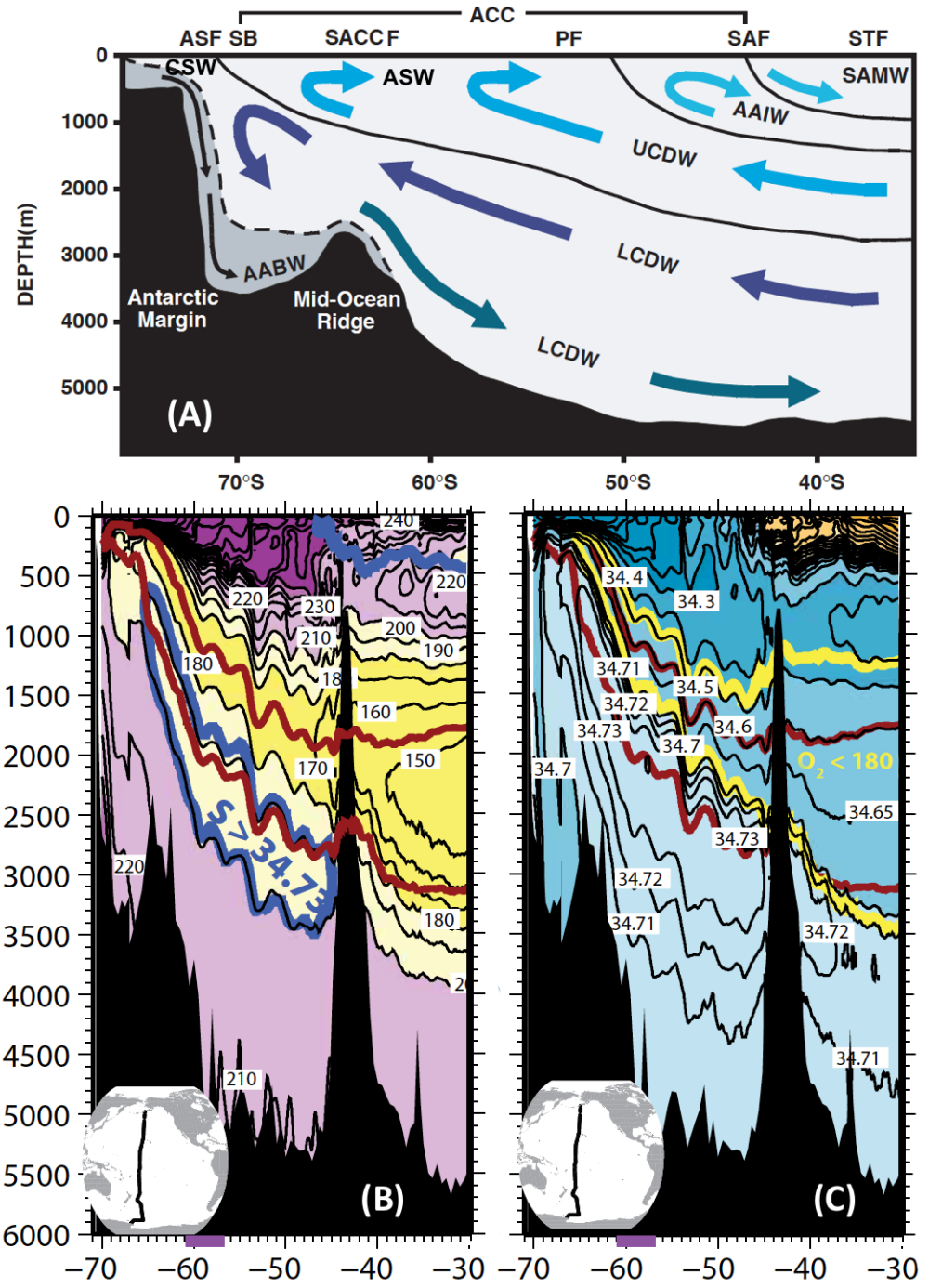

Figure 6-1: (A) A schematic meridional section of the Southern Ocean showing main fronts and water masses. (B) Oxygen concentration and (C) salinity for the South Pacific Ocean. The salinity maximum is shown in (B) by the thick blue lines. The oxygen concentration minimum is also shown in (C) by the thick yellow lines. The two thick dark red lines in (B) and (C) are isoneutral contours of 27.8 and 28.04 kg/m^3, which indicate the core of IDW/PDW and NADW, respectively. (A) is modified from Carter et al. (2008), and (B) and (C) are modified from Talley (2013).

et al., 1993; Belkin and Gordon, 1996). The Southern Boundary (SB) is south of the SACCF, but sometimes merges with the SACCF (Orsi et al., 1995). It is not a dynamical front but the edge of the Upper Circumpolar Deep Water (UCDW). The Antarctic Slope Front (ASF) is south of the ACC and locates mostly along the continental slope.

The fronts separate the Southern Ocean into the zones as shown in Figure 6-1A. From the north to south these zones are: the Subantarctic Zone (SAZ; between the STF and SAF), the Polar Frontal Zone (PFZ; between the SAF and PF), the Antarctic Zone (AZ; between the PF and SACCF), the Southern Zone (SZ; between the SACCF and SB), and the Subpolar Region (south of the SB Orsi et al., 1995).

Water masses. Distribution of surface water masses in the Southern Ocean can largely be defined by the main fronts. The Continental Shelf Water (CSW) south of the ASF is cold and dense. Temperature of the CSW can be close to freezing point in winter, and the density of CSW is comparable to Antarctic Bottom Water (AABW) (> 28.27 kg/m^3) (Whitworth et al., 1998). There could be salinity stratification within the CSW possibly due to brine injection, and the saltiest part of it is the source of the AABW (Talley et al., 2011). The Antarctic Surface Water (ASW), which is a cold (temperature between -1.9 to 1 °C in winter) and fresh (salinity between 33 to 34.5 ‰) water mass, occupies the surface ocean south of the PF. The surface water between the SAF and PF within the PFZ is the transitional water between the ASW and Subantarctic Surface Water (SASW). North of the SAF is the SASW, with a temperature range of 4 to 10 °C and a salinity around 34 ‰ during winter. The Subantarctic Mode Water (SAMW) is formed just north of the SAF as the mixed layer thicken during winter (McCartney and Talley, 1982). It can reach 500 m at depth in the Indian Ocean, and is deeper than 300 m in the Pacific Ocean. The SAMW supplies large amount of the Southern Ocean surface water to the subtropical gyres (Talley et al., 2011).

Below the SAMW is the Antarctic Intermediate Water (AAIW), characterized as a vertical salinity minimum, at about 500 to 1500 m. The AAIW is found north of the SAF and extend to 10 to 20 °N in the Pacific Ocean and 15 to 20 °N in the Atlantic Ocean. It is still under debate whether the AAIW is formed by the sinking ASW across the SAF or locally in the Southeast Pacific and the Drake Passage (Talley et al., 2011).

The Circumpolar Deep Water (CDW) is the largest deep water mass in the Southern Ocean. It is not formed at the sea surface, but a mixture of the deep waters from in three major ocean basins, and deep waters formed around Antarctic (Talley et al., 2011). The North Atlantic Deep Water (NADW), Pacific Deep Water (PDW), and Indian Deep Water (IDW) are mixed upon entering the ACC. The CDW can be divided into the UCDW and the Lower Circumpolar Deep Water (LCDW). The UCDW is characterized by the vertical oxygen minimum (< 180 μmol/kg, Figure 6-1C), as it is contributed by mainly by the PDW and IDW, which have low oxygen and high nutrient concentrations. North of the PF, the UCDW has a depth range of 1400 to 2500 m (Talley et al., 2011). The UCDW upwells to the south across the ACC, and it meets the surface water or outcrops within the PFZ and AZ. The UCDW only upwells north of the SB, within the ACC. As a result, nutrients are supplied to the ASW by the UCDW and are transported northwards by the AAIW and SAMW. The LCDW is characterized by the vertical salinity maximum (~34.72 ‰ in the Pacific, ~34.75 ‰ in the Indian, and 34.8 to 34.9 ‰ in the Atlantic), which is reminiscent of the saline NADW (Figure 6-1B) (Talley et al., 2011). It occupies the depth deeper than 2500 m and reaches the bottoms of Pacific and Indian Ocean north of the PF.

The Antarctic Bottom Water (AABW) is the densest water mass in the Southern Ocean, and it is defined by its neutral density, which is > 28.27 kg/m^3 in a strict sense (Orsi et al., 1999). According to this definition, the AABW is largely restricted to the southern regions by the ocean ridges (Talley et al., 2011). In comparison to the LCDW, the AABW is fresher and colder.

Weddell Sea, Ross Sea, and Adélie coast are the three main locations for the AABW formation (Rintoul and Bullister, 1999). The AABW is formed the mixture of the CSW flowing down slopes and the CDW north of the ASF.

6.1.2 Deep-water $[CO_3^{2-}]$ variations

In this section, I summarize how deepwater $[CO_3^{2-}]$ can be affected by closed-system and open-system processes and deepwater $[CO_3^{2-}]$ variation in the modern ocean.

Closed-system responses. Closed-system responses affect deepwater $[CO_3^{2-}]$ mainly by changing carbon contents in the deep ocean. These processes include changes in the biological pump (Boyle, 1988; Matsumoto, 2007; Martínez-Garcia et al., 2011; Martínez-García et al., 2014) and ocean circulation (Burke and Robinson, 2012; Chen et al., 2015; Ronge et al., 2016).

A strengthened biological pump in the SAZ, driven by increased dust fluxes, has been proposed to explain the atmospheric pCO_2 decline during glaciation (Anderson et al., 2002; Martínez-García et al., 2014). An increased iron-bearing dust input into the nutrient-rich SAZ can enhance the productivity that is currently limited by iron availability (Martin, 1990). In the Atlantic sector of the Southern Ocean, enhanced productivity, as indicated by Alkenone flux, and a higher degree of nitrate consumption have been observed to coincide with the increased dust fluxes during the last glaciation (Martínez-García et al., 2014). This supports that a strengthened biological pump, driven by iron fertilization, assisted to sequester more carbon into the deep Southern Ocean, contributing to the low atmospheric pCO_2 during the last ice age (Martínez-García et al., 2014).

Besides productivity changes, the export rate of organic carbon might change on the glacial-interglacial timescale (Boyle, 1988; Keir, 1988; Matsumoto, 2007). The export rate could be altered along with changes in export productivity (Keir, 1988; Boyle, 1988) or due to reduced regeneration

rate of organic carbon at the colder glacial temperatures (Matsumoto, 2007). The increase in the export rate, the results of increased export productivity and decreased regeneration rates, can shift the depth of maximum regeneration from intermediate depths to deep depths (Boyle, 1988; Keir, 1988; Matsumoto, 2007). Laterally this can shift nutrients from the Atlantic basin to the Indo-Pacific basins (Boyle, 1988; Keir, 1988; Matsumoto, 2007).

Water mass mixing affects deepwater [CO_3^{2-}] by changing relative proportions of various water masses and by changing [CO_3^{2-}] of the end-member water masses.

In the modern ocean, the deep SW Pacific is filled with the LCDW, which retains the NADW imprint (Rintoul and Bullister, 1999). As the NADW shoaled during glacials, the proportion of the NADW entrained into the deep Indo-Pacific decreased (Ferrari et al., 2014). This is supported by reconstructions based on both $\delta^{13}C_b$ (Oppo et al., 1990; Ninnemann and Charles, 2002; Moy et al., 2006) and ε_{Nd} (Piotrowski et al., 2005, 2009; Wilson et al., 2015; Molina-Kescher et al., 2016; Hu et al., 2016). The glacial PDW has been suggested to have a larger influence on the LCDW, as radiocarbon depleted water accumulated in the deep SW Pacific (Skinner et al., 2015; Ronge et al., 2016). The contribution of the AABW to the LCDW during the LGM is less well constrained, but it is speculated that its influence might be stronger during glacials based on $\delta^{13}C_b$ data (Ullermann et al., 2016).

In the modern ocean, [CO_3^{2-}] of the major deep water masses (PDW, AABW, and NADW) are consistent with the trend defined by regeneration of organic matters (Broecker et al., 1982; Yu et al., 2008). In the glacial ocean, [CO_3^{2-}] of major deep water masses may be altered by changes in the ocean stratification (Burke and Robinson, 2012; Skinner et al., 2015; Chen et al., 2015; Ronge et al., 2016) and the air-sea exchange (Stephens and Keeling, 2000). [CO_3^{2-}] of the North Atlantic sourced water, which affects the preformed [CO_3^{2-}] of the global deep ocean, was higher than the modern level owing to low atmospheric pCO_2 (Yu et al., 2010b). [CO_3^{2-}] of the PDW is expected to have

a larger offset from the North Atlantic sourced waters during glacials because the deep ocean was poorly ventilated, as shown by radiocarbon data from all sectors of the deep Southern Ocean (Burke and Robinson, 2012; Skinner et al., 2015; Chen et al., 2015; Ronge et al., 2016). $[CO_3^{2-}]$ of the PDW can be approximated by records from the deep equatorial Pacific (Yu et al., 2013; Kerr et al., 2017), which shows a minimal LGM-Holocene gradient, and a larger offset from $[CO_3^{2-}]$ of the North Atlantic sourced water during glacials (Yu et al., 2013; Kerr et al., 2017). The $[CO_3^{2-}]$ of the AABW is unconstrained because several competing processes can potentially affect deep water $[CO_3^{2-}]$: the air-sea exchange, the alkalinity change, and the biological pump change. Downcore reconstruction for the AABW is also very challenging, and the only deep water $[CO_3^{2-}]$ record available (Rickaby et al., 2010) cannot resolve glacial-interglacial variations (Kerr et al., 2017).

Open-system responses. Open-system responses involve dissolution and preservation of $CaCO_3$ on the seafloor (Broecker and Peng, 1987; Boyle, 1988), and deposition of $CaCO_3$ on the continental shelves (Berger, 1982; Opdyke and Walker, 1992).

When deepwater $[CO_3^{2-}]$ is changed by closed-system processes, carbonate saturation state ($\Delta[CO_3^{2-}]$) would also be modified, affecting the preservation of $CaCO_3$ on the seafloor. This changes the whole ocean ALK, and thus $[CO_3^{2-}]$, acting as a positive feedback to restore ALK fluxes back to a steady state on a timescale of $\sim$7 kyr (Broecker and Peng, 1987). This process is called carbonate compensation (Broecker and Peng, 1987; Boyle, 1988).

Sea level fluctuations can shift the locus of carbonate deposition between deep sea and the continental shelves, affecting the ALK change and $[CO_3^{2-}]$ change (Berger, 1982; Opdyke and Walker, 1992). When sea level falls, the continental shelf area decreases. As a result, $CaCO_3$ deposition on the continental shelves is reduced (Berger, 1982; Opdyke and Walker, 1992). Because of the minimal variation in the global continental weathering rate during the

late Cenozoic (Foster and Vance, 2006; Willenbring and von Blanckenburg, 2010), the reduction of $CaCO_3$ deposition on the continental shelves leads to an increase in the whole ALK and thus $[CO_3^{2-}]$ (Berger, 1982).

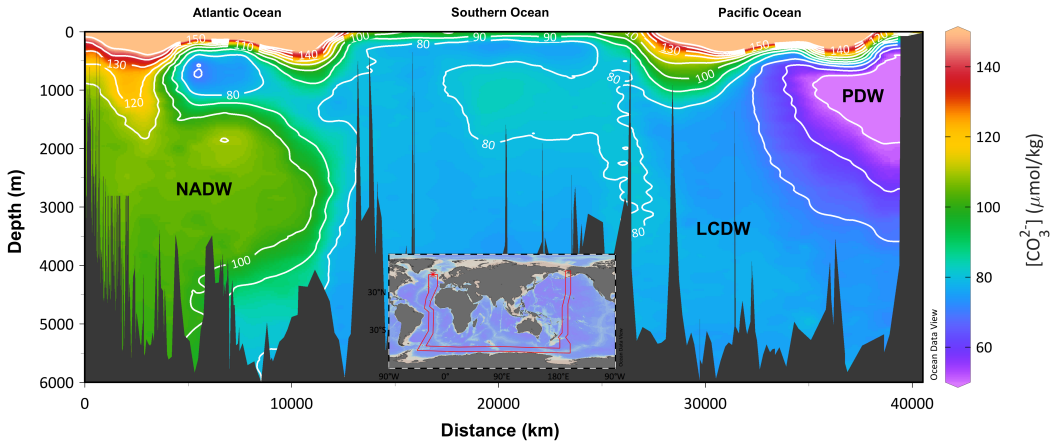

Figure 6-2: A transect showing $[CO_3^{2-}]$ of major deep water masses including NADW, PDW and, PDW.

$[CO_3^{2-}]$ of water masses. Formation of organic matter and carbonate in the surface ocean enhance $[CO_3^{2-}]$ of surface water (Figure 5-1). In the Atlantic and Pacific surface seawater $[CO_3^{2-}]$ is higher than 150 μmol/kg (Figure 6-2). Distribution of $[CO_3^{2-}]$ in the deep ocean reflect the ventilation history of the deep water. As NADW is well-ventilated, it has the highest $[CO_3^{2-}]$ in the deep ocean of about 110 μmol/kg (Figure 6-2). The most poorly-ventilated PDW, on the other hand, has the lowest $[CO_3^{2-}]$ of about 50 μmol/kg (Figure 6-2). In the Southern Ocean, $[CO_3^{2-}]$ of LCDW is between 70 and 80 μmol/kg, owing to the strong upwelling and the contribution of NADW to LCDW (Figure 6-2).

6.2 Materials and methods

6.2.1 Materials

The two studied sediment cores, GC34 and MD97-2106, are located in the Southwestern Pacific at 4.0 and 3.3 km, respectively (Table 6.1, Figure 6-3). The average sediment rate is 2.8 cm/kyr at GC34 during the last 150

kyr. GC34 is sampled every ∼3 cm for the LGM-Holocene interval, and every ∼5 cm for the rest of the last glacial-interglacial cycle. For MD97-2106, the average sediment rate is 9.3 cm/kyr during the last 150 kyr. MD97-2106 is sampled every ∼10 cm for the LGM-Holocene interval, and every ∼20 cm for the rest of the last glacial-interglacial cycle.

Sediment samples are disaggregated and sieved through 63 μm sieves. For each sample, sediments $<$ and $>$ 63 μm are dried and weighed, respectively. All pristine *Cibicidoides wuellerstorfi* shells are preferentially picked from the 250-500 μm size fraction. When insufficient (< 5) shells can be picked from this size fraction, effort was made to pick *C. wuellerstorfi* shells from the 212-250 μm size fraction. *C. wuellerstorfi* shells are checked before crushing to ensure consistent morphology. For each sample, 3 to 20 shells are crushed. If the total number of *C. wuellerstorfi* shells for a sample is larger than 15, these shells are divided into two subsamples and crushed separately for replicate analyses. The crushed shells are cleaned according to the 'Mg-cleaning' method (Barker et al., 2003). All samples are checked under a microscope to remove foreign particles using a single-haired brush before moving on to the oxidative step (Yu et al., 2007a). The reductive cleaning step is not employed. This is because B/Ca is negligibly affected by the reductive step (Yu and Elderfield, 2007), and foraminiferal shells can be partially dissolved during this step (Yu et al., 2007a).

6.2.2 Analytical method

Trace element to calcium ratios of foraminiferal samples were measured on a Varian 820 ICP-MS at the ANU, following the method of Yu et al. (2005). The analytical precision for B/Ca, based on repeated measurements of an in-house solution standard is 2.7% (151.4±4.2 μmol/mol, 2σ). Relative standard deviations of B/Ca for replicate samples are 1.3−2.6 % (N = 4) and 0.1−4.2 % (N = 10) for MD97-2106 and GC34, respectively.

6.2.3 Hydrographic settings

The two studied cores are located in the Subtropical Front Zone (STFZ), and bathed in the LCDW in the modern ocean, making them ideal for reconstructing the Southern Ocean conditions in the Pacific Sector.

Core	Lat. °S	Lon. °E	Water depth m	Sed. rate cm/kyr	$[CO_3^{2-}]$ μmol/kg	$\Delta[CO_3^{2-}]$ μmol/kg	Core type
MD97-2106	45.15	146.28	3310	9.3	80	-2	Piston
GC34	45.10	147.75	4002	2.8	80	-14	Gravity

Table 6.1: Locations, sedimentation rates, deepwater carbonate chemistry of MD97-2106 and GC34.

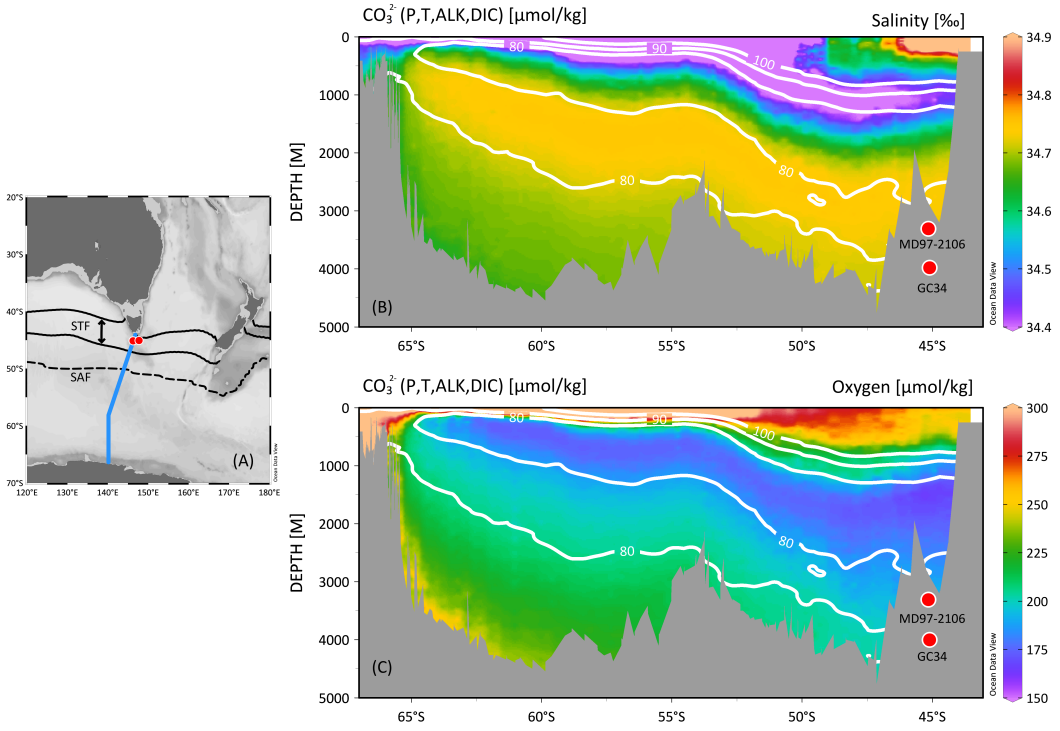

Figure 6-3: Hydrological settings of two cores used in this study. (A) Location of two sediment cores. Black solid lines are northern and southern bounds of STF, and the black dashed line is the SAF (Belkin and Gordon, 1996). (B) and (C) Contours of $[CO_3^{2-}]$ superimposed on salinity (B) and oxygen concentration (C) of the transect indicated by the blue curve in (A).

The STF in the Tasman Region is characterized by a zonal trending band, with the equatorwards limit of the cold and fresh subantarctic water overriding the polarwards limit of the warm salty subtropical water (Hamilton, 2006). Regarding nutrients, subantarctic water is rich in macro-nutrients, whereas

the subtropical water is rich in iron (Boyd et al., 1999). Both macro-nutrients and iron limit the regional productivity (Boyd et al., 1999).

At the latitude of the two studied cores, the salinity maximum is at ~3000 m, indicating the core of the LCDW (Callahan, 1972; Rintoul and Bullister, 1999; Talley, 2013) (Figure 6-3). The oxygen minimum, which defines the UCDW (Callahan, 1972; Rintoul and Bullister, 1999; Talley, 2013) , is about 1500 to 2000 m (Figure 6-3). $[CO_3^{2-}]$ of the LCDW is lower than that of the UCDW, because 1) the LCDW is influenced by the NADW with high $[CO_3^{2-}]$ compared to the south-sourced waters (Yu et al., 2008) and 2) the UCDW is rich in regenerated organic matter. (Figure 6-3).

In the SW Pacific, deep-water carbonate chemistry has been investigated by dissolution proxies (Bostock et al., 2011, and references therein). Based on carbonate content ($\%CaCO_3$) of core-top sediment, the carbonate compensation depth (CCD), the depth at which $\%CaCO_3$ is less than 20% (Broecker et al., 1982), is between 3700 and 4800 m in the Tasman Sea Basin(Bostock et al., 2011). The fragmentation of foraminifera, however, indicates that significant $CaCO_3$ dissolution occurs around 3550 m in the Tasman Basin (Martinez, 1994).

6.2.4 Age model

The age models of two two studied cores are reconstructed based on published data (Moy et al., 2006) and shown in Figure 6-4. Published radiocarbon dates of both cores (Moy et al., 2006) are calibrated to the Marine13 curve (Reimer et al., 2013) assuming a constant surface reservoir age of 400 years, calculated using Calib v7.1 (Stuiver and Reimer, 1993). Published benthic $\delta^{18}O$ data (Moy et al., 2006) are aligned to the global benthic $\delta^{18}O$ stack for the last 150 kyr (Lisiecki and Stern, 2016). The tie-points for both cores are the mid-points between $\delta^{18}O_b$ peaks and troughs.

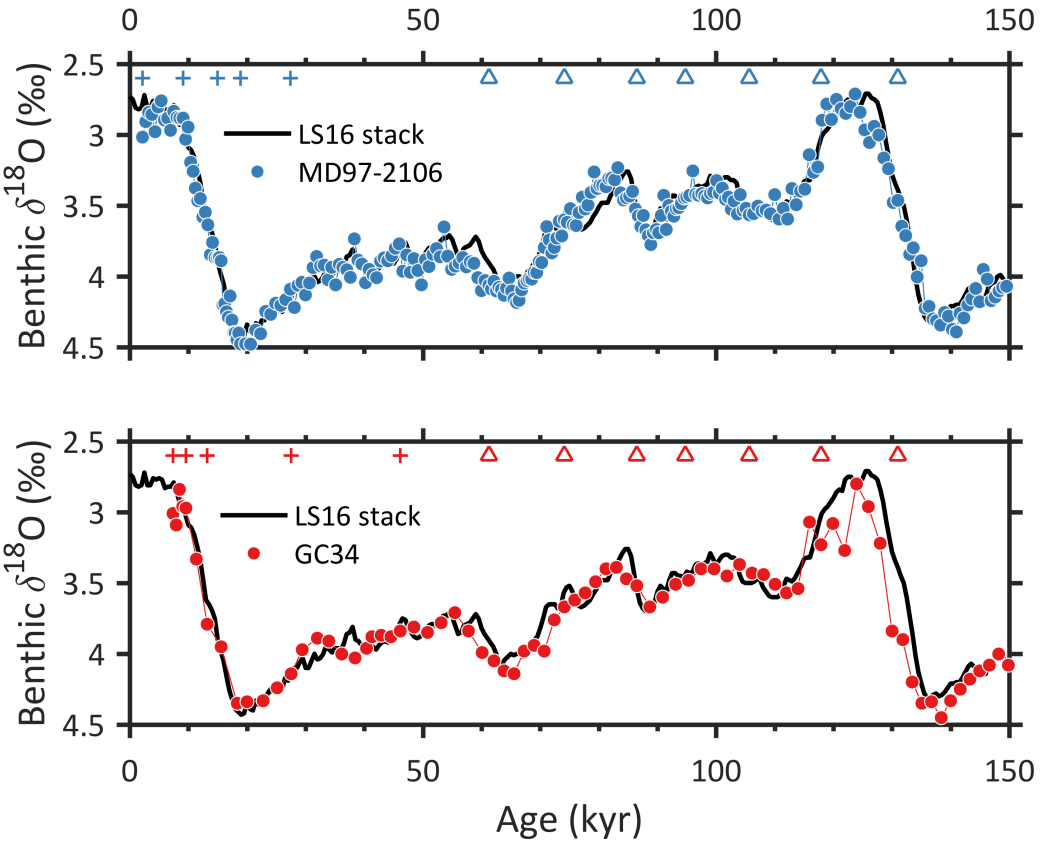

Figure 6-4: Age models of MD97-2106 and GC34. The black curves are the global benthic δ^{18}O stack for the last glacial cycle (Lisiecki and Stern, 2016), vertically shifted to be consistent with downcore benthic δ^{18}O data (Moy et al., 2006).Pluses and triangles along the top x axises represent tie points based on radiocarbon and the benthic δ^{18}O, respectively.

6.2.5 $[CO_3^{2-}]$ calculation

Deepwater $[CO_3^{2-}]$ is calculated from *C. wuellerstorfi* B/Ca based on the core-top calibration of Yu et al. (2013), which combines all published core-top data to date (Yu and Elderfield, 2007; Rae et al., 2011; Raitzsch et al., 2011; Brown et al., 2011; Yu et al., 2013):

$$\begin{aligned} B/Ca &= k \times \Delta[CO_3^{2-}] + b, \\ k &= 1.14 \pm 0.04,\ b = 176.6 \pm 1.0. \end{aligned} \tag{6.1}$$

The saturation $[CO_3^{2-}]$ is largely depth (pressure)-dependent, so that its variation is minimal on the glacial-interglacial timescale. As a result, *in situ* $[CO_3^{2-}]$

can be determined by deepwater $\Delta[CO_3^{2-}]$ reconstructed from benthic B/Ca:

$$[CO_3^{2-}]_{in\ situ} = \Delta[CO_3^{2-}] + [CO_3^{2-}]_{saturation}. \tag{6.2}$$

If the core-top is of Late Holocene in age, and the benthic B/Ca variation is minimal during the Late Holocene, Equation (6.2) can be reorganized into:

$$[CO_3^{2-}]_{in\ situ} = [CO_3^{2-}]_{pre-industrial} + \Delta(B/Ca)_{Sample-LateHolocene}/1.14, \tag{6.3}$$

where only the sensitivity of B/Ca to $\Delta[CO_3^{2-}]$ is involved in the calculation of *in situ* $[CO_3^{2-}]$. The absolute $[CO_3^{2-}]$ value calculated from Equation (6.2) and (6.3) are the same, but the uncertainty of $[CO_3^{2-}]$ yielded from Equation (6.3) is smaller. This is because the intercept of Equation (6.1) is not used in Equation (6.3). For Equation (6.2) and Equation (6.3), the uncertainty of $[CO_3^{2-}]$ is calculated by Equation (6.4) and (6.5), respectively.

$$e_{[CO_3^{2-}]} = \sqrt{\left(\frac{B/Ca}{k} \times \sqrt{(\frac{e_{B/Ca}}{B/Ca})^2 + (\frac{e_k}{k})^2}\right)^2 + \left(\frac{b}{k} \times \sqrt{(\frac{e_b}{b})^2 + (\frac{e_k}{k})^2}\right)^2} \tag{6.4}$$

$$e_{[CO_3^{2-}]} = \frac{B/Ca}{k} \times \sqrt{(\frac{e_{B/Ca}}{B/Ca})^2 + (\frac{e_k}{k})^2} \tag{6.5}$$

As the Late Holocene part is missing for GC34, its $[CO_3^{2-}]$ is calculated using Equation (6.2). Deepwater $[CO_3^{2-}]$ in core MD97-2106 is calculated based on Equation (6.3), owing to the small variation of the Late Holocene B/Ca (174 $\pm$ 4 μmol/mol, n = 3). Given that the relative uncertainty of B/Ca is 2.7 % (2σ), typical uncertainties of $[CO_3^{2-}]$ for GC34 and MD97-2106 are $\sim$4 and $\sim$3 μmol/kg (1σ), respectively.

6.3 Results

Deepwater $[CO_3^{2-}]$ records from GC34 and MD97-2106 are shown in Figure 6-5, along with $\delta^{18}O_b$ data (Moy et al., 2006). These are the first deepwater

[CO_3^{2-}] records reconstructed from benthic B/Ca in the deep SW Pacific.

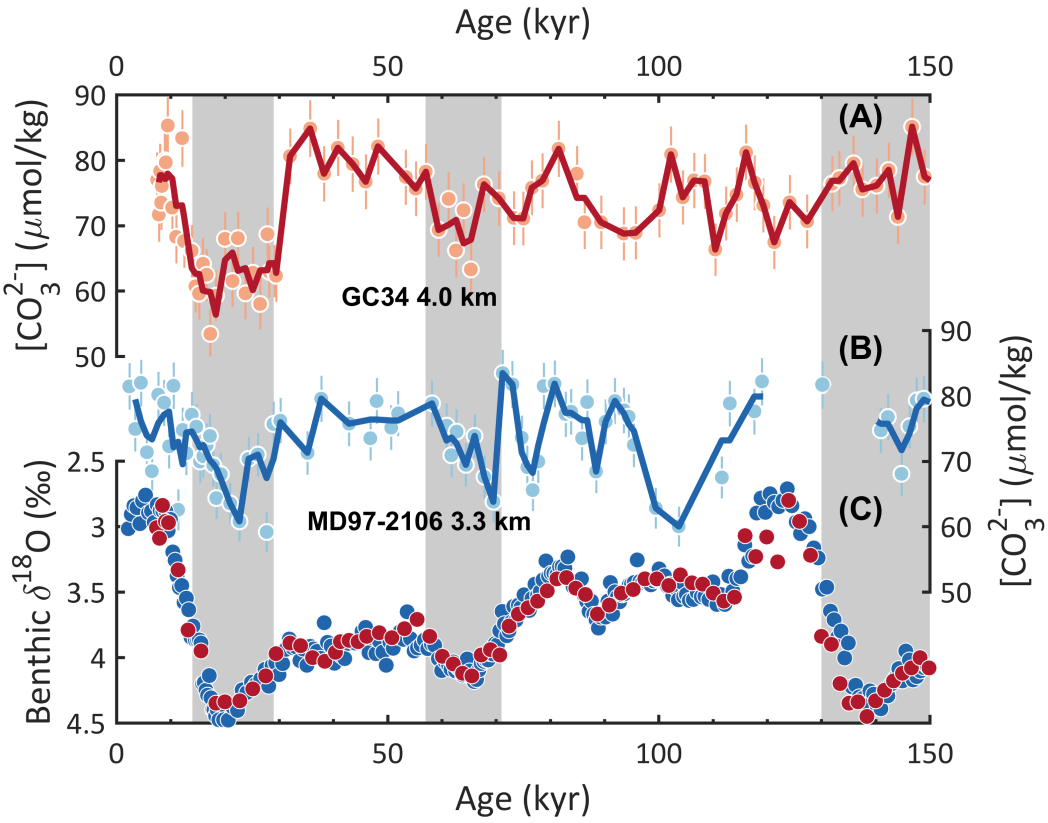

Figure 6-5: Deepwater [CO_3^{2-}] records in cores GC34 (A) and MD97-2106 (B) along with benthic $\delta^{18}O$ data from (Moy et al., 2006) (C). Errorbars of [CO_3^{2-}] data represent $\pm 1\sigma$ ranges. The thick curves in (A) and (B) are 2-kyr window running average. The cold MISs (2, 4, 6) are marked by the grey bars.

Deepwater [CO_3^{2-}] at GC34 varied from ~55 to 85 μmol/kg during the last glacial-interglacial cycle. The lowest [CO_3^{2-}] was observed during the LGM, with an average of 61 $\pm$ 4 μmol/kg (n = 12). From the late MIS 6 to 3, [CO_3^{2-}] fluctuated within a narrower range between ~70 and 85 μmol/kg, compared to Termination I (T I). The highest [CO_3^{2-}] level of ~80 μmol/kg was reached in early Holocene, MIS 3, 5a, 5e-d, and the late MIS 6. Since MIS 5d, these peak [CO_3^{2-}] values were associated with warmer MISs, as indicated by light $\delta^{18}O_b$. This is not the case for MIS 6 and 5e, when the warmer MIS 5e was lower in [CO_3^{2-}] compared to MIS 6. During the MIS 6-5e transition, [CO_3^{2-}] descended from ~77 (n = 9) to ~71 (n = 4) μmol/kg.

Deepwater [CO_3^{2-}] at MD97-2106 shows a similar variability to GC34

from ~65 to ~85 μmol/kg during the last glacial-interglacial cycle. The data resolution is lower during MIS 5e-c compared to the rest of the record, because there are not enough shells in this section of the core. This section will be re-sampled and reanalyzed in the future. The minimal $[CO_3^{2-}]$ values of ~65 μmol/kg were seen in the LGM, MIS 4, and 5d-c. The peak $[CO_3^{2-}]$ values of ~80 μmol/kg were reached during the late Holocene, MIS 3, 5a, and 6.

In the following two sections, deepwater $[CO_3^{2-}]$ records from the deep SW Pacific are compared with 1) sedimentary partial dissolution proxies at these two cores, 2) records from the deep South Atlantic and the deep equatorial Indo-Pacific, and other Southern Ocean proxies for the last 150 kyr.

6.4 Sedimentary partial dissolution

In this section, benthic B/Ca based $[CO_3^{2-}]$ records are compared with three sedimentary dissolution based proxies for deepwater $[CO_3^{2-}]$: coarse fraction content (> 63 μm %) (*e. g.*, Bassinot et al., 1994), carbonate content (%$CaCO_3$) (*e. g.*, Berger, 1973; Farrell and Prell, 1989), and planktonic foraminiferal shell fragmentation (*e. g.*, Barker and Diz, 2014), which is represented by percentage of whole planktonic foraminiferal shells (% WPF) in a previous study (Moy, 2005). In general, stronger partial dissolution can be reflected by lower > 63μm%, lower %$CaCO_3$, and lower % WPF. These proxies can be potentially complicated by variation in surface productivity (Arrhenius, 1952), pore water dissolution (Archer and Maier-Reimer, 1994), and local sediment focusing (Anderson et al., 2002). Benthic B/Ca based $[CO_3^{2-}]$, however, can better represent the bottom water condition and be independent of surface conditions (Yu and Elderfield, 2007). Benthic B/Ca and coarse fraction data are new results from this study. %$CaCO_3$ and %WPF of bothe MD97-2106 and GC34 are from previous work (Moy, 2005; Moy et al., 2006).

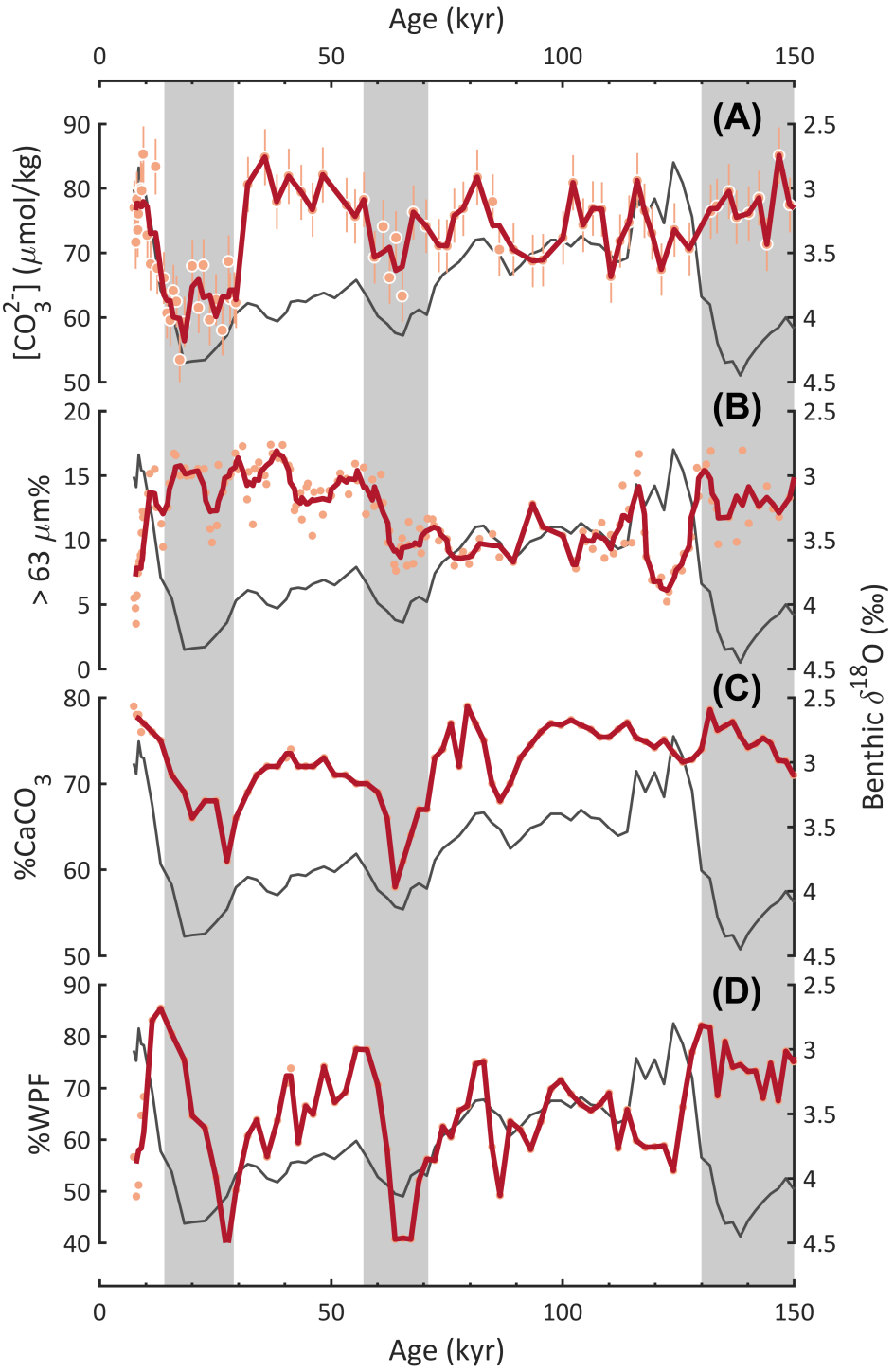

Figure 6-6: Deepwater $[CO_3^{2-}]$ records in core GC34 (A) compared with $> 63\mu$m % (B), %$CaCO_3$ (Moy et al., 2006) (C), and % WPF (Moy, 2005) (D). In all these panels, dots are original data and curves are ±2-kyr moving average. $\delta^{18}O_b$ data are shown in all panels to illustrate MISs. The cold MISs (2, 4, and 6) are shaded.

6.4.1 GC34

Deepwater $[CO_3^{2-}]$ records in cores GC34 with sedimentary partial dissolution proxies are shown in Figure 6-6. Benthic B/Ca based $[CO_3^{2-}]$ decreased during the MIS 3/2, 5a/4, and 6/5e transitions. $\%CaCO_3$ and % WPF both indicated stronger dissolution at MIS 3/2 and 5a/4 transitions. $\%CaCO_3$and % WPF reached the local minimum at the beginning of the MIS 2 and in the mid MIS 4, when the declines in $[CO_3^{2-}]$ stopped. The intensified dissolution at these two transitions, however, is not well registered in the $> 63\mu$m % record. During the course of this $[CO_3^{2-}]$ decrease at the MIS 6/5e transitions (Termination II, T II), all three dissolution proxies indicated overall stronger dissolution, but with a moderate increase in preservation at the end of the MIS 6. Benthic B/Ca based $[CO_3^{2-}]$ increased during the MIS 2/1 and 4/3 transitions. During the early Holocene, there is a decreasing trend in $[CO_3^{2-}]$ with the sediment depth, but this cannot be observed after averaging over a age window. Consistent with the overall increasing trend in $[CO_3^{2-}]$ are $\%CaCO_3$ and % WPF records. % WPF decreased at the beginning of the Holocene, before $[CO_3^{2-}]$ started to decline. > 63 μm % demonstrated a general decreasing trend at this transition. At the MIS 4/3 transition, all three dissolution proxies suggested better preservation at this transition.

6.4.2 MD97-2106

At MD97-2106, benthic B/Ca based $[CO_3^{2-}]$ decreased during the MIS 3/2 and 5a/4 transitions, and increased during the MIS 2/1 and 4/3 transitions 6-7. Among three sediment dissolution proxies investigated, $\%CaCO_3$ demonstrates the most similar trend to $[CO_3^{2-}]$ on the timescale of 10 kyr. Despite that $> 63\mu$m % does not show a similar trend to $[CO_3^{2-}]$ on the timescale of 10 kyr, it can be well aligned with $\%CaCO_3$. However, the long term trends of $> 63\mu$m % and $\%CaCO_3$ differ, especially in the MIS 3. Variation of % WPF does not show clear relation with $[CO_3^{2-}]$ or the other two dissolution proxies.

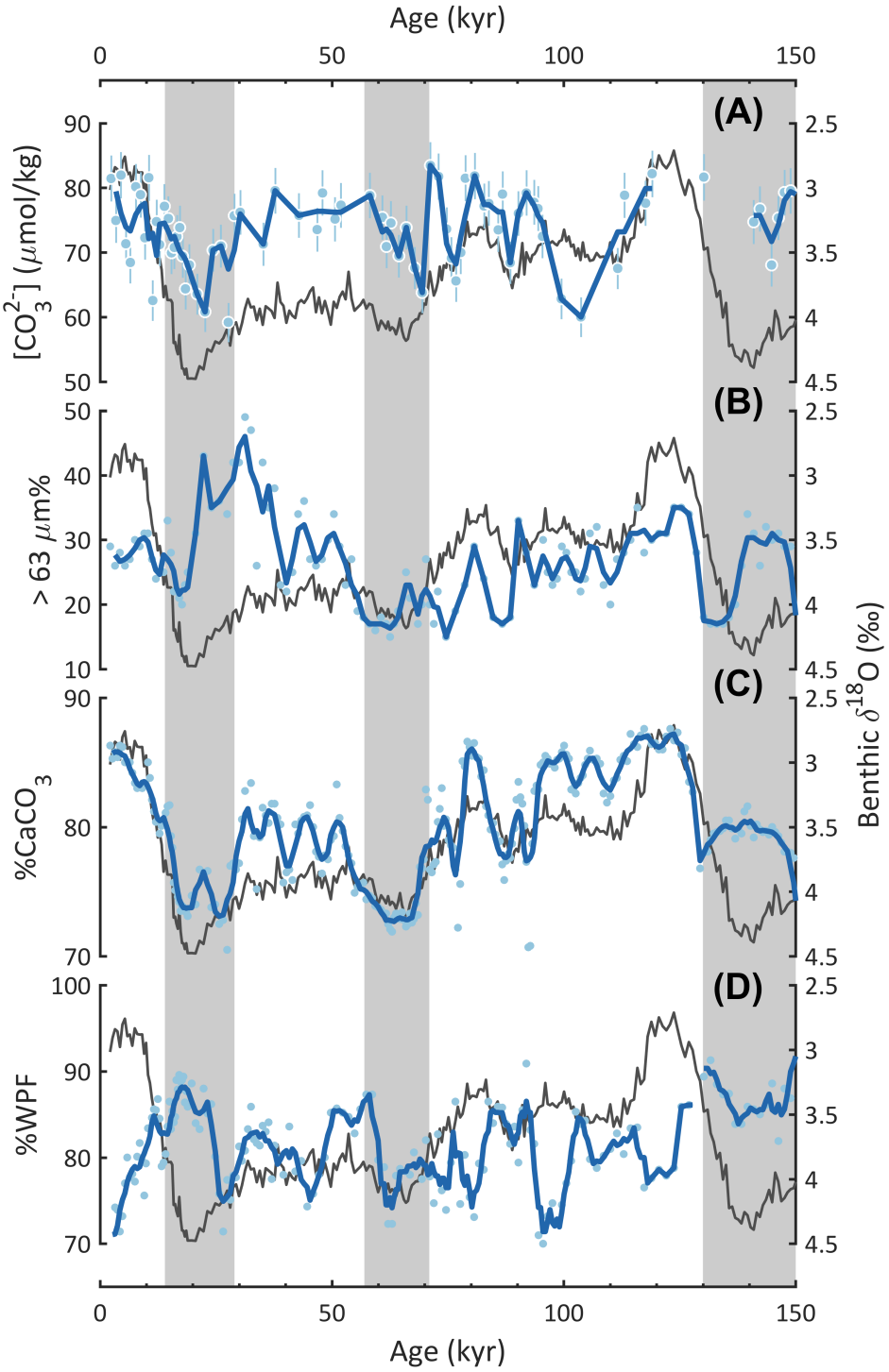

Figure 6-7: Deepwater $[CO_3^{2-}]$ records in core MD97-2106 (A) compared with $> 63\mu$m % (B), %$CaCO_3$ (Moy et al., 2006) (C), and % WPF (Moy, 2005) (D). In all these panels, dots are original data and curves are $\pm$2-kyr moving average. $\delta^{18}O_b$ data are shown in all panels to illustrate MISs. The cold MISs (2, 4, and 6) are shaded.

6.4.3 Deepwater $[CO_3^{2-}]$ and sedimentary partial dissolution proxies

According to previous regional study (Bostock et al., 2011, and references there in), the deeper core GC34 is below the foraminiferal lysocline in the late Holocene, while the shallower core MD97-2106 is above. Nevertheless, $\%CaCO_3$ of both cores during the last 150 kyr are much higher than 20%, suggesting that both cores are above the CCD. Sitting at different water depths, and thus with different carbonate saturation states (preindustrial $\Delta[CO_3^{2-}] = -14$ and -2 μmol/kg for GC34 and MD97-2106, respectively), MD97-2106 an GC34 demonstrate different relations between benthic B/Ca and sedimentary partial dissolution proxies.

$\%CaCO_3$ at both cores show similar trends to $[CO_3^{2-}]$ on the timescale of 10 kyr, despite the non-linear response of $\%CaCO_3$ to the amount of $CaCO_3$ being dissolved (Broecker et al., 1982). While % WPF at core GC34 is mostly consistent with $[CO_3^{2-}]$, % WPF at core MD97-2106 is not. The variability of % WPF at the more undersaturated core GC34 (40-85%) is much larger than that at MD 97-2106 (70-90%). Given the proximity of these two sediment core and thus similar planktonic foraminifera assemblies, this difference suggests that % WPF may be more sensitive to dissolution at more undersaturated deep-water environment. $> 63\mu$m % at neither cores show similar trends to $\%CaCO_3$ at the transitions between MISs. However, $> 63\mu$m % can be aligned with $\%CaCO_3$ on millennial timescale at MD97-2106. This It is speculated that the short-term (millennial) $> 63\mu$m % changes at this core might be linked to sedimentary dissolution, but the long-term (between MISs) changes are affected by other processes, for example, surface productivity.

6.5 Deepwater [CO_3^{2-}] history

6.5.1 Termination I

During Termination I (T I), a prominent feature of [CO_3^{2-}] in the deep SW Pacific is a monotonic increase at both sites (Figure 6-8). At MD97-2106, deepwater [CO_3^{2-}] increases by 12 ± 5 μmol/kgfrom 64 ± 3 μmol/kg (n = 4) to 78 ± 4 μmol/kg (n = 3) in the early Holocene (8−11.5 kyr). At GC34, the LGM [CO_3^{2-}] of 63 ± 4 μmol/kg (n = 5) is 15± 5 μmol/kg lower than the early Holocene [CO_3^{2-}] level of 78 ± 4 μmol/kg (n = 8) .

The deepwater [CO_3^{2-}] pattern during T I at two cores in the deep SW Pacific is similar to that in the Atlantic (Yu et al., 2008; Broecker et al., 2015; Gottschalk et al., 2015) (Figure 6-8). The magnitude of the LGM-Holocene gradient at the SW Pacific sites of ∼15 μmol/kg is smaller than those in the North Atlantic (∼20 μmol/kg, Yu et al., 2008). $\delta^{13}C_b$ of two studied cores increased by ∼0.7‰ during T I, similar to that in the deep Atlantic (Moy et al., 2006; Yu et al., 2008; Broecker et al., 2015).

The [CO_3^{2-}] variations during T I in the deep SW Pacific and the deep Atlantic, paralleled by similar $\delta^{13}C_b$ changes, suggest that [CO_3^{2-}] in the deep SW Pacific is probably affected by the Atlantic processes. In the Atlantic Ocean, the variation of deepwater [CO_3^{2-}] is attributed to the variability of the Atlantic overturning circulation, which changes the relative contributions of the northern sourced (high-[CO_3^{2-}]) and the southern sourced (low-[CO_3^{2-}]) waters (Yu et al., 2008; Gottschalk et al., 2015). In the modern ocean, the LCDW retains the NADW influence (Rintoul and Bullister, 1999; Talley, 2013). The NADW influence on the LCDW was persistent during the glacials, based on ε_{Nd} data (Piotrowski et al., 2005, 2009; Noble et al., 2013; Wilson et al., 2015; Molina-Kescher et al., 2016; Hu et al., 2016), but the contribution of the North Atlantic sourced water to the deep Indo-Pacific is thought to be decreased during the glacials (Piotrowski et al., 2009; Noble et al., 2013; Wilson et al., 2015; Molina-Kescher et al., 2016; Hu et al., 2016). This is also supported by larger

differences in $\delta^{13}C_b$ and $\delta^{18}O_b$ between the South Atlantic and Pacific during the LGM (McCave et al., 2008; Sikes et al., 2017) . The smaller magnitude of the LGM-Holocene $[CO_3^{2-}]$ gradient in the deep SW Pacific compared to the Atlantic is consistent with the persistent but a diminished North Atlantic influence on the deep SW Pacific during the glacials.

Another possible cause for the lower deep water $[CO_3^{2-}]$ during the LGM is the strengthened biological pump in the Subantarctic Zone (SAZ). In the Atlantic sector of the Southern Ocean, biological pump is stronger or more efficient during the LGM, based on ^{230}Th-normalized nutrient fluxes and foraminiferal shell-bounded $\delta^{15}N$ (Martínez-García et al., 2014). However, such a change did not seem to prevail in all sectors of the Southern Ocean. In the SW Pacific, productivity seems to be comparable between the LGM and the late Holocene. The productivity does not seem to be elevated during the LGM in the Pacific Sector of the Southern Ocean (Bostock et al., 2013). Moreover, a recent study based on ^{230}Th-normalized nutrient fluxes shows that despite the higher dust fluxes during the LGM, the productivity in the SAZ is largely invariant from the LGM to Holocene in the Pacific sector of the Southern Ocean (Durand et al., 2017). GC34 and MD97-2106 should not be affected by possible productivity changes induced by front shifting either. These two sites are located south of the North STF in the modern ocean. The STF shifted northwards during the glacial period (e. g., Sikes et al., 2009; Bostock et al., 2015). These two cores should always be within the SAZ so that no productivity change associated with front shifting would be expected. Nevertheless, despite minimal variation of productivity at the core sites, the influence of productivity change on deepwater $[CO_3^{2-}]$ in other sectors of Southern Ocean, *i.e.* in the Atlantic Sector (Martínez-Garcia et al., 2011; Martínez-García et al., 2014), could be transmitted to the SW Pacific through the ACC (McCave et al., 2008, 2014).

In contrast to the deep Atlantic, the LGM-Holocene $[CO_3^{2-}]$ pattern during T I in the equatorial Indo-Pacific (Yu et al., 2010a, 2013) is distinct from

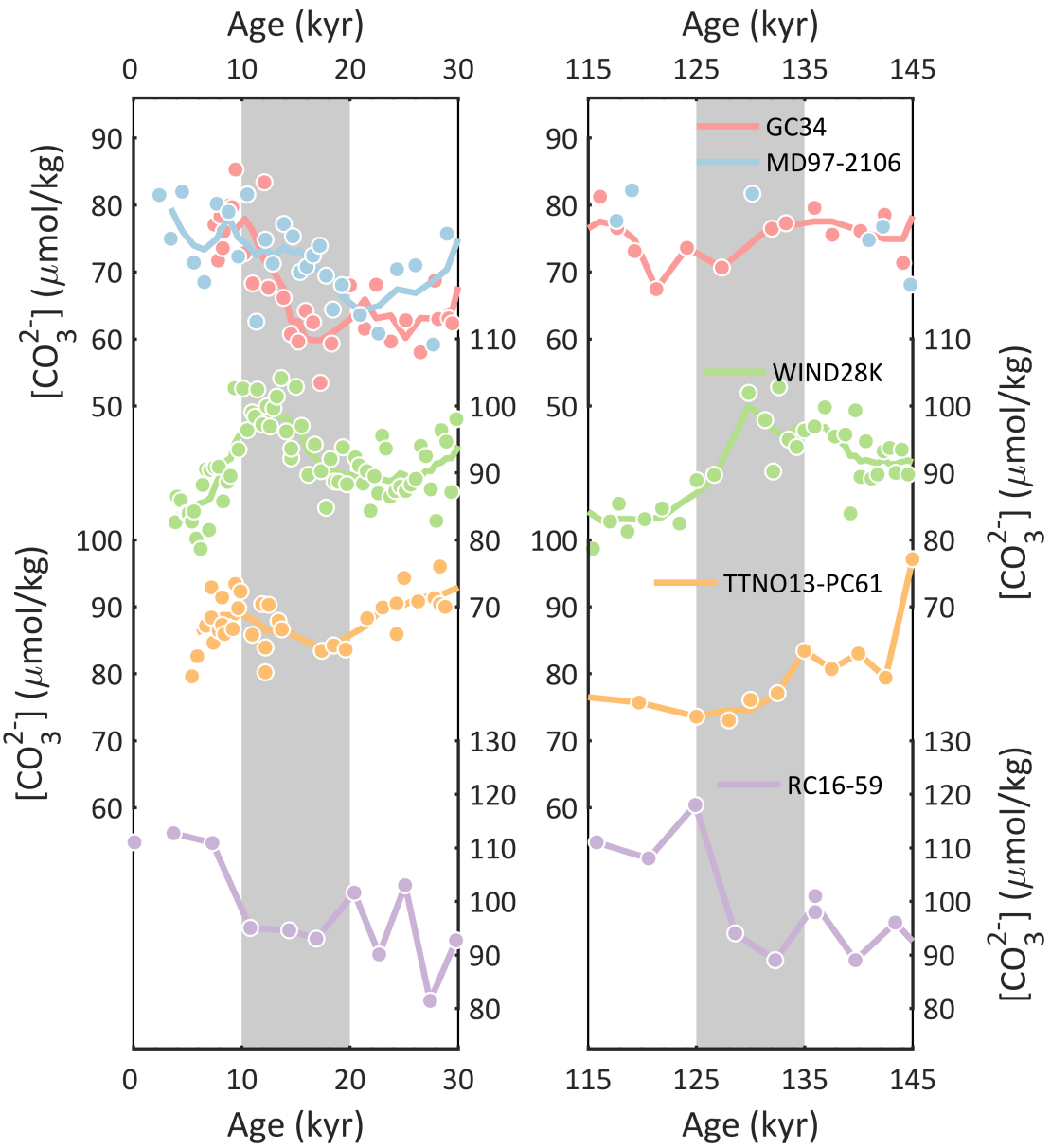

Figure 6-8: Deepwater [CO_3^{2-}] records at different locations during T I and T II. (A) GC34 (45°S, 4.0 km) and MD97-2106 (45°S, 3.3 km) from the SW Pacific, [this study], (B) WIND28K (10°S, 4.1 km) from the equatorial Indian (Yu et al., 2010a; Kerr et al., 2017), (C) TTNO13-PC61 from the equatorial Pacific (1°S, 4.3 km) (Yu et al., 2013), (D) RC16-59 from the Atlantic (4°N, 3.5 km), (Broecker et al., 2015; Yu et al., 2016). In all these panels, dots are original data and curves are ±2-kyr moving average, where possible. Deepwater [CO_3^{2-}] records are all based on *C. wuellerstorfi* B/Ca. Grey bars illustrate terminations.

that in the deep SW Pacific. The LGM-Holocene $[CO_3^{2-}]$ change is close to zero in the deep equatorial Indo-Pacific (Yu et al., 2010a, 2013) (Figure 6-8). Besides, most $[CO_3^{2-}]$ records in the deep equatorial Indo-Pacific display pronounced $[CO_3^{2-}]$ peaks during the deglacial (Yu et al., 2010a, 2013). No deglacial peak is seen in the SW Pacific records. The LGM-Holocene gradients of $\delta^{13}C_b$ in the deep equatorial Indo-Pacific, however, resemble those in the deep SW Pacific, with a smaller amplitude (Yu et al., 2010a, 2013).

The small LGM-Holocene $[CO_3^{2-}]$ variation in the equatorial Indo-Pacific may reflect well-buffered deepwater pH by deep-sea $CaCO_3$ dissolution/dissolution on the timescale of ~10 kyr (Anderson and Archer, 2002; Yu et al., 2013). The deglacial $[CO_3^{2-}]$ peak observed in the deep equatorial Indo-Pacific is a result of carbonate compensation triggered by removal of carbon from the deep ocean (Yu et al., 2010a). Deepwater $[CO_3^{2-}]$ records in the SW Pacific do not show a similar pattern as those in the equatorial Pacific. Nevertheless, it is possible that an influence from carbonate compensation is superimposed on the $[CO_3^{2-}]$ variation in the SW Pacific. This influence is evident from the $[CO_3^{2-}]$ decline at the onset of Holocene at both cores GC34 and MD97-2106 (Figure 6-8). While the late Holocene part of the core GC34 is missing, $[CO_3^{2-}]$ at MD97-2106 began to rise at ~5 kyr. This $[CO_3^{2-}]$ pattern in Holocene suggests that carbonate compensation influenced $[CO_3^{2-}]$ in the deep SW Pacific. Although such an influence is counteracted by changes in circulation and biological pump, it may account for the smaller $[CO_3^{2-}]$ changes in the deep SW Pacific compared to the deep Atlantic.

In summary, deepwater $[CO_3^{2-}]$ change at Termination I in the SW Pacific is likely the result of the combined influence from circulation, biological pump, and carbonate compensation.

6.5.2 MIS 5a to MIS 2

MIS 5a to MIS 4. From MIS 5a to MIS 4, deepwater $[CO_3^{2-}]$ at GC34 and MD97-2106 were both characterized by decreases with a positive spike at the

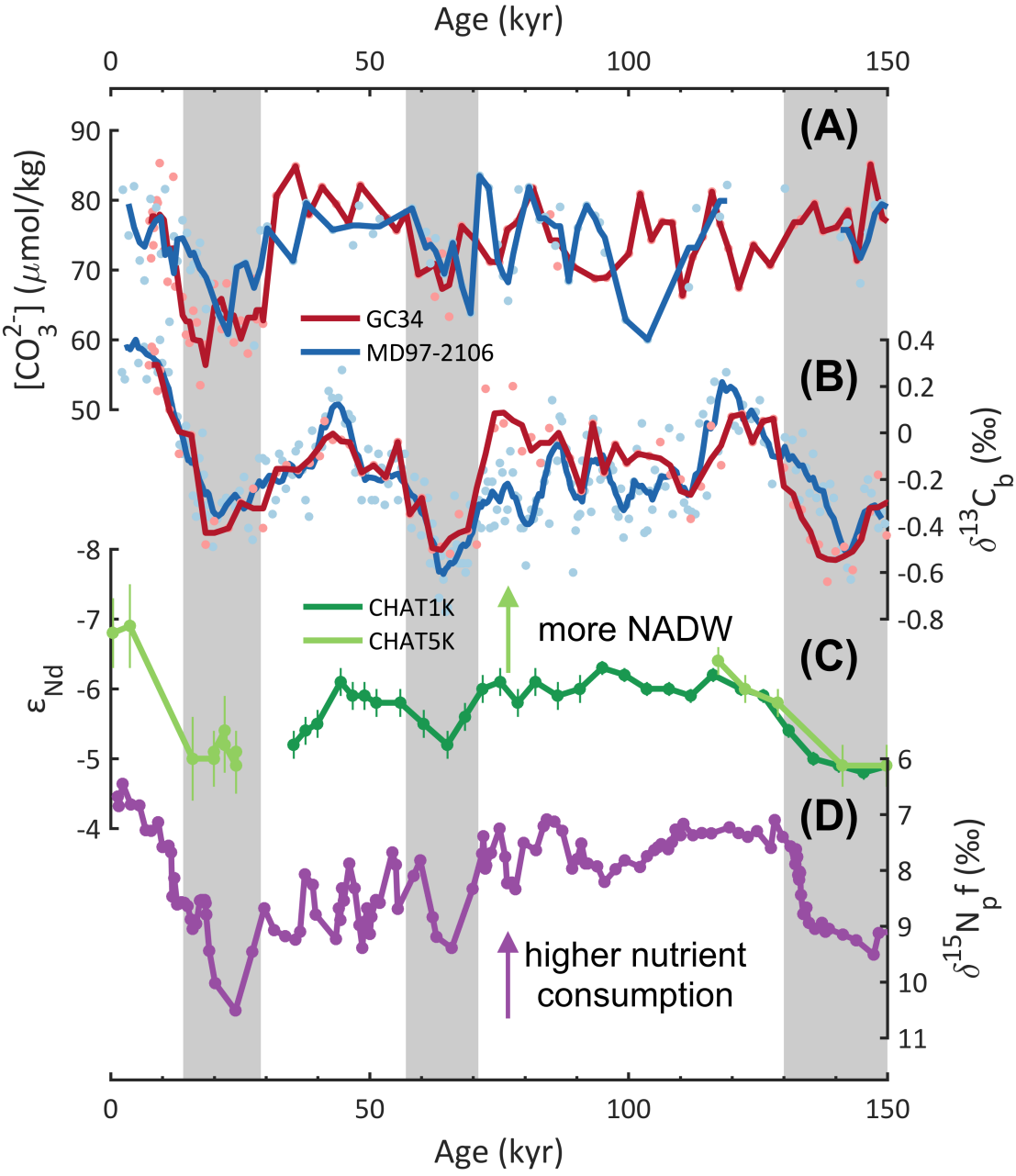

Figure 6-9: The Southern Ocean proxy records in the last 150 kyr. (A) [CO_3^{2-}] in the deep SW Pacific, at GC34 and MD97-2106 [this study]. (B) $\delta^{13}C_b$ in the deep SW Pacific, at GC34 and MD97-2106 (Moy et al., 2006). (C) ε_{Nd} in the deep SW Pacific, at CHAT5K and CHAT1K (Hu et al., 2016). More negative values indicate more influence from the North Atlantic sourced water. Note that the y-axis is in the reverse order. (D) $\delta^{15}N$ in planktonic foraminifera shell in the South Atlantic, at ODP1090 (Martínez-García et al., 2014). High $\delta^{15}N$ indicates efficient nutrient utilization. In Panel (A) and (B), dots are original data and curves are ±2-kyr moving average. Dashed lines divide these records into different marine isotope stages.

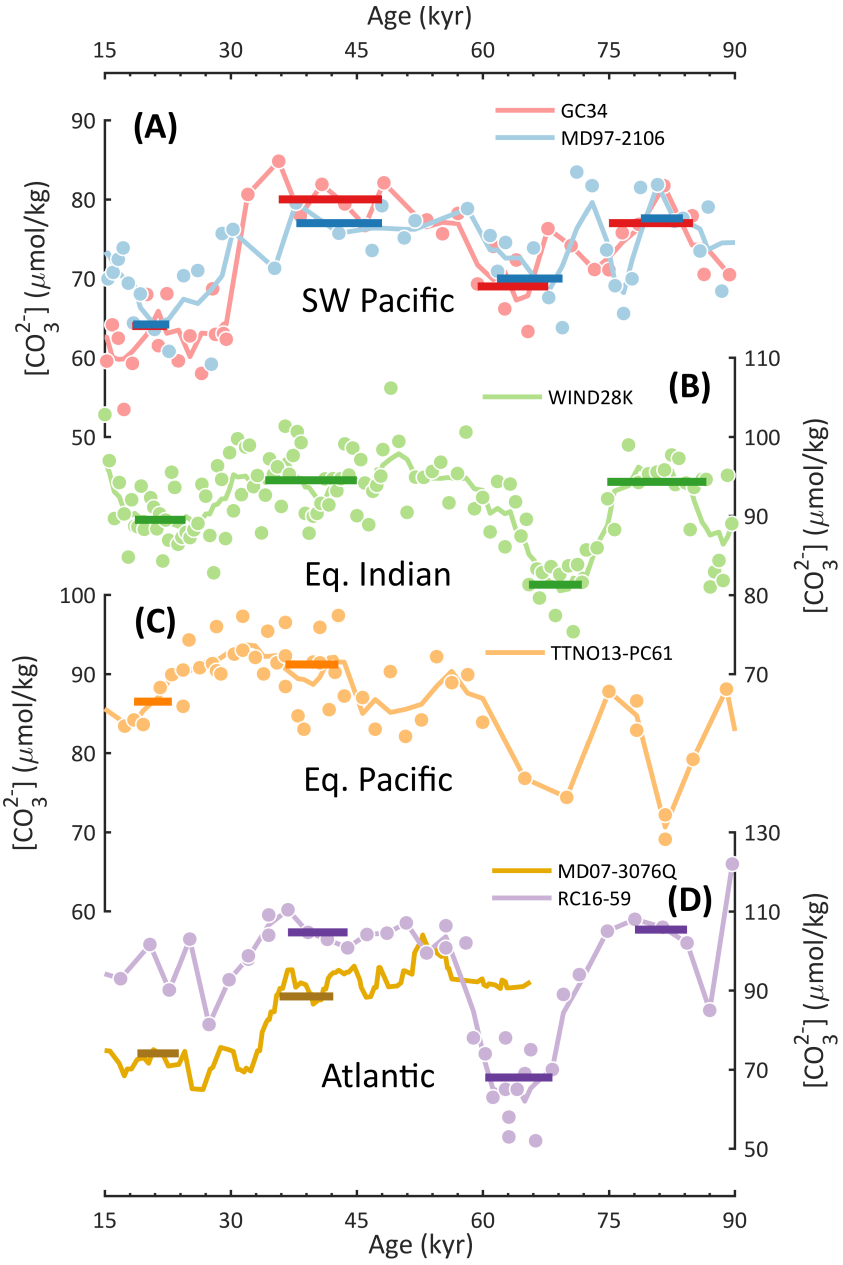

Figure 6-10: (next page) Deepwater $[CO_3^{2-}]$ records from MIS 5a to 2 from different locations. (A) the SW Pacific, GC34 (45°S, 4.0 km) and MD97-2106 (45°S, 3.3 km, this study), (B) the equatorial Indian, WIND28K (10°S, 4.1 km, Yu et al., 2010a; Kerr et al., 2017), (C) the equatorial Pacific, TTNO13-PC61 (1°S, 4.3 km, Yu et al., 2013), (D) the Atlantic, MD07-3076Q (44°S, 3.7 km, Gottschalk et al., 2015), RC16-59 (4°N, 3.5 km, Broecker et al., 2015; Yu et al., 2016). In all these panels, dots are original data and curves are ±2-kyr moving average. Original data of MD07-3076Q are not shown for clarity. Thick bars in all panels represent the average $[CO_3^{2-}]$ level during certain MISs (MIS 5a, 4, mid-3, and 2). Note that a bar is presented when there are >3 data points within that MIS. $[CO_3^{2-}]$ records expect MD07-3076Q are based on *C. wuellerstorfi* B/Ca, while $[CO_3^{2-}]$ record of MD07-3076Q is based on *Cibicidoides mundulus (kullenbergi)* B/Ca.

transition (Figure 6-10). At GC34, deepwater [CO_3^{2-}] descended from 77 ± 4 μmol/kg (n = 5) to 69 ± 4 μmol/kg (n = 4), by 8 ± 6 μmol/kg. At MD97-2106, deepwater [CO_3^{2-}] decreased by 8 ± 6 μmol/kg from 78 ± 5 μmol/kg (n = 4) to 70 ± 4 μmol/kg (n = 6). During this transition, [CO_3^{2-}] in the deep Indian Ocean declined by ∼10 μmol/kg (Kerr et al., 2017). The resolution of available [CO_3^{2-}] records in the deep Pacific is not high enough to resolve the change at this transition (Yu et al., 2013; Kerr et al., 2017). In the deep Atlantic Ocean, a [CO_3^{2-}] decline of ∼25 μmol/kg was observed from a wide range of latitudes of ∼40 °N to ∼40 °S (Yu et al., 2016).

MIS 4 to MIS 3. Deepwater [CO_3^{2-}] increased at GC34 and MD97-2106 during the MIS 4 to MIS 3 transition (Figure 6-10). At MD97-2106, deepwater [CO_3^{2-}] increased by 7 ± 5 μmol/kg from 70 ± 4 μmol/kg (n = 6) to 77 ± 3 μmol/kg (n = 4). At GC34, deepwater [CO_3^{2-}] was elevated from 69 ± 4 μmol/kg (n = 6) by 11 ± 5 μmol/kg to 80 ± 3 μmol/kg (n = 6). In the deep equatorial Indian and Pacific, the [CO_3^{2-}] increases during this period were ∼13 and ∼7 μmol/kg, respectively (Yu et al., 2010a, 2013; Kerr et al., 2017). In the deep equatorial Atlantic, [CO_3^{2-}] climbed by ∼35 μmol/kg at the beginning of MIS 3 (Broecker et al., 2015; Yu et al., 2016).

MIS 3 to MIS 2. At the transition between MIS 3 and MIS 2, deepwater [CO_3^{2-}] at GC34 and MD97-2106 were both marked by a significant decline (Figure 6-10). The magnitude of this decline was comparable to the increase occurred during T I in both cores. At GC34, deepwater [CO_3^{2-}] plunged from 80 ± 3 μmol/kg (n = 6) to 63 ± 4 μmol/kg (n = 4), by 17 ± 5 μmol/kg. At MD97-2106, deepwater [CO_3^{2-}] decreased from 77 ± 4 μmol/kg (n = 6) to 64 ± 4 μmol/kg (n = 5), by 13 ± 6 μmol/kg. Despite similar magnitudes of [CO_3^{2-}] decline at these two cores, the rates of [CO_3^{2-}] change were different. At GC34, the [CO_3^{2-}] decline was rapid, within ∼3 kyr at the MIS 3 to MIS 2 transition, while at MD97-2106, the [CO_3^{2-}] decline was gradual, lasting for ∼15 kyr to the LGM. During this transition, smaller declines in deepwater

$[CO_3^{2-}]$ of ~5 to 8 μmol/kg was observed in the equatorial Indo-Pacific (Yu et al., 2010a, 2013). A larger decline of ~20 μmol/kg was detected in the deep South Atlantic during this transition (Gottschalk et al., 2015).

Since MIS 5a, the deepwater $[CO_3^{2-}]$ variations in two studied cores were in concert with $\delta^{13}C_b$ (Moy et al., 2006) (Figure 6-9). The magnitudes of $\delta^{13}C_b$ change, are between ~0.3 and ~0.4 ‰. The synchronous variation of $[CO_3^{2-}]$ and $\delta^{13}C_b$ in the deep SW Pacific is consistent with $[CO_3^{2-}]$ and $\delta^{13}C_b$ records from the deep Atlantic and equatorial Indo-Pacific (Yu et al., 2010a, 2013, 2016; Kerr et al., 2017). In the Atlantic, larger deepwater $[CO_3^{2-}]$ and $\delta^{13}C_b$ changes are contributed to both changing Atlantic overturning circulation and the biological pump (Gottschalk et al., 2015, 2016; Yu et al., 2016). In the equatorial Indo-Pacific Ocean, the simultaneous changes of deepwater $[CO_3^{2-}]$ and $\delta^{13}C_b$ are argued to be caused by changes in the deep ocean stratification (Lund et al., 2011; Burke and Robinson, 2012; Adkins, 2013) and the strength of the biological pump (Hain et al., 2014).

In the context of deepwater $[CO_3^{2-}]$ records in the South Atlantic and the equatorial Indo-Pacific (Yu et al., 2010a, 2013; Gottschalk et al., 2015; Yu et al., 2016; Kerr et al., 2017), it is argued here that the variation of the deep SW Pacific $[CO_3^{2-}]$ in the last glacial cycle is the result of processes reorganizing carbon in the deep ocean. These processes include changes of biological pump (Martínez-García et al., 2014; Gottschalk et al., 2016), influence of the North Atlantic-sourced water (Molina-Kescher et al., 2016; Hu et al., 2016), and ocean stratification (Lund et al., 2011; Adkins, 2013; Ferrari et al., 2014). Firstly, in accord with the change of Atlantic overturning circulation, the influence of the North Atlantic-sourced water on the deep South Pacific fluctuated during the glacial cycle (Hu et al., 2016; Molina-Kescher et al., 2016) (Figure 6-9C). Secondly, the biological pump was strengthened in the Atlantic Sector of the Southern Ocean at MIS 5a-4 and 3-2 transitions and weakened at MIS 4-3 transition (Martínez-García et al., 2014; Gottschalk et al., 2016) (Figure 6-9D). In the SW Pacific, the strength of the biological pump earlier than the

LGM has not been investigated by ^{230}Th-normalized fluxes. Nevertheless, the effect of biological pump changes on [CO_3^{2-}] in the deep South Atlantic could be transmitted to the SW Pacific through the ACC (McCave et al., 2008, 2014). Thirdly, stratification in the Southern Ocean probably intensified as the Atlantic overturning circulation shoaled during MIS 4 and MIS 2 (Lund et al., 2011; Adkins, 2013; Ferrari et al., 2014).

An additional note is that the positive spikes in the two studied cores at MIS 5a to 4 transition, despite different magnitudes, seem to coincide with the atmospheric pCO_2 spike (Ahn and Brook, 2008; Bereiter et al., 2012). Restricted by the data resolution and uncertainty of the age model, these spikes are not further discussed. However, it demonstrates that the deep SW Pacific carbonate chemistry is possibly also responsive to the transient change of atmospheric pCO_2 like that in the South Atlantic (Gottschalk et al., 2015), which warrants further investigation.

6.5.3 Termination II

Deepwater [CO_3^{2-}] change in the deep SW Pacific during Termination II (T II) is distinct from that during T I 6-8. At GC34, there is no discernible [CO_3^{2-}] change from the late MIS 6 to 5e (from 78 $\pm$ 4 μmol/kg (n = 6) to 74 $\pm$ 3 μmol/kg (n = 5)). At MD97-2106, data resolution is not high enough for MIS 5e. Based on the limited number of data, the increase in [CO_3^{2-}], if any, seems modest during T II. In the deep equatorial Indo-Pacific, deepwater [CO_3^{2-}] variations during T II are also different from T I. Deepwater [CO_3^{2-}] decreased by $\sim$13 μmol/kg during T II in the equatorial Indian, in comparison to modest increase during T I (Yu et al., 2010a; Kerr et al., 2017). In the equatorial Pacific, deepwater declined by $\sim$7 μmol/kg, in contrast to the minimal change during T I (Yu et al., 2010a, 2013). In the deep equatorial Atlantic, however, [CO_3^{2-}] increased for $\sim$19 μmol/kg (Broecker et al., 2015), similar to the magnitude observed during T I.

Despite the different deepwater [CO_3^{2-}] history between T II and T I, other

proxies suggest that the changes in circulation and biological pump that affect $[CO_3^{2-}]$ variation during T I should influence deepwater $[CO_3^{2-}]$ similarly during T II. The magnitudes of $\delta^{13}C_b$ changes at GC34 and MD97-2106 during T II are comparable to those during T I (Moy et al., 2006) (Figure 6-9). Moreover, ε_{Nd} records in the deep SW Pacific cores show that the contribution of North Atlantic sourced water to the deep SW Pacific changed similarly during T II and T I (Hu et al., 2016) (Figure 6-9). The variations in the strength of the biological pump at T II mirrored that during T I (Martínez-García et al., 2014) (Figure 6-9). These proxy data all point to comparable circulation and biological pump changes during T II and T I. Indeed, deepwater $[CO_3^{2-}]$ variations at RC16-59 from the equatorial Atlantic during T II resembled that during T I (Broecker et al., 2015). Should circulation and biological pump affect $[CO_3^{2-}]$ in the deep SW Pacific $[CO_3^{2-}]$ similarly to that during T I, there must be other processes at work with the opposing effect on $[CO_3^{2-}]$ during T II, to cause the different deepwater $[CO_3^{2-}]$ patterns between T II and T I.

One possible cause is different deepwater circulations during MIS 6 and MIS 2. If there were a water mass, which is high in $[CO_3^{2-}]$, influencing the core sites of GC34 during MIS 6 but not MIS 2, the relatively higher $[CO_3^{2-}]$ in core GC34 during the end of the MIS 6 could be explained. If the influence of this water mass withdrew during T II, deepwater $[CO_3^{2-}]$ in GC34 could be decreased consequently, counteracting the influence of biological pump and the NADW influence. Based on the modern Southern Ocean hydrography, there are two candidate water masses: the AABW and the PDW. In the modern ocean, AABW has slightly higher $[CO_3^{2-}]$ compared to LCDW (Figure 6-2). The character of the glacial AABW is largely unknown. It is proposed that AABW could be salty and cold during glacials, because the Glacial North Atlantic Intermediate Water (GNAIW), which contributed to the formation of AABW, was too cold to melt the land based ice to freshen the AABW (Adkins, 2013). The AABW formed in this condition is expected to be salty and low in

DIC, thus high in $[CO_3^{2-}]$. This is consistent with a B/Ca record in the Weddell Sea with a very low resolution(Rickaby et al., 2010). However, as AABW may be more different between different ocean basins during glacial periods (Sikes et al., 2017; McCave et al., 2008). No data are available for Adelie Coast, which is more relevant to AABW in the SW Pacific. If AABW was different for Adelie Coast, during MIS 6, this should be observed in other cores in the Indo-Pacific Sector of the Southern Ocean. However, there is no other high resolution B/Ca records in the region for T II to date, which are needed to test this hypothesis. If the other water mass is the PDW, the Pacific records should show a relatively high $[CO_3^{2-}]$ in MIS 6 to MIS 2, which does not seem to be the case for an equatorial Pacific record (Yu et al., 2013). With currently available records, it is difficult to confirm or deny the possibility that different circulation changes influenced deepwater $[CO_3^{2-}]$ variations in the SW Pacific during T II and T I. Changes in glacial AABW is one possible explanation for the different $[CO_3^{2-}]$ feature seen in the SW Pacific. More records from other locations are needed to test this hypothesis.

Alternatively, the different deepwater $[CO_3^{2-}]$ changes between T II and T I may reflect different open system changes during these two terminations, which would have a global effect. As $[CO_3^{2-}]$ changes are affected by the difference between ALK and DIC, a process causing a decline in $[CO_3^{2-}]$ would be associated with decreased ALK, increased DIC, or both (Broecker et al., 1982). There seems to be no process capable of increasing DIC in the deep ocean during terminations. An ALK decline must be responsible for the $[CO_3^{2-}]$ decline at T II. Two processes can draw down ALK in the deep ocean: improved preservation of $CaCO_3$ in the deep ocean (Broecker and Peng, 1987) and regrowth of coral reefs on continental shelves (Berger, 1982). These two processes remove $CaCO_3$ from the ocean-atmospheric system, reducing the global mean ALK.

If ALK were lowered by more $CaCO_3$ preservation in the deep sea, there should be an increase in $\%CaCO_3$ in the Indo-Pacific Basin. Based on $\%CaCO_3$ data at GC34, there is no clear sign of increased $CaCO_3$ preservation during

T II (Moy et al., 2006). $\%CaCO_3$ increased modestly at the end of MIS 6 and dropped to a similar level to MIS 6 during MIS 5e. This $\%CaCO_3$ feature is also seen at another core in the STR at 4 km water depth (**?**, unpublished data in thesis). In the deep equatorial Indian Ocean, there was a decrease in $\%CaCO_3$ at WIND28K (Kerr et al., 2017). In the equatorial Pacific Ocean, $\%CaCO_3$ also declined at TTNO13-PC61, and such a decline is corroborated by ^{230}Th-normalized $CaCO_3$ flux data at an adjacent core (Anderson et al., 2008). Therefore, there do not seems to be a major improvement in $CaCO_3$ preservation in the deep Indo-Pacific Ocean, suggesting that $CaCO_3$ preservation on the seafloor does not likely cause an ALK decline during T II.

It is therefore deduced that the regrowth of coral reef is responsible for the decline in ALK. The reason that regrowth of coral reef had a larger contribution during T II than T I might be that the major deglaciation represented by the melt water pulse 2B (MWP-2B) was not interrupted by a cold event like the Younger Dryas during T I (Marino et al., 2015). When sea level was above the modern level at the beginning of MIS 5e (Grant et al., 2014), the coral reef growth was already widespread (Stirling et al., 1998). The steady sea level rise facilitated a continuous regrowth of coral reef. This process more efficiently removed ALK from the atmosphere-ocean system and counteracted the $[CO_3^{2-}]$ change caused by the circulation and the biological pump change during T II. The decline of deep water $[CO_3^{2-}]$ observed since the early Holocene (Yu et al., 2014) was interpreted as a result of major coral reef regrowth at ~8 kyr (Vecsei and Berger, 2004). Should regrowth of coral reef appeared in an earlier stage during T II compared to T I, the influence of coral reef regrowth can be synchronous with and thus superimposed on the impact from the circulation and the biological pump.

If the differences in regrowth of coral reef and the basin-to-shelf of carbonate deposition is responsible for the different patterns of deep-water $[CO_3^{2-}]$ during T I and T II in the SW Pacific, this signal should be global. Indeed, deep-water $[CO_3^{2-}]$ changes in other ocean basin is consistent with the obser-

vation in the SW Pacific Ocean. The [CO_3^{2-}] gradient between MIS 6 and MIS 5e is higher than that between the LGM and the early Holocene in both the Equatorial Indian and the Equatorial Pacific Ocean (Yu et al., 2010a; Kerr et al., 2017; Yu et al., 2013, Figure 6-8). In the Atlantic Ocean, at the only one low-resolution deep core with B/Ca dating back to MIS 6, the [CO_3^{2-}] gradient between MIS 5e and MIS 6 seems smaller than that between the early Holocene and the LGM (Yu et al., 2016; Broecker et al., 2015, Figure 6-8). However, there are only a few benthic B/Ca records during T II, to test whether T I and T II are different on the global scale, more records with high resolution and good age controls are needed.

During T I, [CO_3^{2-}] increased in the deep SW Pacific, which was consistent with deep Atlantic changes. The shift in [CO_3^{2-}], together with the variation in $\delta^{13}C_b$, suggests that [CO_3^{2-}] in the deep SW Pacific might be affected by similar processes that affected deep Atlantic [CO_3^{2-}], namely changes in the Atlantic overturning circulation and the biological pump. During T II, the [CO_3^{2-}] in the deep SW Pacific showed little change, despite that the impacts of the Atlantic processes remained similar. The different [CO_3^{2-}] variations in the deep SW Pacific during T II from that during T I hints to a 1) changes in AABW [CO_3^{2-}], 2) substantial impact on the ALK from the coral reef regrowth on continental shelves, or both. Variations of [CO_3^{2-}] change in the deep SW Pacific during different T I and T II emphasize that carbon inventory in the deep ocean might be modulated by distinct mechanisms during different Terminations.

6.6 Conclusions

In this chapter, deepwater carbonate chemistry in the deep SW Pacific for the last 150 kyr is reconstructed using B/Ca in benthic foraminifera *C. wuellerstorfi*. From MIS 5a to Holocene, the variation of the deepwater [CO_3^{2-}] in the SW Pacific is in concert with $\delta^{13}C_b$. During T I, deepwater [CO_3^{2-}] increased by

$\sim$15 μmol/kg. These changes, on the timescale of $\sim$10 kyr, are similar to those from the deep Atlantic. This suggests that $[CO_3^{2-}]$ of the deep SW Pacific is influenced by similar processes affecting $[CO_3^{2-}]$ in the deep Atlantic, which are changes in the Atlantic Overturning Circulation and biological pump. During T II, however, the deep SW Pacific $[CO_3^{2-}]$ did not show any increase, despite similar variations in $\delta^{13}C_b$ and other proxies to T I. Based on the available data, coral reef regrowth on the continental shelves seems to counteract the influences of changes in circulation and the biological pump on deepwater $[CO_3^{2-}]$ during T II. These results highlight different possible mechanisms for the deep ocean to sequester and release carbon during different glacial-deglacial transitions, which warrants more efforts to understand carbon cycle changes during other Terminations.

Chapter 7

Conclusions and future work

7.1 Environmental controls on geochemistry of planktonic foraminiferal shells

The aim of the first part of the thesis is to understand the environmental controls on planktonic B/Ca using shells from the Atlantic meridional core-tops. This is achieved by taking advantage of other trace element to calcium ratios measured together with B/Ca. Along with the achievement of the main aim, there are several findings in other aspects of the geochemistry of planktonic foraminiferal shells.

In Chapter 2, I presented core-top B/Ca in four planktonic foraminiferal species from three depth transects. Based on these data, I demonstrated that dissolution effects on planktonic B/Ca are species-specific. Among the four species examined, B/Ca in *G. ruber* (w) and *G. sacculifer* (w/o sac) decreases with intensified dissolution, while B/Ca in *N. dutertrei* and *P. obliquiloculata* is negligibly influenced by dissolution. The reason for species-specific responses of B/Ca in different species to dissolution might be related to the micro-scale distribution of B in foraminiferal shells. The decline of B/Ca in *G. ruber* (w) and *G. sacculifer* (w/o sac) is empirically correlated to the deepwater $\Delta[CO_3^{2-}]$ and B/Ca in the coexisting benthic foraminifera. The correlation between the

declines in planktonic B/Ca and the deepwater $\Delta[CO_3^{2-}]$ is employed to assess the influence of dissolution effects on the interpretation of core-top B/Ca data. The correlation between the declines in planktonic and coexisting benthic B/Ca provides a means to correct for dissolution effects on downcore planktonic B/Ca.

In Chapter 3, I presented Mg/Ca in *G. ruber* (w) and *G. sacculifer* (w/o sac) from the Atlantic meridional core-tops, to determine the seasonality and calcification depths of these two species. The debate on a salinity effect on planktonic Mg/Ca casts double on whether it is appropriate to compare Mg/Ca to hydrological temperatures to determine the calcification depth and seasonality of *G. ruber* (w) and *G. sacculifer* (w/o sac), two species investigated in this study. To this end, the salinity effect on planktonic Mg/Ca is reevaluated. By comparing Mg/Ca in *G. ruber* (w) and *G. sacculifer* (w/o sac) with hydrological temperatures and temperatures estimated from $\delta^{18}O_c$, I find little salinity effect on *G. sacculifer* (w/o sac) and *G. ruber* (w) Mg/Ca, which is comparable to the results from culture studies. Core-top Mg/Ca data and hydrological data are reconciled by considering the latitude-dependent calcification depths and seasonality of these two species. The negligible influence of salinity on planktonic Mg/Ca derived from core-tops in this thesis resolves the long standing debate between core-top and culture studies. This enhances our confidence in using Mg/Ca as a reliable paleotemperature proxy in the open ocean on the glacial-interglacial timescale. By discounting a strong salinity effect, planktonic Mg/Ca be used to determining the calcification depths and seasonality of the studied species from core-tops.

In Chapter 4, environmental controls on B/Ca in *G. ruber* (w) and *G. sacculifer* (w/o sac) from the Atlantic meridional core-tops were examined. With similar ranges of environmental parameters, *G. ruber* (w) B/Ca at tropical latitudes show higher values than at temperate latitudes. This can be attributed to the higher calcification rates of *G. ruber* (w) at tropical latitudes than that at temperate latitudes, as indicated by higher Sr/Ca. *G. ruber* (w)

B/Ca at temperate latitudes, which is affected by the calcification rate to a lesser degree, and *G. sacculifer* (w/o sac) B/Ca show similar correlations with carbonate chemistry parameters to those observed in culture studies. This confirms the carbonate chemistry as an important environmental controlling factor on planktonic B/Ca. The patterns of core-top B/Ca in these two species from the Atlantic meridional transect are likely to be the result of competing influences from the calcification rates and the seawater carbonate chemistry. The calcification rate control on B/Ca complicates the direct connection between planktonic B/Ca and the seawater carbonate chemistry. Nevertheless, according to the different responses of B/Ca in *G. ruber* (w) and *G. sacculifer* (w/o sac) to the calcification rate, it is possible that B/Ca in some species are less susceptible to such an influence, and can be employed for carbonate chemistry reconstruction.

7.2 Deepwater carbonate chemistry in the SW Pacific

The second part of the thesis investigated the deepwater carbonate chemistry in the SW Pacific using B/Ca in benthic foraminifera *C. wuellerstorfi*. In Chapter 5, the relationship between $[CO_3^{2-}]$ and (ALK-DIC) was refined for the deep Indo- Pacific. It is demonstrated that the correlation between $[CO_3^{2-}]$ and (ALK-DIC) applies to compositions beyond the modern range of ALK and DIC. This suggests that the $[CO_3^{2-}]$-(ALK-DIC) relationship is robust to be employed to quantify DIC changes in the past using $[CO_3^{2-}]$. It is further demonstrated that the sensitivity of $[CO_3^{2-}]$ to (ALK-DIC) depends on $[CO_3^{2-}]$. $[CO_3^{2-}]$ changes more sensitively to (ALK-DIC) changes at high-$[CO_3^{2-}]$ values. The improved relationship between $[CO_3^{2-}]$ and (ALK -DIC) can help better quantify carbon inventory changes in the deep ocean.

In Chapter 6, I presented that the deepwater carbonate chemistry in the SW Pacific for the last 150 kyr was influenced by the Atlantic processes and

growth of coral reef on the continental shelves. Since MIS 5a, the deepwater $[CO_3^{2-}]$ variation in the SW Pacific was in concert with $\delta^{13}C_b$. These changes, on the timescale of ~10 kyr, were similar to those in the deep Atlantic. This suggests that deepwater $[CO_3^{2-}]$ of the deep SW Pacific could be affected by changes in the Atlantic Overturning Circulation and biological pump. However, during T II, the deep SW Pacific $[CO_3^{2-}]$ showed little change, despite that variations of $\delta^{13}C_b$ at the same cores and ε_{Nd} and $\delta^{15}N$ were similar to those during T I. Based on the available deepwater $[CO_3^{2-}]$ records from the deep Indo-Pacific Ocean to date, coral reef regrowth on the continental shelves seems to be the only process that can counteract the influences of Atlantic Overturning Circulation and the biological pump on deep water $[CO_3^{2-}]$ during T II. These results highlight different possible mechanisms for the deep ocean to sequester and release carbon during different climate transitions.

7.3 Future work

7.3.1 Environmental controls on geochemistry of planktonic foraminiferal shells

This study demonstrates that B/Ca in *G. ruber* (w) and *G. sacculifer* (w/o sac) is affected by the calcification rate, based on the covariation between B/Ca and Sr/Ca. This covariation should be further tested in other planktonic species, to test whether the calcification rate is responsible for varying B/Ca in different species. Moreover, it would be useful to test the calcification rate control on planktonic B/Ca in culture experiments, where estimation of instantaneous calcification rates is enabled.

In this study, core-top B/Ca, Mg/Ca, and Sr/Ca in *G. ruber* (w) and *G. sacculifer* (w/o sac) from the meridional Atlantic are investigated. Several other trace element to calcium ratios (*e.g.*, Li/Ca, Cd/Ca, and Ba/Ca) are also measured. The large latitude coverage of the core-tops provides an invaluable

opportunity to investigate the controlling factors of these trace elements in the foraminiferal shells. One future work is to investigate how these trace elements are incorporated into the foraminiferal shells. One possible approach forward is to compare the trace element concentrations in planktonic foraminiferal shells to concentrations of relevant elements in seawater using the GEOTRACES dataset.

7.3.2 Deepwater carbonate chemistry in the SW Pacific

In this thesis, the deepwater carbonate chemistry in the SW Pacific during the last 150 kyr was reconstructed. High resolution deepwater carbonate chemistry records are prepared for these two cores especially for some important climatic transitions. A high resolution $[CO_3^{2-}]$ record in the deep SW Pacific may provide information about what caused transient changes of atmospheric pCO_2 changes. A multi-proxy approach also need to be employed to understand mechanisms for the $[CO_3^{2-}]$ changes in the deep SW Pacific. Proxies like deepwater O_2 and $[PO_4^{3-}]$ can be employed to estimate the $[CO_3^{2-}]$ change caused by changes in the biological pump and the Atlantic overturning circulation. By doing so, the influence of the 'closed-system' and 'open-system' responses on $[CO_3^{2-}]$ may be able to be deconvolved.

Apart from further paleoceanographic reconstructions based on these two deep SW Pacific cores, modeling work should be done to understand the reason for the different deepwater carbonate chemistry changes during the last two terminations. This is necessary because the effect of coral reef regrowth on seawater alkalinity cannot be reconstructed directly by proxies to date. It is also useful to be test by models to explore how differences in timing of deglacial events during terminations can affect responses of the deepwater carbonate chemistry.

Bibliography

Adkins, J. F. The role of deep ocean circulation in setting glacial climates. *Paleoceanography*, 28(3):539–561, 2013.

Ahn, J. and Brook, E. J. Atmospheric CO_2 and climate on millennial time scales during the last glacial period. *Science*, 322(5898):83–85, 2008.

Allen, K. A. and Hönisch, B. The planktic foraminiferal B/Ca proxy for seawater carbonate chemistry: A critical evaluation. *Earth and Planetary Science Letters*, 345:203–211, 2012.

Allen, K. A., Hönisch, B., Eggins, S. M., Yu, J., Spero, H. J., and Elderfield, H. Controls on boron incorporation in cultured tests of the planktic foraminifer *orbulina universa*. *Earth and Planetary Science Letters*, 309(3):291–301, 2011.

Allen, K. A., Hönisch, B., Eggins, S. M., and Rosenthal, Y. Environmental controls on B/Ca in calcite tests of the tropical planktic foraminifer species *Globigerinoides ruber* and *Globigerinoides sacculifer*. *Earth and Planetary Science Letters*, 351:270–280, 2012.

Allen, K. A., Sikes, E. L., Hönisch, B., Elmore, A. C., Guilderson, T. P., Rosenthal, Y., and Anderson, R. F. Southwest Pacific deep water carbonate chemistry linked to high southern latitude climate and atmospheric CO_2 during the last glacial termination. *Quaternary Science Reviews*, 122:180–191, 2015.

Allen, K. A., Hönisch, B., Eggins, S. M., Haynes, L. L., Rosenthal, Y., and Yu, J. Trace element proxies for surface ocean conditions: A synthesis of culture calibrations with planktic foraminifera. *Geochimica et Cosmochimica Acta*, 193:197–221, 2016.

Anand, P., Elderfield, H., and Conte, M. H. Calibration of Mg/Ca thermometry in planktonic foraminifera from a sediment trap time series. *Paleoceanography*, 18(2), 2003. ISSN 08838305. doi: 10.1029/2002pa000846.

Anderson, D. M. and Archer, D. Glacial-interglacial stability of ocean pH inferred from foraminifer dissolution rates. *Nature*, 416(6876):70–73, 2002.

Anderson, R., Fleisher, M., Lao, Y., and Winckler, G. Modern $CaCO_3$ preservation in equatorial Pacific sediments in the context of late-Pleistocene glacial cycles. *Marine Chemistry*, 111(1):30–46, 2008.

Anderson, R., Ali, S., Bradtmiller, L., Nielsen, S., Fleisher, M., Anderson, B., and Burckle, L. Wind-driven upwelling in the Southern Ocean and the deglacial rise in atmospheric CO_2. *science*, 323(5920):1443–1448, 2009.

Anderson, R. F., Chase, Z., Fleisher, M. Q., and Sachs, J. The Southern Ocean's biological pump during the last glacial maximum. *Deep Sea Research Part II: Topical Studies in Oceanography*, 49(9):1909–1938, 2002.

Antonov, J. I., Seidov, D., Boyer, T. P., Locarnini, R. A., Mishonov, A. V., Garcia, H. E., Baranova, O. K., Zweng, M. M., and Johnson, D. R. World Ocean Atlas 2009, Volume 2: Salinity, 2010.

Arbuszewski, J., deMenocal, P., Kaplan, A., and Farmer, E. C. On the fidelity of shell-derived $\delta^{18}O_{seawater}$ estimates. *Earth and Planetary Science Letters*, 300(3-4):185–196, 2010. ISSN 0012821X. doi: 10.1016/j.epsl.2010.10.035.

Archer, D. and Maier-Reimer, E. Effect of deep-sea sedimentary calcite preservation on atmospheric CO_2 concentration. *Nature*, 367:260–263, 1994.

Arrhenius, G. Sediment cores from the East Pacific: Swedish Deep-Sea Exped.(1947-1948) Repts., v. 5, fasc. 1, 89 p. 1963, Pelagic sediments in The Sea: New York, 1952.

Babila, T. L., Rosenthal, Y., and Conte, M. H. Evaluation of the biogeochemical controls on B/Ca of *Globigerinoides ruber* white from the Oceanic Flux Program, Bermuda. *Earth and Planetary Science Letters*, 404:67–76, 2014.

Babila, T. L., Rosenthal, Y., Wright, J. D., and Miller, K. G. A continental shelf perspective of ocean acidification and temperature evolution during the Paleocene-Eocene Thermal Maximum. *Geology*, 44(4):275–278, 2016.

Barker, S. and Diz, P. Timing of the descent into the last ice age determined by the bipolar seesaw. *Paleoceanography*, 29(6):489–507, 2014.

Barker, S., Greaves, M., and Elderfield, H. A study of cleaning procedures used for foraminiferal Mg/Ca paleothermometry. *Geochemistry, Geophysics, Geosystems*, 4(9), 2003.

Bassinot, F. C., Beaufort, L., Vincent, E., Labeyrie, L. D., Rostek, F., Müller, P. J., Quidelleur, X., and Lancelot, Y. Coarse fraction fluctuations in pelagic carbonate sediments from the tropical indian ocean: A 1500-kyr record of carbonate dissolution. *Paleoceanography*, 9(4):579–600, 1994.

Bassinot, F. C., Mélières, F., Gehlen, M., Levi, C., and Labeyrie, L. Crystallinity of foraminifera shells: A proxy to reconstruct past bottom water $CO_3^=$ changes? *Geochemistry Geophysics Geosystems*, 5(8):217–228, 2004.

Bé, A. W. and Hamlin, W. H. Ecology of Recent planktonic foraminifera: part 3: distribution in the North Atlantic during the summer of 1962. *Micropaleontology*, pages 87–106, 1967. ISSN 0026-2803.

Bé, A., Spero, H., and Anderson, O. Effects of symbiont elimination and reinfection on the life processes of the planktonic foraminifer *Globigerinoides sacculifer*. *Marine Biology*, 70(1):73–86, 1982.

Belkin, I. M. and Gordon, A. L. Southern Ocean fronts from the Greenwich meridian to Tasmania. *Journal of Geophysical Research: Oceans*, 101(C2): 3675–3696, 1996.

Bemis, B. E., Spero, H. J., Bijma, J., and Lea, D. W. Reevaluation of the oxygen isotopic composition of planktonic foraminifera: Experimental results and revised paleotemperature equations. *Paleoceanography*, 13(2):150–160, 1998. ISSN 08838305. doi: 10.1029/98pa00070.

Bereiter, B., Lüthi, D., Siegrist, M., Schüpbach, S., Stocker, T. F., and Fischer, H. Mode change of millennial CO_2 variability during the last glacial cycle associated with a bipolar marine carbon seesaw. *Proceedings of the National Academy of Sciences*, 109(25):9755–9760, 2012.

Berger, W. Increase of carbon dioxide in the atmosphere during deglaciation: the coral reef hypothesis. *Naturwissenschaften*, 69(2):87–88, 1982.

Berger, W. H. Planktonic foraminifera: selective solution and the lysocline. *Marine Geology*, 8(2):111–138, 1970. ISSN 0025-3227.

Berger, W. H. Deep-sea carbonates: Pleistocene dissolution cycles. *The Journal of Foraminiferal Research*, 3(4):187–195, 1973.

Bostock, H. C., Hayward, B. W., Neil, H. L., Currie, K. I., and Dunbar, G. B. Deep-water carbonate concentrations in the southwest Pacific. *Deep Sea Research Part I: Oceanographic Research Papers*, 58(1):72–85, 2011.

Bostock, H. C., Barrows, T. T., Carter, L., Chase, Z., Cortese, G., Dunbar, G., Ellwood, M., Hayward, B., Howard, W., Neil, H., et al. A review of the australian–new zealand sector of the southern ocean over the last 30 ka (aus-intimate project). *Quaternary Science Reviews*, 74:35–57, 2013.

Bostock, H. C., Hayward, B. W., Neil, H. L., Sabaa, A. T., and Scott, G. H. Changes in the position of the subtropical front south of new zealand since the last glacial period. *Paleoceanography*, 30(7):824–844, 2015.

Boussetta, S., Bassinot, F., Sabbatini, A., Caillon, N., Nouet, J., Kallel, N., Rebaubier, H., Klinkhammer, G., and Labeyrie, L. Diagenetic Mg-rich calcite in Mediterranean sediments: Quantification and impact on foraminiferal Mg/Ca thermometry. *Marine Geology*, 280(1-4):195–204, 2011. ISSN 00253227. doi: 10.1016/j.margeo.2010.12.011.

Boyd, P., LaRoche, J., Gall, M., Frew, R., and McKay, R. M. L. Role of iron, light, and silicate in controlling algal biomass in subantarctic waters SE of New Zealand. *Journal of Geophysical Research: Oceans*, 104(C6): 13395–13408, 1999.

Boyle, E. and Keigwin, L. Comparison of Atlantic and Pacific paleochemical records for the last 215,000 years: Changes in deep ocean circulation and chemical inventories. *Earth and Planetary Science Letters*, 76(1-2):135–150, 1985.

Boyle, E. A. The role of vertical chemical fractionation in controlling late Quaternary atmospheric carbon dioxide. *Journal of Geophysical Research: Oceans*, 93(C12):15701–15714, 1988.

Branson, O., Redfern, S. A. T., Tyliszczak, T., Sadekov, A., Langer, G., Kimoto, K., and Elderfield, H. The coordination of Mg in foraminiferal calcite. *Earth and Planetary Science Letters*, 383(4):134–141, 2013.

Branson, O., Kaczmarek, K., Redfern, S. A., Misra, S., Langer, G., Tyliszczak, T., Bijma, J., and Elderfield, H. The coordination and distribution of b in foraminiferal calcite. *Earth and Planetary Science Letters*, 416:67–72, 2015.

Broecker, W. S. Glacial to interglacial changes in ocean chemistry. *Progress in Oceanography*, 11(2):151–197, 1982.

Broecker, W. S. and Clark, E. An evaluation of Lohmann's foraminifera weight dissolution index. *Paleoceanography*, 16(5):531–534, 2001a.

Broecker, W. S. and Clark, E. Glacial-to-Holocene Redistribution of Carbonate Ion in the Deep Sea. *Science*, 294(5549):2152–2155, 2001b.

Broecker, W. S. and Peng, T.-H. The role of $CaCO_3$ compensation in the glacial to interglacial atmospherid CO_2 change. *Global Biogeochemical Cycles*, 1(1): 15–29, 1987.

Broecker, W. S., Peng, T.-H., and Beng, Z. *Tracers in the Sea*. Lamont-Doherty Geological Observatory, Columbia University, 1982.

Broecker, W. S., Clark, E., Mccorkle, D. C., Peng, T. H., Hajdas, I., and Bonani, G. Evidence for a reduction in the carbonate ion content of the deep sea during the course of the Holocene. *Paleoceanography*, 14(6):744–752, 1999.

Broecker, W. S., Yu, J., and Putnam, A. E. Two contributors to the glacial CO_2 decline. *Earth and Planetary Science Letters*, 429:191–196, 2015.

Brown, R. E., Anderson, L. D., Thomas, E., and Zachos, J. C. A core-top calibration of B/Ca in the benthic foraminifers *Nuttallides umbonifera* and *Oridorsalis umbonatus*: A proxy for Cenozoic bottom water carbonate saturation. *Earth and Planetary Science Letters*, 310(3):360–368, 2011.

Brown, S. J. and Elderfield, H. Variations in Mg/Ca and Sr/Ca ratios of planktonic foraminifera caused by postdepositional dissolution: Evidence of shallow Mg-dependent dissolution. *Paleoceanography*, 11(5):543–551, 1996.

Burke, A. and Robinson, L. F. The southern ocean's role in carbon exchange during the last deglaciation. *Science*, 335(6068):557–561, 2012.

Callahan, J. E. The structure and circulation of deep water in the Antarctic. In *Deep Sea Research and Oceanographic Abstracts*, volume 19, pages 563–575. Elsevier, 1972.

Carter, L., McCave, I., and Williams, M. J. Circulation and water masses of the southern ocean: a review. In Florindo, F. and Siegert, M., editors, *Developments in earth and environmental sciences*, volume 8, chapter 4, pages 85–114. Elsevier, 2008.

Chen, T., Robinson, L. F., Burke, A., Southon, J., Spooner, P., Morris, P. J., and Ng, H. C. Synchronous centennial abrupt events in the ocean and atmosphere during the last deglaciation. *Science*, 349(6255):1537–1541, 2015.

Cléroux, C., deMenocal, P., Arbuszewski, J., and Linsley, B. Reconstructing the upper water column thermal structure in the Atlantic Ocean. *Paleoceanography*, 2013. ISSN 08838305. doi: 10.1002/palo.20050.

Coadic, R., Bassinot, F., Dissard, D., Douville, E., Greaves, M., and Michel, E. A core-top study of dissolution effect on B/Ca in *Globigerinoides sacculifer* from the tropical Atlantic: Potential bias for paleo-reconstruction of seawater carbonate chemistry. *Geochemistry Geophysics Geosystems*, 14(4): 1053–1068, 2013.

De Nooijer, L., Spero, H., Erez, J., Bijma, J., and Reichart, G. Biomineralization in perforate foraminifera. *Earth-Science Reviews*, 135:48–58, 2014.

De Villiers, S. Optimum growth conditions as opposed to calcite saturation as a control on the calcification rate and shell-weight of marine foraminifera. *Marine Biology*, 144(1):45–49, 2004.

De Villiers, S. Foraminiferal shell-weight evidence for sedimentary calcite dissolution above the lysocline. *Deep Sea Research Part I Oceanographic Research Papers*, 52(5):671–680, 2005.

Dekens, P. S., Lea, D. W., Pak, D. K., and Spero, H. J. Core top calibration of Mg/Ca in tropical foraminifera: Refining paleotemperature estimation. *Geochemistry Geophysics Geosystems*, 3(4):1–29, 2002.

DePaolo, D. J. Surface kinetic model for isotopic and trace element fractionation during precipitation of calcite from aqueous solutions. *Geochimica et Cosmochimica Acta*, 75(4):1039–1056, 2011.

Deuser, W. Seasonal variations in isotopic composition and deep-water fluxes of the tests of perennially abundant planktonic foraminifera of the Sargasso Sea; results from sediment-trap collections and their paleoceanographic significance. *Journal of Foraminiferal Research*, 17(1):14–27, 1987.

Dickson, A. G. Standard potential of the reaction: AgCl (s) + $12H_2$ (g) = Ag (s) + HCl (aq), and and the standard acidity constant of the ion HSO_4^- in synthetic sea water from 273.15 to 318.15 K. *The Journal of Chemical Thermodynamics*, 22(2):113–127, 1990a.

Dickson, A. G. Thermodynamics of the dissociation of boric acid in synthetic seawater from 273.15 to 318.15 k. *Deep Sea Research Part A. Oceanographic Research Papers*, 37(5):755–766, 1990b.

Doss, W. and Marchitto, T. M. Glacial deep ocean sequestration of CO_2 driven by the eastern equatorial Pacific biologic pump. *Earth and Planetary Science Letters*, s 377–378(14):43–54, 2013.

Dueñas-Bohórquez, A., da Rocha, R. E., Kuroyanagi, A., Bijma, J., and Reichart, G.-J. Effect of salinity and seawater calcite saturation state on Mg and Sr incorporation in cultured planktonic foraminifera. *Marine Micropaleontology*, 73(3-4):178–189, 2009.

Duplessy, J.-C., Blanc, P.-L., and Bé, A. W. Oxygen-18 enrichment of planktonic foraminifera due to gametogenic calcification below the euphotic zone. *Science*, 213(4513):1247–1250, 1981.

Durand, A., Chase, Z., Noble, T. L., Bostock, H., Jaccard, S. L., Kitchener, P., Townsend, A. T., Jansen, N., Kinsley, L., Jacobsen, G., et al. Export production in the New-Zealand region since the Last Glacial Maximum. *Earth and Planetary Science Letters*, 469:110–122, 2017.

Edgar, K. M., Anagnostou, E., Pearson, P. N., and Foster, G. L. Assessing the impact of diagenesis on δ^{11}B, δ^{13}C, δ^{18}O, Sr/Ca and B/Ca values in fossil planktic foraminiferal calcite. *Geochimica Et Cosmochimica Acta*, 166:189–209, 2015.

Eggins, S., Deckker, P. D., and Marshall, J. Mg/Ca variation in planktonic foraminifera tests: implications for reconstructing palaeo-seawater temperature and habitat migration. *Earth and Planetary Science Letters*, 212(3–4): 291–306, 2003.

Eggins, S. M., Sadekov, A., and De Deckker, P. Modulation and daily banding of Mg/Ca in *Orbulina universa* tests by symbiont photosynthesis and respiration: a complication for seawater thermometry? *Earth and Planetary Science Letters*, 225(3):411–419, 2004.

Elderfield, H. and Ganssen, G. Past temperature and δ^{18}O of surface ocean waters inferred from foraminiferal Mg/Ca ratios. *Nature*, 405(6785):442–445, 2000.

Elderfield, H., Vautravers, M., and Cooper, M. The relationship between shell size and Mg/Ca, Sr/Ca, δ^{18}O, and δ^{13}C of species of planktonic foraminifera. *Geochemistry, Geophysics, Geosystems*, 3(8):1–13, 2002. ISSN 1525-2027. doi: 10.1029/2001GC000194.

Erez, J. The source of ions for biomineralization in foraminifera and their implications for paleoceanographic proxies. *Reviews in mineralogy and geochemistry*, 54(1):115–149, 2003.

Evans, D., Brierley, C., Raymo, M. E., Erez, J., and Müller, W. Planktic foraminifera shell chemistry response to seawater chemistry: Pliocene-Pleistocene seawater Mg/Ca, temperature and sea level change. *Earth and Planetary Science Letters*, 438:139–148, 2016a. ISSN 0012821X. doi: 10.1016/j.epsl.2016.01.013.

Evans, D., Wade, B. S., Henehan, M., Erez, J., and Müller, W. Revisiting carbonate chemistry controls on planktic foraminifera Mg/Ca: implications for sea surface temperature and hydrology shifts over the Paleocene-Eocene Thermal Maximum and Eocene-Oligocene transition. *Climate of the Past*, 12(4):819–835, 2016b. ISSN 1814-9332. doi: 10.5194/cp-12-819-2016.

Fairbanks, R. G., Wiebe, P. H., and Bé, A. W. Vertical distribution and isotopic composition of living planktonic foraminifera in the western North Atlantic. *Science*, 207(4426):61–63, 1980. ISSN 0036-8075.

Fairbanks, R. G., Sverdlove, M., Free, R., Wiebe, P. H., and Bé, A. W. Vertical distribution and isotopic fractionation of living planktonic foraminifera from the Panama Basin. *Nature*, 298(5877):841–844, 1982. ISSN 0028-0836.

Farrell, J. W. and Prell, W. L. Climatic change and $CaCO_3$ preservation: an 800,000 year bathymetric reconstruction from the central equatorial Pacific Ocean. *Paleoceanography*, 4(4):447–466, 1989.

Ferguson, J. E., Henderson, G. M., Kucera, M., and Rickaby, R. E. M. Systematic change of foraminiferal Mg/Ca ratios across a strong salinity gradient. *Earth and Planetary Science Letters*, 265(1-2):153–166, 2008. ISSN 0012821X. doi: 10.1016/j.epsl.2007.10.011.

Ferrari, R., Jansen, M. F., Adkins, J. F., Burke, A., Stewart, A. L., and Thompson, A. F. Antarctic sea ice control on ocean circulation in present and glacial climates. *Proceedings of the National Academy of Sciences*, 111 (24):8753–8758, 2014.

Foster, G. L. and Rae, J. W. Reconstructing ocean pH with boron isotopes in foraminifera. *Annual Review of Earth and Planetary Sciences*, 44:207–237, 2016.

Foster, G. L. and Vance, D. Negligible glacial–interglacial variation in continental chemical weathering rates. *Nature*, 444(7121):918–921, 2006.

Foster, G. Seawater pH, pCO_2 and $[CO_3^{2-}]$ variations in the Caribbean Sea over the last 130 kyr: A boron isotope and B/Ca study of planktic foraminifera. *Earth and Planetary Science Letters*, 271(1):254–266, 2008.

Foster, G., Pogge von Strandmann, P., and Rae, J. Boron and magnesium isotopic composition of seawater. *Geochemistry, Geophysics, Geosystems*, 11(8), 2010.

Francois, R., Altabet, M., Yu, E., Sigman, D., Bacon, M., Frank, M., Bohrmann, G., Bareille, G., and Labeyrie, L. Water column stratification in the Southern Ocean contributed to the lowering of glacial atmospheric CO_2. *Nature*, 389:929–935, 1997.

Friedrich, O., Schiebel, R., Wilson, P. A., Weldeab, S., Beer, C. J., Cooper, M. J., and Fiebig, J. Influence of test size, water depth, and ecology on Mg/Ca, Sr/Ca, $\delta^{18}O$ and $\delta^{13}C$ in nine modern species of planktic foraminifers. *Earth and Planetary Science Letters*, 319:133–145, 2012.

Gabitov, R. I., Rollion-Bard, C., Tripati, A., and Sadekov, A. In situ study of boron partitioning between calcite and fluid at different crystal growth rates. *Geochimica et Cosmochimica Acta*, 137:81–92, 2014.

Gastrich, M. D. Ultrastructure of a new intracellular symbiotic alga found within planktonic foraminifera. *Journal of Phycology*, 23(4):623–632, 1987.

Gottschalk, J., Skinner, L. C., Misra, S., Waelbroeck, C., Menviel, L., and Timmermann, A. Abrupt changes in the southern extent of North Atlantic Deep Water during Dansgaard-Oeschger events. *Nature Geoscience*, 2015.

Gottschalk, J., Skinner, L. C., Lippold, J., Vogel, H., Frank, N., Jaccard, S. L., and Waelbroeck, C. Biological and physical controls in the Southern Ocean on past millennial-scale atmospheric CO_2 changes. *Nature communications*, 7, 2016.

Grant, K., Rohling, E., Ramsey, C. B., Cheng, H., Edwards, R., Florindo, F., Heslop, D., Marra, F., Roberts, A., Tamisiea, M. E., et al. Sea-level variability over five glacial cycles. *Nature communications*, 5, 2014.

Greaves, M., Caillon, N., Rebaubier, H., Bartoli, G., Bohaty, S., Cacho, I., Clarke, L., Cooper, M., Daunt, C., Delaney, M., deMenocal, P., Dutton, A., Eggins, S., Elderfield, H., Garbe-Schoenberg, D., Goddard, E., Green, D., Groeneveld, J., Hastings, D., Hathorne, E., Kimoto, K., Klinkhammer,

G., Labeyrie, L., Lea, D. W., Marchitto, T., Martínez-Botí, M. A., Mortyn, P. G., Ni, Y., Nuernberg, D., Paradis, G., Pena, L., Quinn, T., Rosenthal, Y., Russell, A., Sagawa, T., Sosdian, S., Stott, L., Tachikawa, K., Tappa, E., Thunell, R., and Wilson, P. A. Interlaboratory comparison study of calibration standards for foraminiferal Mg/Ca thermometry. *Geochemistry, Geophysics, Geosystems*, 9(8):n/a–n/a, 2008. ISSN 15252027. doi: 10.1029/2008gc001974.

Hain, M., Sigman, D., and Haug, G. The biological pump in the past. In Holland, H. D. and Turekian, K. K., editors, *Treatise on Geochemistry (Second Edition)*, pages 485 – 517. Elsevier, Oxford, second edition edition, 2014. ISBN 978-0-08-098300-4.

Hamilton, L. Structure of the subtropical front in the Tasman Sea. *Deep Sea Research Part I: Oceanographic Research Papers*, 53(12):1989–2009, 2006.

Haynes, L. L., Hönisch, B., Dyez, K. A., Holland, K., Rosenthal, Y., Fish, C. R., Subhas, A. V., and Rae, J. W. Calibration of the B/Ca proxy in the planktic foraminifer *Orbulina universa* to Paleocene seawater conditions. *Paleoceanography*, 2017.

He, M., Xiao, Y., Jin, Z., Liu, W., Ma, Y., Zhang, Y., and Luo, C. Quantification of boron incorporation into synthetic calcite under controlled pH and temperature conditions using a differential solubility technique. *Chemical Geology*, 337:67–74, 2013.

Hemleben, C., Spindler, M., and Anderson, O. R. *Modern Planktonic Foraminifera*. Springer, 1989.

Hemming, N. and Hanson, G. Boron isotopic composition and concentration in modern marine carbonates. *Geochimica et Cosmochimica Acta*, 56(1): 537–543, 1992.

Hemming, N., Reeder, R., and Hanson, G. Mineral-fluid partitioning and isotopic fractionation of boron in synthetic calcium carbonate. *Geochimica et Cosmochimica Acta*, 59(2):371–379, 1995.

Henehan, M. J., Foster, G. L., Rae, J. W., Prentice, K. C., Erez, J., Bostock, H. C., Marshall, B. J., and Wilson, P. A. Evaluating the utility of B/Ca ratios in planktic foraminifera as a proxy for the carbonate system: A case study of *Globigerinoides ruber*. *Geochemistry, Geophysics, Geosystems*, 16 (4):1052–1069, 2015.

Henehan, M. J., Foster, G. L., Bostock, H. C., Greenop, R., Marshall, B. J., and Wilson, P. A. A new boron isotope-pH calibration for *Orbulina universa*, with implications for understanding and accounting for 'vital effects'. *Earth and Planetary Science Letters*, 454:282–292, 2016.

Hertzberg, J. E. and Schmidt, M. W. Refining *Globigerinoides ruber* Mg/Ca paleothermometry in the Atlantic Ocean. *Earth and Planetary Science Letters*, 383:123–133, 2013. ISSN 0012821X. doi: 10.1016/j.epsl.2013.09.044.

Hodell, D., Charles, C., and Sierro, F. Late Pleistocene evolution of the ocean's carbonate system. *Earth and Planetary Science Letters*, 192(2):109–124, 2001.

Holland, K., Eggins, S. M., Hönisch, B., Haynes, L. L., and Branson, O. Calcification rate and shell chemistry response of the planktic foraminifer *Orbulina universa* to changes in microenvironment seawater carbonate chemistry. *Earth and Planetary Science Letters*, 464:124–134, 2017.

Hönisch, B., Bijma, J., Russell, A. D., Spero, H. J., Palmer, M. R., Zeebe, R. E., and Eisenhauer, A. The influence of symbiont photosynthesis on the boron isotopic composition of foraminifera shells. *Marine Micropaleontology*, 49(1–2):87–96, 2003.

Hönisch, B., Allen, K. A., Lea, D. W., Spero, H. J., Eggins, S. M., Arbuszewski, J., deMenocal, P., Rosenthal, Y., Russell, A. D., and Elderfield, H. The influence of salinity on Mg/Ca in planktic foraminifers - Evidence from cultures, core-top sediments and complementary δ^{18}O. *Geochimica et Cosmochimica Acta*, 121:196–213, 2013. ISSN 00167037. doi: 10.1016/j.gca.2013.07.028.

Hoogakker, B. A. A., Klinkhammer, G. P., Elderfield, H., Rohling, E. J., and Hayward, C. Mg/Ca paleothermometry in high salinity environments. *Earth and Planetary Science Letters*, 284(3-4):583–589, 2009. ISSN 0012821X. doi: 10.1016/j.epsl.2009.05.027.

Howard, W. R. and Prell, W. L. Late Quaternary $CaCO_3$ production and preservation in the Southern Ocean: Implications for oceanic and atmospheric carbon cycling. *Paleoceanography*, 9(3):453–482, 1994.

Hu, R., Noble, T. L., Piotrowski, A. M., McCave, I. N., Bostock, H. C., and Neil, H. L. Neodymium isotopic evidence for linked changes in Southeast Atlantic and Southwest Pacific circulation over the last 200 kyr. *Earth and Planetary Science Letters*, 455:106–114, 2016.

Johnstone, H. J. H., Schulz, M., Barker, S., and Elderfield, H. Inside story: An X-ray computed tomography method for assessing dissolution in the tests of planktonic foraminifera. *Marine Micropaleontology*, 77(1):58–70, 2010.

Johnstone, H. J. H., Yu, J., Elderfield, H., and Schulz, M. Improving temperature estimates derived from Mg/Ca of planktonic foraminifera using X-ray computed tomography–based dissolution index, XDX. *Paleoceanography*, 26 (1):PA1215, 2011. ISSN 0883-8305. doi: 10.1029/2009pa001902.

Jones, J. I. Significance of the distribution of planktonic foraminifera in the equatorial Atlantic undercurrent. *Micropaleontology*, 13(4):489–501, 1967.

Jonkers, L. and Kučera, M. Global analysis of seasonality in the shell flux of extant planktonic foraminifera. *Biogeosciences*, 12(7):2207–2226, 2015.

Jonkers, L. and Kučera, M. Quantifying the effect of seasonal and vertical habitat tracking on planktonic foraminifera proxies. *Climate of the Past*, 13 (6):573–586, 2017.

Jorgensen, B. B., Erez, J., Revsbech, N. P., and Cohen, Y. Symbiotic photosynthesis in a planktonic foraminiferan, *Globigerinoides sacculifer (Brady)*, studied with microelectrodes. *Limnol. Oceanogr*, 30(6):1253–1267, 1985.

Jouzel, J., Massondelmotte, V., Cattani, O., Dreyfus, G., Falourd, S., Hoffmann, G., Minster, B., Nouet, J., Barnola, J. M., and Chappellaz, J. Orbital and millennial Antarctic climate variability over the past 800,000 years. *Science*, 317(5839):793, 2007.

Kaczmarek, K., Nehrke, G., Misra, S., Bijma, J., and Elderfield, H. Investigating the effects of growth rate and temperature on the B/Ca ratio and δ^{11}B during inorganic calcite formation. *Chemical Geology*, 421:81–92, 2016.

Keir, R. S. On the late Pleistocene ocean geochemistry and circulation. *Paleoceanography*, 3(4):413–445, 1988.

Kerr, J., Rickaby, R., Yu, J., Elderfield, H., and Sadekov, A. Y. The effect of ocean alkalinity and carbon transfer on deep-sea carbonate ion concentration during the past five glacial cycles. *Earth and Planetary Science Letters*, 471: 42–53, 2017.

Key, R. M., Kozyr, A., Sabine, C. L., Lee, K., Wanninkhof, R., Bullister, J. L., Feely, R. A., Millero, F. J., Mordy, C., and Peng, T.-H. A global ocean carbon climatology: Results from Global Data Analysis Project (GLODAP). *Global Biogeochemical Cycles*, 18(4), 2004.

Kısakurek, B., Eisenhauer, A., Böhm, F., Garbe-Schönberg, D., and Erez, J. Controls on shell Mg/Ca and Sr/Ca in cultured planktonic foraminiferan, *Globigerinoides ruber* (white). *Earth and Planetary Science Letters*, 273 (3-4):260–269, 2008.

Kısakürek, B., Eisenhauer, A., Böhm, F., Hathorne, E. C., and Erez, J. Controls on calcium isotope fractionation in cultured planktic foraminifera, *Globigerinoides ruber* and *Globigerinella siphonifera*. *Geochimica et Cosmochimica Acta*, 75(2):427–443, 2011.

Klochko, K., Kaufman, A. J., Yao, W., Byrne, R. H., and Tossell, J. A. Experimental measurement of boron isotope fractionation in seawater. *Earth and Planetary Science Letters*, 248(1):276–285, 2006.

Krupinski, N. B. Q., Russell, A. D., Pak, D. K., and Paytan, A. Core-top calibration of B/Ca in Pacific Ocean *Neogloboquadrina incompta* and *Globigerina bulloides* as a surface water carbonate system proxy. *Earth and Planetary Science Letters*, 466:139–151, 2017.

Lea, D. W., Mashiotta, T. A., and Spero, H. J. Controls on magnesium and strontium uptake in planktonic foraminifera determined by live culturing. *Geochimica et Cosmochimica Acta*, 63(16):2369–2379, 1999.

Lea, D. W., Pak, D. K., and Spero, H. J. Climate impact of late Quaternary equatorial Pacific sea surface temperature variations. *Science*, 289(5485): 1719–1724, 2000.

Lea, D. W., Pak, D. K., Peterson, L. C., and Hughen, K. A. Synchroneity of tropical and high-latitude Atlantic temperatures over the last glacial termination. *Science*, 301(5638):1361–1364, 2003.

Lee, K., Kim, T.-W., Byrne, R. H., Millero, F. J., Feely, R. A., and Liu, Y.-M. The universal ratio of boron to chlorinity for the North Pacific and North Atlantic oceans. *Geochimica et Cosmochimica Acta*, 74(6):1801–1811, 2010.

LeGrande, A. N. and Schmidt, G. A. Global gridded data set of the oxygen isotopic composition in seawater. *Geophysical Research Letters*, 33(12), 2006. ISSN 0094-8276. doi: 10.1029/2006gl026011.

Lewis, E., Wallace, D., and Allison, L. J. *Program developed for CO_2 system calculations*. Carbon Dioxide Information Analysis Center, managed by Lockheed Martin Energy Research Corporation for the US Department of Energy Tennessee, 1998.

Lisiecki, L. E. and Stern, J. V. Regional and global benthic δ^{18}O stacks for the last glacial cycle. *Paleoceanography*, 31(10):1368–1394, 2016.

Locarnini, R. A., Mishonov, A. V., Antonov, J. I., Boyer, T. P., Garcia, H. E., Baranova, O. K., Zweng, M. M., and Johnson, D. R. World Ocean Atlas 2009, Volume 1: Temperature, 2010.

Lohmann, G. P. A model for variation in the chemistry of planktonic foraminifera due to secondary calcification and selective dissolution. *Paleoceanography*, 10(10):445–457, 1995.

Lorens, R. B. Sr, Cd, Mn and Co distribution coefficients in calcite as a function of calcite precipitation rate. *Geochimica et Cosmochimica Acta*, 45 (4):553–561, 1981.

Lund, D., Adkins, J., and Ferrari, R. Abyssal Atlantic circulation during the Last Glacial Maximum: Constraining the ratio between transport and vertical mixing. *Paleoceanography*, 26(1), 2011.

Lüthi, D., Le, F. M., Bereiter, B., Blunier, T., Barnola, J. M., Siegenthaler, U., Raynaud, D., Jouzel, J., Fischer, H., and Kawamura, K. High-resolution carbon dioxide concentration record 650,000-800,000 years before present. *Nature*, 453(453):379–82, 2008.

Marchitto, T. M., Lynch-Stieglitz, J., and Hemming, S. R. Deep Pacific $CaCO_3$ compensation and glacial/interglacial atmospheric CO_2. *Earth and Planetary Science Letters*, 231(3–4):317–336, 2005.

Marino, G., Rohling, E., Rodríguez-Sanz, L., Grant, K., Heslop, D., Roberts, A., Stanford, J., and Yu, J. Bipolar seesaw control on last interglacial sea level. *Nature*, 522(7555):197, 2015.

Martin, J. H. Glacial-interglacial CO_2 change: The iron hypothesis. *Paleoceanography*, 5(1):1–13, 1990.

Martinez, J. Late pleistocene carbonate dissolution patterns in the tasman sea. *Evolution of the Tasman Sea basin*, pages 215–228, 1994.

Martínez-Garcia, A., Rosell-Melé, A., Jaccard, S. L., Geibert, W., Sigman, D. M., and Haug, G. H. Southern ocean dust-climate coupling over the past four million years. *Nature*, 476(7360):312–315, 2011.

Martínez-García, A., Sigman, D. M., Ren, H., Anderson, R. F., Straub, M., Hodell, D. A., Jaccard, S. L., Eglinton, T. I., and Haug, G. H. Iron fertilization of the Subantarctic Ocean during the last ice age. *Science*, 343(6177): 1347–1350, 2014.

Mathien-Blard, E. and Bassinot, F. Salinity bias on the foraminifera Mg/Ca thermometry: Correction procedure and implications for past ocean hydrographic reconstructions. *Geochemistry, Geophysics, Geosystems*, 10(12): n/a–n/a, 2009. ISSN 15252027. doi: 10.1029/2008gc002353.

Matsumoto, K. Biology-mediated temperature control on atmospheric pCO_2 and ocean biogeochemistry. *Geophysical Research Letters*, 34(20), 2007.

McCartney, M. S. and Talley, L. D. The subpolar mode water of the north atlantic ocean. *Journal of Physical Oceanography*, 12(11):1169–1188, 1982.

McCave, I., Carter, L., and Hall, I. R. Glacial-interglacial changes in water mass structure and flow in the SW Pacific Ocean. *Quaternary Science Reviews*, 27(19):1886–1908, 2008.

McCave, I., Crowhurst, S., Kuhn, G., Hillenbrand, C., and Meredith, M. Minimal change in Antarctic Circumpolar Current flow speed between the last glacial and Holocene. *Nature geoscience*, 7(2):113–116, 2014.

McConnell, M. C. and Thunell, R. C. Calibration of the planktonic foraminiferal Mg/Ca paleothermometer: Sediment trap results from the Guaymas Basin, Gulf of California. *Paleoceanography*, 20(2), 2005.

Mehrbach, C., Culberson, C., Hawley, J., and Pytkowicx, R. Measurement of the apparent dissociation constants of carbonic acid in seawater at atmospheric pressure. *Limnology and Oceanography*, 18(6):897–907, 1973.

Molina-Kescher, M., Frank, M., Tapia, R., Ronge, T. A., Nürnberg, D., and Tiedemann, R. Reduced admixture of North Atlantic Deep Water to the deep central South Pacific during the last two glacial periods. *Paleoceanography*, 31(6):651–668, 2016.

Monnin, E. and Barnola, J. M. Atmospheric CO_2 concentrations over the last glacial termination. *Science*, 291(5501):112–4, 2001.

Moy, A. D., Howard, W. R., and Gagan, M. K. Late Quaternary palaeoceanography of the circumpolar deep water from the South Tasman Rise. *Journal of Quaternary Science*, 21(7):763–777, 2006.

Moy, A. D. *Late Pleistocene palaeoceanographic and geochemical evolution of the South Tasman Rise*. PhD thesis, University of Tasmania, 2005.

Ni, Y., Foster, G. L., Bailey, T., Elliott, T., Schmidt, D. N., Pearson, P., Haley, B., and Coath, C. A core top assessment of proxies for the ocean carbonate system in surface-dwelling foraminifers. *Paleoceanography*, 22(3), 2007.

Ninnemann, U. S. and Charles, C. D. Changes in the mode of Southern Ocean circulation over the last glacial cycle revealed by foraminiferal stable isotopic variability. *Earth and Planetary Science Letters*, 201(2):383–396, 2002.

Noble, T. L., Piotrowski, A. M., and McCave, I. N. Neodymium isotopic composition of intermediate and deep waters in the glacial southwest pacific. *Earth and Planetary Science Letters*, 384:27–36, 2013.

Noireaux, J., Mavromatis, V., Gaillardet, J., Schott, J., Montouillout, V., Louvat, P., Rollion-Bard, C., and Neuville, D. Crystallographic control on the boron isotope paleo-pH proxy. *Earth and Planetary Science Letters*, 430: 398–407, 2015.

Nürnberg, D., Bijma, J., and Hemleben, C. Assessing the reliability of magnesium in foraminiferal calcite as a proxy for water mass temperatures. *Geochimica et Cosmochimica Acta*, 60(5):803–814, 1996.

Opdyke, B. N. and Walker, J. C. Return of the coral reef hypothesis: Basin to shelf partitioning of $CaCO_3$ and its effect on atmospheric CO_2. *Geology*, 20(8):733–736, 1992.

Oppo, D. W., Fairbanks, R. G., Gordon, A. L., and Shackleton, N. J. Late Pleistocene southern Ocean $\delta^{13}C$ variability. *Paleoceanography*, 5(1):43–54, 1990.

Orsi, A., Johnson, G., and Bullister, J. Circulation, mixing, and production of Antarctic Bottom Water. *Progress in Oceanography*, 43(1):55–109, 1999.

Orsi, A. H., Nowlin, W. D., and Whitworth, T. On the circulation and stratification of the weddell gyre. *Deep Sea Research Part I: Oceanographic Research Papers*, 40(1):169–203, 1993.

Orsi, A. H., Whitworth, T., and Nowlin, W. D. On the meridional extent and fronts of the antarctic circumpolar current. *Deep Sea Research Part I: Oceanographic Research Papers*, 42(5):641–673, 1995.

Palmer, M. R., Brummer, G. J., Cooper, M. J., Elderfield, H., Greaves, M. J., Reichart, G. J., Schouten, S., and Yu, J. M. Multi-proxy reconstruction of surface water pCO_2in the northern Arabian Sea since 29 ka. *Earth and Planetary Science Letters*, 295(1–2):49–57, 2010.

Penman, D. E., Hönisch, B., Zeebe, R. E., Thomas, E., and Zachos, J. C. Rapid and sustained surface ocean acidification during the Paleocene-Eocene Thermal Maximum. *Paleoceanography*, 29(5):357–369, 2014.

Petit, J. R., Jouzel, J., Raynaud, D., Barkov, N. I., Barnola, J. M., Basile, I., Bender, M., Chappellaz, J., Davis, M., and Delaygue, G. Climate and atmospheric history of the past 420,000 years from the Vostok ice core, Antarctica. *Nature*, 399(6735):429, 1999.

Piotrowski, A. M., Goldstein, S. L., Hemming, S. R., and Fairbanks, R. G. Temporal relationships of carbon cycling and ocean circulation at glacial boundaries. *Science*, 307(5717):1933–1938, 2005.

Piotrowski, A. M., Banakar, V. K., Scrivner, A. E., Elderfield, H., Galy, A., and Dennis, A. Indian Ocean circulation and productivity during the last glacial cycle. *Earth and Planetary Science Letters*, 285(1):179–189, 2009.

Rae, J. W., Foster, G. L., Schmidt, D. N., and Elliott, T. Boron isotopes and B/Ca in benthic foraminifera: proxies for the deep ocean carbonate system. *Earth and Planetary Science Letters*, 302(3):403–413, 2011.

Raitzsch, M., Hathorne, E. C., Kuhnert, H., Groeneveld, J., and Bickert, T. Modern and late Pleistocene B/Ca ratios of the benthic foraminifer *Planulina wuellerstorfi* determined with laser ablation ICP-MS. *Geology*, 39 (11):1039–1042, 2011.

Ravelo, A. and Fairbanks, R. Oxygen isotopic composition of multiple species of planktonic foraminifera: Recorders of the modern photic zone temperature gradient. *Paleoceanography*, 7(6):815–831, 1992.

Redfield, A. C. On the proportions of organic derivatives in a sea water and their relation to the composition of plankton. *James Johnstone memorial volume*, pages 177–192, 1934.

Regenberg, M., Nürnberg, D., Steph, S., Groeneveld, J., Garbe-Schönberg, D., Tiedemann, R., and Dullo, W.-C. Assessing the effect of dissolution on planktonic foraminiferal Mg/Ca ratios: Evidence from Caribbean core tops. *Geochemistry, Geophysics, Geosystems*, 7(7), 2006.

Regenberg, M., Regenberg, A., Garbe-Schönberg, D., and Lea, D. W. Global dissolution effects on planktonic foraminiferal Mg/Ca ratios controlled by the calcite-saturation state of bottom waters. *Paleoceanography*, 19, 2014. ISSN 08838305. doi: 10.1002/2013pa002492.

Reimer, P. J., Bard, E., Bayliss, A., Beck, J. W., Blackwell, P. G., Ramsey, C. B., Buck, C. E., Cheng, H., Edwards, R. L., Friedrich, M., et al. IntCal13 and Marine13 Radiocarbon Age Calibration Curves 0-50,000 Years cal BP. *Radiocarbon*, 55(4):1869–1887, 2013.

Rickaby, R., Schrag, D., Zondervan, I., and Riebesell, U. Growth rate dependence of Sr incorporation during calcification of *Emiliania huxleyi*. *Global biogeochemical cycles*, 16(1), 2002.

Rickaby, R., Elderfield, H., Roberts, N., Hillenbrand, C.-D., and Mackensen, A. Evidence for elevated alkalinity in the glacial Southern Ocean. *Paleoceanography*, 25(1), 2010.

Rink, S., Kühl, M., Bijma, J., and Spero, H. Microsensor studies of photosynthesis and respiration in the symbiotic foraminifer *Orbulina universa*. *Marine Biology*, 131(4):583–595, 1998.

Rintoul, S. R. and Bullister, J. L. A late winter hydrographic section from Tasmania to Antarctica. *Deep Sea Research Part I: Oceanographic Research Papers*, 46(8):1417–1454, 1999.

Rollion-Bard, C. and Erez, J. Intra-shell boron isotope ratios in the symbiont-bearing benthic foraminiferan *Amphistegina lobifera*: implications for δ^{11}B vital effects and paleo-pH reconstructions. *Geochimica et Cosmochimica Acta*, 74(5):1530–1536, 2010.

Ronge, T., Tiedemann, R., Lamy, F., Köhler, P., Alloway, B., De Pol-Holz, R., Pahnke, K., Southon, J., and Wacker, L. Radiocarbon constraints on the extent and evolution of the South Pacific glacial carbon pool. *Nature communications*, 7, 2016.

Rosman, K. and Taylor, P. Isotopic compositions of the elements. *Journal of Physical and Chemical Reference Data*, 27(6):1275–1287, 1998.

Russell, A. D., Emerson, S., Nelson, B. K., Erez, J., and Lea, D. W. Uranium in foraminiferal calcite as a recorder of seawater uranium concentrations. *Geochimica Et Cosmochimica Acta*, 58(2):671–681, 1994.

Russell, A. D., Hønisch, B., Spero, H. J., and Lea, D. W. Effects of seawater carbonate ion concentration and temperature on shell U, Mg, and Sr in cultured planktonic foraminifera. *Geochimica et Cosmochimica Acta*, 68 (21):4347–4361, 2004.

Sabine, C. L., Feely, R. A., Gruber, N., Key, R. M., Lee, K., Bullister, J. L., Wanninkhof, R., Wong, C., Wallace, D. W., Tilbrook, B., et al. The oceanic sink for anthropogenic CO_2. *Science*, 305(5682):367–371, 2004.

Sadekov, A., Eggins, S. M., De Deckker, P., and Kroon, D. Uncertainties in seawater thermometry deriving from intratest and intertest Mg/Ca variability in *Globigerinoides ruber*. *Paleoceanography*, 23(1), 2008.

Sadekov, A. Y., Eggins, S. M., and Deckker, P. D. Characterization of Mg/Ca distributions in planktonic foraminifera species by electron microprobe mapping. *Geochemistry Geophysics Geosystems*, 6(12):238–239, 2013.

Salmon, K. H., Anand, P., Sexton, P. F., and Conte, M. Calcification and growth processes in planktonic foraminifera complicate the use of B/Ca and U/Ca as carbonate chemistry proxies. *Earth and Planetary Science Letters*, 2016.

Sanyal, A., Nugent, M., Reeder, R., and Bijma, J. Seawater pH control on the boron isotopic composition of calcite: Evidence from inorganic calcite precipitation experiments. *Geochimica et Cosmochimica Acta*, 64(9):1551–1555, 2000.

Schmidt, G., Bigg, G., and Rohling, E. Global seawater oxygen-18 database, 1999.

Seki, O., Foster, G. L., Schmidt, D. N., Mackensen, A., Kawamura, K., and Pancost, R. D. Alkenone and boron-based Pliocene pCO_2 records. *Earth and Planetary Science Letters*, 292(1):201–211, 2010.

Sigman, D. M. and Boyle, E. A. Glacial/interglacial variations in atmospheric carbon dioxide. *Nature*, 407(6806):859–69, 2000.

Sigman, D. M., Hain, M. P., and Haug, G. H. The polar ocean and glacial cycles in atmospheric CO_2 concentration. *Nature*, 466(7302):47–55, 2010.

Sikes, E., Howard, W., Samson, C., Mahan, T., Robertson, L., and Volkman, J. Southern Ocean seasonal temperature and Subtropical Front movement on the South Tasman Rise in the late Quaternary. *Paleoceanography*, 24(2), 2009.

Sikes, E. L., Allen, K. A., and Lund, D. C. Enhanced δ13c and δ18o differences between the south atlantic and south pacific during the last glaciation: The deep gateway hypothesis. *Paleoceanography*, 32(10):1000–1017, 2017.

Skinner, L., McCave, I., Carter, L., Fallon, S., Scrivner, A., and Primeau, F. Reduced ventilation and enhanced magnitude of the deep Pacific carbon pool during the last glacial period. *Earth and Planetary Science Letters*, 411:45–52, 2015.

Spero, H. J., Eggins, S. M., Russell, A. D., Vetter, L., Kilburn, M. R., and Hönisch, B. Timing and mechanism for intratest Mg/Ca variability in a living planktic foraminifer. *Earth and Planetary Science Letters*, 409:32–42, 2015.

Stephens, B. B. and Keeling, R. F. The influence of Antarctic sea ice on glacial-interglacial CO_2 variations. *Nature*, 404(6774):171–174, 2000.

Stirling, C., Esat, T., Lambeck, K., and McCulloch, M. Timing and duration of the last interglacial: evidence for a restricted interval of widespread coral reef growth. *Earth and Planetary Science Letters*, 160(3):745–762, 1998.

Stoll, H. M., Klaas, C. M., Probert, I., Encinar, J. R., and Alonso, J. I. G. Calcification rate and temperature effects on Sr partitioning in coccoliths of multiple species of coccolithophorids in culture. *Global and Planetary Change*, 34(3):153–171, 2002.

Stuiver, M. and Reimer, P. J. Extended ^{14}C data base and revised CALIB 3.0 ^{14}C age calibration program. *Radiocarbon*, 35(01):215–230, 1993.

Takahashi, T., Sutherland, S. C., Wanninkhof, R., Sweeney, C., Feely, R. A., Chipman, D. W., Hales, B., Friederich, G., Chavez, F., and Sabine, C. Climatological mean and decadal change in surface ocean pCO_2 , and net sea-air CO_2 flux over the global oceans. *Deep Sea Research Part II Topical Studies in Oceanography*, 56(8–10):554–577, 2009.

Talley, L. D. Closure of the global overturning circulation through the Indian, Pacific, and Southern Oceans: Schematics and transports. *Oceanography*, 26(1):80–97, 2013.

Talley, L. D., Pickard, G. L., Emery, W. J., and Swift, J. H. *Descriptive physical oceanography: an introduction*. Academic Press, 2011.

Tang, J., Köhler, S. J., and Dietzel, M. Sr^{2+}/Ca^{2+} and $^{44}Ca/^{40}Ca$ fractionation during inorganic calcite formation: I. Sr incorporation. *Geochimica et Cosmochimica Acta*, 72(15):3718–3732, 2008.

Teng, Y.-C., Primeau, F. W., Moore, J. K., Lomas, M. W., and Martiny, A. C. Global-scale variations of the ratios of carbon to phosphorus in exported marine organic matter. *Nature Geoscience*, 7(12):895–898, 2014.

Tesoriero, A. J. and Pankow, J. F. Solid solution partitioning of Sr^{2+}, Ba^{2+}, and Cd^{2+} to calcite. *Geochimica et Cosmochimica Acta*, 60(6):1053–1063, 1996.

Toggweiler, J. R., Russell, J. L., and Carson, S. R. Midlatitude westerlies, atmospheric CO_2, and climate change during the ice ages. *Paleoceanography*, 21(2), 2006.

Tolderlund, D. S. and Bé, A. W. H. Seasonal distribution of planktonic foraminifera in the western North Atlantic. *Micropaleontology*, 17(3):297–329, 1971.

Uchikawa, J., Penman, D. E., Zachos, J. C., and Zeebe, R. E. Experimental evidence for kinetic effects on B/Ca in synthetic calcite: Implications for potential $B(OH)_4^-$ and $B(OH)_3$ incorporation. *Geochimica et Cosmochimica Acta*, 150:171–191, 2015.

Ullermann, J., Lamy, F., Ninnemann, U., Lembke-Jene, L., Gersonde, R., and Tiedemann, R. Pacific-Atlantic Circumpolar Deep Water coupling during the last 500 ka. *Paleoceanography*, 31(6):639–650, 2016.

Vecsei, A. and Berger, W. H. Increase of atmospheric CO_2 during deglaciation: constraints on the coral reef hypothesis from patterns of deposition. *Global Biogeochemical Cycles*, 18(1), 2004.

Wang, L. Isotopic signals in two morphotypes of *Globigerinoides ruber* (white) from the South China Sea: implications for monsoon climate change during the last glacial cycle. *Palaeogeography, Palaeoclimatology, Palaeoecology*, 161 (3):381–394, 2000.

Wara, M. W., Delaney, M. L., Bullen, T. D., and Ravelo, A. C. Possible roles of pH, temperature, and partial dissolution in determining boron concentration and isotopic composition in planktonic foraminifera. *Paleoceanography*, 18 (4), 2003.

Whitworth, T., Orsi, A., Kim, S.-J., Nowlin, W., and Locarnini, R. Water masses and mixing near the antarctic slope front. Antarctic Research Series 75, pages 1–27. American Geophysical Union, Washington, 1998.

Willenbring, J. K. and von Blanckenburg, F. Long-term stability of global erosion rates and weathering during late-cenozoic cooling. *Nature*, 465(7295): 211–214, 2010.

Wilson, D. J., Piotrowski, A. M., Galy, A., and Mccave, I. N. A boundary exchange influence on deglacial neodymium isotope records from the deep western Indian Ocean. *Earth and Planetary Science Letters*, 341-344(8): 35–47, 2012.

Wilson, D. J., Piotrowski, A. M., Galy, A., and Banakar, V. K. Interhemispheric controls on deep ocean circulation and carbon chemistry during the last two glacial cycles. *Paleoceanography*, 30(6):621–641, 2015.

Wolf-Gladrow, D. A., Bijma, J., and Zeebe, R. E. Model simulation of the carbonate chemistry in the microenvironment of symbiont bearing foraminifera. *Marine Chemistry*, 64(3):181–198, 1999.

Yu, J., Menviel, L., Jin, Z., Thornalley, D., Barker, S., Marino, G., Rohling, E., Cai, Y., Zhang, F., Wang, X., et al. Sequestration of carbon in the deep Atlantic during the last glaciation. *Nature Geoscience*, 2016.

Yu, J. and Elderfield, H. Benthic foraminiferal B/Ca ratios reflect deep water carbonate saturation state. *Earth and Planetary Science Letters*, 258(1): 73–86, 2007.

Yu, J., Day, J., Greaves, M., and Elderfield, H. Determination of multiple element/calcium ratios in foraminiferal calcite by quadrupole ICP-MS. *Geochemistry, Geophysics, Geosystems*, 6(8), 2005.

Yu, J., Elderfield, H., Greaves, M., and Day, J. Preferential dissolution of benthic foraminiferal calcite during laboratory reductive cleaning. *Geochemistry, Geophysics, Geosystems*, 8(6), 2007a.

Yu, J., Elderfield, H., and Hönisch, B. B/Ca in planktonic foraminifera as a proxy for surface seawater pH. *Paleoceanography*, 22(2), 2007b.

Yu, J., Elderfield, H., and Piotrowski, A. M. Seawater carbonate ion-δ^{13}C systematics and application to glacial-interglacial North Atlantic ocean circulation. *Earth and Planetary Science Letters*, 271(1):209–220, 2008.

Yu, J., Broecker, W. S., Elderfield, H., Jin, Z., McManus, J., and Zhang, F. Loss of carbon from the deep sea since the Last Glacial Maximum. *Science*, 330(6007):1084–1087, 2010a.

Yu, J., Foster, G. L., Elderfield, H., Broecker, W. S., and Clark, E. An evaluation of benthic foraminiferal B/Ca and δ^{11} B for deep ocean carbonate ion and pH reconstructions. *Earth and Planetary Science Letters*, 293(1): 114–120, 2010b.

Yu, J., Anderson, R. F., Jin, Z., Rae, J. W., Opdyke, B. N., and Eggins, S. M. Responses of the deep ocean carbonate system to carbon reorganization during the Last Glacial-interglacial cycle. *Quaternary Science Reviews*, 76: 39–52, 2013.

Yu, J., Anderson, R. F., Jin, Z., Menviel, L., Zhang, F., Ryerson, F. J., and Rohling, E. J. Deep South Atlantic carbonate chemistry and increased interocean deep water exchange during last deglaciation. *Quaternary Science Reviews*, 90:80–89, 2014.

Žarić, S., Donner, B., Fischer, G., Mulitza, S., and Wefer, G. Sensitivity of planktic foraminifera to sea surface temperature and export production as

derived from sediment trap data. *Marine Micropaleontology*, 55(1):75–105, 2005.

Zeebe, R. E. and Sanyal, A. Comparison of two potential strategies of planktonic foraminifera for house building: Mg^{2+} or H^+ removal? *Geochimica et Cosmochimica Acta*, 66(7):1159–1169, 2002.

Zeebe, R. E. and Wolf-Gladrow, D. A. *CO_2 in seawater: equilibrium, kinetics, isotopes*. Number 65. Gulf Professional Publishing, 2001.

Zeebe, R. E., Bijma, J., and Wolf-Gladrow, D. A. A diffusion-reaction model of carbon isotope fractionation in foraminifera. *Marine Chemistry*, 64(3): 199–227, 1999.

Zeebe, R. E., WolfâĂŘGladrow, D. A., Bijma, J., and Hönisch, B. Vital effects in foraminifera do not compromise the use of $\delta^{11}B$ as a paleoâĂŘpH indicator: Evidence from modeling. *Paleoceanography*, 18(2):21–1, 2003.

Appendix

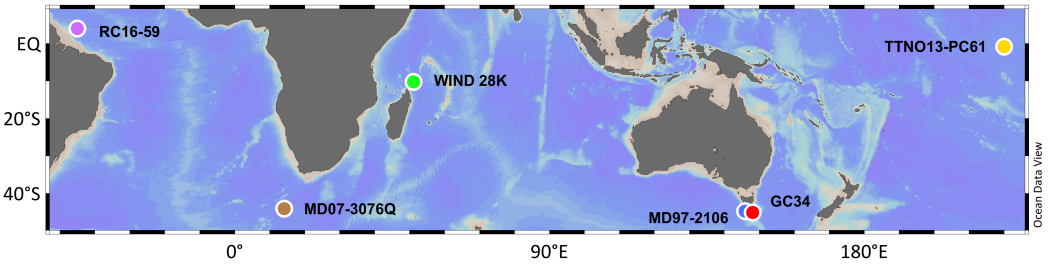

Figure 7-1: Locations of cores mentioned in discussion in Chapter 6.

Table A1: Core-top B/Ca in four species from three depth transects.

Core	planktonic foraminiferal B/Ca (μmol/mol)			
	G. ruber (w)	*G. sacculifer* (w/o sac)	*N. dutertrei*	*P. obliquiloculata*
		Ontong Java Plateau		
1BC3	115	75	72	64
1.5BC33	112	70	66	63
2BC13	106	64	66	62
2.5BC37	102	63	64	
3BC16	93	61	65	
3BC24	106	61	67	66
4BC51		56	69	66
4.5BC53			72	67
5BC54			68	64
5.5BC58			71	
6BC66				69
		Southwestern Indian Ocean		
WIND 20B	138	91	70	71
WIND 11B	111	98	67	
WIND 10B	122	93	67	
WIND 33B	111	74	58	66
WIND 5B	98	87	67	69
WIND 25B	99	83	62	64
WIND 23B		69		65
WIND 13B	97	79	68	74
WIND 28B			56	60
WIND 6B			66	
WIND 12B			66	
		Caribbean Sea		
M35013-3	138	94		
M35014-1	133	96		
M35020-1	139	94		
M35010-2	139	104		
M35004-1	132	89		
M35026-2	132	87		
M35024-6	112	79		

Table A2: Core-top trace element to calcium ratios in *G. ruber* (w) from the meridional Atlantic core tops.

Core-top	Lon.	Lat.	Water depth	B/Ca	Mg/Ca	Sr/Ca	Al/Ca	Mn/Ca
	°E	°N	m	μmol/mol	mmol/mol	mmol/mol	μmol/mol	μmol/mol
VM24-235TW	-19.6	-33.3	3722	93	2.38	1.42	3.6	7.7
VM26-70TW	-17.9	-30.9	3933	87	2.49	1.41	26.5	9.1
V26-68RB	-15.8	-30.4	3660	88	2.89	1.40	6.4	9.6
RC8-27TW	-10.6	-26.2	3678	96	3.36	1.41	2.3	10.6
RC8-19RB	-14.7	-24.3	3640	98	3.36	1.43	2.2	8.3
RC8-18RB	-15.1	-24.1	3977	96	3.18	1.40	10.2	15.4
V16-37TW	-9.0	-21.3	3908	98	2.83	1.41	3.5	12.3
V16-36	-11.4	-19.4	3329	103	2.63	1.39	11.2	64.8
V16-35RB	-15.1	-17.7	3891	94	3.87	1.45	-0.1	18.2
VM22-169TW	-5.7	-16.3	3499	99	2.91	1.44	133.3	8.8
RC16-77	-13.4	-12.7	3400	99	3.43	1.42	8.3	16.0
RC13-210RB	-10.6	-9.1	3658	105	3.66	1.46	20.3	8.0
V22-175	-14.3	-8.8	2950	105	3.26	1.43	1.4	4.9
RC24-21	-10.1	-8.2	3718	110	3.31	1.45	5.1	1.0
RC24-19	-10.0	-7.0	3581	108	3.33	1.44	2.6	1.8
RC24-17RB	-10.2	-5.1	3559	114	3.00	1.43	8.6	3.5
RC24-16RB	-10.2	-5.0	3559	110	3.05	1.44	0.8	2.6
V22-179	-15.7	-4.9	3576	101	2.93	1.42	4.1	7.3
RC24-13	-10.9	-3.7	3921	121	2.93	1.41	11.1	5.8
V26-100	-34.7	-1.6	4308	110	3.29	1.44	0.8	116.4
V12-79RB	-11.8	-1.5	3823	111	3.19	1.43	2.9	68.5
V30-40RB	-23.2	-0.2	3706	109	3.35	1.43	8.2	8.0
VM27-181RB	-25.5	0.1	3601	109	3.54	1.44	1.7	13.4
VM25-50TW	-42.8	0.2	3749	118	3.90	1.45	13.0	12.5
RC13-189RB	-30.0	1.9	3233	122	3.93	1.45	2.6	19.9
G1504RB	-31.3	2.3	2980	119	3.75	1.47	5.0	10.1
VM25-60RB	-34.8	3.3	3749	104	3.92	1.44	16.2	21.1
KNR110-75GGC	-43.4	4.3	3063	118	4.10	1.47	0.6	1.7
KNR110-71GGC	-43.7	4.4	3164	123	4.23	1.48	0.8	1.3
V22-188	-20.9	4.7	2600	118	3.38	1.44	13.3	14.8
K110-58RB	-43.0	4.8	4341	108	3.73	1.46	21.2	4.3
KNR110-91GGC	-43.3	4.8	3810	117	3.97	1.49	1.0	1.3
V20-234	-33.0	5.3	3133	116	3.86	1.48	1.8	7.8
RC25-35RB	-46.7	5.5	3616	120	3.99	1.49	2.3	4.3
VM22-26TW	-41.3	8.7	3720	112	3.65	1.46	43.3	10.4
V16-203RB	-39.9	9.4	4158	108	3.73	1.47	3.2	124.3
VM32-67RB	-42.5	11.3	4082	106	3.27	1.42	1.9	11.5
V25-44TWT	-45.2	11.5	4049	113	3.17	1.44	3.9	23.0
VM16-22RB	-45.8	16.4	3948	107	3.97	1.43	50.3	13.2
G4420-1RB	-46.5	16.5	2763	116	3.67	1.41	15.0	3.7

Table A2: Core-top trace element to calcium ratios in *G. ruber* (w) from the meridional Atlantic core tops, continued.

Core-top	Lon.	Lat.	Water depth	B/Ca	Mg/Ca	Sr/Ca	Al/Ca	Mn/Ca
	°E	°N	m	μmol/mol	mmol/mol	mmol/mol	μmol/mol	μmol/mol
G4421-2RB	-46.0	17.0	3176	117	3.80	1.43	0.4	7.5
V16-21RB	-48.4	17.3	3975	104	3.84	1.43	13.4	98.9
V10-90	-47.1	23.0	4149	114	3.94	1.44	1.4	187.7
VM16-206RB	-46.5	23.3	3733	119	4.24	1.43	17.1	41.5
V10-93RB	-47.5	24.2	3574	111	4.18	1.47	10.0	42.5
VM20-244TWT	-48.3	26.0	3953	112	3.98	1.44	1.4	7.6
VM25-17RB	-46.3	26.6	3983	104	4.04	1.45	3.4	15.9
VM22-219TW	-43.6	27.9	2582	99	3.97	1.45	1.8	3.0
VM19-308TW	-41.4	29.0	3197	107	3.52	1.46	2.8	6.8
VM27-261TW	-36.0	31.4	3253	94	3.03	1.43	11.7	11.4
V17-165RB	-41.9	32.8	3924	109	2.81	1.42	2.6	11.2
V27-161	-14.0	33.6	4446	103	2.35	1.44	3.2	1.4
V27-263RB	-40.9	35.0	3704	110	3.02	1.42	5.6	14.8
VM4-8RB	-33.1	37.2	1697	101	2.77	1.44	1.7	3.2
V30-96RB	-33.1	40.0	3188	104	2.61	1.43	4.3	58.9
VM30-97TW	-32.9	41.0	3371	110	2.21	1.44	20.8	4.9
VM29-178RB	-25.2	42.9	3448	98	2.10	1.36	12.3	9.1

Table A3: Trace element to calcium ratios in *G. sacculifer* (w/o sac) from the meridional Atlantic core tops.

Core-top	Lon.	Lat.	Water depth	B/Ca	Mg/Ca	Sr/Ca	Al/Ca	Mn/Ca
	°E	°N	m	μmol/mol	mmol/mol	mmol/mol	μmol/mol	μmol/mol
VM24-235	-19.6	-33.3	3722	82.1	2.347	1.337	4.9	8.6
VM26-70	-17.9	-30.9	3933	85.2	2.855	1.360	8.2	23.5
V26-68	-15.8	-30.4	3660	81.0	2.804	1.322	24.7	19.9
RC8-27	-10.6	-26.2	3678	85.3	2.978	1.377	5.1	14.4
RC8-23	-12.77	-25.15	3338	86.6	2.972	1.365	4.3	14.8
RC8-19	-14.70	-24.30	3640	84.2	3.198	1.367	2.8	12.8
V16-37	-8.95	-21.33	3908	87.4	2.790	1.336	1.4	16.6
V16-36	-11.43	-19.37	3329	91.3	2.707	1.358	2.0	68.8
V16-35	-15.10	-17.65	3891	84.1	3.049	1.370	0.8	22.0
VM22-169	-5.7	-16.3	3499	82.2	2.710	1.364	13.9	9.3
RC16-77	-13.40	-12.70	3400	83.4	2.931	1.361	3.4	22.3
VM26-55	-15.6	-11.6	3457	78.9	2.627	1.329	3.6	11.2
VM22-174	-12.8	-10.1	2630	84.3	3.316	1.371	11.8	12.0
RC13-210	-10.60	-9.13	3658	88.1	3.168	1.371	7.1	15.8
V22-175	-14.28	-8.77	2950	83.8	3.343	1.382	5.4	15.5
RC24-21	-10.12	-8.18	3718	84.3	2.975	1.338	3.3	3.0
RC24-19	-10.00	-7.02	3581	83.9	3.068	1.367	1.7	5.1
RC11-17	-33.43	-5.28	4490	88.4	3.895	1.369	8.1	
RC24-16	-10.18	-5.03	3559	80.0	2.957	1.337	2.5	1.8
RC24-15	-10.87	-4.10	3504	80.8	2.677	1.322	11.5	17.1
VM20-233	-39.0	-2.0	3294	82.7	3.641	1.365	6.7	34.5
RC24-08	-11.9	-1.3	3882	85.8	2.637	1.335	10.3	19.6
V30-40	-23.15	-0.20	3706	82.1	2.988	1.356	14.9	10.0
V30-40	-23.2	-0.2	3706	83.6	3.026	1.345	7.5	10.1
VM25-50	-42.77	0.20	3749	84.3	3.841	1.379	3.6	8.1
VM25-59	-33.5	1.4	3824	83.5	3.567	1.364	3.8	14.2
RC13-190	-25.43	1.78	3797	75.7	3.206	1.374	9.6	18.5
VM22-31	-32.5	1.9	3436	82.0	3.669	1.388	8.6	13.4
VM20-230	-35.9	2.0	3884	84.5	3.710	1.363	8.0	12.8
GEOB1503-2	-30.6	2.3	2298	85.8	3.591	1.382	9.6	7.1
KNR110-71	-43.7	4.4	3164	90.8	3.633	1.407	7.1	3.1
KNR110-50	-43.2	4.9	3995	79.5	3.821	1.382	5.6	4.4
GEOB4416	-45.1	5.7	3903	79.6	3.693	1.400	8.9	8.9
GEOB4413	-44.2	6.1	4291	74.1	3.398	1.351	13.1	6.0
VM22-26	-41.3	8.7	3720	84.6	3.199	1.377	9.2	11.5
VM16-203	-39.87	9.35	4158	79.5	3.350	1.380	7.1	92.8
VM32-67	-42.50	11.28	4082	80.8	3.134	1.352	2.8	12.3
V25-44	-45.15	11.50	4049	85.0	3.324	1.384	17.8	50.1
V22-202	-21.2	14.4	4310	82.9	2.354	1.326	18.5	32.2
GEOB4420	-46.5	16.5	2763	93.0	3.863	1.395	2.8	5.2

Table A2: Core-top trace element to calcium ratios in *G. ruber* (w) from the meridional Atlantic core tops, continued.

Core-top	Lon.	Lat.	Water depth	B/Ca	Mg/Ca	Sr/Ca	Al/Ca	Mn/Ca
	°E	°N	m	μmol/mol	mmol/mol	mmol/mol	μmol/mol	μmol/mol
GEOB4421	-46.0	17.0	3176	94.4	3.670	1.350	1.3	5.3
GEOB4424	-44.0	18.2	4779	82.9	3.374	1.371	6.8	3.9
VM14-2	-49.4	20.7	4171	93.2	3.352	1.352	12.9	28.6
VM10-89	-43.8	23.0	3523	91.5	3.199	1.362	32.2	127.7
VM16-206	-46.48	23.33	3733	97.4	3.689	1.371	3.6	41.8
VM10-93	-47.47	24.20	3574	103.9	3.843	1.383	2.1	66.6
VM20-244	-48.3	26.0	3953	91.5	3.572	1.364	13.1	12.6
VM25-17	-46.3	26.6	3983	101.3	3.692	1.391	5.1	25.5
VM22-219	-43.6	27.9	2582	97.9	3.644	1.358	6.6	8.3
VM19-308	-41.4	29.0	3197	94.4	3.266	1.383	0.8	18.1
VM27-261	-36.0	31.4	3253	93.9	3.090	1.331	9.8	14.3
VM17-165	-41.90	32.75	3924	99.7	3.167	1.381	27.1	15.6
V27-161	-14.0	33.6	4446	93.8	2.338	1.374	110.4	1.3
V27-263	-40.9	35.0	3704	92.1	2.895	1.376	13.3	19.2
VM4-8	-33.1	37.2	1697	93.8	2.392	1.391	0.7	6.4
VM23-12	-45.3	38.3	5205	89.0	2.490	1.357	20.2	15.5
VM30-96	-33.13	39.95	3188	86.4	2.550	1.382	6.2	82.3
VM30-97	-32.93	41.00	3371	98.2	2.624	1.379	4.6	16.5
V29-177	-25.7	41.5	3391	84.3	2.647	1.368	3.7	18.8
VM29-178	-25.15	42.85	3448	81.7	2.172	1.357	3.3	12.7

Table A4: *C. wuellerstorfi* B/Ca in GC34.

Depth (mid)	Age	B/Ca
cm	kyr	μmol/mol
1	7.5	157
4	7.8	151
6	8.0	159
8	8.2	153
9	8.4	156
14	8.9	161
16	9.1	160
19	9.4	167
22	10.3	152
24	11.0	147
27	12.1	164
28	12.5	147
32	13.9	145
34	14.6	139
36	15.2	137
38	15.9	143
40	16.6	141
42	17.3	130
45	18.3	137
50	20.0	147
54	21.4	140
57	22.4	147
61	23.8	137
65	25.1	141
69	26.5	136
73	27.8	148
74	28.2	141
77	29.1	141
78	29.4	140
86	32.0	161
97.5	35.7	166
105.5	38.3	158
113.5	40.8	163
122	43.6	160
129.5	46.0	157
134.5	48.2	163
138.5	50.1	171
145.5	53.3	158
149.5	55.2	156
153.5	57.1	159
158.5	59.4	148

Table A4: *C. wuellerstorfi* B/Ca in GC34, continued.

Depth (mid)	Age	B/Ca
cm	kyr	μmol/mol
162.5	61.3	154
166.5	62.6	145
170.5	64.0	152
174.5	65.4	142
181.5	67.8	156
189.5	70.5	154
197.5	73.3	151
202.5	75.0	150
207	76.6	156
212.5	78.5	157
221	81.6	163
230.5	84.9	158
234.5	86.3	150
241.5	89.4	150
251	93.5	148
256	95.7	148
266	100.1	152
271	102.3	162
276	104.4	154
281	106.5	157
286	108.5	157
291	110.4	145
296	112.4	151
301	114.3	155
305.5	116.1	162
309.5	117.7	157
313.5	119.3	153
318.5	121.3	146
325.5	124.1	153
333.5	127.4	150
345.5	132.0	157
349.5	133.3	158
357.5	135.9	160
362.5	137.6	156
370.5	140.2	156
377.25	142.4	159
382.5	144.1	151
390.5	146.7	166
397.5	149.0	158
406.5	152.0	156
421.5	156.9	161
430.5	159.9	157

Table A4: *C. wuellerstorfi* B/Ca in GC34, continued.

Depth (mid)	Age	B/Ca
cm	kyr	μmol/mol
438.5	162.5	161
446.5	165.1	151
450.5	166.4	150
458.5	169.0	152
466.5	171.7	161
470.5	173.0	164

Table A5: *C. wuellerstorfi* B/Ca in MD97-2106.

Depth (mid)	Age	B/Ca
cm	kyr	μmol/mol
5	2.4	176
15	3.5	169
25	4.5	177
35	5.6	164
44	6.5	161
55	7.7	174
65	8.8	173
75	9.7	166
85	10.5	176
95	11.4	154
105	12.2	168
113	12.9	164
125	13.9	171
135	14.7	169
145	15.4	163
155	16.0	164
165	16.6	166
175	17.2	167
185	17.8	162
195	18.4	157
205	19.2	161
215	21.0	156
225	22.7	151
225	22.7	154
235	24.4	163
245	26.1	164
255	27.7	148
255	27.7	153
265	29.0	169
275	30.2	170
314	35.2	164
334	37.8	174
374	42.9	169
405	46.8	167
414	48.0	173
435	50.7	169
445	51.9	171
494	58.2	173
515	60.9	169
524	61.8	164

Table A5: *C. wuellerstorfi* B/Ca in MD97-2106, continued.

Depth (mid)	Age	B/Ca
cm	kyr	μmol/mol
535	62.7	168
555	64.4	162
574	66.1	167
595	67.9	160
614	69.5	156
634	71.2	178
655	73.0	175
655	73.0	178
674	74.7	167
684	75.7	162
694	76.8	158
704	77.8	163
714	78.8	176
734	80.8	176
754	82.8	171
764	83.8	172
784	85.8	167
794	86.8	173
813	88.5	161
833	90.2	170
853	91.9	173
872	93.6	172
882	94.4	171
892	95.4	163
892	95.4	168
932	99.5	155
974	103.7	152
1034	111.6	160
1044	113.1	173
1075	117.6	172
1084	119.0	177
1153	130.2	176
1233	140.9	168
1243	142.3	171
1262	144.8	161
1273	146.2	169
1283	147.6	174
1293	148.9	174
1333	154.2	175
1343	155.5	167
1375	159.8	159